X-ray Study of Temperature and Metallicity in Groups and Clusters of Galaxies with *Suzaku*

Kosuke Sato

Department of Physics, Tokyo Metropolitan University
1-1 Minami-Ohsawa, Hachioji, Tokyo 192-0397, Japan

February 2007

Abstract

Clusters of galaxies are the largest structure among the gravitationally bound systems in the universe, which contain 10–1000 galaxies and extend over spatial scales of $\sim 10^{25}$ cm, while groups of galaxies are smaller systems consisting of several galaxies. Clusters and groups of galaxies contain X-ray emitting hot plasma (ICM) with typical temperatures of a few times 10^7 K. Metal abundances of ICM give us important information in understanding the chemical history and the evolution process of clusters. Metals in the ICM are mainly produced by supernovae (SN) in galaxies which are classified into Type Ia (SN Ia) and Type II (SN II). Si, S and Fe are synthesized in both SN Ia and SN II, while alpha elements such as O, Ne, and Mg are mainly in SN II, which are explosions of massive stars with initial mass above ~ 10 solar mass.

We studied the properties of the ICM in two groups (HCG 62 and NGC 507) and in two clusters of galaxies (A 1060 and AWM 7) with the X-ray astronomy satellite *Suzaku*. Based on the spatially resolved energy spectra, we obtained precise temperature profiles and metal abundance distributions for various elements. As a result, the ICM temperatures in the observed systems commonly show decrease from the centers to the outskirt regions. The temperature drop from the peak level (taking place at around $\sim 0.1\ r_{\rm vir}$) to the value at $0.3\ r_{\rm vir}$ is typically 30%, which agrees with the results from numerical simulation of cluster formation based on the ΛCDM framework. Metal abundances of Si, S, Fe show significant decrease from the center to the outer, while O and Mg show fairly constant abundance distribution compared with the Fe gradient. These abundance features are commonly observed in both the cD and non-cD systems. Observed metal distribution supports the view that iron and silicon are produced by type Ia supernovae with major contributions from the central galaxies, while galactic winds caused by type II supernovae have caused wider distribution of oxygen.

CONTENTS

List of Figures

List of Tables

Chapter 1

Introduction

Clusters of galaxies, being the largest virialized system in the universe, are filled with hot intracluster medium (ICM), which consists of X-ray emitting hot plasma with typical temperatures of a few times 10^7 K. X-ray spectroscopy of the ICM can immediately determine its temperature and metal abundances. The metal abundances of ICM have a lot of information to understand the chemical history and evolution of clusters. A large amount of metals in the ICM are mainly produced by supernovae (SN) in galaxies (Arnaud et al. 1992; Renzini et al. 1993) and are classified roughly as Type Ia (SN Ia) and Type II (SN II). Elements such as Si, S and Fe are synthesized in both SN Ia and SN II, while lighter α elements such as O, Ne, and Mg are mainly produced in SN II, which are explosions of massive stars with initial mass above $\sim 10\ M_{\odot}$. The metals produced in the galaxies are transfered into the ICM by galactic wind and/or ram pressure strippings.

ASCA first measured the distributions of Si and Fe in the ICM (Fukazawa et al. 1998; Fukazawa et al. 2000; Finoguenov et al. 2000; Finoguenov et al. 2001). The derived iron-mass-to-light ratios (IMLR) are nearly constant in rich clusters and decrease toward poorer systems Makishima et al. (2001). Recent observations with *Chandra* and *XMM-Newton* allowed detailed studies of the metals in the ICM. These observations, however, showed abundance profiles of O, Mg, Si and Fe only for the central regions of very bright clusters or groups of galaxies dominated by cD galaxies in a reliable manner (Finoguenov et al. 2002; Fukazawa et al. 2004; Matsushita et al. 2003; Tamura et al. 2003). The abundance profiles of O and Mg, in particular for outer regions of clusters, are still poorly determined, because data from *Chandra* and *XMM-Newton* both show relatively high intrinsic background levels. Tamura et al. (2004) derived IMLR for five clusters within 250 h_{100}^{-1} kpc to be $\sim 0.01\ M_{\odot}/L_{\odot}$, and the oxygen mass within 50 h_{100}^{-1} kpc for several clusters. However, oxygen-mass-to-light ratios (OMLR) for rich clusters are not reliable due to the low emissivity of O_{VII} and O_{VIII} lines in high temperatures. De Grandi & Molendi (2002) and Hayakawa et al. (2006) found that clusters associated with cD galaxies and central cool components showed abundance concentration in the cluster center, while clusters without cD galaxies indicated flatter profiles. The central metallicity enhancement in the cool core clusters were further studied and the excess metals were shown to be supplied from the cD galaxies (De Grandi et al. 2004).

This thesis reports results from *Suzaku* observations of A 1060, AWM 7, HCG 62 and NGC 507 and several other systems. The sample covers from elliptical galaxies to poor clusters, and the targets are suitable to look into the distribution of O in the ICM. Owing to the low-background nature of the *Suzaku* XIS, we are able to measure the temperature and abundance profiles to further outer regions than the previous XMM-Newton measuremetns. We use $H_0 = 70$ km s^{-1} Mpc^{-1}, $\Omega_{\Lambda} = 1 - \Omega_M = 0.73$ in this thesis. Otherwise noted, the solar abundance table is given by Anders & Grevesse (1989),

and errors are 90% confidence level.

Chapter 2

Review of Cluster and Group Structure

2.1 Cluster of Galaxies

Clusters of galaxies are the largest well-defined structures in the universe, with a typical linear dimension of 1-3 Mpc. A cluster consists of 100-1000 member galaxies, ranging from the cD galaxy, which belongs to the most luminous galaxy class in the universe, to dwarf galaxies.

In the early 1930s, Zwicky measured velocities of member galaxies in the Coma cluster, and found that they are traveling too fast ($\sim$ 1000 km s^{-1} in average) to be gravitationally bound unless the total mass in the cluster greatly exceeds that expected from optical luminosities of member galaxies. This is the first evidence for large-scale dark matter. Through sub sequent measurements velocity dispersions of rich clusters were found typically to be 700 km s^{-1}, implying mass-to-light ratios of $M_{total}/L_{total} \sim 150 - 400\ M_{\odot}/L_{\odot}$ (e.g., Peebles 1993). Here M_{total} and L_{total} are the total dynamical mass and the total optical luminosity, respectively. In contrast, individual galaxies typically have mass-to-light ratios of 10 $M_{\odot}/L_{\odot}$ in their luminous central regions.

With cosmic X-ray observation, witch started in the 1960s, clusters were found to be the most luminous class of X-ray sources in the universe after some types of active galactic nuclei (AGNs). The X-ray emission originates from the intracluster medium (ICM), a hot ($10^7 - 10^8$ K) and low density ($10^{-4} - 10^{-2}$ cm^{-3}) plasma in the intracluster space. Extensive observation with previous X-ray satellites such as *HEAO-1*, *Einstein*, *Ginga*, *ROSAT*, *ASCA*, *Chandra* and *XMM-Newton* provided measurements of densities and temperatures of the ICM. These results implied that the mass if the ICM is comparable to, or even greater than that of the stellar component in member galaxies. Characteristic emission lines from ionized heavy elements (mainly from iron) were detected in the X-ray spectra of clusters. The implied sub-solar metallicity of the ICM indicates that the ICM is a mixture of the primordial gas and that reprocessed in the stellar interior. Moreover, X-ray observations of the ICM have provided independent and more accurate measurements of the total mass, and hence of the dark matter, in clusters of galaxies. A rough agreement between the optical and X-ray measurements of the total cluster mass supports the basic assumption that the ICM is in hydrostatic equilibrium. According to a contemporary consensus, about $5-10$ % of a cluster mass is in the stellar component, another $10-20$ % is in the ICM, and the rest is in dark matter.

2.2 Group of Galaxies

Groups of galaxies are smaller systems than clusters of galaxies, with a typical group containing only a few luminous galaxies, and have a scale of 250 $\sim$ 500 kpc. They are also mainly identified on optical plates. At present, the hierarchical clustering scenario is widely supported, as it is naturally expected from the cold dark matter model. Also, the fact that the galaxies at redshifts of ~ 5 have been observed, whereas the most distant observed clusters are at $z \sim 1$, indicating that the smaller systems have been formed earlier. According to the bottom-up scenario, large-scale structures of the universe have been formed from infinitesimally small density perturbations at the early universe through the gravitational interaction. A number of numerical simulations for the structure formation show hierarchical clustering of the hot gas and dark matter, and indicate that the clusters are formed through subcluster mergers and/or acquisition of groups of galaxies. Groups should thus provide useful probes of structure formation in the universe, yet their physical nature is still highly unclear [see Hickson (1997) and Mulchaey (2000) for reviews].

Hickson (1982) cataloged 100 compact groups (Hickson's Compact Groups; HCGs), which form one of the best studied catalogs among the groups searched by Palomer Observatory Sky Survey red points. A group is called "compact" when there are several galaxies within a limited radius (Hickson 1982), and called "loose" when there are not. According to Hickson (1982), a compact group is defined by the following criteria: $N \geq 4$, $\theta_{\rm N} \geq 3\theta_{\rm G}$, $\bar{\mu_{\rm G}} < 26.0$, where N is the total number of galaxies within 3 mag of the brightest one, $\bar{\mu_{\rm G}}$ is the total magnitude of these galaxies per arcsec^{2}a averaged over the smallest circle (angular diameter $\theta_{\rm G}$) that contains their geometric centers, and $\theta_{\rm N}$ is the angular diameter of the largest concentric circle that contains no other galaxies within this magnitude range or brighter. The radius is about 100 kpc. The short crossing times implied for HCGs suggest either they are chance alignments of unrelated galaxies within looser systems (Mamon 1986; Walke & Mamon 1989) or short-lived ($\sim$ 1 Gyr) bound configurations within loose groups (Diaferio et al. 1994; Governato et al. 1996).

The observation of clusters/groups began in the optical band historically. We can understand this immediately, since it is defined by the distribution of member galaxies which are identified in the optical band. However, the discovery that many groups are X-ray sources has provided considerable new insight. X-ray observations indicate that about half of all poor groups are luminous X-ray sources. The diffuse X-ray emission can be interpreted in the following way. For example, we assume a group which is concentrated in a sphere of radius $\sim$ 250 kpc with a mass of $10^{13} M_{\odot}$. If this system is under hydrostatic equilibrium, the kinetic energy is approximately equal to the gravitational potential energy. This gives an emission in the typical X-ray energy band, if we calculate the temperature corresponding to this energy. X-ray analysis provides a powerful tool to measure the temperature, the metal abundance, and the gravitational mass in groups.

In many cases, the X-ray emission is extended, often beyond the optical extent of the group. The spatial and spectral properties of the X-ray emission suggest the entire volume of a group is filled with hot, low-density ($\sim 10^{-3}$ cm^{-3}) gas. The derived gas temperatures are in the range 0.3 $\sim$ 1.8 keV, which is roughly what is expected given the range of observed velocity dispersions for groups (Ponman et al. 1996; Mulchaey et al. 1996; Mulchaey & Zabludoff 1998; Helsdon & Ponman 2000). X-ray hot gas component is referred to as the intragroup medium, in analogy with the diffuse X-ray emitting intracluster medium found in rich clusters (Forman & Jones 1982). The total kinetic energy contained in a group becomes $\sim 10^{61-62}$ erg, so that it is one of the most energetic objects in the universe.

2.3 Scenario of the evolution in the universe

The evolution of the universe is divided broadly into the structure formation and the chemical evolution. The former is dynamical processes of celestial objects, and the latter represents the production of heavy elements in galaxies. Clusters of galaxies are regarded as useful probes to study both evolutions by several reasons: 1) since the dynamical time-scale of clusters is close to Hubble time, clusters retain the cosmological initial conditions well, 2) clusters can be approximated that they consist of dark matter, hot gas, and galaxies, and also the shape is almost spherical, thus they are easy to deal with, 3) though a part of metals produced in galaxies run away into ICM, they do not escape from clusters. We can thus obtain the total metal abundance without omission. In order to obtain the properties of clusters, X-ray observations are particularly suited, because the X-ray-emitting gas gives us the physical parameters such as temperature, mass, and metal abundance.

2.4 Observational studies of clusters and gourds

2.4.1 X-ray emission process

The X-ray spectrum emitted from an ionized plasma of the low density ($\sim 10^{-3}$ cm^{-3}) ICM is described with a combination of thermal bremsstrahlung (free-free) emission and line emission from heavy elements. In the temperature range of typical cluster (1 keV$<$ $kT < 10$ keV) the total emission is dominated by the free-free emission if the abundance of heavy elements does not exceed the solar abundance by very much. The emissivity of the free-free emission at a frequency ν from a hot plasma with an electron temperature of T_g is given by

$$\epsilon_\nu = \frac{2^5\pi e^6}{3m_e c^3}\left(\frac{2\pi}{2m_e k}\right)^{1/2} n_e \sum_i Z_i^2 n_i g_{ff}(Z, T_g, \nu) \times T_g^{-1/2} \exp(-h\nu/kT_g) \quad (2.1)$$

$$= \Lambda(T, Z, \nu) n_e^2 \quad (2.2)$$

where Z_i and n_i are the charge and number density of the ion i, respectively, and n_e is the electrons number density (e.g. Rybicki & Lightman 1979). The Gaunt factor is a correction factor for quantum mechanical effects and is approximately $g_{ff} \sim 0.9(h\nu/kT)^{-0.3}$. The emissivity in a given bandpass, $\nu_1 < \nu < \nu_2$, is then

$$\epsilon^{ff} = \int_{\nu_1}^{\nu_2} \epsilon_\nu^{ff} d\nu \quad (2.3)$$

$$= \Lambda(T, Z) n_e^2. \quad (2.4)$$

The $\Lambda(T, Z)$ is the cooling function, with T and Z representing the plasma temperature and the heavy element abundance, respectively. Figure 2.1 shows the cooling function as a function of the plasma temperature assuming the cosmic abundances. The contribution of the bremsstrahlung continuum to Λ increases as $\propto T^{1/2}$.

We can obtain the total X-ray luminosity by integrating equation 2.4. It is useful to define the emission integral as

$$EI = \int n_e^2 dV, \quad (2.5)$$

where V is the volume of the cluster. If we assume that th ICM has a spatially-uniform temperature and abundance in the volume V, and that the ICM density is constant over

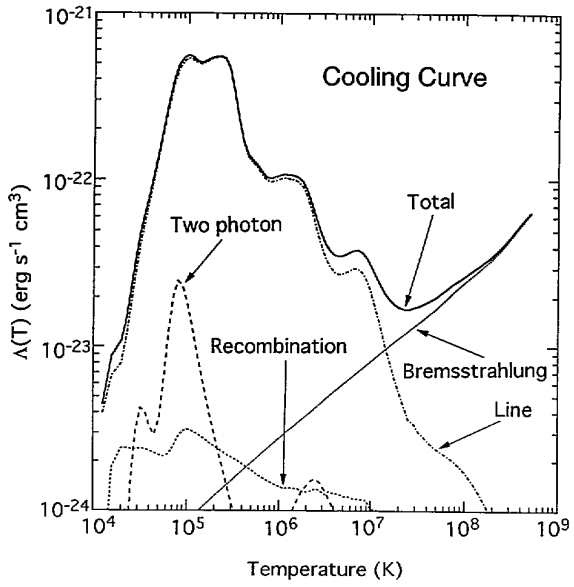

Fig. 2.1: Temperature dependence of the cooling function with its components for optically thin plasma containing cosmic abundances of elements (Gehrels & Williams 1993).

the projected sky area S, then the luminosity L_X is given as

$$\begin{aligned} L_X &= \int \epsilon^{ff} dV & (2.6)\\ &= EI \times \Lambda(T, Z) & (2.7)\\ &= EM \times S \times \Lambda(T, Z). & (2.8) \end{aligned}$$

The EM is the emission measure defined as

$$EM = \int n_e^2 dl, \tag{2.9}$$

where l is the depth of the plasma along the line of sight. The emission integral determines the normalization of the spectrum, and the shape of the spectrum depends only on the temperature T and the heavy element abundance Z, and EI (or EM if S is known) from the observed X-ray spectra.

Emission of atomic lines becomes significant when the ICM temperature falls below a few keV. Since the temperature of the ICM is of the same order as the K-shell ionization potentials of heavy elements such as O, Ne, Mg, Si, S and Fe, these elements become mainly He/H-like ions and are completely ionized. These ions are collisionally excited, and then emit their resonance K-lines. In lower temperature clusters, in which Fe ions are not only He-like but also of a low ionization status, the spectrum exhibits resonance L-lines at $\sim$ 1 keV. We show predicted X-ray spectra for various temperature in figure 2.2.

The emission lines and continuum spectra from the ionization equilibrium plasma have been calculated by various authors, e.g. Mewe et al. (1985); Mewe et al. (1986). In this thesis, we use the APEC code, which is based on the model calculations of Smith et al. (2001), in the XSPEC data analysis Package.

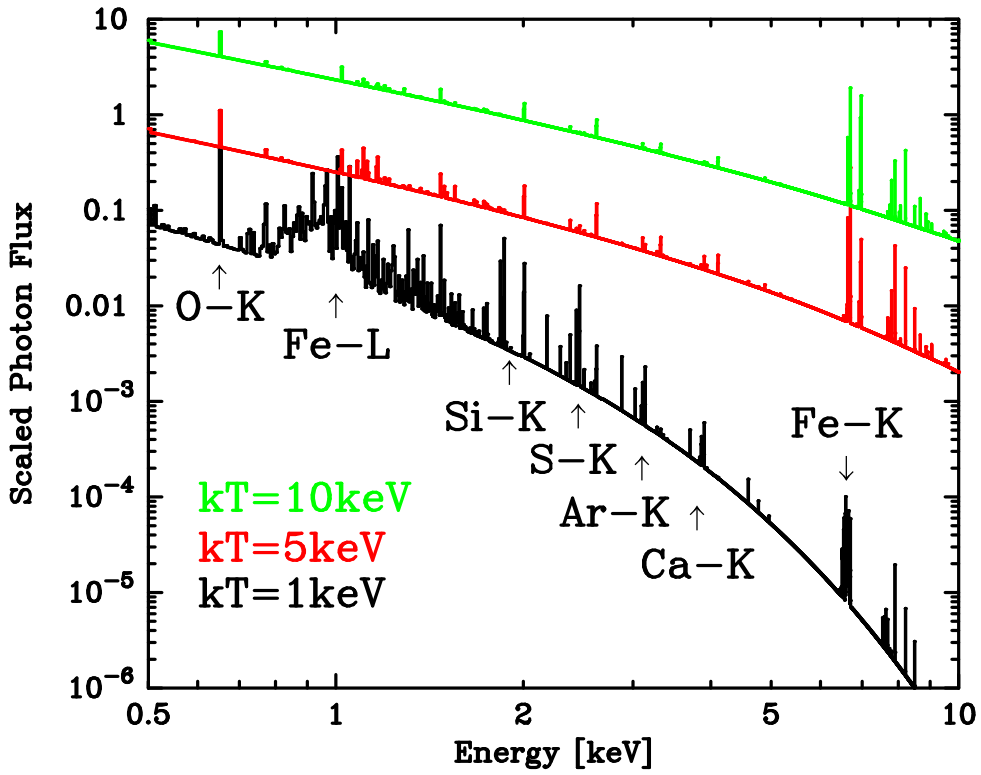

Fig. 2.2: Calculated X-ray spectra from optically thin hot plasmas with various temperatures. The MEKAL plasma emission code is used, assuming a metal abundance of 0.3 solar. Vertical scale is arbitrary.

2.4.2 Morphology

The X–ray morphology of clusters is classified by Jones & Forman (1984) as shown in table 2.1. Roughly speaking, there are two types of the X-ray morphology. One type has a circularly symmetric X-ray emission sharply centered on the cD galaxy (XD type), and the other type does not have such a sharp X-ray peak associated with any galaxies (nXD typ). Moreover, either type is subdivided into two groups; so-called early systems and late systems. Early systems have a high X-ray luminosity and a low fraction of spiral galaxies, and they are thought to be dynamically evolved according to their galaxy distribution. Rich clusters are typical early systems. Late systems have a low X-ray luminosity and a high fraction of spiral galaxies, and a thought to be dynamically young. Poor clusters are examples of typical late systems.

2.4.3 Temperature structure

Recent experiments made it possible to obtain spatially resolved spectra of clusters, and are revealing the temperature structure. Markevitch et al. (1998) analyzed spatially resolved X-ray spectra of 30 nearby clusters with ASCA and ROSAT. They reported that most of them show a similar temperature decline at large radii, and about a half of the sample shows signs of merging. Recent measurements of 13 nearby relaxed clusters (excluding A 1060) with *Chandra* by Vikhlinin et al. (2005) showed that the temperature reaches at a peak at $r \sim 0.15\ r_{180}$ and then declines to ~ 0.5 of its peak value at $r \simeq 0.5\ r_{180}$, in good agreement with Markevitch et al. (1998). They also found that clusters whose temperature profiles peak at $r < 70$ kpc $\ll 0.15\ r_{180}$ (MKW4 and RX

nXD	XD
Large core radius ($\sim$400–800 kpc)	Small core radius ($<$300 kpc)
	Central, dominant galaxy
Early system—A1367:	Early systems—Virgo, A262:
Low X-ray luminosity ($<10^{44}$ ergs s^{-1})	Low X-ray luminosity ($<10^{44}$ ergs s^{-1})
Cool X-ray gas (1–4 keV)	Cool X-ray gas (1–4 keV)
No central cooling flows	Central cooling flows
X-ray emission around galaxies	X-ray emission from halo of central galaxy
High spiral fraction ($>40\%$)	High spiral fraction ($>40\%$)
Low central galaxy density	Low central galaxy density
Irregular cluster structure	Irregular cluster structure
Evolved systems—Coma, A2255, A2256:	Evolved systems—A85, A1795, Perseus:
High X-ray luminosity ($>10^{44}$ ergs s^{-1})	High X-ray luminosity ($>10^{44}$ ergs s^{-1})
Hot X-ray gas ($\geq$6 keV)	Hot X-ray gas ($\geq$6 keV)
No central cooling flows	Central cooling flows
High velocity dispersion	High velocity dispersion
Low spiral fraction ($\lesssim 20\%$)	Low spiral fraction ($\lesssim 20\%$)
High central galaxy density	High central galaxy density
Regular, symmetric cluster structure	

Table 2.1: Classifications of galaxies based on the X-ray morphology by Jones & Forman (1984).

J1159+5531) shows a larger peak-temperature-ratio of $T_{\rm p}/\langle T\rangle \sim 1.35$. Determination of the dynamical structure of the clusters can constrain cosmological models because clusters should be dynamically more relaxed in a low-density universe than in a high-density one (e.g. Richstone et al. (1992)). Comparing the temperature profiles with the results of cluster hydrodynamic simulations, Markevitch et al. (1998) found the low Ω (< 0.3) cosmological models are suitable to explain the temperature profiles.

For example, we cite two instances of 2-dimensional temperature structures of the Coma cluster and A754. Figure 2.3 shows color-coded temperature map of the Coma cluster obtained from ASCA (Watanabe et al. 1999) and *XMM-Newton* (Arnaud et al. 2000). The extended north-west region is clearly hotter than the surrounding regions. This result indicates the evidence of a recent merger in the Coma cluster. It is interesting to see no substructure in the X-ray image around the hot region. Hence, the temperature structure gives us much information of merging, which is not given by the morphology only. Note that the Coma cluster also shows that the abundance distribution is almost uniform. This probably mean that the metals in the Coma cluster are mixed by mergers. Figure 2.4 shows temperature map with CXO (Markevitch et al. 2000) and simulated result for A754 (Roettiger et al. 1998). The north small region of substructure shows a hot spot (fig. 2.4 left), which is expected to be due to the shock heating. The numerical simulation for A754 represents quite similar structure of the temperature map.

2.4.4 Metal product and distribution

The existence and distribution of the chemical elements and their isotopes are a consequence of nuclear processes that have taken place in the past in the Big Bang and subsequently in stars and in the interstellar medium where they are still ongoing. These processes have been studied theoretically and observationally. Based on the optical study, the element and star formation history of the universe is derived as shown in figure 2.5 (Madau 1999). The results appear the existence of a decline in the universal metal production rate at the redshift $z < 1$ irrespective of being uncorrected or corrected for dust extinction.

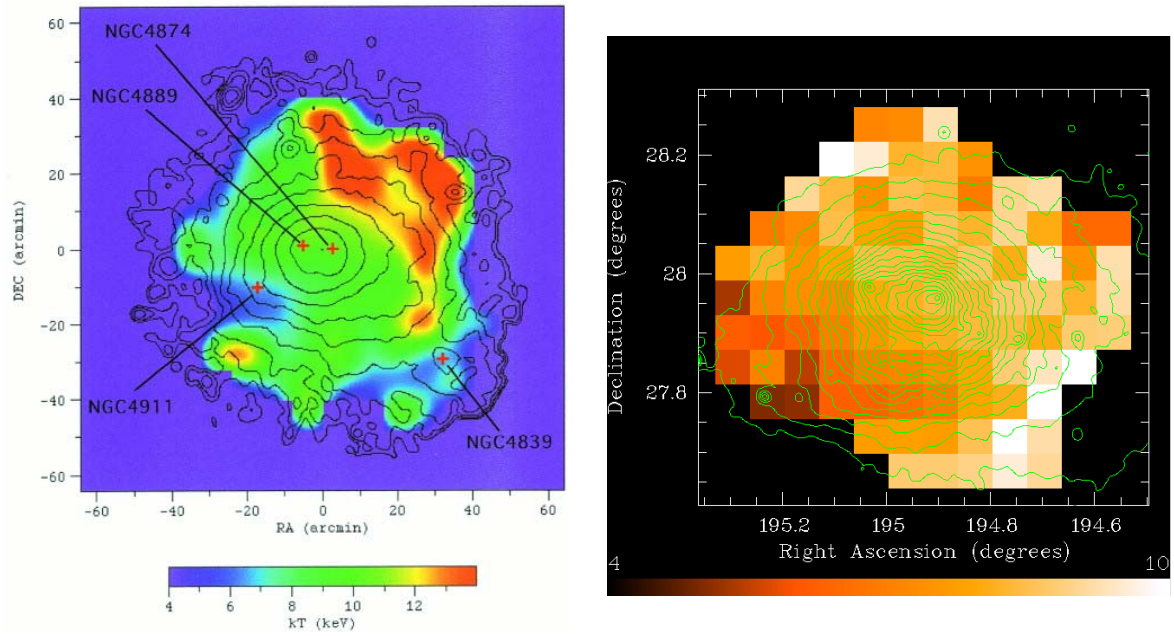

Fig. 2.3: Color coded temperature map of the Coma cluster with ASCA (Watanabe et al. 1999) and *XMM-Newton* (Arnaud et al. 2000).

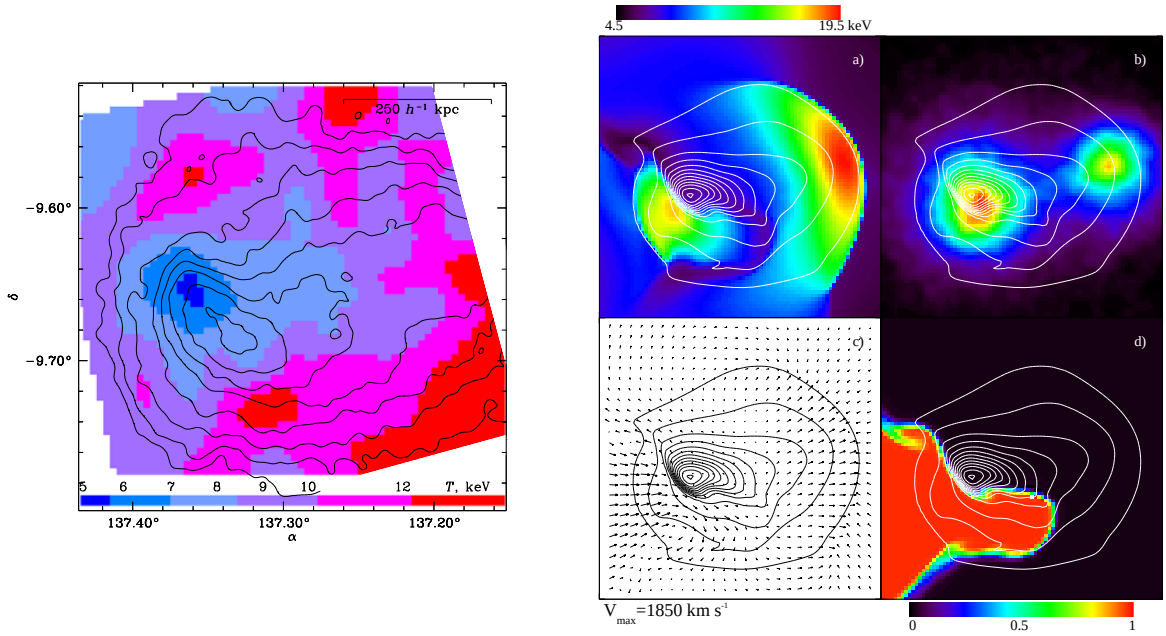

Fig. 2.4: A754 temperature map with CXO (Markevitch et al. 2000) and simulation (Roettiger et al. 1998).

The main source of metal production is supernovae (SN), which are classified roughly into Type Ia and Type II. Type Ia supernovae (SN Ia) are important contributers to iron-group elements in the galaxy. Type Ia SN are the thermonuclear explosions of mass accreting white dwarfs in binary systems and spectroscopically characterized by the lack of H and He and the presence of strong Si lines. Massive stars in the range of 8 to ∼130 $M_\odot$ undergo collapse at the end of their evolution and become Type II and Ib/c SN unless the entire star collapses into a black hole with no mass ejection. Here, SN are classified based on the maximum light spectra as follows. Type II supernovae (SN II) are defined by the presence of hydrogen, which implies that the progenitors are red (or blue) supergiants

keeping their hydrogen-rich envelope. Type Ib supernovae (SN Ib) are characterized by the lack of hydrogen but the presence of prominent He lines, so that their progenitors are Wolf-Rayet (WN) or He stars losing their H-rich envelope in a stellar wind or by Roche lobe overflow in binary systems. Type Ic supernovae (SN Ic) do not show prominent He lines as well as H, which implies that their progenitors have lost even most of He layers to become WC/WO Wolf-Rayet stars or C+O stars in binary systems. Type II SN produce mainly α elements such as O, Ne, Mg, Si, and S. The metal abundances for the elements are given by X-ray spectroscopy of the ICM. Since part of metals are transfered into the ICM by galactic wind or ram pressure stripping, observation of the ICM, not galaxy only, gives total abundance. The observed ratio of Fe to α elements constrains the ratio of Type Ia to Type II and the explosion rate. This enables us to study other essential subjects such as the initial mass function, and star formation rate based on z-evolution. The amount of products from SN Ia and SN II are calculated by Nomoto et al. (1984); Tsujimoto et al. (1995); Thielemann et al. (1996); Iwamoto et al. (1999) in table 2.2. The total amounts of metals produced by SN II's is obtained integrating the yield per star $M^{\rm SNII}_{\rm metal}(M)$ over the stellar initial mass function (IMF) or, equivalently, by the product of the mass-weighted average of yield per star times the total number of SN II's. As usual, for the stellar IMF we assume a power-law,

$$\psi(M) = AM^{-(1+x)} \tag{2.10}$$

where $x = 1.35$, 1.7 corresponds to a Salpeter and Scalco IMF, respectively. Table 2.2 shows a list of nucleosynthesis products in unit of solar from SN II and Ia models, and SN II products are calculated by the average over the mass range from 10 $M_\odot$ to 50 $M_\odot$ assuming a Salpeter IMF.

In order to estimate the amount of metals till now, the SN rate is important for the calculations. Cappellaro et al. (1999) shows the SN rate from 137 SN in a sample of about 10^4 galaxies near $z \sim 0$ (figure 2.3). Combined the value of Table 2.2 and Table 2.3, we can estimate the amount of the metal produced by SN. For example, using SN Ia (W7) model and SN rate in elliptical galaxy, iron is produced 0.749 $M_\odot$ per a SN Ia, which occur 0.18 per 100 years per $10^{10}L^{\rm B}_\odot$,

$$M^{\rm SNIa}_{\rm Fe} = \frac{0.18 \times 0.749 M_\odot \times 1.5 \times 10^{10}{\rm yr}}{100{\rm yr} \times 10^{10} L^{\rm B}_\odot} = 2 \times 10^{-3} \frac{M_\odot}{L^{\rm B}_\odot} \tag{2.11}$$

where we use the life time of a star to be about Hubble time, $1.5{\times}10^{10}$ yr. The unit of $M_\odot/L^{\rm B}_\odot$ is a mass-to-light ratio (see subsection 2.4.5).

Since heavy elements can be produced only by thermonuclear reactions in stars and supernovae, the presence of the emission lines found in the spectra from the ICM implies that heavy elements processed in galaxies largely contaminate the ICM.

Koyama et al. (1991) discovered Fe abundance increases at the center of the Virgo cluster with Ginga. From the ASCA observation, similar central abundance increases were found in several clusters (Fukazawa et al. 1994; David et al. 1996; Xu et al. 1997; Kikuchi et al. 1999)

Moreover, recent observational studies of the clusters with *Chandra* and *XMM-Newton* unveil a lot of new interesting abundance distribution in the cluster. Figure 2.6 shows the steep metallicity concentration and the two high-metallicity blobs located symmetrically with respect to the center of the poor cluster AWM 7 (Furusho et al. 2003). Even Abell 1060 cluster which has been regarded as one of the most uniform cluster shows the blob like metallisity excess in the extended region located at $\sim 1'.5$ north-east of central galaxy NGC 3311 (figure 2.7), discovered by *Chandra* observation (Hayakawa et al. 2004).

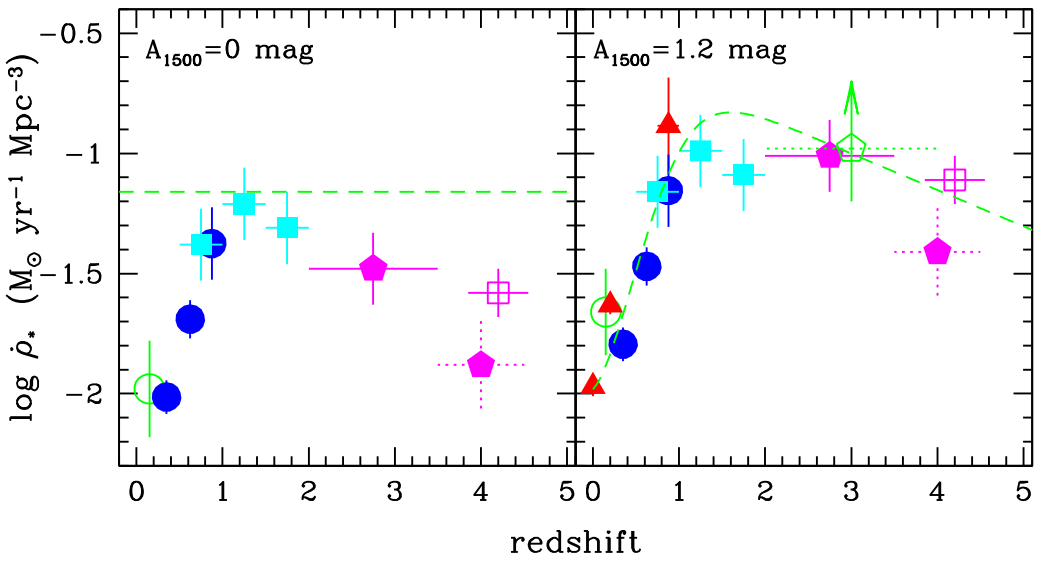

Fig. 2.5: *left:* Mean comoving density of star formation as a function of cosmic time. The data points with error bars have been inferred from the UV-continuum luminosity densities. The dotted line shows the fiducial rate, $< \dot{\rho}_* >= 0.054 M_\odot$ yr^{-1} Mpc^{-3}, required to generate the observed extragalactic background light. *right:* dust corrected values ($A_{1500} = 1.2$ mag). The Hα determinations (filled triangles) together with the SCUBA lower limit (empty pentagon) have been added for comparison (Madau 1999).

2.4.5 Mass to light ratio

In clusters, metals, especially iron, are partly dispersed in the ICM and and is partly locked in to the stellar component of galaxies. The ISM of individual galaxies also contains some iron, but its total amount is negligible compared to the two former contributions.

The amounts of metals is the various components of a cluster can be expressed in several ways, the most traditional being the abundance, i.e., the mass fractions of metals in either the ICM or in stars. In order to know the history of chemical evolution of clusters, this is the most useful way of describing metal contents of clusters. For example, in the case of the ICM, metal abundances in a region depend not only on the total amounts of metal produced in the region, but also on its dispersion as time passes. Renzini et al. (1993) introduced the concept of mass-to-light ratio (MLR), defined as the ratio of the metal mass (either in a specific cluster component, or total) to the total light of the cluster, i.e.,

$$\frac{M_{\mathrm{metal},\ \leq R}}{L_{\mathrm{B},\ \leq R}} = \frac{M_{\mathrm{metal},\ \leq R}}{\Sigma_{\mathrm{i}} L^{\mathrm{i}}_{\mathrm{B},\ \leq R}} \qquad [\frac{M_\odot}{L_\odot}] \tag{2.12}$$

where the $M_{\mathrm{metal},\ \leq R}$ is the total of the metal mass within radius of R in unit of $M_\odot$, and the $\Sigma_{\mathrm{i}} L^{\mathrm{i}}_{\mathrm{B},\ \leq R}$'s are the (blue) luminosities of the individual galaxies of the cluster. The MLR is expressed in terms of quantities whose link with real observable is most direct and presents several other advantages that will become apparent. we investigate the MLR for several metals such as oxygen, magnesium and iron, and the MLRs of oxygen, magnesium and iron are named OMLR, MMLR and IMLR, respectively.

Makishima et al. (2001) summarize the IMLR of various objects, as a function of their plasma temperature serving as a measure of the system richness with *ASCA* (figure 2.8:left). The figure 2.8 left includes clusters with different richness, galaxy groups, and

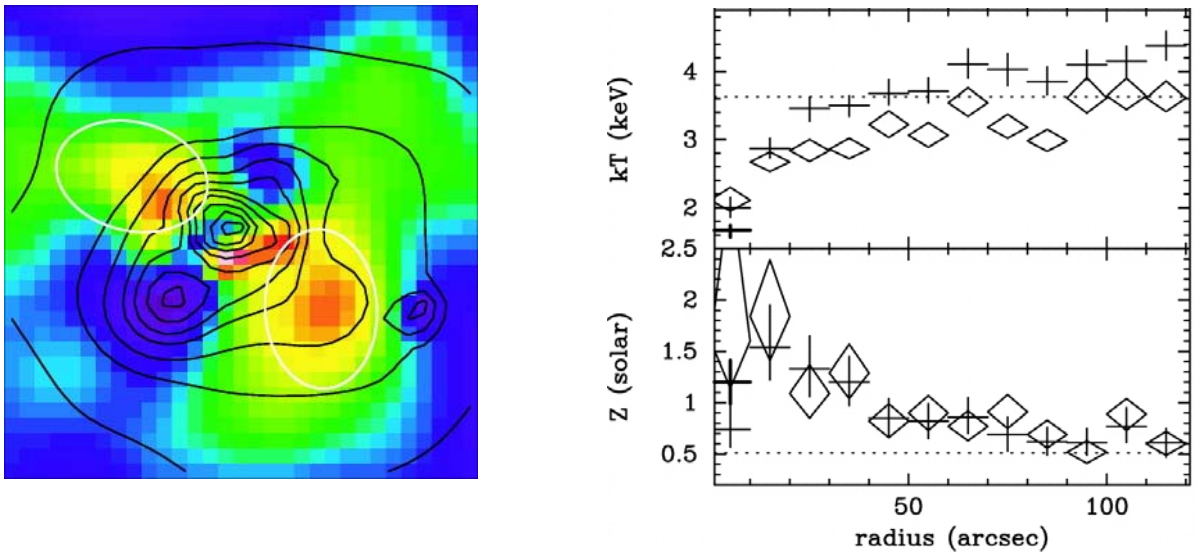

Fig. 2.6: Left: The 6-7 keV image of the central $1^{'}$ square region of the AWM 7 cluster with the 2-10 keV intensity contours (Furusho et al. (2003) with *Chandra*). The white ellipses indicate the Fe blob region to extract a spectrum analysis. Right: The radial temperature (top) and abundance (bottom) distribution of AWM 7. The crosses and diamonds show the results of 1-9 keV and 2-9 keV band fits.

elliptical galaxies. Thus, the IMLR clearly decreases as the system becomes poorer. Evidently, poorer systems have lost most of the heavy elements produced in them, presumably because they have too low an efficiency of gravitational confinement of the metal-enriched SN products (Fukazawa 1997; Matsushita 1997; Fukazawa et al. 2000). The heavy elements are thus inferred to be escaping extensively from objects of lower hierarchy, and the escaped materials enrich the systems of higher hierarchy. Fukazawa (1997) and Fukazawa et al. (2000) have discovered that the silicon over-abundance gradually disappears towards poorer clusters, and that the poorest ones exhibit solar-like Si/Fe ratios, implying a significant contribution from SN Ia as well. In other words, the silicon mass-to-light ratio of the ICM decreases considerably, e.g. by a factor of 2, from rich clusters to the poorest ones, whereas the IMLR is approximately constant among clusters (figure 2.8). As pointedout by Fukazawa et al. (1998), one possible explanation of this effect is a selective escape of silicon; presumably, silicon has been supplied early in the cluster evolution mainly in the form of galactic winds created by SN II, which were energetic enough to escape from poorer systems. In contrast, iron is likely to have been supplied by more prolonged activity of SN Ia without forming such energetic outflows. Tamura et al. (2004) derived IMLR for five clusters within 250 h_{100}^{-1} kpc to be $\sim 0.01\ M_{\odot}/L_{\odot}$, and the oxygen mass within 50 h_{100}^{-1} kpc for several clusters. However, OMLR for rich clusters are not reliable due to the lower emissivity of O_{VII} and O_{VIII} lines in higher temperatures.

Calculation of metal mass

The metal mass in unit of solar , $M_{\rm metal}$, is written as,

$$M_{\rm metal} = M_{\rm gas} \times F_{mass} \times abundance \tag{2.13}$$

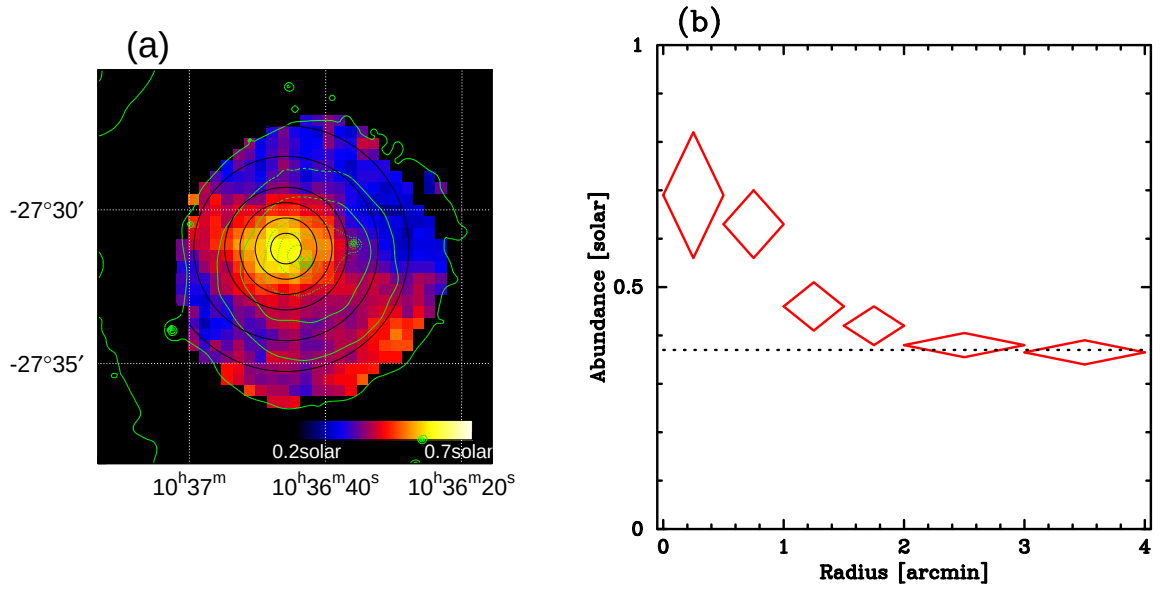

Fig. 2.7: (a) Metal abundance distribution in the central $r < 5'$ region of the Abell 1060 cluster with *XMM-Newton* based on spectral analysis (Hayakawa et al. 2004). The pixel size is $22'' \times 22''$ (5kpc across). Spectral analysis is carried out for a square region of 3×3 pixels. The overlaid contours show smoothed X-ray surface brightness. (b) Radial metallicity distribution in annuli centered on the position of the high metallicity blob, according to the concentric annuli of (a). The crosses show the projected metallicity distribution.

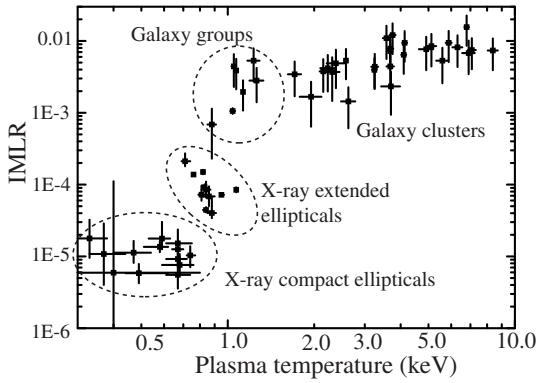

Fig. 2.8: Iron Mass-to-Light Ratio as a function of the system mass (Makishima et al. 2001). Data for clusters and galaxy groups are taken from Fukazawa (1997), where the IMLR is calculated within a radius where the ICM density falls below 3×10^{-4} cm^{-1}. Those for elliptical galaxies refer to Matsushita (1997), where the IMLR is calculated within 4-times the optical effective radius.

where $M_{\rm gas}$ is a 3-dimensional gas mass, $R_{\rm mass}$ is a tranform factor from number to mass ratio, and *abundance* is the results of the spectral fit. In actual calculations, $F_{\rm mass}$ is written as,

$$F_{\rm mass} = N_{\rm table} \times M_{\rm number} \times 0.7 \tag{2.14}$$

where $N_{\rm table}$ is the number ralative to hydrogen of the abundance table for the spectral fit, $M_{\rm number}$ is the mass number of the metal, using mass ratio of solar, X+Y+Z=1 (X=hydrogen=0.7, Y=helium=0.28, Z=others=0.02). For example, when we use Anders

& Grevesse (1989)as the abandance table for spectral fit, oxygen mass, $M_{\rm O}$, is written as,

$$M_{\rm O} = M_{\rm gas} \times 8.51 \times 10^{-4} \times 15.999 \times 0.7 \times abundance. \quad (2.15)$$

calculation of (blue) luminosities

We selected the member galaxies of the clusters and groups by the photometry catalogues of each obgject within the radius of R form the cluters and groups center. In order to correct the 3-denmensional position of the member galaxies form the cluters or groups center, we use the following method. First, we investigated the dispersion of the redsift z and the coordinate (RA, DEC) of each member galay. Second, using the distance coresponded to be 1 sigma of the redshift , d_z, and Declination, $d_{\rm dec}$ and the redshift of the cluster center, $z_{\rm cen}$, and each member galaxy, z_{mem}, the distance, $d_{\rm 3d}$, of line-of-sight from the cluster center is $d_{rm3d} = (z_{\rm mem} - z_{\rm cen}) \times d_{\rm dec}/d_z$.

The observed magunitude of each member galaxy, $m_{\rm X}$ (the X means the band such as V, R, etc.), is translated to a blue magunitude, $m_{\rm B}$, by the equation, $m_{\rm B} = m_{\rm X}+(A_{\rm B}-A_{\rm X})$, where $A_{\rm B}$ and $A_{\rm X}$ are the the magnitude between B-band and X-band (see NASA/IPAC Extragalactic Database(NED)). The relation between the $m_{\rm B}$ and an absolute blue mabnitude, $M_{\rm B}$, is written as,

$$m_{\rm B} - M_{\rm B} = 5 \times \log_{10}(d/1 \text{ pc}) - 5 \quad (2.16)$$

where d is the luminosity distance to the object. The each (blue) luminosity, $L_{\rm B}$, is written as,

$$L_{\rm B} = 10^{-0.4\times(M_{\rm B}-5.48)} \times L_{\odot} \quad (2.17)$$

where we use the $M_{\rm B}$ of the sun to be 5.48.

Table 2.2: Nucleosynthesis products in unit of solar from SN II and Ia models by table 3. of (Iwamoto et al. 1999). SN II products are calculated by the average over the mass range from 10 $M_\odot$ to 50 $M_\odot$ assuming a Salpeter IMF.

TABLE 3

NUCLEOSYNTHESIS PRODUCTS OF SN II AND IA MODELS

	Synthesized Mass ($M_\odot$)							
	Type II	Type Ia						
Species	10–50 $M_\odot$	W7	W70	WDD1	WDD2	WDD3	CDD1	CDD2
^{12}C	7.93E-02	4.83E-02	5.08E-02	5.42E-03	8.99E-03	1.66E-02	9.93E-03	5.08E-03
^{13}C	3.80E-09	1.40E-06	1.56E-09	5.06E-07	3.30E-07	3.17E-07	8.46E-07	4.16E-07
^{14}N.....	1.56E-03	1.16E-06	3.31E-08	2.84E-04	2.69E-04	1.82E-04	9.06E-05	9.03E-05
^{15}N.....	1.66E-08	1.32E-09	4.13E-07	9.99E-07	5.32E-07	1.21E-07	2.53E-07	2.47E-07
^{16}O.....	1.80	1.43E-01	1.33E-01	8.82E-02	6.58E-02	5.58E-02	9.34E-02	5.83E-02
^{17}O.....	9.88E-08	3.54E-08	3.33E-10	3.77E-06	4.58E-06	3.60E-06	9.55E-07	1.01E-06
^{18}O.....	4.61E-03	8.25E-10	2.69E-10	6.88E-07	6.35E-07	2.39E-07	2.08E-07	1.92E-07
^{19}F	1.16E-09	5.67E-10	1.37E-10	1.70E-09	4.50E-10	2.30E-10	5.83E-10	4.24E-10
^{20}Ne	2.12E-01	2.02E-03	2.29E-03	1.29E-03	6.22E-04	4.55E-04	1.16E-03	6.05E-04
^{21}Ne	1.08E-03	8.46E-06	2.81E-08	1.16E-05	1.39E-06	1.72E-06	3.63E-06	1.99E-06
^{22}Ne	1.83E-02	2.49E-03	2.15E-08	1.51E-04	4.21E-04	8.25E-04	4.41E-04	2.11E-04
^{23}Na	6.51E-03	6.32E-05	1.41E-05	8.77E-05	2.61E-05	3.01E-05	5.10E-05	3.50E-05
^{24}Mg.....	8.83E-02	8.50E-03	1.58E-02	7.55E-03	4.47E-03	2.62E-03	7.72E-03	4.20E-03
^{25}Mg.....	1.44E-02	4.05E-05	1.64E-07	8.23E-05	2.66E-05	2.68E-05	4.85E-05	3.25E-05
^{26}Mg.....	2.01E-02	3.18E-05	1.87E-07	6.25E-05	2.59E-05	1.41E-05	4.96E-05	2.97E-05
^{27}Al	1.48E-02	9.86E-04	1.13E-04	4.38E-04	2.47E-04	1.41E-04	4.45E-04	2.35E-04
^{28}Si.....	1.05E-01	1.54E-01	1.42E-01	2.72E-01	2.06E-01	1.58E-01	2.77E-01	1.98E-01
^{29}Si.....	8.99E-03	9.08E-04	5.79E-05	5.47E-04	3.40E-04	2.13E-04	5.52E-04	3.22E-04
^{30}Si.....	8.05E-03	1.69E-03	7.12E-05	1.03E-03	6.41E-04	3.88E-04	1.05E-03	6.14E-04
^{31}P	1.21E-03	3.57E-04	9.12E-05	2.38E-04	1.60E-04	1.07E-04	2.40E-04	1.52E-04
^{32}S	3.84E-02	8.46E-02	9.14E-02	1.60E-01	1.22E-01	9.37E-02	1.63E-01	1.17E-01
^{33}S	1.78E-04	4.24E-04	6.07E-05	2.74E-04	1.92E-04	1.34E-04	2.71E-04	1.79E-04
^{34}S	2.62E-03	1.98E-03	1.74E-05	2.76E-03	2.04E-03	1.46E-03	2.77E-03	1.90E-03
^{36}S	1.78E-06	4.18E-07	3.41E-11	2.23E-07	1.31E-07	7.44E-08	2.22E-07	1.25E-07
^{35}Cl	1.01E-04	1.37E-04	1.06E-05	9.28E-05	7.07E-05	5.33E-05	9.03E-05	6.56E-05
^{37}Cl	1.88E-05	3.67E-05	5.56E-06	2.94E-05	2.26E-05	1.71E-05	2.86E-05	2.11E-05
^{36}Ar	6.62E-03	1.47E-02	1.91E-02	3.11E-02	2.41E-02	1.87E-02	3.18E-02	2.34E-02
^{38}Ar	1.37E-03	9.50E-04	6.60E-07	1.23E-03	9.90E-04	7.44E-04	1.20E-03	9.26E-04
^{40}Ar	2.27E-08	1.87E-08	3.42E-12	7.81E-09	5.19E-09	3.56E-09	7.56E-09	4.82E-09
^{39}K.....	6.23E-05	7.23E-05	1.67E-06	6.76E-05	5.67E-05	4.52E-05	6.39E-05	5.34E-05
^{41}K.....	5.07E-06	6.11E-06	4.83E-07	5.43E-06	4.52E-06	3.62E-06	5.20E-06	4.25E-06
^{40}Ca	5.77E-03	1.19E-02	1.81E-02	3.10E-02	2.43E-02	1.88E-02	3.18E-02	2.38E-02
^{42}Ca	4.23E-05	2.82E-05	1.06E-08	3.09E-05	2.55E-05	1.93E-05	2.97E-05	2.36E-05
^{43}Ca	1.08E-06	9.64E-08	6.17E-08	6.60E-08	2.22E-07	4.18E-07	5.15E-08	2.96E-07
^{44}Ca	5.53E-05	8.02E-06	1.38E-05	1.44E-05	2.95E-05	4.66E-05	1.37E-05	3.62E-05
^{46}Ca	1.43E-10	4.16E-09	1.01E-09	5.01E-09	4.73E-09	4.47E-09	8.79E-10	1.18E-09
^{48}Ca	5.33E-14	2.60E-09	2.47E-09	1.63E-06	1.64E-06	1.55E-06	3.54E-11	4.93E-10
^{45}Sc	2.29E-07	2.21E-07	3.85E-08	2.49E-07	2.09E-07	1.76E-07	2.47E-07	2.02E-07
^{46}Ti	7.48E-06	1.33E-05	3.49E-07	1.34E-05	1.12E-05	8.58E-06	1.27E-05	1.05E-05
^{47}Ti	2.11E-06	5.10E-07	4.08E-07	5.65E-07	1.56E-06	2.57E-06	4.93E-07	1.95E-06
^{48}Ti	1.16E-04	2.05E-04	3.13E-04	7.10E-04	6.11E-04	5.23E-04	7.32E-04	6.20E-04
^{49}Ti	5.98E-06	1.71E-05	2.94E-06	5.27E-05	4.39E-05	3.59E-05	5.22E-05	4.17E-05
^{50}Ti	3.81E-10	1.07E-04	1.04E-04	3.52E-04	3.51E-04	3.51E-04	2.08E-05	7.28E-05
^{50}V	7.25E-10	1.55E-08	1.22E-08	9.74E-09	9.33E-09	9.07E-09	4.94E-09	1.20E-08
^{51}V	1.00E-05	7.49E-05	4.27E-05	1.33E-04	1.16E-04	1.02E-04	1.11E-04	1.09E-04
^{50}Cr	4.64E-05	2.73E-04	6.65E-05	4.44E-04	3.53E-04	2.84E-04	4.49E-04	3.36E-04
^{52}Cr	1.15E-03	6.36E-03	7.73E-03	1.68E-02	1.37E-02	1.13E-02	1.65E-02	1.40E-02
^{53}Cr	1.19E-04	9.22E-04	5.66E-04	1.66E-03	1.38E-03	1.17E-03	1.59E-03	1.33E-03
^{54}Cr	2.33E-08	9.24E-04	9.04E-04	1.60E-03	1.60E-03	1.60E-03	2.31E-04	8.02E-04
^{55}Mn.....	3.86E-04	8.87E-03	6.66E-03	8.48E-03	7.05E-03	6.16E-03	8.10E-03	6.77E-03
^{54}Fe	3.62E-03	9.55E-02	7.30E-02	7.08E-02	5.91E-02	5.15E-02	7.20E-02	5.64E-02
^{56}Fe	8.44E-02	6.26E-01	6.80E-01	5.87E-01	7.13E-01	7.95E-01	5.65E-01	7.57E-01
^{57}Fe	2.72E-03	2.45E-02	1.92E-02	1.08E-02	1.67E-02	2.06E-02	1.01E-02	1.80E-02
^{58}Fe	7.22E-09	3.03E-03	2.96E-03	3.23E-03	3.23E-03	3.24E-03	8.63E-04	3.06E-03
^{59}Co	7.27E-05	1.04E-03	9.68E-04	3.95E-04	6.25E-04	7.75E-04	2.91E-04	6.35E-04
^{58}Ni	3.63E-03	1.10E-01	8.34E-02	3.14E-02	4.29E-02	4.97E-02	3.15E-02	4.47E-02
^{60}Ni	1.75E-03	1.24E-02	1.47E-02	5.08E-03	1.15E-02	1.67E-02	2.81E-03	1.21E-02
^{61}Ni	8.35E-05	2.35E-04	2.15E-04	7.00E-05	3.58E-04	5.92E-04	4.00E-05	4.27E-04
^{62}Ni	5.09E-04	3.07E-03	1.85E-03	1.37E-03	3.69E-03	5.46E-03	6.51E-04	4.60E-03
^{64}Ni	3.20E-14	1.70E-05	1.65E-05	2.32E-04	2.31E-04	2.32E-04	2.47E-06	9.29E-06
^{63}Cu	8.37E-07	2.32E-06	3.00E-06	2.77E-06	4.88E-06	5.92E-06	6.14E-07	3.97E-06
^{65}Cu	4.07E-07	6.84E-07	8.33E-07	7.08E-07	2.04E-06	3.38E-06	1.14E-07	2.05E-06
^{64}Zn	1.03E-05	1.06E-05	7.01E-05	3.71E-06	3.10E-05	5.76E-05	1.87E-06	3.96E-05
^{66}Zn	8.61E-06	1.76E-05	6.26E-06	2.16E-05	6.42E-05	1.04E-04	2.84E-06	6.11E-05
^{67}Zn	1.52E-08	1.58E-08	7.28E-09	6.35E-07	6.55E-07	6.27E-07	1.69E-09	4.01E-08
^{68}Zn	3.92E-09	1.74E-08	1.13E-08	7.44E-08	8.81E-08	9.42E-08	3.08E-09	3.03E-08

Table 2.3: SN rate in unit of 1 SN $(100\mathrm{yr})^{-1}$ $(10^{10}L_{\odot}^{rmB})$ from 137 SN in a sample of about 10^4 galaxies (Cappellaro et al. 1999).

galaxy	N. SNe*			rate [SNu]			
type	Ia	Ib/c	II	Ia	Ib/c	II	All
E-S0	22.0			0.18 ± 0.06	< 0.01	< 0.02	0.18 ± 0.06
S0a-Sb	18.5	5.5	16.0	0.18 ± 0.07	0.11 ± 0.06	0.42 ± 0.19	0.72 ± 0.21
Sbc-Sd	22.4	7.1	31.5	0.21 ± 0.08	0.14 ± 0.07	0.86 ± 0.35	1.21 ± 0.37
Others#	6.8	2.2	5.0	0.40 ± 0.16	0.22 ± 0.16	0.65 ± 0.39	1.26 ± 0.45
All	69.6	14.9	52.5	0.20 ± 0.06	0.08 ± 0.04	0.40 ± 0.19	0.68 ± 0.20

Chapter 3

Instrumentation

3.1 The *Suzaku* satellite

3.1.1 Mission Description

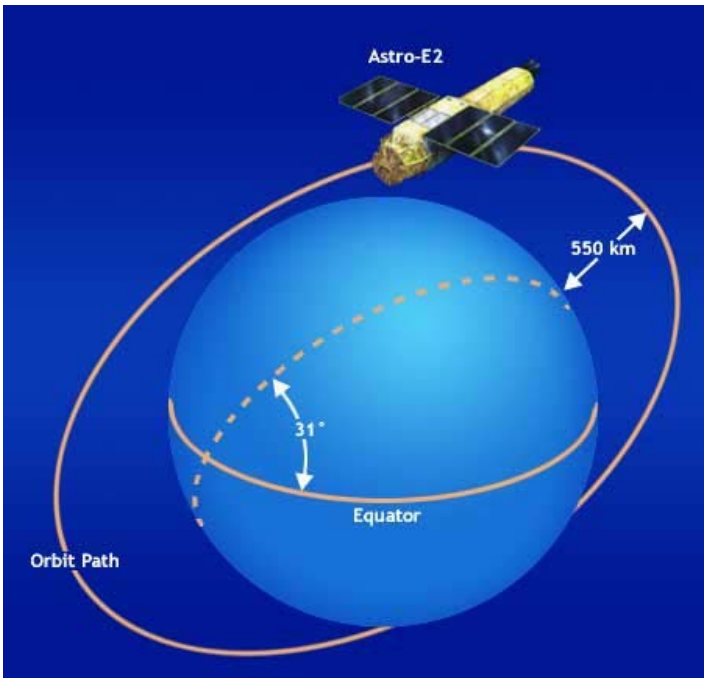

Fig. 3.1: The 96 minute *Suzaku* orbit (The *Suzaku* technical Discription).

Suzaku, the Japanese 5th X-ray astronomical satellite, was launched on July, 2005 (Mitsuda 2007; Serlemitsos 2007; Koyama 2007; Takahashi 2007; Kokubun et al. 2006). *Suzaku* is placed in a near-circular orbit with an apogee of 568 km, an inclination of 31.9 degrees, and an orbital period of about 96 minutes. The maximum slew rate of the spacecraft is 6 degrees/min, and settling to the final attitude takes $\sim$ 10 minutes, using the star trackers.

A Brief Introduction of *Suzaku*

The scientific payload of *Suzaku* (Fig. 3.2) initially consisted of three distinct co-aligned scientific instruments. There are four X-ray sensitive imaging CCD cameras (X-ray Imag-

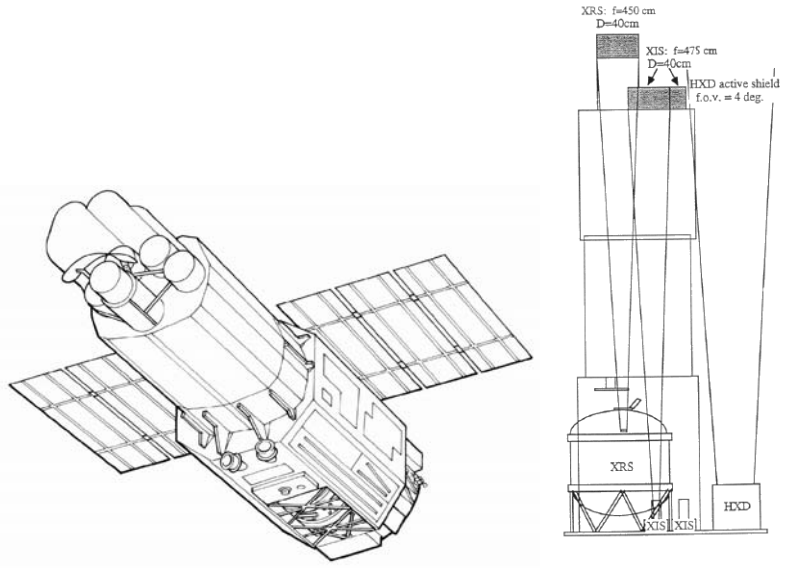

Fig. 3.2: Left: Schematic picture of the *Suzaku* satellite. Right: A side view of the instruments and telescopes on *Suzaku* (Serlemitsos 2007).

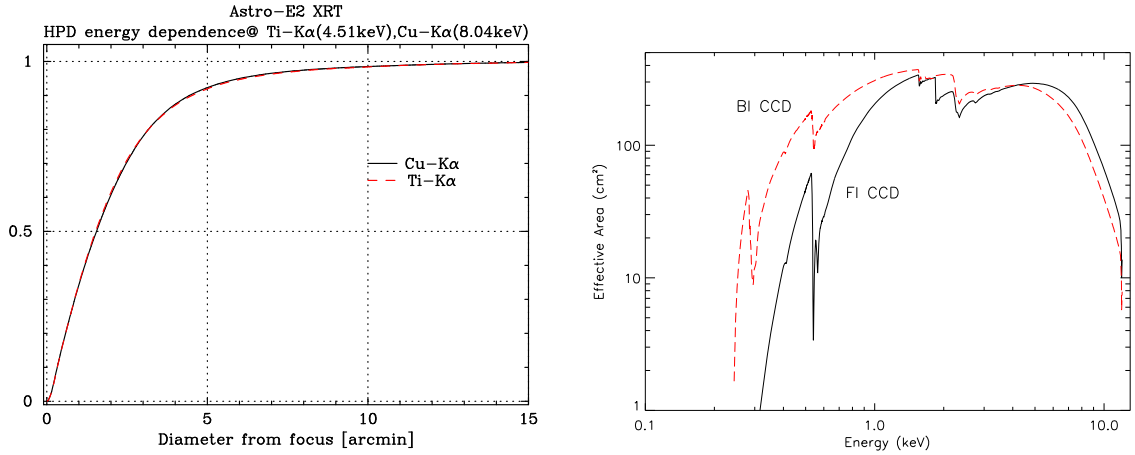

Fig. 3.3: Left: XIS Effective area of one XRT + XIS system, for the FI and BI CCDs. no contamination. Right: The Encircled Energy Function (EEF) showing the fractional energy within a given radius for one quadrant of the XRT-I telescopes on *Suzaku* at 4.5 and 8.0 keV(Serlemitsos 2007).

ing Spectrometers, or XISs), three front-side illuminated (FI; energy range 0.4-12 keV corresponding to XIS0, XIS2 and XIS3) and one back-side illuminated (BI; energy range 0.2-12 keV for XIS1), capable of moderate energy resolution. Each XIS is located in the focal plane of a dedicated X-ray telescope. The second instrument is the non-imaging, collimated Hard X-ray Detector (HXD), which extends the bandpass of the observatory to much higher energies with its 10–600 keV pointed bandpass. The X–Ray Spectrometer (XRS) is no longer operational.

All of the instruments on *Suzaku* operate simultaneously. Each of the co-aligned XRTs features an X-ray mirror with an angular resolution (expressed as Half-Power Diameter, or HPD) of $\sim 2'$ (Fig. 3.3). Figure 3.3 shows the total effective area of the XIS+XRT. K-shell absorption edges from the oxygen (0.54 keV) and aluminum (1.56 keV) in the blocking filters are present, as well as a number of weak M-shell features between 2–3 keV

Table 3.1: Overview of *Suzaku* capabilities

S/C	Orbit Apogee	568 km
	Orbital Period	96 minutes
	Observing Efficiency	$\sim 45\%$
XRT	Focal length	4.75 m
	Field of View	$17'$ at 1.5 keV
		$13'$ at 8 keV
	Plate scale	0.724 arcmin/mm
	Effective Area	440 cm^2 at 1.5 keV
		250 cm^2 at 8 keV
	Angular Resolution	$2'$ (HPD)
XIS	Field of View	$17.8' \times 17.8'$
	Bandpass	0.2–12 keV
	Pixel grid	1024×1024
	Pixel size	24 μm× 24 μm
	Energy Resolution	~ 130 eV at 6 keV
	Effective Area	340 cm^2 (FI), 390 cm^2 (BI) at 1.5 keV
	(incl XRT-I)	150 cm^2 (FI), 100 cm^2 (BI) at 8 keV
	Time Resolution	8 s (Normal mode), 7.8 ms (P-Sum mode)
HXD	Field of View	$4.5^\circ \times 4.5^\circ$ (≥ 100 keV)
	Field of View	$34' \times 34'$ (≤ 100 keV)
	Bandpass	10 – 600 keV
	– PIN	10 – 60 keV
	– GSO	30 – 600 keV
	Energy Resolution (PIN)	~ 3.0 keV (FWHM)
	Energy Resolution (GSO)	$7.6/\sqrt{E_{MeV}}$ % (FWHM)
	Effective area	$\sim 160\,cm^2$ at 20 keV, $\sim 260\,cm^2$ at 100 keV
	Time Resolution	61 μs
HXD-WAM	Field of View	2π (non-pointing)
	Bandpass	50 keV – 5 MeV
	Effective Area	800 cm^2 at 100 keV / 400 cm^2 at 1 MeV
	Time Resolution	31.25 ms for GRB, 1 s for All-Sky-Monitor

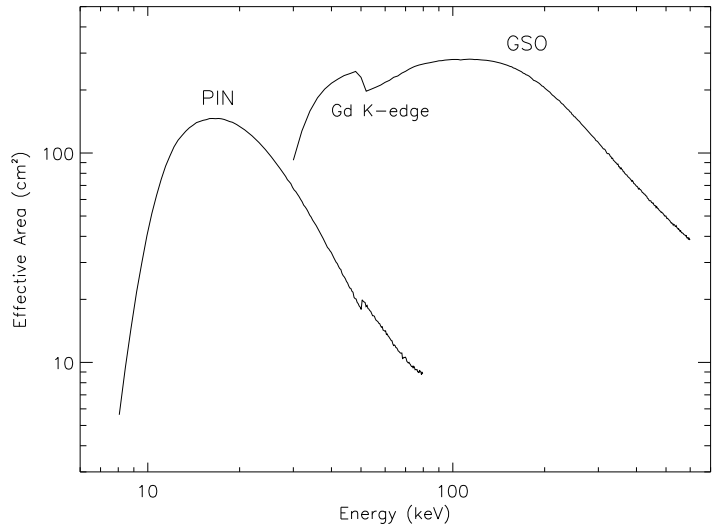

Fig. 3.4: Total effective area of the HXD detectors, PIN and GSO, as a function of energy (Kokubun et al. 2006).

arising from the gold coated on the front surface of the XRT reflector.

The four XISs are true imagers, with a large field of view ($\sim 18' \times 18'$), and moderate spectral resolution.

The HXD is a non-imaging instrument with an effective area of $\sim 260\,\mathrm{cm}^2$, featuring a compound-eye configuration and an extremely low background. It extends the bandpass of the mission with its nominal sensitivity over the 10 – 600 keV band (cf. Fig. 3.4). The HXD consists of two types of sensors: 2 mm thick silicon PIN diodes sensitive over 10 – 60 keV, and GSO crystal scintillators placed behind the PIN diodes covering 30 – 600 keV. The HXD field of view is actively collimated to $4.5° \times 4.5°$ by the well-shaped BGO scintillators, which, in combination with the GSO scintillators, are arranged in the so-called phoswich configuration. At energies below $\sim$ 100 keV, an additional passive collimation further reduces the field of view to $34' \times 34'$. The energy resolution is ~ 3.0 keV (FWHM) for the PIN diodes, and $7.6/\sqrt{E}$ % (FWHM) for the scintillators (where E is energy in MeV). The HXD time resolution for both sensors is 61 μs. While the HXD is intended mainly to explore the faintest hard X-ray sources, it can also tolerate very bright sources up to $\sim$ 10 Crab. The HXD also has an all-sky monitor (the Wide-band All-sky Monitor (WAM), which can detect GRB and other sources (3.1). In this paper, we do not use HXD.

3.1.2 X–Ray Telescopes (XRTs)

Suzaku has five light-weight thin-foil X–Ray Telescopes (XRTs). The XRTs have been developed jointly by NASA/GSFC, Nagoya University, Tokyo Metropolitan University, and ISAS/JAXA. These are grazing-incidence reflective optics consisting of compactly nested, thin conical elements. Because of the reflectors' small thickness, they permit high density nesting and thus provide large collecting efficiency with a moderate imaging capability in the energy range of 0.2-12 keV, all accomplished in telescope units under 20 kg each.

Four XRTs onboard *Suzaku* (XRT-I) are used for the XIS, and the other XRT (XRT-S) is for the XRS. The XRTs are arranged on the top plate of the Extensible Optical Bench

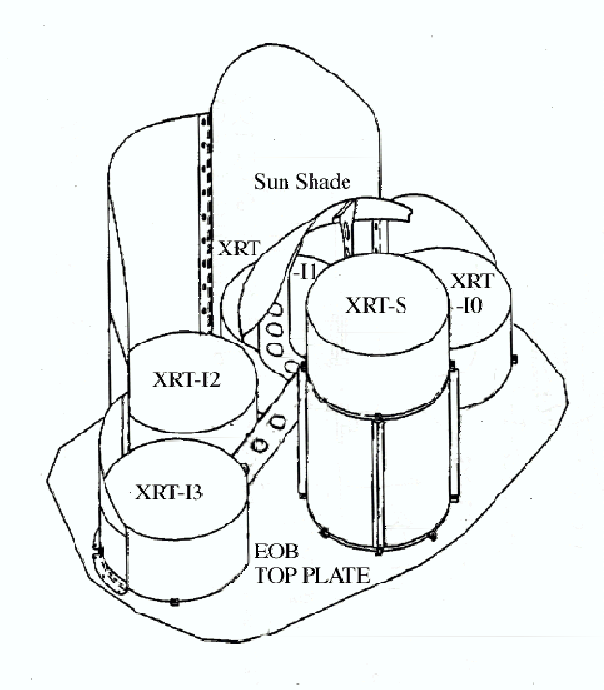

Fig. 3.5: Layout of the XRTs on the *Suzaku* spacecraft (Serlemitsos 2007).

Table 3.2: Telescope dimensions and design parameters of XRT-I, compared with ASCA XRT.

	Suzaku XRT-I	ASCA
Number of telescopes	4	4
Focal length	4.75 m	3.5 m
Inner Diameter	118 mm	120 mm
Outer Diameter	399 mm	345 mm
Height	279 mm	220 mm
Mass/Telescope	19.5 kg	9.8 kg
Number of nested shells	175	120
Reflectors/Telescope	1400	960
Geometric area/Telescope	873 cm^2	558 cm^2
Reflecting surface	Gold	Gold
Substrate material	Aluminum	Aluminum
Substrate thickness	155 μm	127 μm
Reflector slant height	101.6 mm	101.6 mm

(EOB) in the manner shown in Figure 3.5. The external dimensions of the 4 XRT-Is are the same (See Table 3.2, which also includes a comparison with the ASCA telescopes).

The HPD of the XRTs range from 1.8′ to 2.3′, which is the diameter within which half of the focused X-ray is enclosed. The angular resolution does not significantly depend on the energy of the incident X-ray in the energy range of *Suzaku*, 0.2-12 keV. The effective areas are typically 440 cm^2 at 1.5 keV and 250 cm^2 at 8 keV. The focal lengths are 4.75 m for the XRT-I. Individual XRT quadrants have their component focal lengths deviated from the design values by a few cm. The optical axis of the quadrants of each XRT are aligned within 2′ from the mechanical axis. The field of view (the diameter for a half of the effective area) for XRT-Is is about 17′ at 1.5 keV and 13′ at 8 keV.

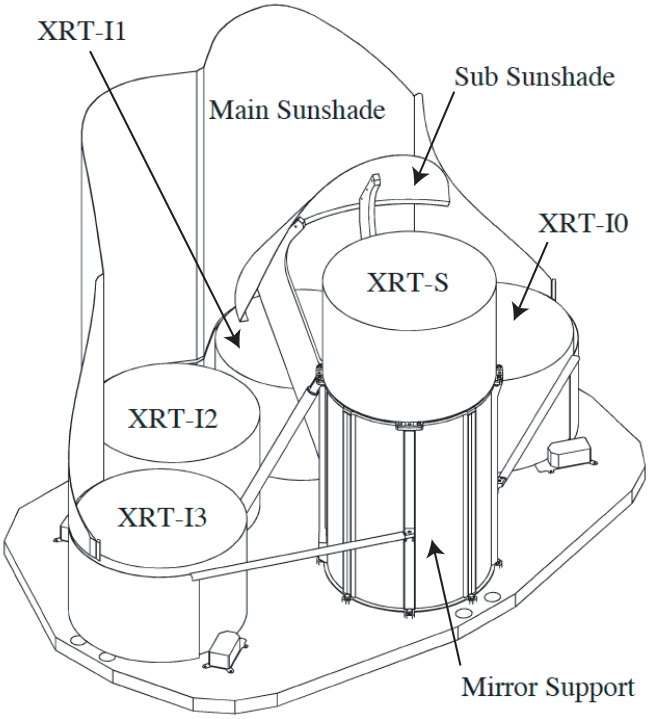

Fig. 3.6: A *Suzaku* X–Ray Telescope (Serlemitsos 2007).

Basic Components of XRT

The *Suzaku* XRTs consist of closely nested thin-foil reflectors, reflecting X-ray at small grazing angles. An XRT is a cylindrical structure, having the following layered components: 1. a thermal shield at the entrance aperture to help maintain a uniform temperature; 2. a pre-collimator mounted on metal rings for stray light elimination; 3. a primary stage for the first X-ray reflection; 4. a secondary stage for the second X-ray reflection; 5. a base ring for structural integrity and interface with the EOB. All these components, except the base rings, are constructed in 90° segments. Four of these quadrants are coupled together by interconnect-couplers and also by the top and base rings (Figure 3.6). The telescope housings are made of aluminum for an optimal strength to mass ratio.

Including the alignment bars, collimating pieces, screws and washers, couplers, retaining plates, housing panels and rings, each XRT-I consists of over 4112 mechanically separated parts. In total, nearly 7000 qualified reflectors were used and over 1 million cm^2 of gold surface was coated.

Reflectors Each reflector consists of a substrate also made of aluminum and an epoxy layer that couples the reflecting gold surface to the substrate. The reflectors are nominally 178 μm in thickness. In shape, each reflector is a 90° segment of a section of a cone. The cone angle is designed to be the angle of on-axis incidence for the primary stage and 3 times that for the secondary stage. They are 101.6 mm in slant length and with radii extending approximately from 60 mm at the inner part to 200 mm at the outer part. All reflectors are positioned with grooved alignment bars, which hold the foils at their circular edges. There are 13 alignment bars at each face of each quadrant, separated at approximately 6.4° apart.

In the *Suzaku* XRTs, the conical approximation of the Wolter-I type geometry is used. This approximation fundamentally limits the angle resolution achievable. More

Table 3.3: Design parameters for pre-collimator

	XRT-I
Number of Collimators	4
Height	32 mm
Blade Substrate	Aluminum
Blade Thickness	120 μm
Blade Height	22 mm
Height from Blade Top to Reflector Top	30 mm
Number of nested shells	175
Blade/Telescope	700
Mass/Collimator	2.7 kg

significantly, the combination of the figure error in the replication mandrels and the imperfection in the thermo-forming process (to about 4 micrometers in the low frequency components of the figure error in the axial direction) limits the angular resolution to about 1 minute of arc (Misaki et al. 2004).

Pre-collimator The pre-collimator, which blocks off stray light that otherwise would enter the detector at a larger angle than intended, consists of concentrically nested aluminum foils similar to that of the reflector substrates (Mori et al. 2005). They are shorter, 22 mm in length, and thinner, 120 μm in thickness. They are positioned in a fashion similar to that of the reflectors, by 13 grooved aluminum plates at each circular edge of the pieces. They are installed on top of their respective primary reflectors along the axial direction. Due to their smaller thickness, they do not significantly reduce the entrance aperture in that direction more than the reflectors already do. Pre-collimator foils do not have reflective surfaces (neither front nor back). The relevant dimensions are listed in Table 3.3.

Thermal Shields The *Suzaku* XRTs are designed to function in a thermal environment of 20$\pm$7.5 °C (figure 3.7). The thermal shield is mechanically sustained by a frame made of aluminum, with a thickness of 4 mm. The frame has thirteen spokes which are along the alignment bars of the XRT. A stainless steel mesh with a wire pitch, width and thickness of 3 mm, 0.1 mm and 0.15 mm, respectively. Finally, polyethylene teleftalate (PET) film as thin as 0.24 μm, coated with aluminum layer with thickness of 30 nm on the surface oriented to the space, is adhered to the mesh with epoxy. The reflectors, due to its composite nature and thus its mismatch in coefficients of thermal expansion, suffer from thermal distortion that degrades the angular resolution of the telescopes in temperature outside this range. Thermal gradient also distorts the telescope in a larger scale. Even though sun shields and other heating elements on the spacecraft help in maintaining a reasonable thermal environment, thermal shields are integrated on top of the pre-collimator stage to provide the needed thermal control.

XRT Performance in Orbit

Focal Positions and Angular Resolutions Verification of the imaging capability of the XRTs has been made with the data of SS Cyg in quiescence taken during 2005 November 2 01:02UT–23:39UT. The total exposure time was 41.3 ks. SS cyg is selected for this purpose because it is a point source and moderately bright (3.6, 5.9, 3.7 and 3.5

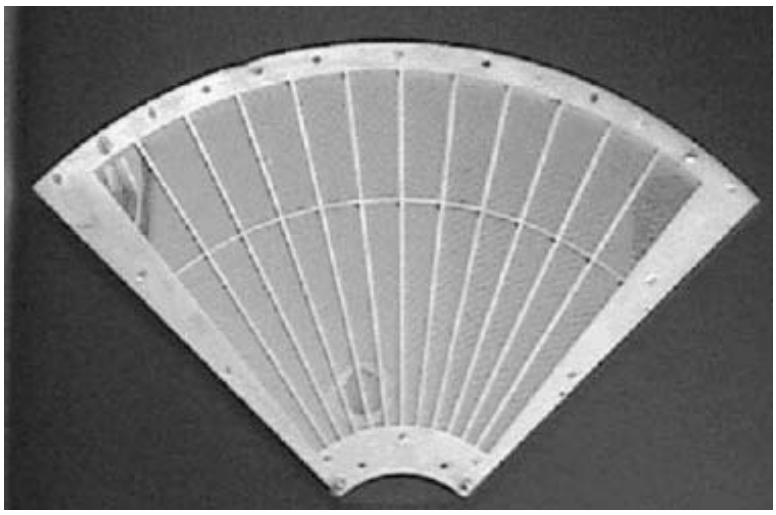

Fig. 3.7: A thermal shield (Serlemitsos 2007).

c s^{-1} for XIS0 through XIS3), and hence, it is needless to care about pile-up even at the image core. A constant value, evaluated from source-free corner regions was subtracted as a background, from all the pixels. The data taken only during the star-tracker calibration is on was used. Fig. 3.8 shows the images and the point spread functions (PSFs) of all the XRT-I+XIS modules. The HPD is obtained to be 1.′8, 2.′3, 2.′0, and 2.′0 for XRT-I0, 1, 2 and 3, respectively. These values are in general consistent with those expected from ground-based calibration measurements.

Figure 3.9 shows the focal position of the XRT-Is, that the source is focused when the satellite points at the XIS aimpoint. The focal positions locate roughly within 0.′5 from the detector center with an deviation of $\sim 0.'3$. This implies that the fields of view of the XIS coinsides each other within $\sim 0.'3$.

Optical Axes, Effective Area and Vignetting Functions A series of offset observations of the Crab observations were carried out in August and September at various off-axis angles of $0'$, $3.'5$, $7'$. The intensity of the Crab nebula is evaluated for each pointing and for each XIS module separately. By finding the maximum throughput angle, we also have obtained a direction of the optical axis of each telescope. The result is shown in Fig. 3.10 The optical axes locate roughly within $1'$ from the XIS aim point. This implies that the efficiency of all the XRT-Is is more than 97 % even at 10 keV when we observe a point source on the XIS aimpoint.

The vignetting curves calculated by the ray-tracing simulator are compared with the observed intensities of the Crab Nebula at various off-axis angles in 3.11. These figures roughly show that effective area is calibrated to within $\sim 10\%$ over the XIS field of view. We expect most of these deviations can be attributed to scattering of the optical axis orientations of the four quadrants within a telescope.

Stray Light In-flight stray-light observations were carried out with Crab at off-axis angles of $20'$ (4 pointings), $50'$ (4 pointing) and $120'$ (4 pointing) in August and September. Fig. 3.12 shows an example of $20'$-off image of XRT-I3 together with simulation results of the same off-axis angle for the cases with and without the pre-collimator.

It is seen that the pre-collimator works for reducing the stray light in orbit.

Figure 3.13 shows angular responses of the XRT-I at 1.5 and 4.5 keV up to 2 degrees. The effective area is normalized at on-axis. The integration area is corresponding to the

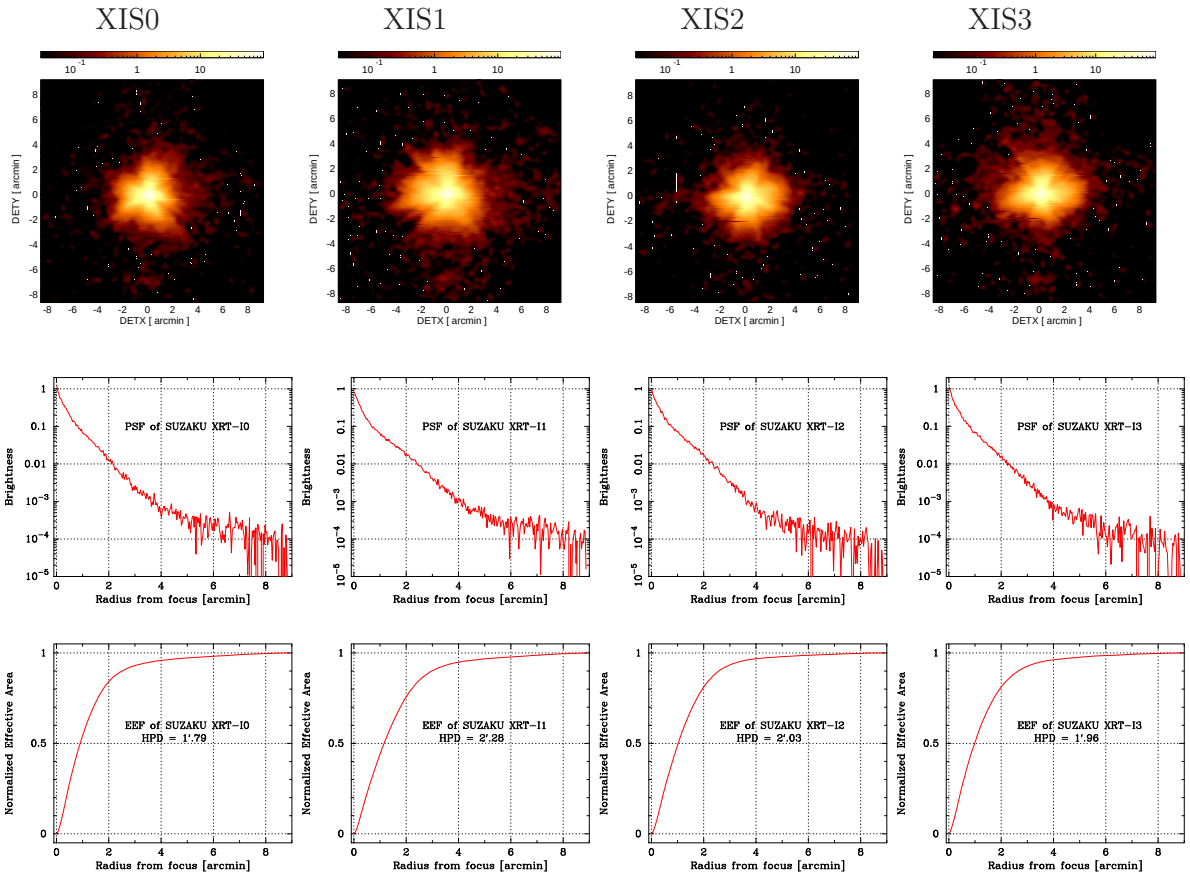

Fig. 3.8: Image, Point-Spread Function (PSF), and EEF of the four XRT-I modules in the focal plane (Serlemitsos 2007). All the images are binned with 2×2 pixels followed by being smoothed with a Gaussian with a sigma of 3 pixels, where the pixel size is 24 μm. The EEF is normalized to unity at the edge of the CCD chip (a square of $17'.8$ on a side). With this normalization, the HPD of the XRT-I0 through I3 is $1'.8$, $2'.3$, $2'.0$ and $2'.0$, respectively.

detector size of XIS ($17'.8 \times 17'.8$). The plots are necessary to plan observations of diffuse sources or faint emissions near bright sources, such as outskirts of cluster of galaxies.

The three solid lines in the plots correspond to different parameters of ray-tracing program while the crosses are the normalized effective area using the Crab pointings. For example, the effective area of the stray lights at 1.5 keV is $\sim 10^{-3}$ at angles smaller than 70 arcmin off axis and $< 10^{-3}$ at angles larger than 70 arcmin off. The measured flux of stray lights are in good agreement with that of raytracing within an order.

3.1.3 X-ray Imaging Spectrometer (XIS)

Overview of the XIS

Suzaku has four X-ray Imaging Spectrometers (XISs), which are shown in Figure 3.14. These employ X-ray sensitive silicon charge-coupled devices (CCDs), which are operated in a photon-counting mode, similar to that used in the ASCA SIS, *Chandra* ACIS, and *XMM-Newton* EPIC. In general, X-ray CCDs operate by converting an incident X-ray photon into a charge cloud, with the magnitude of charge proportional to the energy of

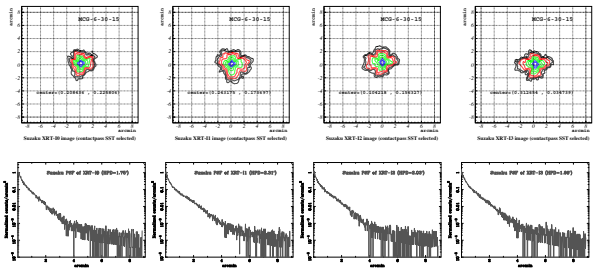

Fig. 3.9: Images and PSFs are shown in the upper, middle, and lower panels for the XIR-I0 through XRT-I3 from left to right. In each image drawn are ten contours in logarithmic spacing with the outermost contour being 1% surface brightness of the peak. the position of the maximum surface brightness is written as a caption in each panel in a unit of arcmin. Its typical error is $\pm 0.1'$. Each PSF is normalized by the number of total photons collected over the entire XIS aperture.

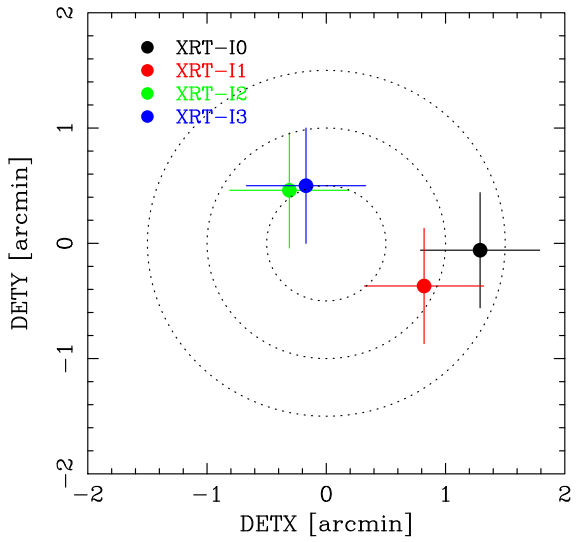

Fig. 3.10: Locations of the optical axis of each XRT-I module in the focal plane determined from the observations of the Crab Nebula in 2005 August-September. This figure implies that the image on each XIS detector becomes brightest when a target star is placed at the position of the corresponding cross. The dotted circles are drawn every $30''$ in radius from the XIS-default position.

the absorbed X-ray. This charge is then shifted out onto the gate of an output transistor via an application of time-varying electrical potential. This results in a voltage level (often referred to as "pulse height") proportional to the energy of the X-ray photon.

The four *Suzaku* XISs are named XIS0, XIS1, XIS2 and XIS3, each located in the focal plane of an X-ray Telescope; those telescopes are known respectively as XRT-I0, XRT-I1, XRT-I2, and XRT-I3. Each CCD camera has a single CCD chip with an array of 1024 $\times$ 1024 picture elements ("pixels"), and covers an $17.8' \times 17.8'$ region on the sky. Each pixel is 24 μm square, and the size of the CCD is 25 mm $\times$ 25 mm. One of the XISs, XIS1, uses a back-side illuminated (BI) CCDs, while the other three use front-side illuminated (FI) CCDs. The XIS has been partially developed at MIT (CCD sensors, analog electronics, thermo-electric coolers, and temperature control electronics), while the digital electronics and a part of the sensor housing were developed in Japan, jointly by Kyoto University, Osaka University, Rikkyo University, Ehime University, and ISAS.

A CCD has a gate structure on one surface to transfer the charge packets to the readout gate. The surface of the chip with the gate structure is called the "front side". A front-side illuminated CCD (FI CCD) detects X-ray photons that pass through its gate structures, i.e. from the front side. Because of the additional photo-electric absorption at the gate structure, the low-energy quantum detection efficiency (QDE) of the FI CCD is

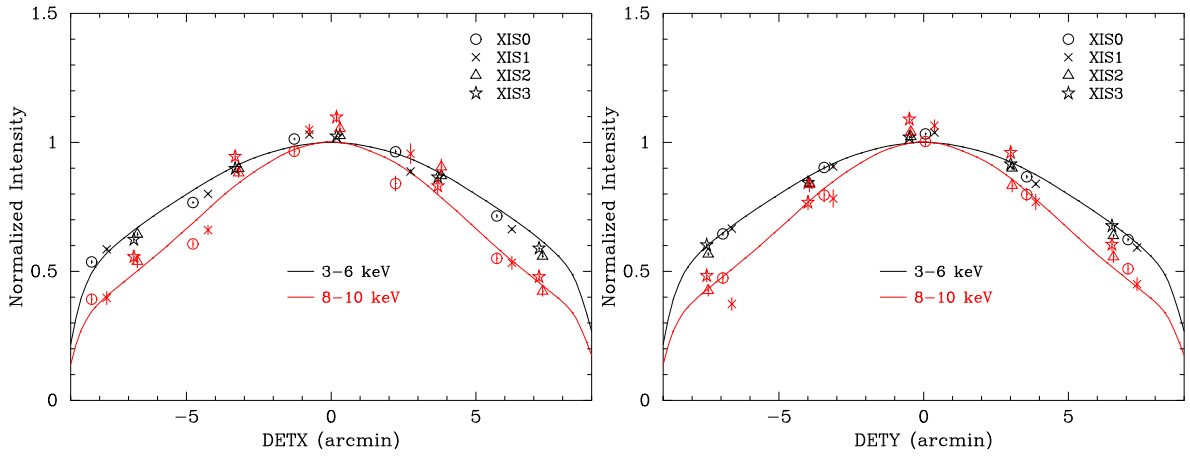

Fig. 3.11: Vignetting of the four XRT-I modules using the data of the Crab Nebula taken during 2005 August 22−27 in the two energy bands 3−6 keV and 8−10 keV. The model curves are calculated with the ray-tracing simulator with the spectral parameters of $N_{\rm H} = 0.33 \times 10^{22}$ cm^{-2}, photon index = 2.09, and the normalization = 9.845 photons cm^{-2} s^{-1} keV^{-1} at 1 keV. Note that the abrupt drop of the model curves at $\sim 8'$ is due to the source approaching the detector edge. The excess of the data points of XIS1 is probably due to insufficient calibration of the BI CCD.

rather limited. Conversely, a back-side illuminated CCD (BI CCD) receives photons from "back," or the side without the gate structures. For this purpose, the undepleted layer of the CCD is completely removed in the BI CCD, and a thin layer to enhance the electron collection efficiency is added in the back surface. A BI CCD retains a high QDE even in sub-keV energy band because of the absence of gate structure on the photon-detection side. However, a BI CCD tends to have a slightly thinner depletion layer, and the QDE is therefore slightly lower in the high energy band. The decision to use only one BI CCD and three FI CCDs was made because of both the slight additional risk involved in the new technology BI CCDs and the need to balance the overall efficiency for both low and high energy photons.

To minimize the thermal noise, the sensors need to be kept at ~ -90°C during observations. This is accomplished by thermo-electric coolers (TECs), controlled by TEC Control Electronics, or TCE. The Analog Electronics (AE) drives the CCD clocks, reads and amplifies the data from the CCDs, performs the analog-to-digital conversion, and routes the signals to the Digital Electronics (DE). The AE and TCE are located in the same housing, and together, they are called the AE/TCE. *Suzaku* has two AE/TCEs; AE/TCE01 is used for XIS-S0 and S1, and AE/TCE23 is used for XIS-S2 and S3. The digital electronics system for the XISs consists of two Pixel Processing Units (PPU) and one Main Processing Unit (MPU); PPU01 is associated with AE/TCE01, and PPU23 is associated with AE/TCE23. The PPUs receive the raw data from AE, carry out event detection, and send event data to the MPU. The MPU edits and packets the event data, and sends them to the satellite's main digital processor.

To reduce contamination of the X-ray signal by optical and UV light, each XIS has an Optical Blocking Filter (OBF) located in front of it. The OBF is made of polyimide with a thickness of 1000 Å, coated with a total of 1200 Å of aluminum (400 Å on one side and 800 Å on the other side). To facilitate the in-flight calibration of the XISs, each CCD sensor has two ^{55}Fe calibration sources. One is installed on the door to illuminate

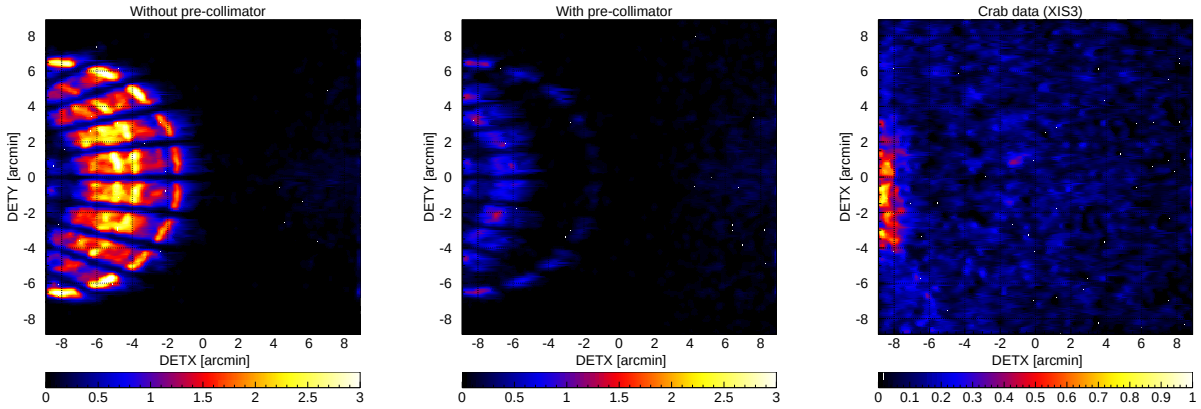

Fig. 3.12: Focal plane images formed by stray light (Serlemitsos 2007). The left and middle panels show simulated images of a monochromatic point-like source of 4.51 keV locating at (DETX, DETY)=($-20'$,0′) in the cases of without and with the pre-collimator, respectively. The radial dark lanes are the shades of the alignment bars. The right panels is the in-flight stray image of the Crab Nebula in the 2.5−5.5 keV band located at the same off-axis angle. The unit of the color scale of this panel is counts per 16 pixels over the entire exposure time of 8428.8 s. The counting rate from the whole image is 0.78±0.01 c s^{-1} including background. Note that the intensity of the Crab Nebula measured with XIS3 at the XIS-default position is 458±3 c s^{-1} in the same 2.5-5.5 keV band. All the images are binned with 4×4 pixels followed by being smoothed with a Gaussian with a sigma of 2 pixels, where the pixel size is 24 μm.

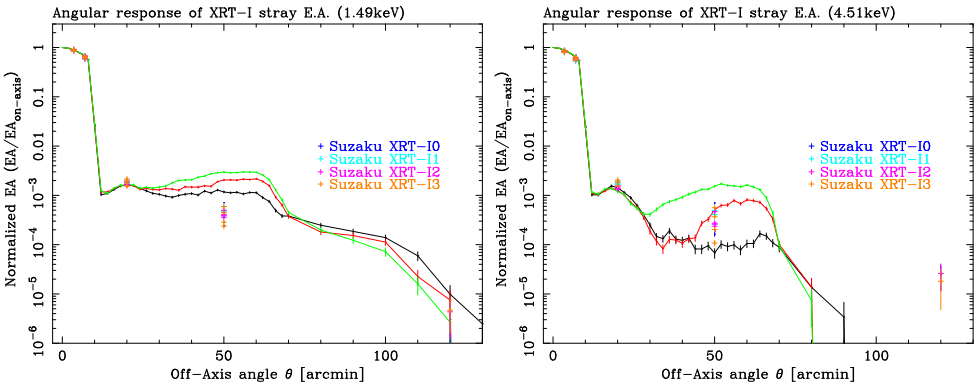

Fig. 3.13: Angular responses of the XRT-I at 1.5 (left) and 4.5 keV (right) up to 2 degrees (Serlemitsos 2007). The effective area is normalized at on-axis. The integration area is corresponding to the detector size of XIS ($17'.8 \times 17'.8$). The three solid lines in the plots correspond to different parameters of ray-tracing program while the crosses are the normalized effective area using the Crab pointings.

the whole chip, while the other is located on the side wall of the housing and is collimated in order to illuminate two corners of the CCD. The door-mounted source will be used for initial calibration only; once the door is opened, it will not illuminate the CCD. The collimated source can easily be seen in two corners of each CCD. A small number of these X-rays scatter onto the entire CCD. In addition to the emission lines created by these sources, we can utilize a new feature of the XIS CCDs, "charge injection capability," to assist with calibration. This allows an arbitrary amount of charge to be input to the pixels at the top row of the imaging region (exposure area), i.e. the far side from the

Fig. 3.14: The four XIS detectors before installation onto *Suzaku* (Koyama 2007).

frame-store region. The charge injection capability may be used to measure the CTI (charge transfer inefficiency) of each column, or even to reduce the CTI. How the charge injection capability will be used is still in progress as of this writing.

Pulse Height Determination, Residual Dark-current Distribution, and Hot Pixels

When a CCD pixel absorbs an X-ray photon, the X-ray is converted to an electric charge, which in turn produces a voltage at the analog output of the CCD. This voltage ("pulse-height") is proportional to the energy of the incident X-ray. In order to determine the true pulse-height corresponding to the input X-ray energy, it is necessary to subtract the *Dark Levels* and correct possible *optical Light Leaks*.

Dark Levels are non-zero pixel pulse-heights caused by leakage currents in the CCD. In addition, optical and UV light may enter the sensor due to imperfect shielding ("light leak"), producing pulse heights that are not related to X-rays. In the case of the ASCA SIS, these were handled via a single mechanism: Dark Levels of 16×16 pixels were sampled and their (truncated) average was calculated for every exposure. Then the same average Dark Level was used to determine the pulse-height of each pixel in the sample. After the launch of ASCA, it was found that the Dark Levels of different pixels were actually different, and their distribution around the average did not necessarily follow a Gaussian. The non-Gaussian distribution evolved with time (referred to as Residual Dark-current Distribution or RDD), and resulted in a degradation of the energy resolution due to incorrect Dark Levels.

For the *Suzaku* XIS, Dark Levels and Light Leaks are calculated separately in normal mode. Dark Levels are defined for each pixel; those are expected to be constant for a given observation. The PPU calculates the Dark Levels in the Dark Initial mode (one of

the special diagnostic modes of the XIS); those are stored in the Dark Level RAM. The average Dark Level is determined for each pixel, and if the dark level is higher than the hot-pixel threshold, this pixel is labeled as a *hot pixel*. Dark Levels can be updated by the Dark Update mode, and sent to the telemetry by the Dark Frame mode. Unlike the case of ASCA, Dark Levels are not determined for every exposure, but the same Dark Levels are used for many exposures unless they are initialized or updated. Analysis of the ASCA data showed that Dark Levels tend to change mostly during the SAA passage of the satellite. Dark Update mode may be employed several times a day after the SAA passage.

Hot pixels are pixels which always output over threshold pulse-heights even without input signals. Hot pixels are not usable for observation, and their output has to be disregarded during scientific analysis. The ASCA SIS did not identify hot pixels on-board, and all the hot pixel data were telemetered and removed during the data analysis procedure. The number of hot pixels increased with time, and eventually occupied significant parts of the telemetry. In the case of XIS, hot pixels are detected on-board by the Dark Initial/Update mode, and their positions and pulse-heights are stored in the Hot-pixel RAM and sent to the telemetry. Thus, hot pixels can be recognized on-board, and they are excluded from the event detection processes. It is also possible to specify the hot pixels manually. There are, however, some pixels which output over threshold pulse-heights intermittently. Such pixels are called flickering pixels. It is difficult to identify and remove the flickering pixels on board; they are inevitably output to the telemetry and need to be removed during the ground processing. Flickering pixels sometimes cluster around specific columns, which makes it relatively easy to identify.

The Light Leaks are calculated on board with the pulse height data after the subtraction of the Dark Levels. A truncated average is calculated for 64×64 pixels (this size may be changed in the future) in every exposure and its running average produces the Light Leak. Thus, the Light Leak is basically the same as the Dark Level in ASCA SIS.

The Dark Levels and the Light Leaks are merged in the parallel-sum (P-Sum) mode, so Dark Update mode is not available in P-Sum mode. The Dark Levels, which are defined for each pixel as the case of the normal mode, are updated every exposure. It may be considered that the Light Leak is defined for each pixel in P-Sum mode.

On-board Event Analysis

The main purpose of the on-board processing of the CCD data is to reduce the total amount transmitted to ground. For this purpose, the PPU searches for a characteristic pattern of charge distribution (called an event) in the pre-processed (post- Dark Levels and Light Leaks subtraction) frame data. When an X-ray photon is absorbed in a pixel, the photoionized electrons can spread into at most four adjacent pixels. An event is recognized when a valid pulse-height (one between the Event Lower and Upper Thresholds) is found that exceeds the pulse-heights in the eight adjacent pixels (e.g. it is the peak value in the 3×3 pixel grid). The coordinates of the central pixel are considered the location of the event. Pulse-height data for the adjacent 5×5 square pixels are sent to the Event RAM as well as the pixel location.

The MPU reads the Event RAM and edits the data to the telemetry format. The amount of information sent to telemetry depends on the editing mode of the XIS. All the editing modes (in normal mode) are designed to send the pulse heights of at least 4 central pixels of an event to the telemetry, because the charge cloud produced by an X-ray photon can spread into at most 4 pixels. Information of the surrounding pixels

may or may not output to the telemetry depending on the editing mode. The 5×5 mode outputs the most detailed information to the telemetry, i.e. all 25 pulse-heights from the 5×5 pixels containing the event. The size of the telemetry data per event is reduced by a factor of 2 in 3×3 mode.

Photon pile-up

The XIS is essentially a position-sensitive integrating instrument, with the nominal interval between readouts of 8 s. If during the integration time one or more photons strike the same CCD pixel, or one of its immediate neighbors, these cannot be correctly detected as independent photons: this is the phenomenon of photon pile-up. Here, the modest angular resolution of the *Suzaku* XRT is an advantage: the central 3×3 pixel area receives 2% of the total counts of a point source, and ∼10% of the counts fall within ∼0.15 arcmin of the image center. We calculated the count rate at which 50% of the events within the central 3×3 pixels are piled-up (the pile-up fraction goes down as we move out of the image center; this fraction is <5% for the 0.15 arcmin radius) — although we offer no formal justification for this particular limit, this is compatible with our ASCA SIS experience (i.e., at this level, the pile-up effects do not dominate the systematic uncertainties).

XIS background rate

All four XISs have low backgrounds, due to a combination of the *Suzaku* orbit and the instrumental design. Below 1 keV, the high sensitivity and energy resolution of the XIS-S1 combined with this low background means that *Suzaku* is the superior instrument for observing soft sources with low surface brightness. At the same time, the large effective area at Fe K (comparable to the XMM pn) combined with this low background make *Suzaku* a powerful tool for investigating hot and/or high energy sources as well.

In the XIS, the background originates from the cosmic X-ray background (CXB) combined with charged particles (the non-X-ray background, or NXB). Currently, flickering pixels are a negligible component of the background. When observing the dark earth (*i.e.* the NXB), the background rate between 1-12 keV in is 0.11 cts/s in the FI CCDs and 0.40 cts/s in the BI CCD; see Figure 3.15:left. Note that these are the fluxes after the grade selection is applied with only grade 0, 2, 3, 4 and 6 selected. There are also fluorescence features arising from the calibration source as well as material in the XIS and XRTs. The Mn lines are due to the scattered X-rays from the calibration sources. As shown in Table 3.4 the Mn lines are almost negligible except for XIS-S0. The O lines are mostly contamination from the day earth (3.1.3). The other lines are fluorescent lines from the material used for the sensor. Table 3.4 shows the current best estimates for the strength of these emission features, along with their 90% upper and lower limits.

The background rate on the FI chips (including all the grades) is normally less than 400 counts/frame (50 cts/s) when no class discriminator is applied. On the BI chip, the rate is normally less than 150 counts/frame (18.75 cts/s). The background rate on the FI chips is expected to reduce significantly when the class discriminator is applied. But little change is anticipated for the BI chip. Since 5×5, 3×3, and 2×2 modes require on average 40, 20, and 10 bytes per event, the minimum telemetry required for any source is ~ 58 kbits/s for 5×5 mode, ~ 31 kbits/s for 3×3, and ~ 17 kbits/s for 2×2 mode, if no class discriminator is used.

Table 3.4: Major XIS Background Emission Lines

Line	Energy	XIS-S0	XIS-S1	XIS-S2	XIS-S3
	keV	10^{-9} ct/s/pix	10^{-9} ct/s/pix	10^{-9} ct/s/pix	10^{-9} ct/s/pix
O K	0.5249	18.5 ± 0.5	$69.3^{+2.7}_{-2.6}$	$14.3^{+1.5}_{-1.3}$	$14.1^{+1.1}_{-1.2}$
Al K	1.846	1.98 ± 0.23	3.01 ± 0.51	$1.50^{+0.31}_{-0.28}$	$1.57^{+0.25}_{-0.23}$
Si K	2.307	$0.299^{+0.2080}_{-0.2074}$	2.21 ± 0.45	$0.0644(< 0.282)$	$0.543^{+0.212}_{-0.213}$
Au M	2.1229	0.581 ± 0.234	$1.13^{+0.280}_{-0.291}$	$0.359^{+0.211}_{-0.212}$	$6.69^{+2.91}_{-2.90}$
Mn Kα	5.898	$8.35^{+0.36}_{-0.34}$	0.648 ± 0.289	$0.299^{+0.209}_{-0.2086}$	$0.394^{+0.181}_{-0.18}$
Mn Kβ	6.490	$1.03^{+0.22}_{-0.216}$	$0.294(< 0.649)$	$0.00(< 0.111)$	$0.428^{+0.225}_{-0.226}$
Ni Kα	7.470	7.20 ± 0.31	6.24 ± 0.53	$3.78^{+0.26}_{-0.25}$	$7.13^{+0.36}_{-0.37}$
Ni Kβ	8.265	0.583 ± 0.183	$1.15^{+0.5}_{-0.489}$	0.622 ± 0.206	$0.983^{+0.247}_{-0.249}$
Au Lα	9.671	$3.52^{+0.27}_{-0.28}$	$3.28^{+1.16}_{-0.99}$	$1.88^{+0.31}_{-0.28}$	$3.54^{+0.36}_{-0.35}$
Au Lβ	11.514	$2.25^{+0.73}_{-0.59}$	2.91 ± 1.29	$0.752^{+0.428}_{-0.304}$	$2.67^{+0.61}_{-0.53}$

Note: Typical accumulation time are 110-160 ks

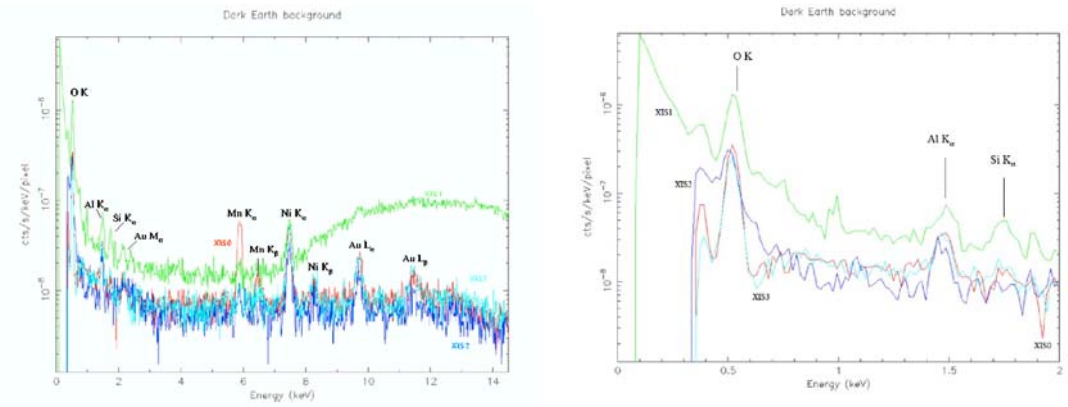

Fig. 3.15: Left: The XIS background rate for each of the four XIS detectors, with prominent fluorescent lines marked. These spectra are based on $\sim 110 - 160$ ksec of observations towards the dark Earth. These spectra does not included Cosmic X-ray background (CXB). Right: The XIS background rate for each of the four XIS detectors, showing only energies between 0.1-2.0 keV. Below 0.3 keV the background rate for the FI chips cannot be determined due to their low effective area.

Out-of-time events X-ray photons detected during the frame-store transfer do not correspond to the true image, but instead appear as a streak or blur in the readout direction. These events are called out-of-time events., and they are an intrinsic feature of CCD detectors. Similar streaks are seen from bright sources observed with *Chandra* and *XMM-Newton*. Out-of-time events produce a tail in the image, which can be an obstacle to detecting a low surface brightness feature in an image around a bright source. Thus the out-of-time events reduce the dynamic range of the detector. Since XIS spends 25 ms in the frame-store transfer, about 0.3% ($= 0.025/8 \times 100$) of all events will be out-of-time events. However, because the orientation of the CCD chip is different among the sensors, one can in principle distinguish a true feature of low surface brightness and the artifact due to the out-of-time events by comparing the images from two or more XISs.

Day Earth Contamination When the XIS field of view is close to the day earth (i.e. Sun lit Earth), fluorescent lines from the atmosphere contaminate low-energy part of the

XIS data, especially in the BI chip. Most prominent is the oxygen line, but the nitrogen line may be also noticed (Fig. 3.15:right). These lines are mostly removed when we apply the standard data screening criteria (XIS FOV is at least 20 degree away from the day earth) during the ground processing. However, small amount of contamination can remain. This contamination may be further reduced if we subtract appropriate background. This subtraction, however, may be imperfect. Thus, when neutral oxygen or nitrogen lines are detected in the XIS data, contamination from day earth should be suspected.

Radiation Damage and On-board Calibration of the XIS

The performance of X-ray CCDs gradually degrades in the space environment due to the radiation damage. This generally causes an increase in the dark current and a decrease of the charge transfer efficiency (CTE). In the case of XIS, the increase of the dark current is expected to be small due to the low (–90°C) operating temperature of the CCD. However, a decrease in CTE is unavoidable. Thus, continuous calibration of CCD on orbit is essential to the good performance of the XIS. For this purpose, we use a radio isotope source and charge injection as explained below:
(i) Each XIS carries ^{55}Fe calibration sources near the two corners of the chip, which will be used to monitor the instrument gain.
(ii) Each XIS CCD is equipped with charge injection capability, which may be useful to measure and even suppress CTI.

Nonetheless, it is difficult to predict based on existing data how well we can calibrate the long-term performance change of XIS on orbit.

On-ground event selection

Internal (non X-ray) background events can be effectively removed using the pattern on CCD pixels (GRADE), the position (STATUS) and time of an event. The definition of GRADE is shown in Figure 3.16. Most of X-ray events take GRADE = 0, 2, 3, 4, or 6. On the other hand, most of the events of other GRADEs are dominated by non X-ray events, and should be excluded. STATUS parameter stores the information of pixel quality of an event. Known hot pixels, bad CTE columns, flickering pixels, and pixels on the segment boundaries can be removed by selecting the events with STATUS$<$ 131072. The parameters used in good time interval (GTI) selection are shown in Table 3.5. The signal to noise ratio can be improved with an appropreate GTI criteria, indicated in Table 3.5.

Table 3.5: Parameters used in GTI selection of *Suzaku*

Parameter	Definition	Recommended value to use
SAA	Whether the satellite was in the SAA[a] or not	eq.0
T_SAA	Time after the last SAA duration (s)	> 255
ELV	Elevetion angle from the Earth limb (degree)	> 5
DYE_ELV	Elevation angle from the day Earth limb (degree)	> 20
COR	Cut off rigidity of the cosmic ray (GeV/c/particle)	> 8

[a]: South Atlantic anomaly

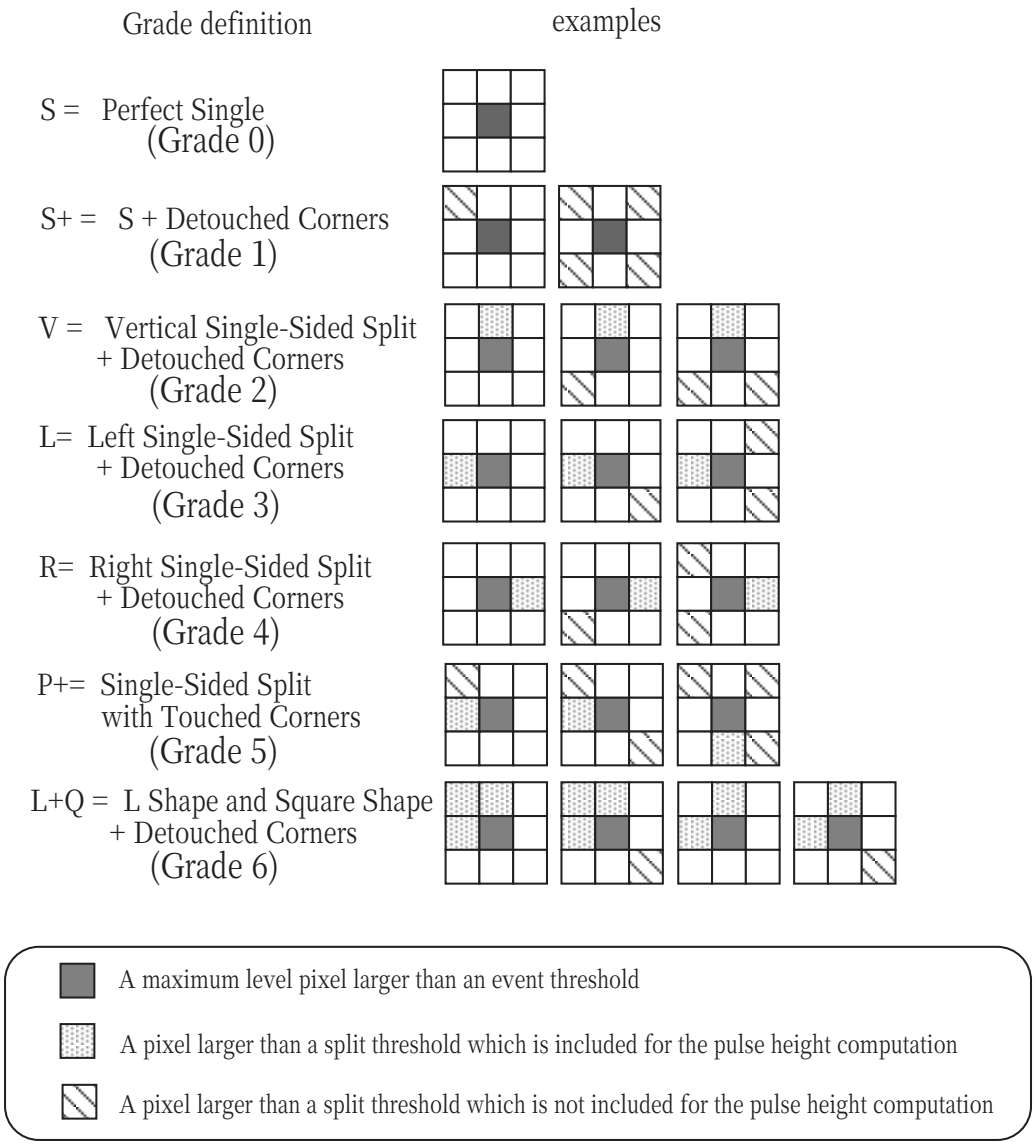

Fig. 3.16: Definition of GRADE of CCD events.

Contamination crrection

The OBF has been gradually contaminated in time by out-gassing from the satellite. The contamination rate af- ter the XIS door-open is unexpectedly high, and the rate is dierent from sensor to sensor. Moreover, the thickness of the contamination varies with position on the OBF.

The contamination has caused a signicant reduction in low-energy response since launch. We therefore need to include additional, time-varying low energy absorption in the response function. This is given as a function of both the observation date after the XIS door-open, and of de- tector coordinates (specifying the position on the OBF). For this purpose, we measured the on-axis extra absorp- tion by observing a SNR 1E0102–72 and an isolated neu- tron star RX J1856.5–3754. At the time of writing, we have not conclusively determined the chemical composi- tion for the contamination material(s). From the overall spectral shape in the low energy absorption for all the available X-ray sources and the best guess for the out- gassing source in *Suzaku*, we assume that the contami- nant contains predominantly C and O with the number ratio C/O 6. Figure 3.17 shows the time histories of the contamination accumulated on the OBF. Empirically,

the time dependence of the contamination thickness is assumed to follow the exponential form as; $N_c = a - b \times \exp -day/c$, where N_c is the carbon column density in units of 10^{18} cm^{-2} (C/O = 6). To measure the off-axis absorption, we used diuse X-rays from the bright Earth rim and the Cygnus Loop. The former emits characteristic K lines of N_I and O_I (neutral atoms) and the latter provides K lines from C_{VI}, N_{VII}, O_{VII} and O_{VIII} (He-like or H-like atoms). Since the for-mer can be observed frequently, we trace the time history of o-axis absorption over successive one-month periods after the XIS door-open (13 August, 2005). With the two reasonable assumptions that (1) the N:O line ratio is uniform over the eld of view and (2) the contamination is azimuthally constant, we can derive the radial prole of the dierence of contamination thickness from the center value. We show the radial proles of the column den- sity of carbon in gure 15 for one month and ve months after the door-open. This radial prole is approximated by a function of $1/[1 + \{r/a(t)\}^{b(t)}]$. The time dependent parameters, $a(t)$ and $b(t)$ are determined and up-dated regularly.

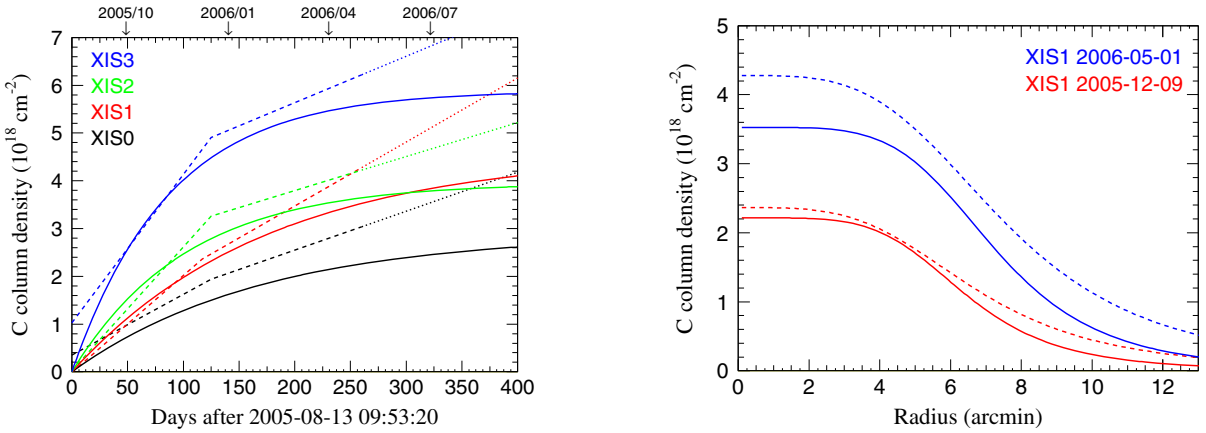

Fig. 3.17: Left: The time history of the contamination of all four XIS detectors, measured at the center of the OBF. The dotted and solid line denoted the models used by CALDB file of 2006-5-24 and 2006-10-24 version, respectively. Right: The radial prole of the contamination of the BI (XIS1).

3.1.4 Uncertainties of metal abundance

We must consider three uncertaities for metal abundance, especially oxygen and magnesium, analizing the spectra of XIS.

1. Systematic uncertainties (NXB and CXB level, gain and CTI correction and so on.)
2. Our Galactic components
3. Contamination on XIS

(1): We check the effects by changing the NXB and CXB levels by ±10%. (2): Because the O VII and O VIII lines emitted from ICM are coupled with these emitted from our Galaxy, the estimation of the emission from our Galaxy is very impotant to decide the oxygen abundance of ICM. (3): As descibed in 3.1.3, because the observed spectra are absorbed by the contaminant on XIS, the effect are taken into account with the arfs,

and we also check the uncertainty of the arfs by changing the amount of contaminant by $10 \sim 20\%$.

It is the negligible effects for the central brightness region of the cluster, however it is the severe effects, especially (2) and (3), for the faint region such as the outskirts of the cluster. Especialy the soft X-ray band (below $\sim$1 keV), the effects of (2) and (3) are impotant. Thus, we are careful to analyze the spectra for the decision of the oxygen and magnesium abundance. In addtion, the abundance may vary whether we use a one or multi temperature model.

3.2 *XMM-Newton*

The ESA (European Space Agency) X-ray satellite *XMM-Newton* was launched on 10 December 1999 from Kourou (French Guiana), by the Ariane-V rocket (Jansen et al. 2001). It was placed into a highly eccentric orbit, with an apogee of about 115,000 km, a perigee of about 6,000 km, and an orbital inclination of 33°, which provides the best visibility in the southern celestial sky. Although the orbital period is 48 hours, the exposure available for scientific data analysis is limited to 39 hours (140 ksec) per orbit. This is because observations are not carried out when the satellite altitude is less than 46,000 km, where the radiation background related to the Earth's magnetosphere is severe. *XMM-Newton* provides the following three types of science instrument.

- European Photon Imaging Camera (EPIC)
- Reflection Grating Spectrometer (RGS)
- Optical Monitor (OM)

The three EPIC cameras; the two different types of CCD camera, MOS and pn, and the two detectors of the RGS spectrometers reside in the focal planes of the X-ray telescopes, while the OM has its own telescope. A sketch of the *XMM-Newton* payload is displayed in Fig.3.18.

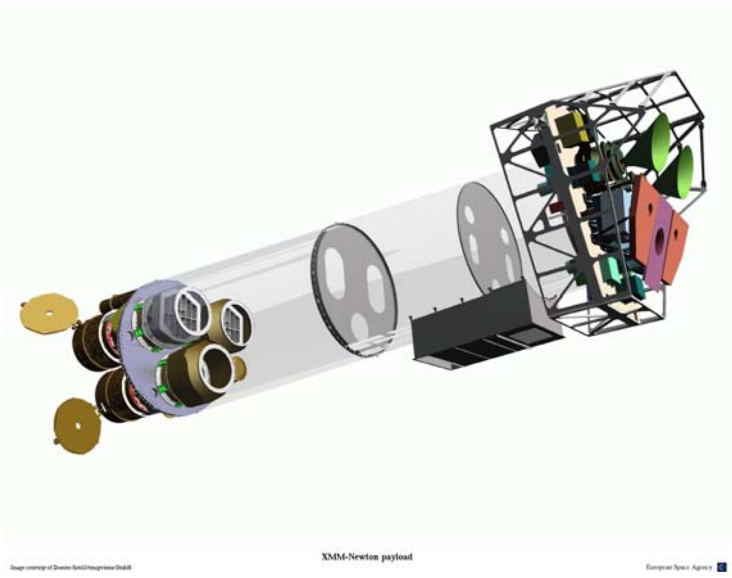

Fig. 3.18: Sketch of the *XMM-Newton* payload. The mirror modules, two of which are equipped with Reflection Grating Arrays, are visible at the lower left. At the right end of the assembly, the focal X-ray instruments are shown: The EPIC MOS cameras with their radiators (black/green horns), the radiator of the EPIC pn camera (violet) and those of the (light blue) RGS detectors (in pink). The OM telescope is obscured by the lower mirror module.

There are in total six science instruments on board *XMM-Newton*, which are operated simultaneously. The instruments can be operated independently and each in different modes of data acquisition.

In the following sections, we describe the X-ray telescopes and EPIC cameras, because we mainly use these instruments in our study. We summarize the basic performance of the EPIC cameras in table 3.6.

Table 3.6: Basic performance of the EPIC detectors

	EPIC-MOS	EPIC-pn
Illumination method	Front illuminated	Back illuminated
Pixel size	40 μm	150 μm
	$1.1''$	$4.1''$
Field of view (FOV)	$30'$	$30'$
PSF (FWHM/HEW)	$5''/14''$	$6''/15''$
Spectral resolution	$\sim$70 eV	$\sim$80 eV
Timing resolution	1.5 ms	0.03 ms
Bandpass	0.15-12keV	0.15-15keV

3.2.1 X-ray Telescopes

Design Structure

XMM-Newton's three XRTs are co-aligned with an accuracy of better than about 1 arcmin. Each of the three telescopes consists of 58 Wolter type-I mirrors, and the mirror grazing incidence angles range between 17 and 42 arcmin. The focal length is 7.5 m and the diameter of the largest mirrors is 70 cm. One telescope with the PN camera at the focal point has a light path as shown in Figure 3.19. The two others have grating assemblies in their light paths, diffracting part of the incoming radiation onto their secondary focus (see Figure 3.20). About 44 % of the incoming light focused by the XRT is directed onto the MOS camera at the prime focus, while 40 % of the radiation is dispersed by a grating array onto a linear strip of CCDs. The remaining light is absorbed by the support structures of the RGAs.

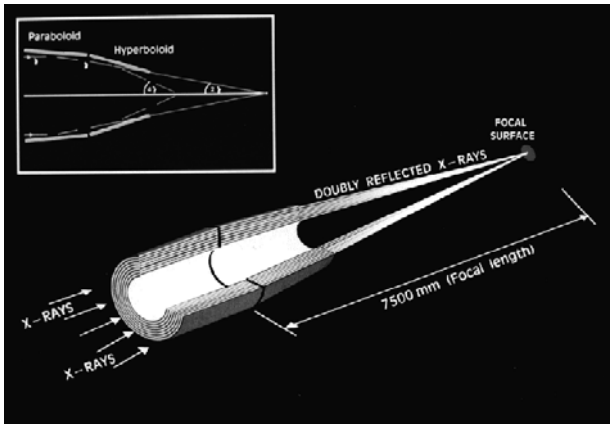

Fig. 3.19: The light path in *XMM-Newton*'s XRT with the PN camera in focus.

Point-spread function (PSF) of XRTs

A point-spread function (PSF) determines the imaging quality of an XRT. Figure 3.21 shows the in orbit on-axis images obtained by each detector. The radial substructures are caused by the spiders holding the mirror shells. Figure 3.22 displays the azimuthally averaged profile of the PSF of one XRT together with the best-fit King profile, which has the form $A(1/[\{1 + (r/r_c)^2\}^{\alpha}])$, where r is the radial distance from the center of

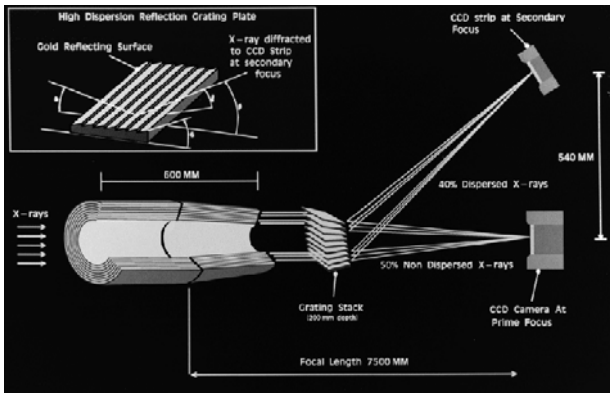

Fig. 3.20: The light path in *XMM-Newton*'s XRT with the MOS camera and RGA.

the PSF, r_c is the core radius and α is the slope of the King model. Figure 3.22 shows the encircled energy function (EEF) as a function of radius from the center of the PSF for several different energies. For on-axis source, high energy photons are reflected and focused predominantly by the inner shells of the XRTs. The inner shells apparently give better focus than the average of all shells, hence the EEF increase with increasing photon energy. A half energy width (HEW), which means the width including half of all the reflected photons, of the PSF can be derived from EEF. Table 3.7 lists the on-axis HEW of the different XRTs measured in orbit and on ground.

The PSFs of the XRTs depend on the source off-axis angle. As the off-axis angle increases, the HEW of PSF becomes larger.

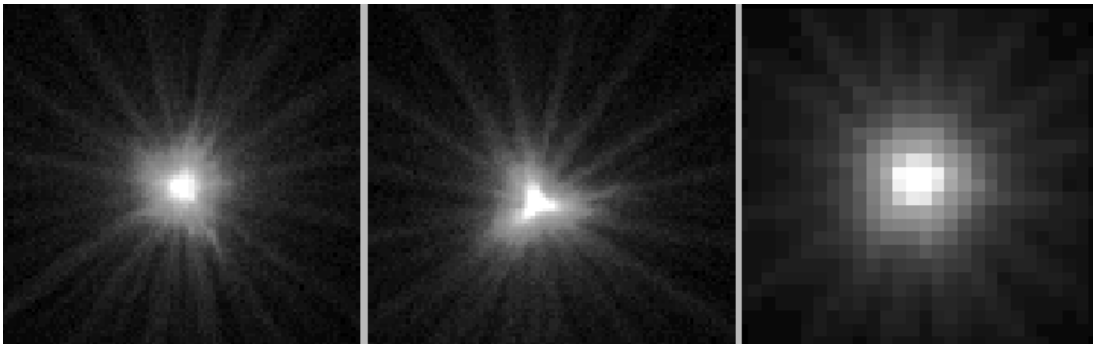

Fig. 3.21: On-axis images of the MOS1, MOS2 and PN XRTs (left to right). The images are 110 arcsec wide and a logarithmic scale has been used to visualize the wings of the point spread function.

Table 3.7: The on-axis in orbit and on ground 1.5 keV HEW of the different XRT.

Instr.	PN	MOS1	MOS2
	orbit/ground	orbit/ground	orbit/ground
HEW [arcsec]	15.2/15.1	13.8/13.6	13.0/12.8

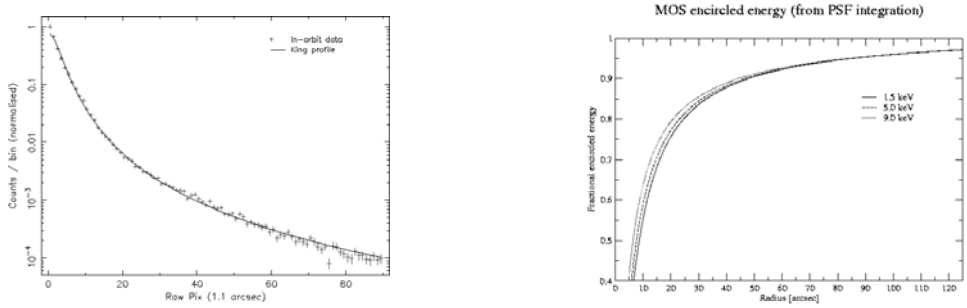

Fig. 3.22: Left: Radial counts distribution for the on-axis PSF of the MOS1 XRT in the 0.75–2.25 keV energy range. The solid line indicates the best-fit King profile. Right: The encircled energy function as a function of angular radius (on-axis) at different energies. The curves are calculated assuming a fractional encircled energy of 100 % at a radial distance of 5 arcmin.

Effective Area (EA) of XRTs

An effective area is an indicator of ability of collecting photons. *XMM-Newton* carries the XRT with the largest effective area of focusing telescope ever. The total mirror geometric effective area (EA) at 1.5 keV energy is about 1,550 cm^2 for each telescope, i.e., 4,650 cm^2 in total. Figure 3.23 shows the on-axis effective area of all *XMM-Newton* XRTs. The EAs of the two MOS cameras are lower than that of the pn, because only part of the incoming radiation falls onto these detectors, which are partially obscured by the RGAs (see Figure 3.20). Not only the shape of the X-ray PSF, but also the effective area of the XRT is a function of off-axis angle within the field of view. Decreasing of photons reflected effectively in the XRT arises from an increasing off-axis angle. This effect is called vignetting. Figure 3.23 displays the vignetting function as a function of off-axis angle for several different energies. The vertical axis is normalized by the on-axis effective area.

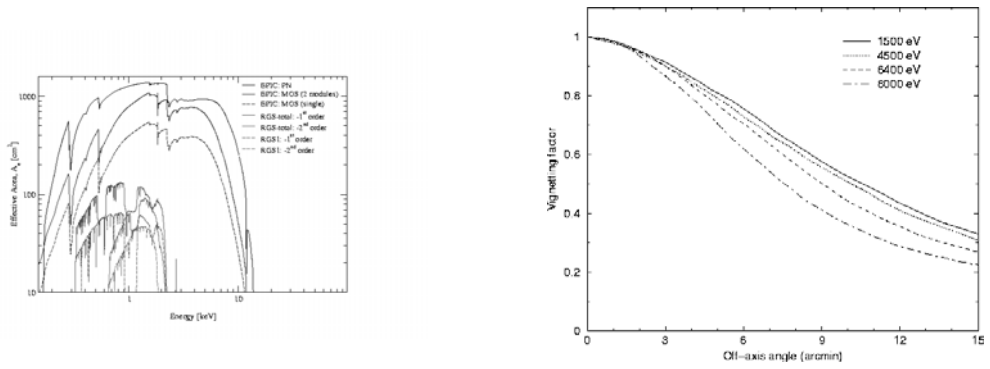

Fig. 3.23: Left: The net effective area of all *XMM-Newton* XRT, combined with the response characteristics of the focal detectors. Right: Vignetting function as a function of off-axis angle at several different energies (based on simulations).

Straylight Rejection

X-ray straylight is produced by rays which are singly reflected by the mirror hyperbolas and which reach the sensitive area of the focal plain detectors. Thus, an X-ray baffle was implemented to shadow those singly reflected rays. It consists of two sieve plates made of concentric annular aperture stops located in front of the mirrors at 85 mm and 145 mm, respectively. The design is such that the entrance annular aperture of each mirror remains unobstructed for on-axis rays. The collecting area of straylight in the EPIC detector as a function of off-axis angle for a point source is about 3 cm^2 for stray sources located between 20 arcmin and 1.4° from the optical axis. The ratio of the X-ray straylight collecting area to the on-axis effective area is smaller than 0.2 % at 1.5 keV for a point source located at off-axis angles of 0.4–1.4° and negligible at higher off-axis angles. Figure 3.24 displays the effect of straylight, which is obtained from the observation of GRS 1758-258 (a black hole candidate near the Galactic center). Some sharp arcs are caused by single mirror reflections of photons possibly from GX 5-1 which is located at off-axis angle of 40 arcmin to the north and outside the field of view.

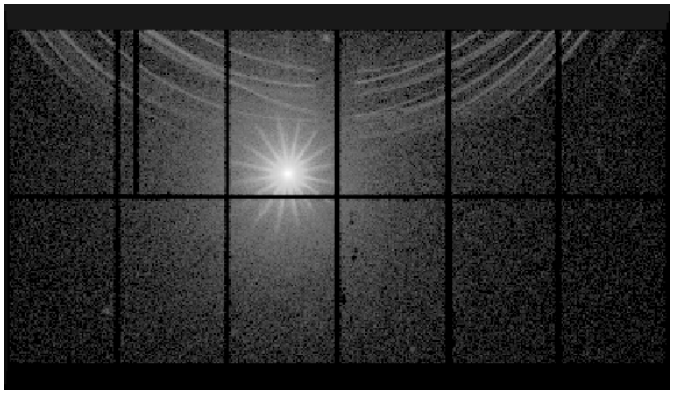

Fig. 3.24: The effect of straylight appeared in PN image of GRS 1758-258.

3.2.2 European Photon Imaging Camera (EPIC)

Two of *XMM-Newton*'s X-ray telescopes are equipped with EPIC MOS (Metal Oxide Semi-conductor, Turner et al. (2001)) CCD arrays, the third carries a different CCD camera called EPIC PN (Strüder et al. 2001). The EPIC cameras offer the possibility to perform extremely sensitive imaging observations over a field of view of 30 arcmin and the energy range from 0.15 to 15 keV, with moderate spectral ($E/\Delta E \sim$ 20–50) and angular resolution (15 arcsec HEW). The detector layout and the baffled X-ray telescope FOV of both types of EPIC cameras are shown in Figure 3.25. The PN chip array is slightly offset with respect to the optical axis of its X-ray telescope so that the nominal, on-axis observing position does not fall on the central chip boundary. This ensures that more than 90 % of the energy of an on-axis point source are collected on one PN CCD chip. Two EPIC MOS cameras are rotated by 90° with respect to each other. The dead spaces between the MOS chips are not gaps, but unusable areas due to detector edges (the MOS chip physically overlap each other, the central one being located slightly behind the ones in the outer ring). All EPIC cameras are operated in photon counting mode with a fixed, mode dependent frame read-out frequency.

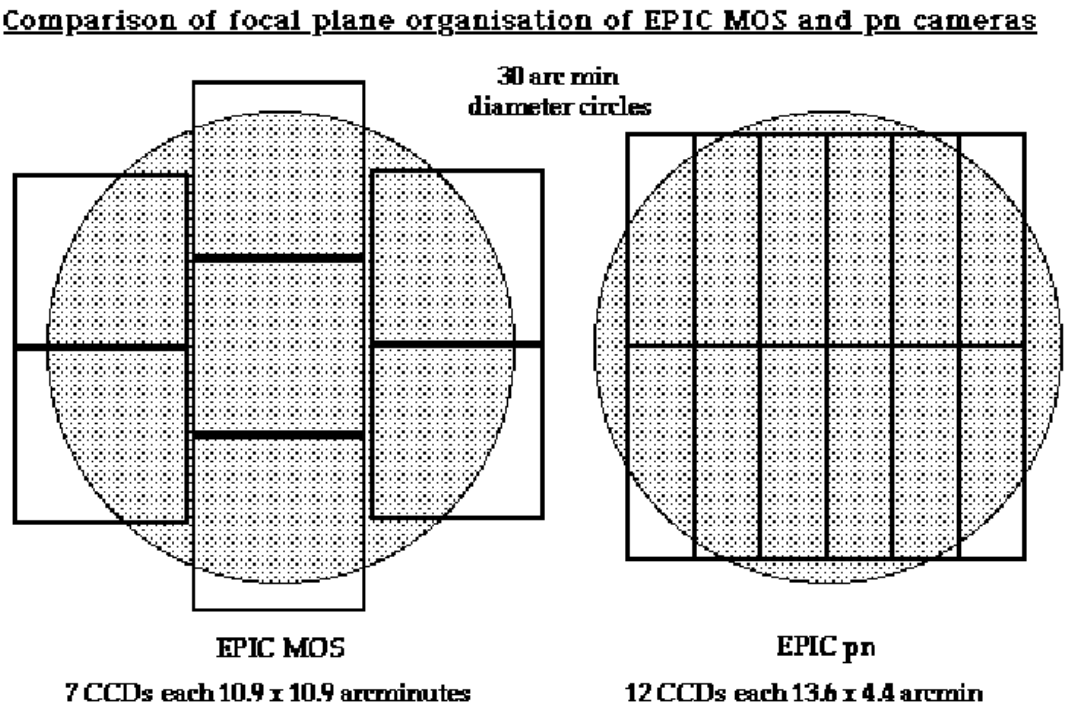

Fig. 3.25: A rough sketch of the field of view of the two types of EPIC cameras (MOS, left; PN, right). The shaded circle depicts a 30 arcmin diameter area which is equivalent with the XRT field of view.

Angular resolution

The EPIC MOS and PN cameras have pixels with sizes of 40 and 150 μm, respectively. For the focal length of the X-ray telescopes (7.5 m), these pexel size corresponds to 1.1 arcsec and 4.1 arcsec on the sky. Since they are smaller than the HEW of XRT (15 arcsec), EPIC's angular resolution is basically determined by the PSF of the mirror modules.

Energy resolution

The resolving power of EPIC cameras is determined by the intrinsic energy resolution of the individual pixels. Figure 3.26 and 3.26 show the energy resolution (FWHM) of MOS and PN, respectively. The measured in-flight FWHM of the Al Kα (1.5 keV) and Mn Kα (5.9 keV), which are the on-board calibration lines, are also plotted in Figure 3.26. It is well known that the energy resolution of MOS cameras has been gradually decrease due to the CTI (charge transfer inefficiency) effect, which means the imperfect transfer of charge as it is transported through the CCD to the output amplifiers. The latest calibration status is found at *XMM-Newton* Science Operation Centre.[1] The accuracy of the energy determination is about 10 eV over the full energy range and for all modes except for MOS timing mode.

Quantum efficiencies

The quantum efficiency of both types of EPIC CCD chips as a function of photon energy is displayed in Figure 3.27 and 3.27. These chips were calibrated using laboratory

[1] *http://xmm.vilspa.esa.es/external/xmm_sw_cal/calib/documentation.shtml#EPIC*

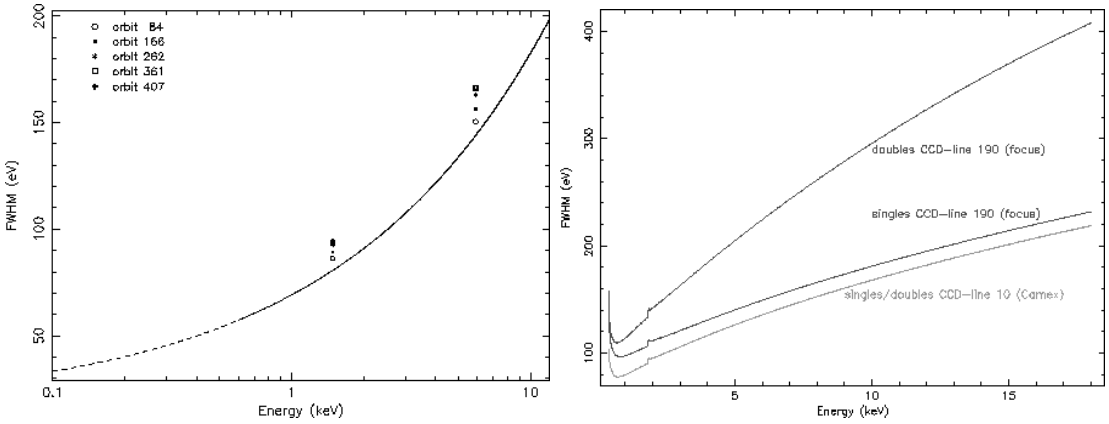

Fig. 3.26: Left: The EPIC MOS energy resolution (FWHM) as a function of energy. The solid curve is a best-fit $E^{0.5}$ function to ground calibration data between 0.1–12.0 keV. Below around 0.6 keV (shown by the dotted region), surface charge loss effects distort the main photopeak significantly from a Gaussian form and, hence the effective energy resolution. The measured in-flight FWHM of the Al Kα (1.487 keV) and Mn Kα (5.893 keV) lines are also plotted. Right: The EPIC PN energy resolution (FWHM) as a function of energy. Curves are given for single and double events (full frame mode) at the focus position node.

X-ray beams, synchrotron generated monochromatic X-ray beams, before launch, and celestial X-ray source measurements. We can see the typical X-ray absorption fine structure (XAFS) behavior around the silicon K edge at 1.838 keV. Ground calibration measurements have shown that the quantum efficiency of MOS CCDs is uniform above 400 eV. Below this energy, spatial variations are seen as patches in the outer parts of the CCDs where the response is degraded. This inhomogeneity is currently not taken into account by the *XMM-Newton* science analysis system (SAS).

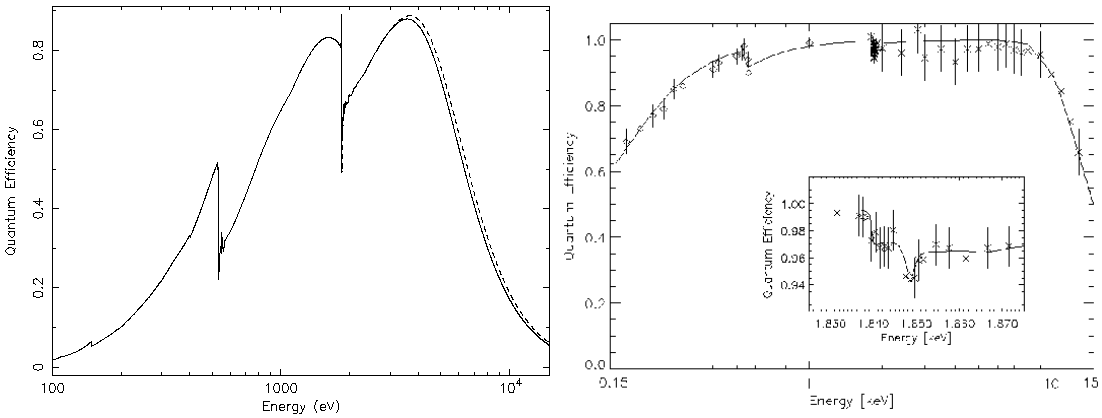

Fig. 3.27: Left: Quantum efficiency of the EPIC MOS camera as a function of photon energy. Right: Quantum efficiency of the EPIC PN camera as a function of photon energy.

EPIC Filters

The EPIC CCDs are not only sensitive to X-ray photons, but also to IR, visible and UV light. Therefore, if an astronomical target has a high optical to X-ray flux ratio, there is

a possibility that the X-ray signal becomes contaminated by those photons. To prevent such a contribution, each EPIC camera is equipped with a set of 3 separate aluminised optical blocking filters, named *thick*, *medium* and *thin*. The thick filter should be used for all point source targets up to m_V of 1–4 (MOS) or 0–3 (PN). The medium filter is about 10^3 less efficient than the thick filter, therefore, it is useful for preventing optical contamination from point sources as bright as $m_V = 8$–10. The thin filter is about 10^5 less efficient than the thick filter, so the use of this filter will be limited to point sources with optical magnitudes about 14 magnitudes fainter than the corresponding thick filter limitations.

Event pattern

An absorbed sometimes deposits its energy over more than one pixels. This is called split event, and in this case the charges mus be summed up over the relevent pixels. This process is automatically done by analysis software. The split pattern is classified in Figure 3.28. The patterns 0-12 for MOS and 0-4 for pn are considered to be X-ray events, while the others are false events induced by charged particles. Because of its much larger pixel size than MOS, the charge split occurs less frequently in pn (Turner et al. 2001).

Any events which located at around an edge or bad pixel are flagged by negative value. These events have possibility that the energy of these events are not correct. If we make a condition that the events have flag=0, we remove the events which are rocated around the edge ore bad pixel.

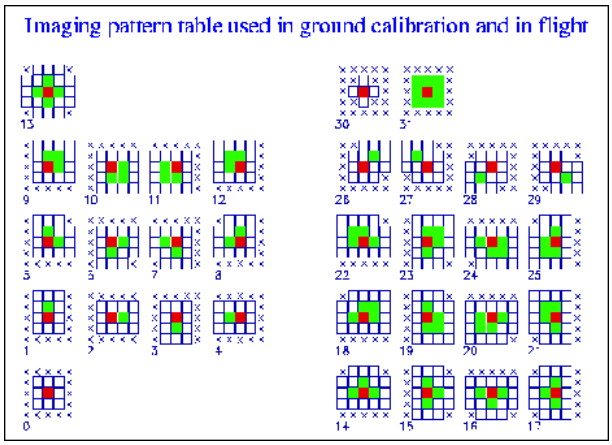

Fig. 3.28: Event patterns recognized by the MOS (pn) detectore. The red pixel is the centre pixel, its signal is above threshold and is the largest signal in the 3×3 inner matrix. The green pixels have signals above threshold. The white pixels have signal below threshold. The crosses indicate pixels no considered.

3.2.3 EPIC Background

The EPIC background can be divided into two parts: a cosmic X-ray background (CXB), and an instrumental background. The latter component may be further divided into a detector noise component, which becomes important at low energies (i.e. below 200eV) and a second component which is due to the particles interaction. This component is characterized by a flat spectrum and is particularly important at high energies (i.e. above a few keV).

The particle induced background can be divided into two components: an external 'flaring' component, characterized by strong and rapid variability, which is often totally absent and a second more stable internal component. The flaring component is currently attributed to soft protons, which are presumably funneled towards the detectors by the X-ray mirrors. The stable component is due to the interaction of high-energy particles with the structure surrounding the detectors and possibly the detectors themselves. We summarize the all background component below.

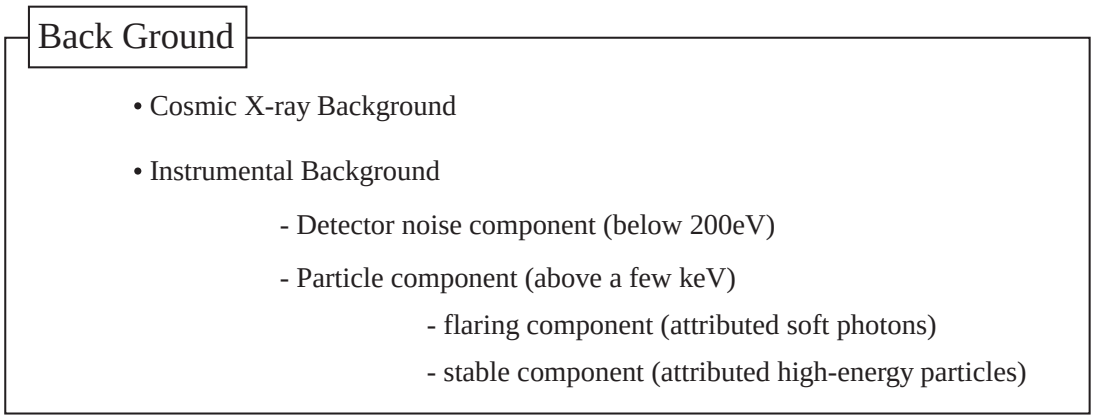

In the following we describe some of the main properties of both components.

Temporal properties

As shown in Figure 3.29, the EPIC background count rate often exhibits sudden increases by as large as two orders of magnitudes, called 'flares'. Such phenomena are not observed in the *ASCA* SIS. This is mainly due to the difference in their orbits. *ASCA* had an almost circular orbit with an altitude of 520-620 km, while XMM-Newton take highly eccentric orbits, with apogees of $\sim 115,000$ km and perigees of $\sim 6,000$ km. Therefore, XMM-Newton fly mostly outside the Earth's magneto-sphere. Now it is known that the background flares are caused by soft protons with energies below 1 MeV, reflected and focused by the X-ray mirrors. The spectra of soft proton flares are variable and no clear correlation is found between intensity and spectral shape. The current understanding is that soft protons are most likely organized in clouds populating the Earth's magneto-sphere. The number of such clouds encountered by XMM-Newton in its orbit depends upon many factors, such as the altitude of the satellite, its position with respect to the magneto-sphere, and the amount of solar activity.

The EPIC background events in quiescent (non-flaring) periods are produced mainly by the interaction of high energy particles with the structure surrounding the detectors, and the detectors themselves. This component varies only by a small fraction, and on relatively longer timescales. On a representative time scale of several tens ksec, the standard deviation of both PN and MOS count rates is about 8 % (Katayama et al. 2004; Pizzolato 2001; Read & Ponman 2003).

Spectral properties

In Figure 3.30, we show the MOS1 and PN spectra extracted from a blank sky region. These background spectra consist of non X-ray background (NXB) and cosmic X-ray background (CXB). The NXB is induced mainly by charged particles. The CXB is mainly

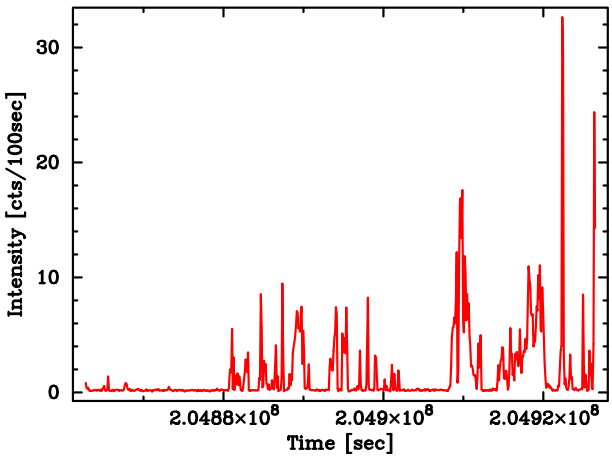

Fig. 3.29: An example of light Curve from a MOS1 observation badly affected by proton flares.

dominates at lower energies by soft thermal emission around the solar system. The entire background spectra are dominated by the NXB at high energy regions, and the CXB becomes more important as the energy decreases. Their contributions are comparable at the energy of ~ 1 keV.

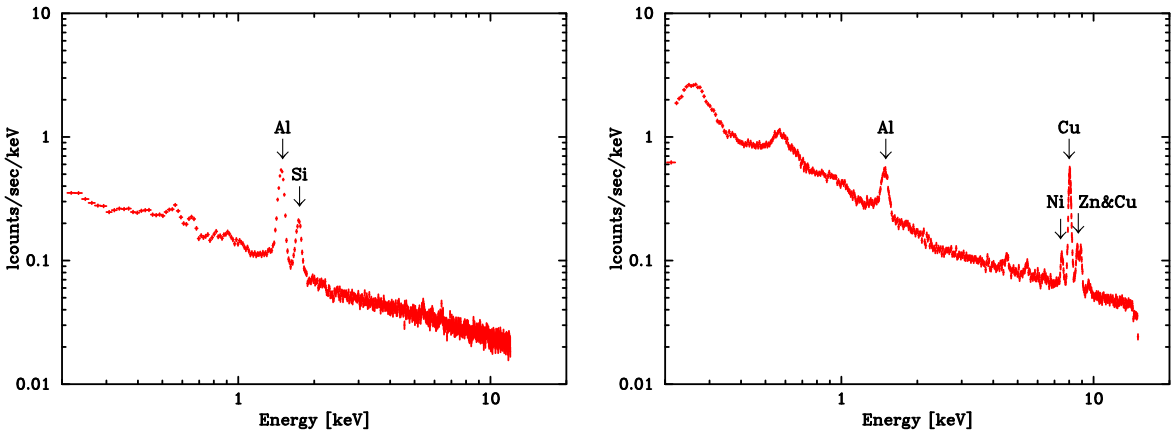

Fig. 3.30: MOS1(left) and PN(right) background spectrum from a blank sky region. In the left figure, the prominent features around 1.5 and 1.7 keV are Al K and Si K fluorescence lines, respectively. On the other hands, he prominent features, in right figure, are identified as Al-K (1.5 keV), Cr-K (5.5 keV), Ni-K, Cu-K, Zn-K (8.0 keV) and Mo-K (17.5 keV), respectively.

Fig. 3.30 shows several distinct fluorescence lines. In PN spectra, Al-K, Ni, Cu, and Zn-K complex lines are prominent, while Al and Si-K lines are outstanding in the MOS. These lines are emitted from surrounding materials such as electronic circuit boards for the signal readout, excited by high energy charged particles. Both the PN and MOS spectra rise below ~ 0.5 keV, due to the detector noise which is more time variable than the continuum above 0.5keV.

Spatial properties

Because the CXB surface brightness is highly uniform, its brightness distribution on the focal plane obeys the effective area. Due to the vignetting effect, the CXB brightness is highest at the detector center, and gradually decreases toward the periphery.

The distribution of the Si-K line in the MOS is concentrated along the edges of some CCDs. This is attributed to Si-K X-rays escaping from the back side of a neighboring CCD. The asymmetric distribution arises because the 7 CCD chips slightly overlap with one another when viewed from the telescope, although their 3-dimensional positions are offset along the optical axis. This layout is intended to reduce the gaps between CCD chips.

Spatial distributions of emission lines are rather complicated. Figure 3.31 show some background images in limited energy bands. The emission in the Cu-K band is very weak at the center of PN (fig. 3.31 right). Actually, the Cu-K line is insignificant in the spectrum extracted there. The Cu-K line image with the central hole agrees with the layout of electronics boards beneath the PN CCDs, indicating that the Cu-K photons come from them. The same mechanism produces semicircular dark regions at the right and reft sides.

The continuum components of the NXB also have inhomogeneous distribution on the focal plane. The NXB image shows central excess brightness, by about 25 %. The shape is similar to the central hole seen in the Cu-K band image (fig. 3.31), although in this case the brightness shows excess, not a deficit.

As is implied by these non-uniform distributions of various components, the background spectrum strongly depends on the detector position. Therefore, when we use other observations as the background fields, we must extract the background spectrum from the same detector region as the analyzing target.

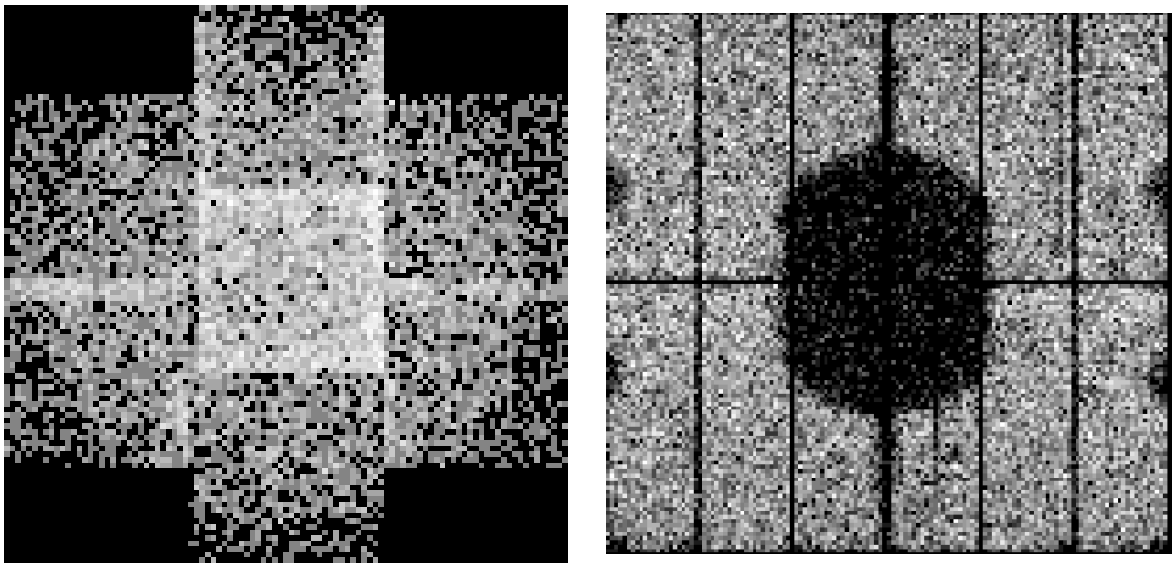

Fig. 3.31: The MOS(left) and PN(right) background image. The MOS image in the energy band centered on Si-K fluorescent line region. As the same, the PN image in the Cu-K fluorescent line energy region.

Chapter 4

Observation and Data Reduction

4.1 *Suzaku*

4.1.1 Observation log

We selected two clusters, A 1060 and AWM 7, and three groups, HCG 62 and NGC 507 to study the temperature and metallicity with *Suzaku*. The basic properties of these clusters and groups are shown in table.4.1. These clusters and groups are nearby, bright and observed with *Suzaku*.

Table 4.1: Basic properties of cluster and groups.

Object	z	D^* [Mpc]	$1'^*$ [kpc]	virial radius† [Mpc/arcmin]	$N_{\rm H}^{\ddagger}$ [$\times 10^{20}$ cm^{-2}]	Coordinates§ R.A(J2000)	Dec(J2000)	l	b	Morphology§ [BM]
A 1060	0.0114‖	49.3	14.0	1.53/109	4.90	$10^{\rm h}36^{\rm m}51^{\rm s}$	$-27°31'.6$	$269.^{\circ}63$	$26.^{\circ}51$	III
AWM 7	0.01724§	74.9	21.0	1.65/78.6	9.83	$2^{\rm h}54^{\rm m}32^{\rm s}$	$+41°35'.2$	$146.^{\circ}35$	$-15.^{\circ}62$	I
HCG 62	0.0145♯	62.8	17.8	1.08/60.7	3.03	$12^{\rm h}53^{\rm m}08^{\rm s}$	$-9°13'.4$	$303.^{\circ}64$	$53.^{\circ}65$	Compact group
NGC 507	0.01646§	71.4	20.1	1.08/53.7	5.24	$1^{\rm h}23^{\rm m}40^{\rm s}$	$+33°15'.3$	$130.^{\circ}64$	$-29.^{\circ}13$	
NGC 720	0.005821§	25.1	7.2	0.653/90.7	1.54	$1^{\rm h}53^{\rm m}00^{\rm s}$	$-13°44'.3$	$173.^{\circ}02$	$-70.^{\circ}36$	

* H_0 =70 km/s/Mpc, $\Omega_\Lambda = 1 - \Omega_M = 0.73$

† $r_{180} = 1.95\ h_{100}^{-1}\sqrt{k\langle T\rangle/10\ \mathrm{keV}}$ Mpc (Markevitch et al. 1998)

‡ Dickey & Lockman (1990)

§ NASA/IPAC EXTRAGALACTIC DATABASE (NED)

‖ Yamasaki et al. (2002)

♯ Morita et al. (2006)

Table 4.2: *Suzaku* Observation Logs for the Clusters and Groups.

Object	Seq. No.	Obs. date	Coordinates(J2000) RA_NOM	DEC_NOM	Exp. ksec	After screening (BI/FI) ksec
A 1060 center	800003010	2005-11-22T14:56:45	$10^{\rm h}36^{\rm m}42.^{\rm s}8$	$-27°31'42''$	40.5	40.2/40.2
A 1060 offset	800004010	2005-11-20T23:24:45	$10^{\rm h}38^{\rm m}03.^{\rm s}8$	$-27°31'42''$	55.5	52.9/54.6
AWM 7 center	801035010	2006-08-07T05:38:14	$2^{\rm h}54^{\rm m}32.^{\rm s}0$	$+41°35'15''$	19.0	18.9/18.9
AWM 7 east	801036010	2006-08-05T06:25:29	$2^{\rm h}56^{\rm m}08.^{\rm s}4$	$+41°35'18''$	38.5	38.3/38.3
AWM 7 west	801037010	2006-08-06T05:46:37	$2^{\rm h}52^{\rm m}55.^{\rm s}8$	$+41°35'16''$	39.8	39.6/39.7
HCG 62	800013020	2006-01-20T09:00:20	$12^{\rm h}53^{\rm m}06.^{\rm s}0$	$-9°12'15''$	119.4	118.0/118.2
NGC 507	801017010	2006-07-28T14:51:16	$1^{\rm h}23^{\rm m}40.^{\rm s}0$	$+33°15'21''$	79.6	79.2/79.2
NGC 720	800009010	2005-12-30T13:29:48	$1^{\rm h}53^{\rm m}00.^{\rm s}5$	$-13°44'19''$	160.4	159.5/150.7

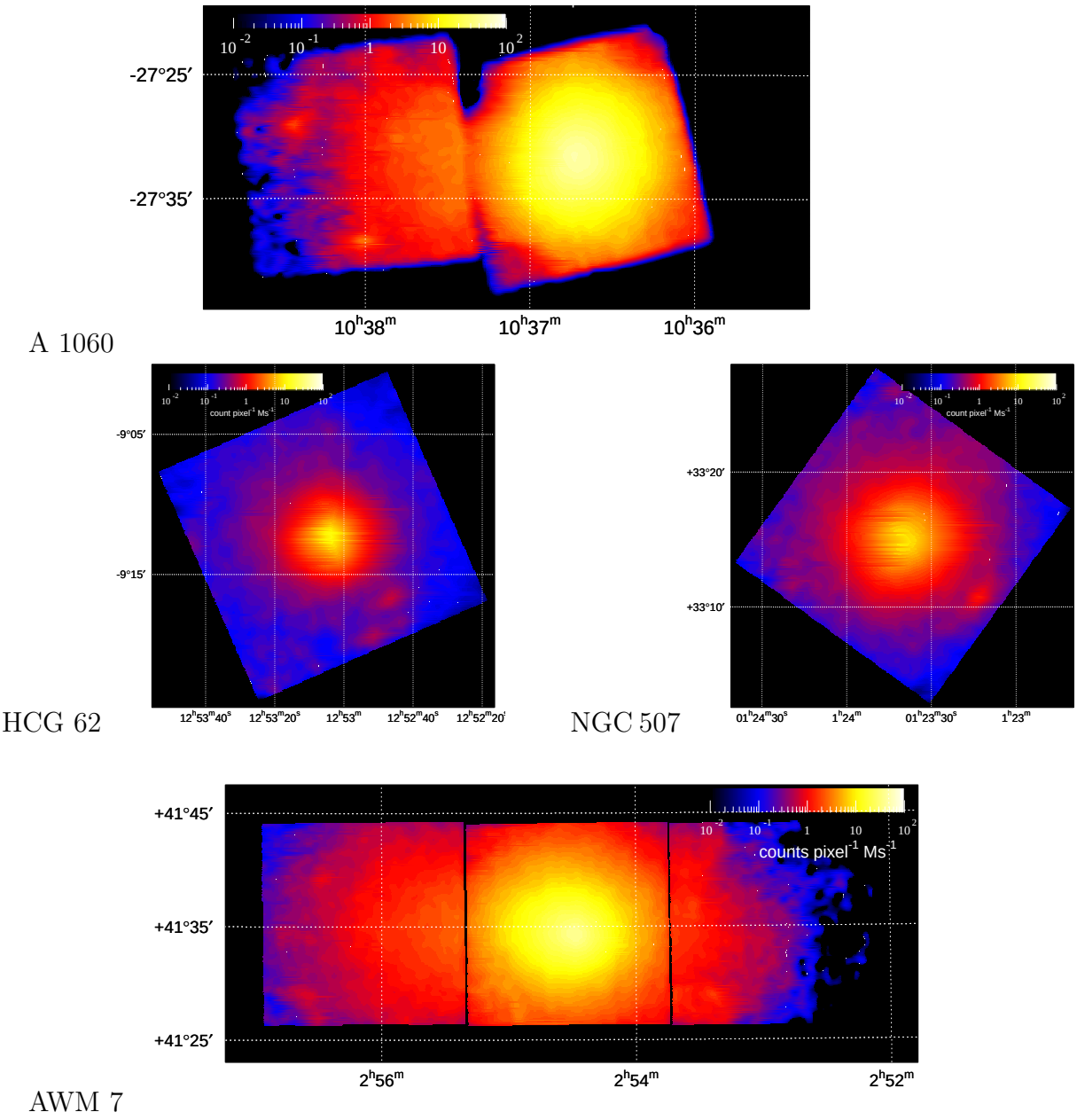

Fig. 4.1: Combined XIS image of the central and offset observations in the 0.5–7.0 keV energy range for A 1060(top), 0.5–4.0 keV energy range for HCG 62(middle:left) and NGC 507(middle:right), and 0.5–7.0 keV energy range for AWM 7(bottom). The observed XIS0-3 images are added on the sky coordinate after removing each calibration source region, and smoothed with $\sigma = 16$ pixel $\simeq 17''$ Gaussian. Estimated components of extragalactic X-ray background (CXB) and instrumental background (NXB) are subtracted, and exposure is corrected.

The observation log is summarized in table 4.2, and the combined XIS (Koyama 2007) images is shown in figure 4.1. We utilize only the XIS data in this paper. The XIS is an X-ray CCD camera, which consists of one back-illuminated sensor (BI = XIS1) and three front-illuminated sensors (FI = XIS0, XIS2, XIS3). The BI and FI sensors have different advantages. The former has higher quantum efficiency in the soft energy band ($E \leq 1$ keV), while the latter shows lower instrumental non X-ray background (NXB). The XIS was operated in the Normal clocking mode (no window nor burst option, so 8 s

Table 4.3: Estimated column density of the contaminant for each sensor at the center of CCD in unit of 10^{18} cm^{-2}.

	XIS0	XIS1	XIS2	XIS3
A 1060				
Carbon	1.37	1.83	2.52	4.04
Oxygen	0.228	0.305	0.420	0.673
AWM 7				
Carbon	2.53	3.97	3.83	5.79
Oxygen	0.422	0.662	0.639	0.964
HCG 62				
Carbon	1.76	2.73	3.13	4.94
Oxygen	0.293	0.454	0.521	0.824
NGC 507				
Carbon	2.52	3.94	3.83	5.78
Oxygen	0.419	0.657	0.638	0.963
NGC 720				
Carbon	1.61	2.49	2.93	4.69
Oxygen	0.268	0.415	0.489	0.781

exposure per frame), with the standard 5×5 or 3×3 editing mode (Koyama 2007).

The optical blocking filters (OBF) of the XIS have been gradually contaminated in time by out-gas from the satellite, and the degradation of the low energy transmission was already significant in November 2005. The thickness of the contaminant is different among sensors, and is also dependent on the location on the CCD. The estimated column density (C/O=6 in number ratio is assumed) at the center of the CCD is listed in table 4.3, and the calculated X-ray transmission for XIS1 (BI) at each annular region is plotted in figure 4.2.[1] This effect is considered in the calculation of the Ancillary Response File (ARF) by the "xissimarfgen" Ftools task (Ishisaki et al. 2006). The energy resolution was also degraded slightly (FWHM $\sim$ 150 eV at 5.9 keV) after the launch, due to the radiation damage of the CCD.

4.1.2 Data Reduction

We used the version 0.7 and 1.2 processing data (Mitsuda 2007), and the analysis was performed with HEAsoft version 6.0.6 and XSPEC 11.3.2t for A 1060 and HEAsoft version 6.1.1 and XSPEC 11.3.2t for AWM 7, HCG 62, and NGC 507. We started the event screening from the cleaned event file, in which selection of the event grade and bad CCD column, disposal of non-observational intervals (during maneuver, data-rate low, South Atlantic Anomaly, Earth occultation, bright Earth rim to avoid scattered solar X-ray), and removal of hot and flickering pixels by the "cleansis" Ftools, were already conducted. The exposure time given in table 4.2 is for the cleaned event file. We further applied the Good-Time Intervals (GTI) given for excluding the telemetry saturation by the XIS team. The light curve of each sensor in the 0.3–10 keV range with 16 s time bin was also

[1]The calibration database file of `ae_xiN_contami_20060525.fits` for A 1060, and `ae_xiN_contami_20061024.fits` for AWM 7, HCG 62, and NGC 507 was used for the estimation of the XIS contamination ($N = 0, 1, 2, 3$ corresponding to the XIS sensor).

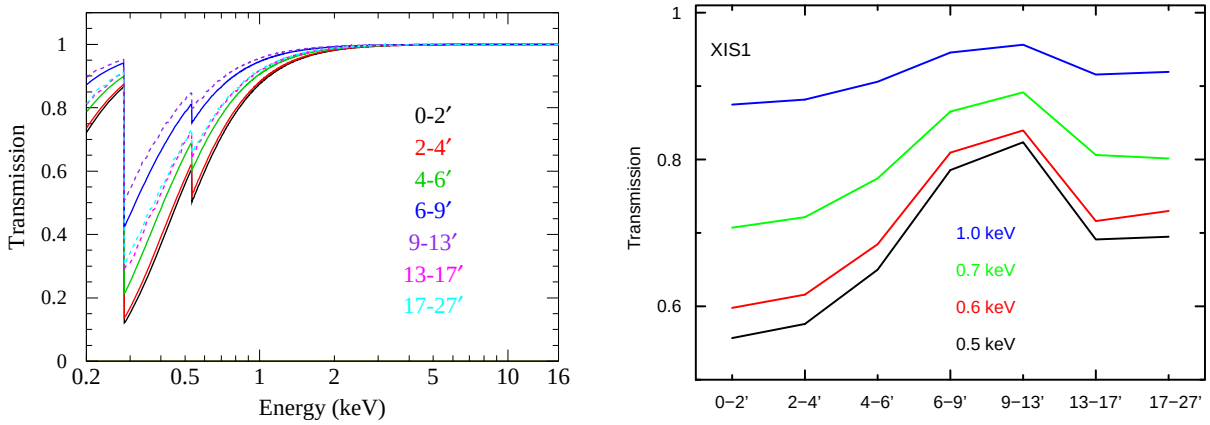

Fig. 4.2: Left: Estimated transmission of the contaminant on the XIS1 sensor for each annular region used in the spectral analysis plotted against the X-ray energy. Transmissions in the central observations are drawn by solid lines, and the offset observations are by dashed lines. These transmissions are calculated by "xissimarfgen" with a calibration file of `ae_xi1_contami_20060525.fits`, and written in the CONTAMI_TRANSMIS column of the ARF response. Right: The calculated transmission plotted against each annular region in the energies of 0.5, 0.6, 0.7, and 1.0 keV.

examined to reject periods of anomalous event rate greater or less than $\pm 3\sigma$ around the mean. After the above screenings, remaining exposure of the central observation shows in figure 4.2. These exposures are not so different from those in table 4.2, which represent that the NXB was almost stable during the both observations. The event screening with the cut-off rigidity (COR) was not performed in our data.

4.1.3 NXB & CXB Subtraction

In order to subtract the NXB and the extra-galactic cosmic X-ray background (CXB; see Brandt & Hasinger (2005) for review), we used the night earth database of 770 ks exposure provided by the XIS team for the NXB, and estimated the CXB component using the ASCA results.

The night-earth spectra were extracted from the same detector region as each observation in order to cancel positional variation of the NXB. Furthermore, we divided the night-earth data referring to COR in the ranges of < 4 GV, 4–13 GV in 1 GV step, and > 13 GV, because it is known that the intensity and energy spectrum of the NXB are primarily correlated with COR at the orbital location of the satellite. The NXB spectra to be subtracted in the spectral fitting were estimated by adding these COR-sorted night-earth spectra weighted with exposure times of each observation in the corresponding COR range.

The CXB component was estimated by the "fake" command of XSPEC using uniform-sky ARFs. We assumed a power-law spectrum for the CXB with the values by Kushino et al. (2002), $\Gamma = 1.4$ and $S_X = 5.97 \times 10^{-8}$ erg cm^{-2} s^{-1} sr^{-1} (2–10 keV), absorbed with the neutral hydrogen column in table 4.2. The above CXB intensity is taken from table 3 of Kushino et al. (2002), for the integrated spectrum with source elimination brighter than $S_0 = 2 \times 10^{-13}$ erg cm^{-2} s^{-1} (2–10 keV) in the GIS filed of view with $\Gamma = 1.4$ (fix) and the nominal NXB level (0%). It is confirmed that this gives a reasonable estimate of the CXB contribution for the XIS in subsection 6.2 of Ishisaki et al. (2006) and Fujimoto et al. (2006).

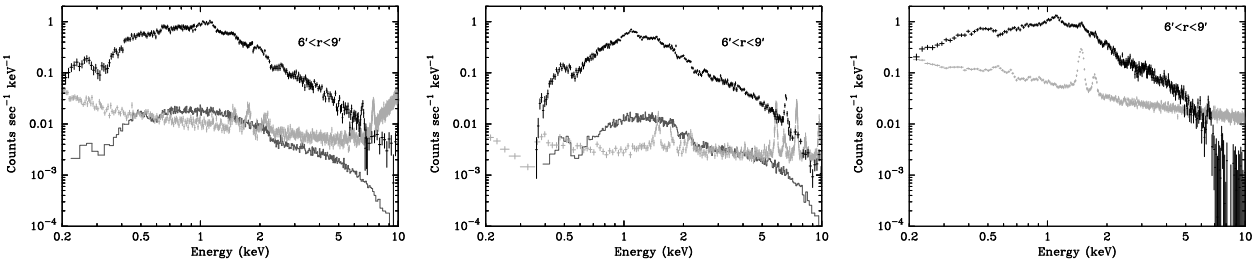

Fig. 4.3: Left: The observed spectrum at the annular region of 6–9′ of A 1060 with the *Suzaku* BI (XIS1) sensor is plotted in black crosses after subtracting the estimated CXB and NXB components, which are plotted by gray crosses and a black histogram, respectively. Middle: Same as (a) but for the FI (XIS0+XIS2+XIS3) sensors. The count rate drop below ≤ 0.4 keV is due to the event threshold of the FI CCDs (Koyama 2007). Although 0.2–10 keV energy range is shown here, only 0.4–7.1 keV band was utilized for the spectral fitting for both BI and FI. Right: Same as (a) but for the XMM-Newton MOS1 sensor, and the estimated CXB+NXB component using blank-sky observations are plotted in gray. The 0.5–8.0 keV energy range was used for the spectral fitting with XMM-Newton.

Table 4.4: The best-fit parameters of figure 4.4.

	$r_{\rm in}$	$\beta_{\rm in}$	$Norm_{\rm in}$	$r_{\rm out}$	$\beta_{\rm out}$	$Norm_{\rm out}$
A 1060	3.7′	1.3	1.26	7.3′	0.69	0.96
AWM 7	0.51′	0.44	9.0	5.06′	0.60	2.26
HCG 62*	0.1′/0.48′	0.65	0.83/0.29	9.0	0.63	0.0018
NGC 507	1.0′	0.48	5.1	-	-	-
NGC 720†	0.08′	0.42	-	-	-	-

* Morita et al. (2006)

† Buote et al. (2002)

Figures 4.3 show the background level for *Suzaku* BI, FI sensors, and XMM-Newton MOS1, at the same 6–9′ annulus of A 1060. The observed spectrum after the CXB and NXB subtraction are compared with the estimated CXB and NXB spectra separately for *Suzaku*, while sum of the CXB and NXB are indicated for the XMM-Newton because the blank-sky data was used as the background. These figures show the background level of *Suzaku* XIS is $\sim 50\%$ lower than that of XMM-Newton. It is also notable that there is a strong Al-K$_\alpha$ peak at 1.49 keV for the XMM-Newton background, which makes the determination of the Mg abundance quite difficult. The S/N ratio of the *Suzaku* XIS BI/FI sensors are by about 1.8/2.0 times higher than that of the XMM-Newton MOS at 1 keV, and 1.3/1.8 times higher at 4 keV. The particle background is more stable for *Suzaku* than XMM-Newton due to its low-earth orbit.

4.2 XMM-Newton

4.2.1 Observation & Analysis

The same dataset with Hayakawa et al. (2006) was utilized. We used only the MOS data, and data reduction and analysis were performed with SAS version 6.0 and HEAsoft version 6.0.6. As for the XMM-Newton data, data reduction and spectral analysis were based on

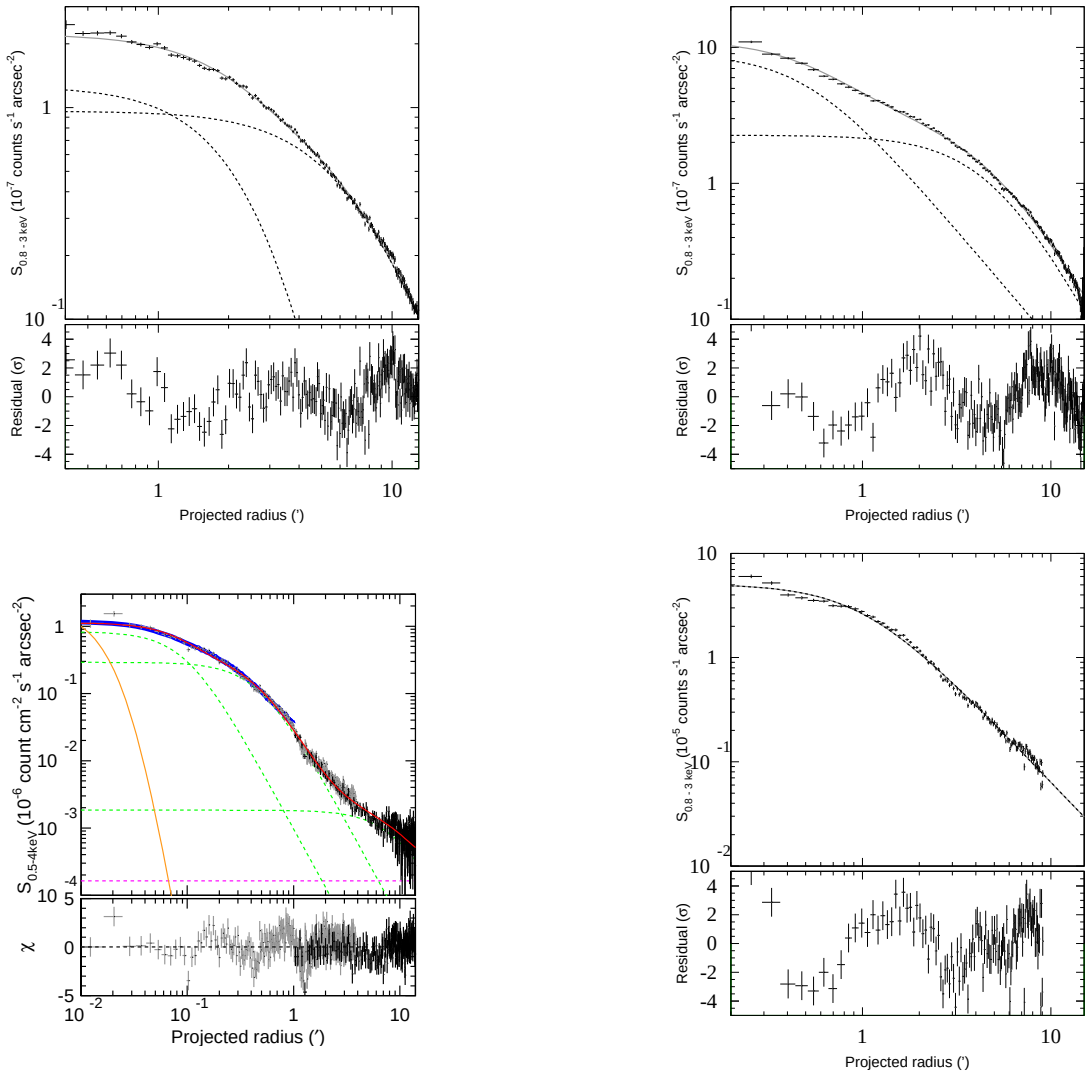

Fig. 4.4: In the upper panel, radial profiles of the surface brightness of A 1060(top:left), AWM 7(top:right) and NGC 507(bottomright) in the 0.8–3 keV band are plotted for XMM-Newton MOS1+2 ($r < 13'$) and a radial profile of surface brightness of HCG 62 (bottom:left) in the 0.5–4 keV band (Morita et al. 2006). The best-fit double-β model is shown by the solid gray line, and the two β-components are indicated by dashed lines. In the bottom panel, fit residuals are shown in unit of σ.

Sato et al. (2005) and Hayakawa et al. (2006). Hayakawa et al. (2006) have reported the temperature and abundance profiles of A 1060 with XMM-Newton observation, however, we reanalyzed the A 1060 data in order to compare with the *Suzaku* results on the same criterion. The differences form Hayakawa et al. (2006) are: *(1)* the event extraction region, *(2)* using the *vapec* thin thermal plasma model (Smith et al. 2001) instead of *vmekal* (Mewe et al. 1985; Mewe et al. 1986), and *(3)* deriving the element abundances separately.

We also derived the surface brightness profile of A 1060, AWM 7, and NGC 507 with XMM-Newton, because it was needed to generate the *Suzaku* ARFs. Figure 4.4 shows a radial profile of A 1060, AWM 7, NGC 507 in the 0.8–3 keV energy range, fitted with a double-β model. For HCG 62, we used the value in Morita et al. (2006), the radial profile is placed in figure 4.4. The best-fit parameters are summarized in table 4.4.

Chapter 5

Spectral Analysis and Results

5.1 A 1060

5.1.1 *Suzaku* XIS Spectra

We extracted spectra from seven annular regions of 0–2′, 2–4′, 4–6′, 6–9′, 9–13′, 13–17′ and 17–27′, centered on (RA, Dec) = ($10^{\rm h}36^{\rm m}42\overset{\rm s}{.}8$, $-27^\circ31'42''$). The first four annuli were taken from the central observation, and the rest of thee annuli were from the offset observation. Table 5.1 lists areas of the extraction regions (arcmin^2), coverage of the whole annulus (%), the SOURCE_RATIO_REG values (%; see caption for its definition) and the observed counts in 0.4–7.1 keV including NXB and CXB for the BI and FI sensors.

Although the thickness of the OBF contamination is different among sensors as shown in table 4.3 and figure 5.1(b), we have confirmed that the four sensors give quite consistent fit results after incorporating the contamination effect into the ARFs, as demonstrated in figure 5.1(a). We therefore add the three FI spectra (XIS0, XIS2, XIS3), hereafter.

Each annular spectrum is shown in figure 5.2. The ionized Mg, Si, S, Fe lines are clearly seen in each ring. The O VII and O VIII lines are prominent in the outer rings, however, most of the O VII emission is supposed to come from the local Galactic emission, which will be examined in detail in subsections 5.1.3–5.1.5.

5.1.2 Strategy of Spectral Fit

The basic strategy of the spectral fit is described in subsection 6.3 of Ishisaki et al. (2006). The observed spectrum is assumed to contain (A) thin thermal plasma emission from the ICM, (B) local Galactic emission, (C) CXB, and (D) NXB. The estimation of (C) and (D) is described in subsection 4.1.3, and both are subtracted from the observed spectrum. The spectrum of (B) can be represented by one or two thin-thermal plasma model(s), *apec*, with 1 solar abundance, however, it may vary from field to field by more than an order of magnitude (Kushino et al. 2002). The ICM spectrum (A) can be represented by a variable abundance thin-thermal plasma model, *vapec*, whose best-fit parameters are what we want. An important point is that the spatial distributions are different between (A) and (B). The former follows the surface brightness of the cluster, while the latter is supposed to have almost a uniform distribution in the XIS field of view.

We therefore generated two different ARFs for the spectrum of each annulus, $A^{\rm U}$ and $A^{\rm B}$, which respectively assume the uniform-sky emission and $\sim 1^\circ \times 1^\circ$ size of the double-β surface brightness profile obtained with the XMM-Newton data (table 4.4). $A^{\rm U}$ was used to evaluate the CXB, and the surface brightness of the Galactic component (B) at each annulus in combination with the XSPEC "fakeit" command, and $A^{\rm B}$ was used

Table 5.1: Area, coverage of whole annulus, SOURCE_RATIO_ REG and observed counts for each annular region of A 1060. SOURCE_ RATIO_REG represents the flux ratio in the assumed spatial distribution on the sky (double-β model) inside the accumulation region to the entire model, and written in the header keyword of the calculated ARF response by "xissimarfgen".

Region *	Area † (arcmin^2)	Coverage †	SOURCE_ * RATIO_REG	Counts ‡ BI	FI
0–2′	12.6	100.0%	7.7%	30,549	64,606
2–4′	37.7	100.0%	13.7%	55,186	114,220
4–6′	62.8	100.0%	13.8%	49,259	100,080
6–9′	137.0	96.9%	17.2%	52,719	100,750
9–13′	49.1	17.8%	2.8%	10,696	17,329
13–17′	76.2	20.2%	2.2%	11,032	21,010
17–27′	167.3	12.1%	2.0%	18,055	28,834

* The first four annuli are extracted from the central observation, and others are from the offset observation.

† The largest values among four sensors are presented.

‡ Observed counts including NXB and CXB in 0.4–7.1 keV.

for the actual fitting. We have confirmed that the assumed double-β surface brightness profile is consistent with the observed *Suzaku* image by about $\pm 15\%$ in figure 5 of Ishisaki et al. (2006). We further constrained that the surface brightness of the Galactic component (B) is nearly constant among all the extraction annuli, whereas its spectral shape is determined from the spectral fit of our *Suzaku* data. Details will be described in the next subsection.

We adopted the nominal Redistribution Matrix Files (RMF) of `ae_xi`N`_20060213.rmf` for spectral fitting, although slight degradation in energy resolution is expected. The ARFs were generated by "xissimarfgen", and were convolved with the RMFs and added for three FI sensors, using the "marfrmf" and "addrmf" tasks in Ftools. The spectra from BI and FI are fitted simultaneously in the 0.4–7.1 keV band except for energy range of anomalous response around the Si K-edge (1.825–1.840 keV). We ignored below 0.4 keV because the C edge (0.284 keV) seen in the BI spectra could not be reproduced perfectly in our data. Energy range above 7.1 keV was also ignored because background Ni line ($\sim$ 7.5 keV) left artificial structures after the NXB subtraction at large radii. It is also known that the XIS response in $E \sim 8$ keV are not fully understood at the present stage. In the simultaneous fit of BI and FI, only the normalization are allowed to be different between them, although we found that the derived normalizations are quite consistent between the two.

5.1.3 Estimation of Galactic Component

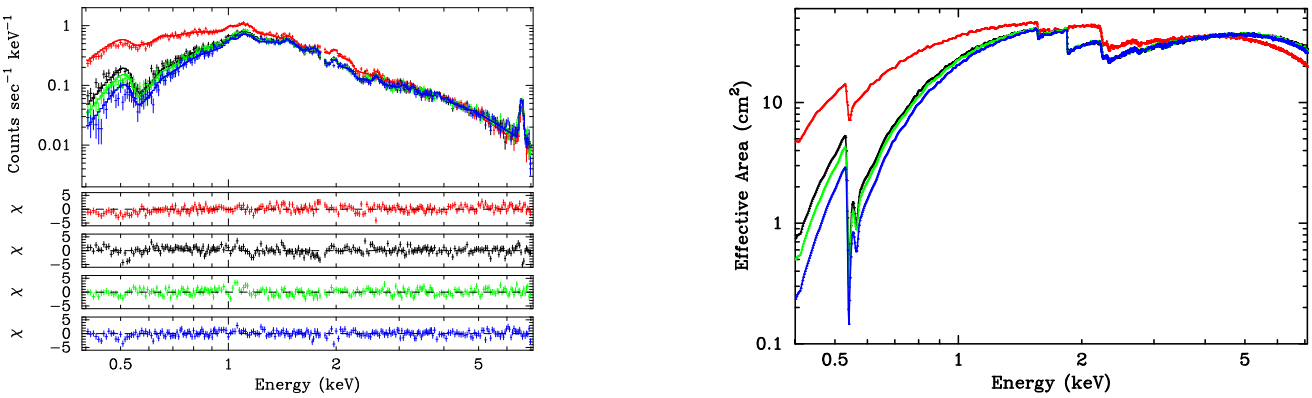

Fig. 5.1: (a) The uppermost panel show the observed spectra after subtracting the estimated CXB and NXB components at the annular region of 2–4′ plotted separately for the XIS0 (black), XIS1 (red), XIS2 (green), and XIS3 (blue) sensors. The cross markers denote the observed spectra and the solid lines show the best-fit model with $apec_1 + apec_2 + phabs \times vapec$. The energy range around the Si K-edge (1.825–1.840 keV) is ignored for the spectral fit. Lower three panels show the residuals of the fit in unit of σ for XIS1, XIS0, XIS2, and XIS3 from upper to lower, respectively. (b) Plots of the calculated XIS effective area (ARF + RMF) including the XIS quantum efficiency. These responses are used in the spectral fit in (a) with the same colors. The quantum efficiency is much higher for BI (XIS1; red) than FI sensors, while the OBF contamination is thicker in the order of XIS3, XIS2, XIS1, and XIS0.

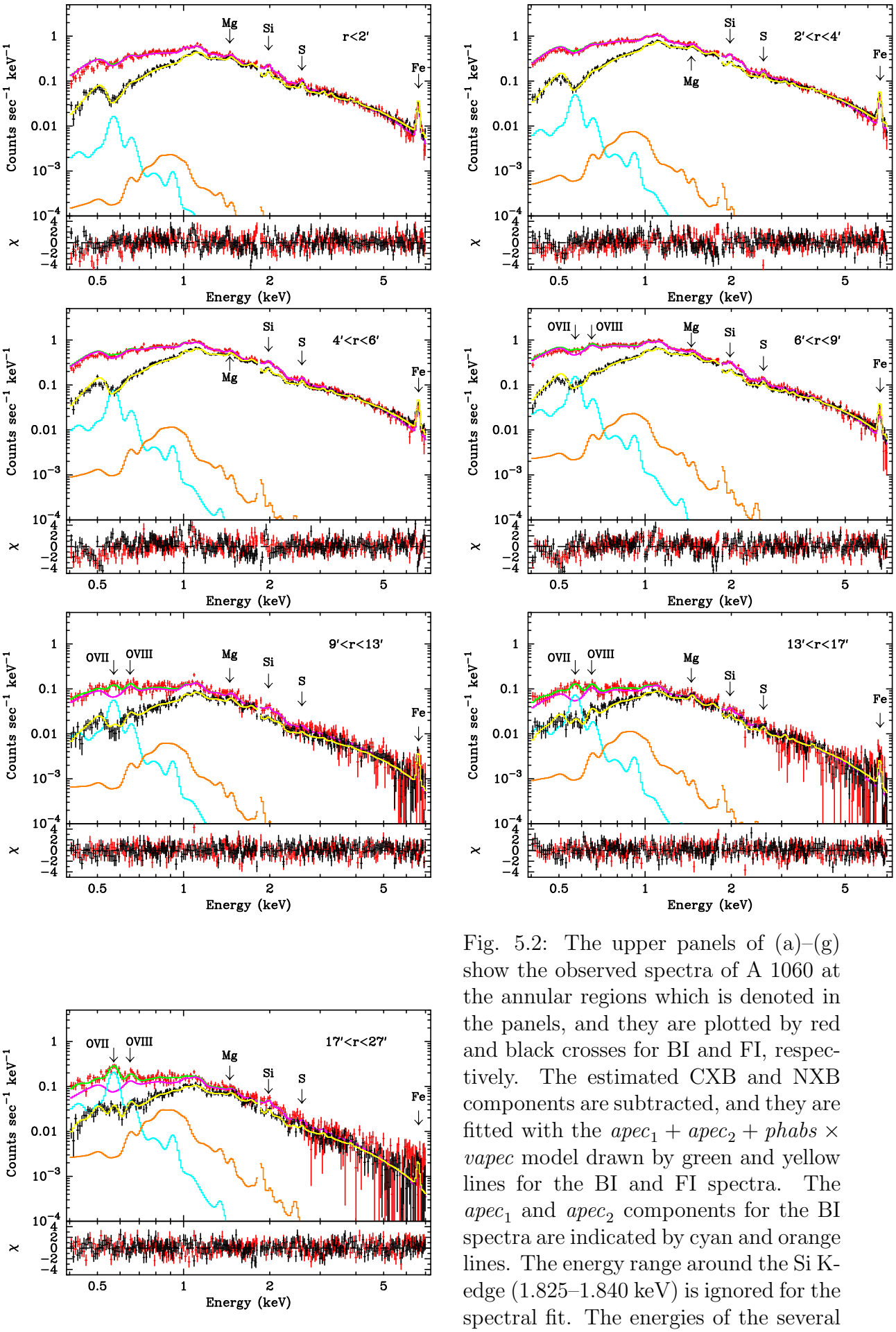

Fig. 5.2: The upper panels of (a)–(g) show the observed spectra of A 1060 at the annular regions which is denoted in the panels, and they are plotted by red and black crosses for BI and FI, respectively. The estimated CXB and NXB components are subtracted, and they are fitted with the $apec_1 + apec_2 + phabs \times vapec$ model drawn by green and yellow lines for the BI and FI spectra. The $apec_1$ and $apec_2$ components for the BI spectra are indicated by cyan and orange lines. The energy range around the Si K-edge (1.825–1.840 keV) is ignored for the spectral fit. The energies of the several prominent lines are also indicated in the panels. The lower panels show the fit residuals in unit of σ.

Table 5.2: The best-fit parameters of the *apec* component(s) for the simultaneous fit of the spectra in 13–17′ and 17–27′ annuli of A 1060.

Fit model	$Norm_1$ *	kT_1 (keV)	$Norm_2$ *	kT_2 (keV)	χ^2/dof
(a) $apec_1 + phabs \times vapec$	1.20 ± 0.07	$0.179^{+0.006}_{-0.012}$	—	—	1128/994
(b) $apec_1 + apec_2 + phabs \times vapec$	1.66 ± 0.35	$0.143^{+0.014}_{-0.015}$	0.21 ± 0.05	$0.737^{+0.063}_{-0.088}$	1082/992

* Normalization of the *apec* component divided by the solid angle, $\Omega^{\rm U}$, assumed in the uniform-sky ARF calculation (20′ radius), $Norm = \int n_{\rm e} n_{\rm H} dV \,/\, (4\pi\,(1+z)^2 D_{\rm A}^2) \,/\, \Omega^{\rm U}$ $\times 10^{-20}$ cm^{-5} arcmin^{-2}, where $D_{\rm A}$ is the angular distance to the source.

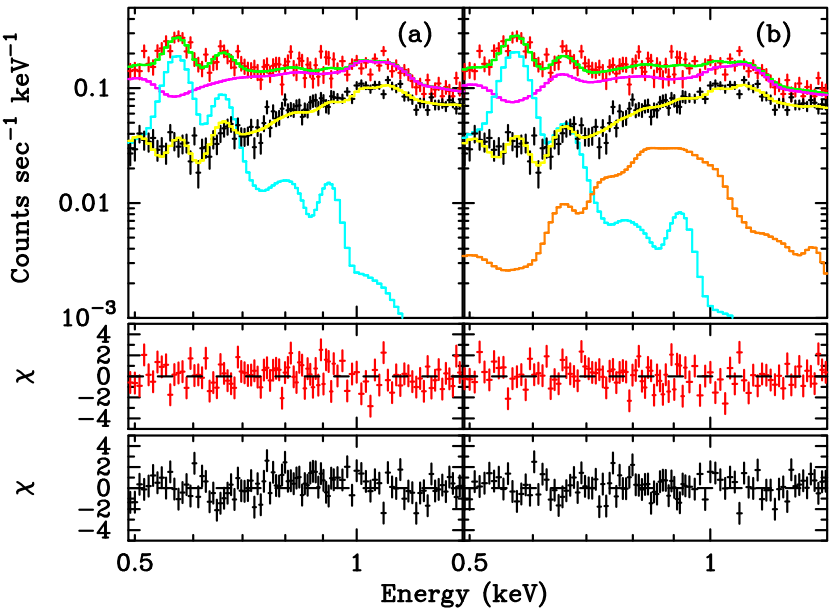

Fig. 5.3: (a) A magnification of 0.49–1.4 keV range of the BI (red) and FI (black) spectra in the 17–27′ annulus of A 1060. They are fitted with the $apec_1 + phabs \times vapec$ model, and the best-fit model are drawn by green and yellow lines. The estimated CXB and NXB components were subtracted, and a simultaneously fit with the 13–17′ annulus was conducted in the entire energy range of 0.4–7.1 keV. The $apec_1$ or *vapec* component for BI is indicated by a cyan or magenta line, respectively. Lower two panels show the fit residuals for BI and FI in unit of σ. The orange dotted lines in figure 5.6 correspond to this modeling of the Galactic component. (b) Same as (a) but fitted with the $apec_1+apec_2+phabs\times vapec$ model, and the $apec_2$ component for BI is indicated by an orange line. We adopt this model in the spectral fit. See subsection 5.1.3 for details.

We found that the estimation of the Galactic component significantly affect the determination of the oxygen abundance, because both the ICM and the Galactic component contribute to the O VIII emission line (0.653 keV), and the XIS cannot resolve them by redshift due to the limited energy resolution. On the other hand, most of the O VII emission is supposed to originate in the Galactic component, because the ICM temperature $kT \sim 2$ keV $\simeq 2.3 \times 10^7$ K is too high to emit the O VII lines (0.561, 0.568, 0.574 keV). See, e.g., figure 3 of Yoshikawa et al. (2003) for the oxygen line emissivity.

It is therefore important to estimate the Galactic component precisely, which is possible using the offset observation of A 1060 with *Suzaku*. In order to determine the surface brightness and the spectral shape of the Galactic component, we performed the simultaneous fit of the 13–17′ and 17–27′ annuli. The Galactic component is prominent in these annuli as shown in figure 5.2, however the ICM component is still dominant almost all the energy range except for the O VII line. We made the simultaneous fit in the whole 0.4–7.1 keV range (except 1.825–1.840 keV), assuming one or two *apec* models for the Galactic component, and the fit results are presented in table 5.2 and figure 5.3. The resultant normalization of the *apec* model in table 5.2 is scaled so that it gives the surface brightness in the unit solid angle of arcmin^2.

It may appear that the difference between these two models are not large in figure 5.3, however, it is notable that the derived O VIII line intensity for the Galactic component is by about twice larger for (a). We examined the improvement of the χ^2 ($\Delta\chi^2 = 46$) with the F-test, and adding the $apec_2$ component was justified with a large significance (false probability $\sim 10^{-9}$). We further allowed the normalization of the $apec_2$ to become free

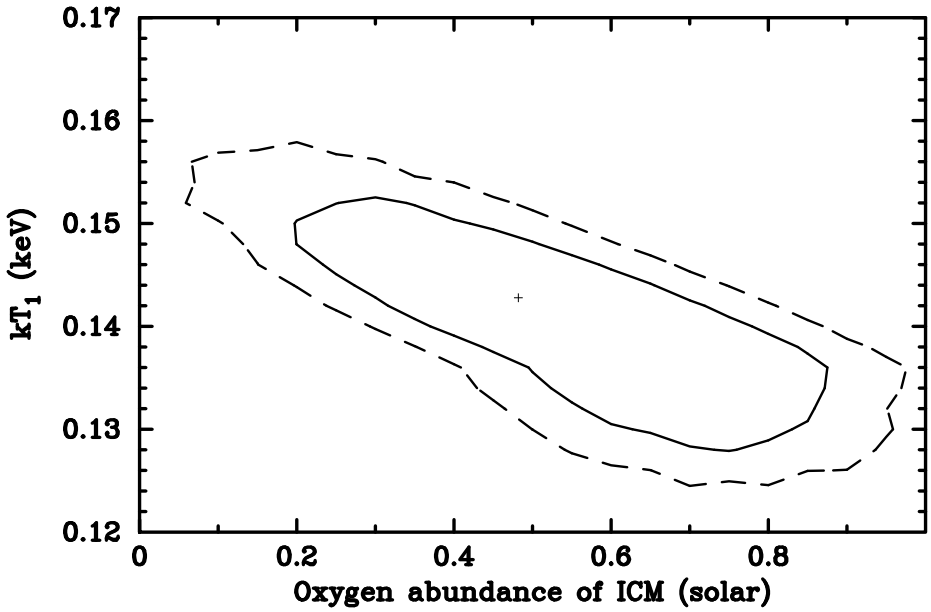

Fig. 5.4: A plot of confidence contour between kT_1 (temperature of the cooler part of the two *apec* components) and the O abundance of *vapec* for the 17–27′ annulus, in the simultaneous fitting of 13–17′ and 17–27′ annuli with the $apec_1 + apec_2 + phabs \times vapec$ model. The cross denotes the best-fit location, and the two contours represent 1σ and 90% confidence ranges, from inner to outer, respectively.

between the two annuli. The derived surface brightness ratio of the 13–17′ annulus to 17–27′ was 0.9 ± 0.2, hence it was consistent to be constant. We also confirmed that the 9–13′ annulus gave the same result. We therefore concluded that the two *apec* models are required to account for the Galactic component. Hereafter, the $apec_1 + apec_2 + phabs \times vapec$ model are utilized for the spectral fitting, otherwise stated.

To demonstrate how sensitive the O abundance of the ICM is to the assumed Galactic component model, we present a confidence contour between kT_1 (keV) of the $apec_1$ component and the O abundance (solar) of *vapec* for the outermost annulus (17–27′) in figure 5.4. There appears to exist a negative correlation between the two parameters, because higher temperature of the Galactic component produces more O VIII emission line relative to O VII, which contribute to reduce the O VIII line from the ICM (*vapec* component). Influences on the derived temperature and abundance by the modeling of the Galactic component will be tested in subsection 5.1.4, too.

In order to take into account both existence of the Galactic component itself and propagation of its statistical error, we simultaneously fitted each annulus with the outermost annulus of 17–27′. As mentioned in the previous subsection, the normalization of the $apec_1 + apec_2$ component are constrained to give the same surface brightness between the two annuli. The temperatures of the two *apec* models were also common between the two, however their values (two normalizations and two temperatures) themselves are left free. It is confirmed that the derived normalizations, $Norm_1$ and $Norm_2$, and temperatures, kT_1 and kT_2, are consistent with the values in table 5.2(b) within the quoted errors.

5.1.4 Radial Temperature & Abundance Profiles

Table 5.3: Result of the spectral fit in the central region of 0–6′ of A 1060, with the $apec_1 + apec_2 + phabs \times vapec$ model. Only the parameters for the *vapec* component are presented. The abundance of each element (except for He, C, and N, which are fixed to 1 solar with the assumed abundance ratio of *angr*) is allowed to be free in the spectral fit. Errors are 90% confidence range of statistical errors, and do not include systematic errors.

Region	kT (keV)	O (solar)	Ne (solar)	Mg (solar)	Al (solar)	Si (solar)	χ^2/dof
0–6′	$3.54^{+0.03}_{-0.03}$	$0.31^{+0.08}_{-0.08}$	$1.21^{+0.10}_{-0.10}$	$0.70^{+0.10}_{-0.09}$	$0.00^{+0.13}_{-0.00}$	$0.57^{+0.05}_{-0.05}$	1871/986
	Norm *	S (solar)	Ar (solar)	Ca (solar)	Fe (solar)	Ni (solar)	
	302 ± 3	$0.57^{+0.07}_{-0.07}$	$0.53^{+0.16}_{-0.16}$	$0.44^{+0.17}_{-0.17}$	$0.43^{+0.01}_{-0.01}$	$0.83^{+0.23}_{-0.23}$	

* Normalization of the *vapec* component scaled with a factor of SOURCE_RATIO_REG / AREA in table 5.1,
$Norm = \frac{\text{SOURCE\_RATIO\_REG}}{\text{AREA}} \int n_\mathrm{e} n_\mathrm{H} dV \,/\, (4\pi\,(1+z)^2 D_\mathrm{A}^2) \times 10^{-20}$ cm^{-5} arcmin^{-2}, where D_A is the angular distance to the source.

Table 5.4: Results of the spectral fits in the central region of 0–6′ of A 1060 by changing the amount of the OBF contaminant.

Contaminant	O (solar)	Ne (solar)	Mg (solar)	Al (solar)	Si (solar)	S (solar)	Ar (solar)	Ca (solar)	Fe (solar)	Ni (solar)
nominal	0.31	1.21	0.70	0.00	0.57	0.57	0.53	0.44	0.43	0.83
+20%	0.43	1.05	0.48	0.00	0.47	0.50	0.45	0.46	0.41	0.41
free *	0.38	1.12	0.57	0.00	0.51	0.53	0.47	0.43	0.42	0.54

Contaminant	kT (keV)	$Norm$ †	kT_1 (keV)	$Norm_1$ ‡	kT_2 (keV)	$Norm_2$ ‡	$N_{\mathrm{CO}_{1/6}}$ § BI	FI	χ^2/dof
nominal	3.54	302	0.159	1.00	0.752	1.00	1.74	2.32	1878/986
+20%	3.36	298	0.148	1.40	0.721	1.09	2.11	2.72	1746/986
free *	3.50	301	0.159	0.96	0.765	0.95	2.18	2.38	1681/982

* We fitted the amount of the OBF contaminant as a free parameter with the C/O number ratio fixed to 6.
† Normalization of the *vapec* model, calculated in the same way with table 5.3 .
‡ Ratio to the normalization of the "nominal" ARF.
§ Column density of the $\mathrm{CO}_{1/6}$ for BI and FI in unit of 10^{18} cm^{-2}.

Table 5.5: Summary of the best-fit parameters of the *vapec* component for each annular region of A 1060 with the $apec_1+apec_2+phabs\times vapec$ model. Each annulus is simultaneous fitted with the the outermost 17–27′ annulus. Errors are 90% confidence range of statistical errors, and do not include systematic errors. The solar abundance ratio of *angr* is assumed. These results are plotted in figure 5.6. The O abundance in the outer two regions becomes lower when the Galactic component is expressed by a single *apec* model, which is drawn by orange dotted lines in figure 5.6. The kT, O, and Mg columns at $r < 6'$ are slightly different when the OBF contaminant is increased by "+20%", which is drawn by black dotted lines in figure 5.6. The Ne abundance is probably not reliable because the *Suzaku* XIS cannot resolve the ionized Ne lines from the Fe-L line complex.

Region	*Norm**	kT (keV)	O (solar)	Ne (solar)	Mg (solar)	Si (solar)	S, Ar, Ca (solar)	Fe (solar)	Ni (solar)	χ^2/dof
0–2′	605 ± 12	$3.34^{+0.04}_{-0.04}$	$0.38^{+0.16}_{-0.15}$	$1.20^{+0.20}_{-0.20}$	$0.76^{+0.19}_{-0.19}$	$0.69^{+0.11}_{-0.11}$	$0.82^{+0.12}_{-0.12}$	$0.49^{+0.03}_{-0.03}$	$1.13^{+0.46}_{-0.45}$	1240/992
2–4′	352 ± 5	$3.39^{+0.03}_{-0.03}$	$0.28^{+0.11}_{-0.12}$	$1.11^{+0.16}_{-0.15}$	$0.65^{+0.14}_{-0.14}$	$0.52^{+0.08}_{-0.08}$	$0.52^{+0.08}_{-0.08}$	$0.42^{+0.02}_{-0.02}$	$0.90^{+0.34}_{-0.34}$	1290/992
4–6′	198 ± 3	$3.42^{+0.04}_{-0.04}$	$0.29^{+0.13}_{-0.13}$	$1.24^{+0.18}_{-0.16}$	$0.67^{+0.15}_{-0.15}$	$0.58^{+0.09}_{-0.09}$	$0.53^{+0.09}_{-0.10}$	$0.41^{+0.02}_{-0.02}$	$0.87^{+0.38}_{-0.37}$	1345/992
6–9′	109 ± 2	$3.25^{+0.04}_{-0.04}$	$0.58^{+0.14}_{-0.14}$	$1.17^{+0.16}_{-0.15}$	$0.59^{+0.15}_{-0.15}$	$0.50^{+0.08}_{-0.08}$	$0.55^{+0.09}_{-0.09}$	$0.40^{+0.02}_{-0.02}$	$1.17^{+0.36}_{-0.35}$	1329/992
9–13′	44 ± 2	$2.87^{+0.10}_{-0.10}$	$0.65^{+0.34}_{-0.29}$	$0.89^{+0.35}_{-0.33}$	$0.75^{+0.33}_{-0.32}$	$0.27^{+0.17}_{-0.17}$	$0.19^{+0.20}_{-0.19}$	$0.40^{+0.05}_{-0.05}$	$1.13^{+0.77}_{-0.72}$	1057/992
13–17′	26 ± 1	$2.50^{+0.09}_{-0.09}$	$0.72^{+0.29}_{-0.38}$	$0.44^{+0.29}_{-0.28}$	$0.78^{+0.29}_{-0.27}$	$0.30^{+0.15}_{-0.14}$	$0.44^{+0.18}_{-0.17}$	$0.25^{+0.05}_{-0.05}$	$0.16^{+0.60}_{-0.16}$	1082/992
17–27′	13 ± 1	$2.22^{+0.11}_{-0.12}$	$0.48^{+0.41}_{-0.37}$	$0.30^{+0.29}_{-0.26}$	$0.21^{+0.22}_{-0.21}$	$0.28^{+0.12}_{-0.12}$	$0.21^{+0.14}_{-0.14}$	$0.21^{+0.04}_{-0.04}$	$0.00^{+0.41}_{-0.00}$	—†

* Normalization of the *vapec* model, calculated in the same way with table 5.3.

† The 17–27′ annulus was fitted simultaneously with other annuli, and the best-fit values with the 13–17′ annulus are presented here.

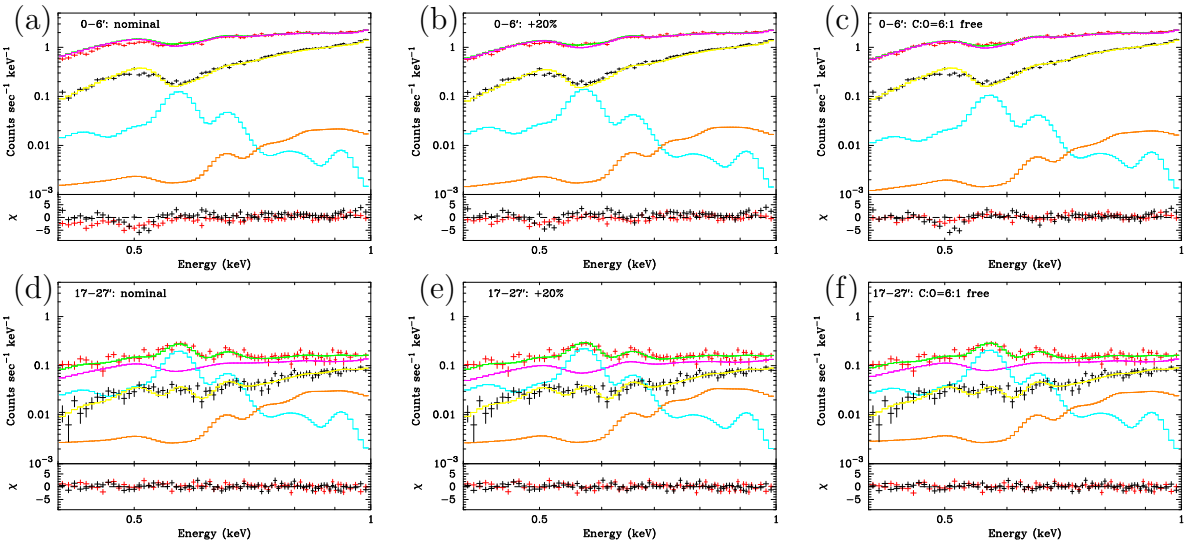

Fig. 5.5: (a) A magnification of the best-fit spectrum at 0–6′ annulus in the energy range of 0.4–1.0 keV with the "nominal" ARF response, in which transmission of the OBF contaminant was estimated according to the calibration files `ae_xi`N`_contami_20060525.fits` ($N = 0, 1, 2, 3$). Table 5.3 and the "nominal" row of table 5.4 show the best-fit parameters. (b) The best-fit spectrum with the "+20%" ARF, in which amount of the OBF contaminant was increased by +20% than the "nominal" ARF. The "+20%" row of table 5.4 shows the best-fit parameters. (c) The best-fit spectrum with the no-contaminant ARF but fitted with $varabs \times (apec_1 + apec_2 + phabs \times vapec)$ model to consider the transmission of the OBF contaminant in the XSPEC *varabs* model with chemical composition of $\mathrm{C\,O}_{1/6}$. The "free" row of table 5.4 shows the best-fit parameters. (d), (e), (f) Same as (a), (b), (c) but for the 17–27′ annulus, respectively. Each spectrum was simultaneously fitted with (a), (b), (c).

Before entering the spectral fit at each annulus, we investigate the fit result in the central 0–6′ region to test the capability in the abundance determination with the *Suzaku* XIS. This region exhibits nearly constant temperature and metal abundances (figure 5.6), and the contribution of the Galactic component is almost negligible (figure 5.2). The fit result is presented in table 5.3, in which most of element abundances are allowed to be free in the spectral fit, except for He, C, and N, which are fixed to 1 solar with the assumed abundance ratio of *angr*.

Although the fit was not acceptable due mainly to the very high photon statistics than the systematic errors in the instrumental response, this result was useful to assess whether each element abundance was reasonably determined or not. The Ar and Ca abundances were reasonably determined although the errors are larger than other elements. We therefore decided to link the S, Ar, and Ca abundances to be the same, because they showed similar values. The Al abundance became 0.0, which is physically strange, therefore we fixed the Al abundance to 1 solar. The χ^2/dof was increased to 1898/988 with this treatment, however we confirmed that other parameters did not change beyond the quoted error range in table 5.3. Somehow, the Ne and Ni abundances were larger than other elements. This might be due to these element lines could not be resolved from the Fe-L line complex. Note that the Ni abundance was also determined by Ni-L lines because we ignored energy range above 7.1 keV, while the Fe abundance was determined by both Fe-L and Fe-K lines. Anyway, we left these Ne and Ni abundances to move freely during the spectral fit. We also present results when the O, Ne, and Mg abundances are linked

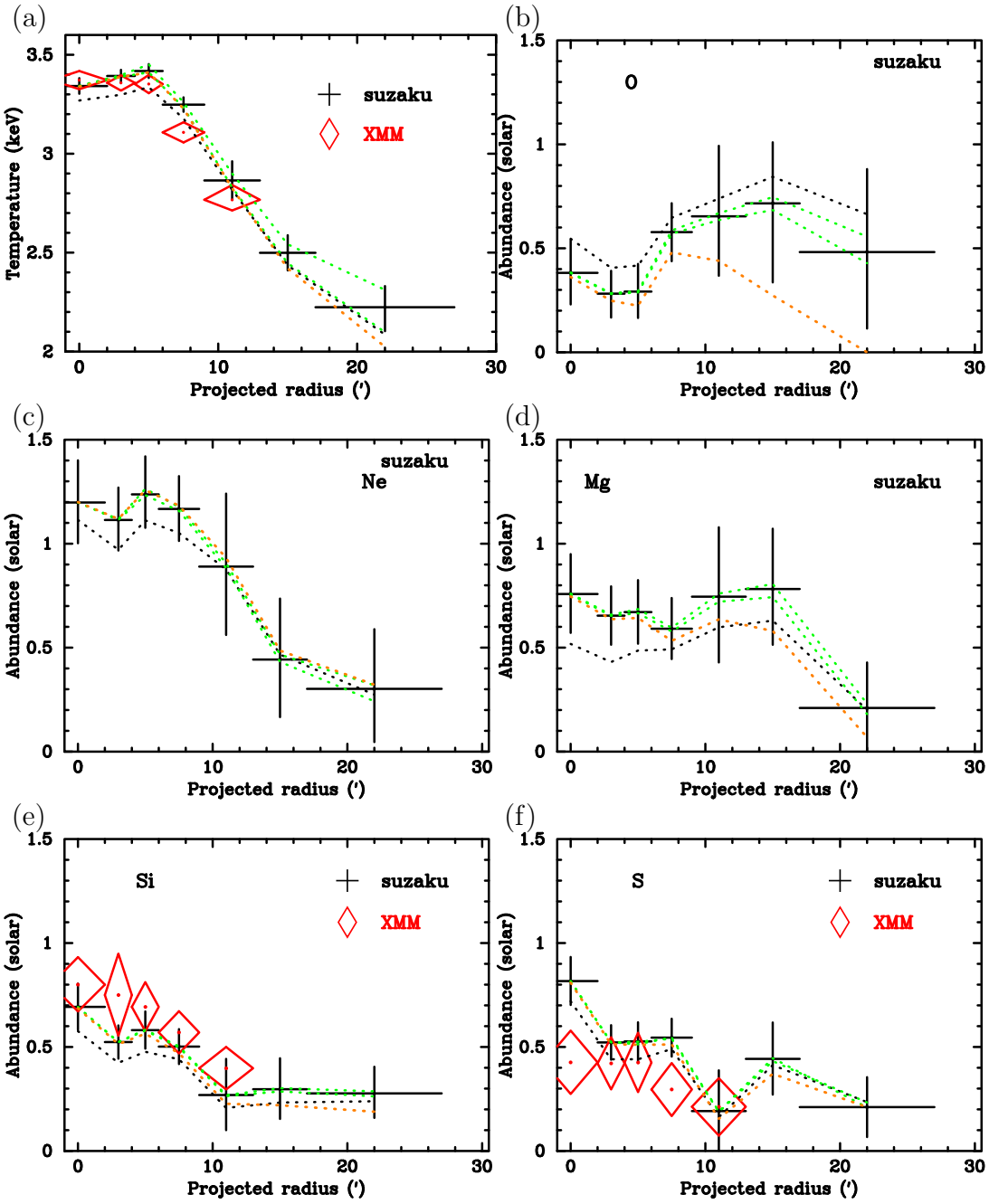

Fig. 5.6:

to have the same value in Appendix B.

We also found that the assumed abundance table, which defines the "1 solar" of each element relative to H, significantly affects the determination of temperature and abundance. In fact, difference in the abundance table affects the fit results in three ways. Firstly, we assume the Galactic component to have the $apec_1 + apec_2$ model with "1 solar". Secondly, the Galactic absorption model of *phabs* is also changed by the assumed abundance table. Lastly, the derived abundances are given in unit of "solar" by the *vapec* model. The first two effects are rather complicated, and details are investigated in Appendix B. In this section, we treat only the solar abundance ratio of *angr* (Anders & Grevesse 1989) with the *phabs* absorption model, simply because they are the *default standard* of XSPEC. In terms of the χ^2, it appears to give the minimum χ^2 with the *lodd* (Lodders 2003) abundance table in combination with the *wabs* (Morrison & McCammon

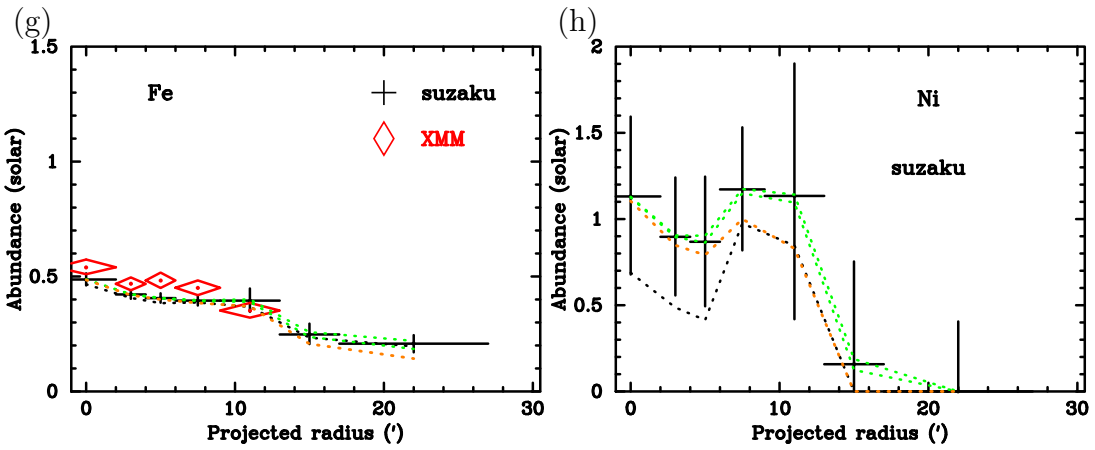

Fig. 5.6: (a) Radial temperature profiles of A 1060 derived from spectral fit of the *Suzaku* (black) and XMM-Newton (red) spectra at each annulus. The horizontal axis denotes the projected radius and deprojection are not conducted. The same data with table 5.5 are used for *Suzaku*. The black dotted lines correspond to shifts of the best-fit values by changing thickness of the OBF contaminant by +20%. The green dotted lines denote those when the estimated CXB and NXB levels are changed by ±10%. The orange dotted line shows the best-fit value when the Galactic component is modeled by a single *apec*. Regarding XMM-Newton, the *phabs* × *vapec* model are used for the spectral fit, and the O, Ne, Mg, and Ni abundances are fixed to 1 solar in the assumed abundance table of *angr*. (b)–(h) Radial abundance profiles derived and plotted in the same way as (a).

1983) absorption model which utilizes the abundance table of *aneb* (Anders & Ebihara 1982) built-in the code (table B.1).

We then examined the influence of uncertainty in the OBF contaminant using the spectrum within 6′. Figure 5.5(a) shows a magnification of the best-fit spectrum in the energy range of 0.4–1.0 keV with the "nominal" ARF response, in which transmission of the OBF contaminant was estimated according to the calibration files `ae_xi`N`_contami_20060525.fits` ($N = 0, 1, 2, 3$), as shown in figures 4.2 and 5.1(b). As described in subsection 5.1.2, the spectrum was simultaneously fitted with the 17–27′ annulus shown in figure 5.5(d). In this figure, it is suggested that the absorption in the low energy band is slightly inconsistent between BI and FI sensors, namely, the BI spectrum appears to need more absorption in 0–6′ where the amount of contamination is larger than 17–27′ (see figure 4.2). We also found that the contamination measurement by RXJ1856.5−3754 on October 25, 2005 in the XIS hardware paper (figure 14 of Koyama (2007)) indicates by about 20% larger amount of the OBF contaminant than the "nominal" value for the XIS1.

We therefore generated ARF responses changing the amount of the OBF contaminant by +20%. The fit result is shown in figure 5.5(b), (e) and table 5.4 ("+20%" row). Note that the CXB background to subtract was also modified in this fit. The fit residual for 0–6′ was improved, and the χ^2 was decreased by $\Delta\chi^2 = 132$. We further tested the fit by adding an absorption of the OBF contaminant with chemical composition of $\mathrm{C\,O}_{1/6}$ to the fit model using the XSPEC *varabs* model.[1] The fit result is shown in figure 5.5(c) and (f). The best-fit values are summarized in table 5.4 ("free" row), and the χ^2 was improved by $\Delta\chi^2 = 197$. The derived amount of contaminant for BI was by 25% larger than the "nominal" value, and by 3% larger for FI. We think that the deviation from the "nominal" value for BI is beyond the calibration uncertainty, however, almost all of

[1]In this method, we used the same CXB background with the "nominal" ARF, and the surface brightness of the Galactic component was slightly different between 0–6′ and 17–27′.

the best-fit values at the "free" row in table 5.4 are between values at "nominal" and "+20%". We therefore consider the +20% result as the systematic error range due to the uncertainty in the OBF contaminant.

Considering these systematics, results of the spectral fit at each annulus are summarized in table 5.5 and figure 5.6. We tested the results by changing the background normalization by ±10%, and they are plotted in green dotted lines in figure 5.6. The systematic error due to the background estimation is almost negligible. Difference in the best-fit values by modeling the Galactic component with a single *apec* was investigated, and they were indicated by orange dotted lines. The differences are within the statistical error for the inner five annuli, however, O abundance becomes lower than the 90% confidence error at the outer two annuli as indicated in figure 5.3, and temperature and Fe abundance become lower at the outermost annulus. This is due mainly to the fact that the XIS cannot resolve the ICM O VIII line from the Galactic O VIII by redshift. The systematic error range due to the uncertainty in the OBF contaminant is indicated by black dotted lines. It is sometimes larger than the statistical errors at small radii ($r \leq 6'$), particularly for kT, O, and Mg abundances. Though Ne abundance is significantly larger than other elements at small radii ($r < 9'$), it is probably not reliable because the *Suzaku* XIS cannot resolve the ionized Ne lines from the Fe-L line complex.

We also plot the XMM-Newton results for the inner five annuli with red diamonds, in which the *phabs* × *vapec* model are used for the spectral fit, and the Ne, Ar, Ca and Ni abundances are fixed to 1 solar. Namely, the Galactic component is ignored. They are almost consistent with the *Suzaku* results, although XMM-Newton appears to give slightly higher abundance for Fe and Si, while lower abundance for S.

5.1.5 Direct Comparison of O VII and O VIII Intensities

Table 5.6: Line intensities of O VII and O VIII at each annulus of A 1060 and the NGC 2992 field in unit of photons cm^{-2} s^{-1} sr^{-1}. These intensities are derived from the spectral fit with *power-law* + *gaussian* + *gaussian* model (see figure 5.8 for the NGC 2992 field), assuming the uniform-sky ARF response. Intensities by McCammon et al. (2002) measured with a high resolution microcalorimeter array for a large sky area of ∼ 1 sr are also presented.

Region	O VII	O VIII
A 1060 center (0–2′)	$11.9^{+15.5}_{-11.9}$	17.1±9.2
A 1060 center (2–4′)	7.2±7.2	12.1±5.0
A 1060 center (4–6′)	10.0±4.4	8.6±3.3
A 1060 center (6–9′)	7.3±2.0	6.9±1.4
A 1060 offset (9–13′)	8.3±2.8	5.7±1.8
A 1060 offset (13–17′)	8.6±1.7	3.5±0.9
A 1060 offset (17–27′)	8.6±1.2	2.0±0.5
NGC 2992 field	4.1±0.6	0.6±0.2
Galactic average (McCammon et al. 2002)	4.8±0.8	1.6±0.4

We also investigated the surface brightness of the O VII and O VIII emission lines in order to estimate the O abundance of the ICM directly from the line intensities. The surface brightness of the O VII and O VIII were derived by fitting the annular spectrum

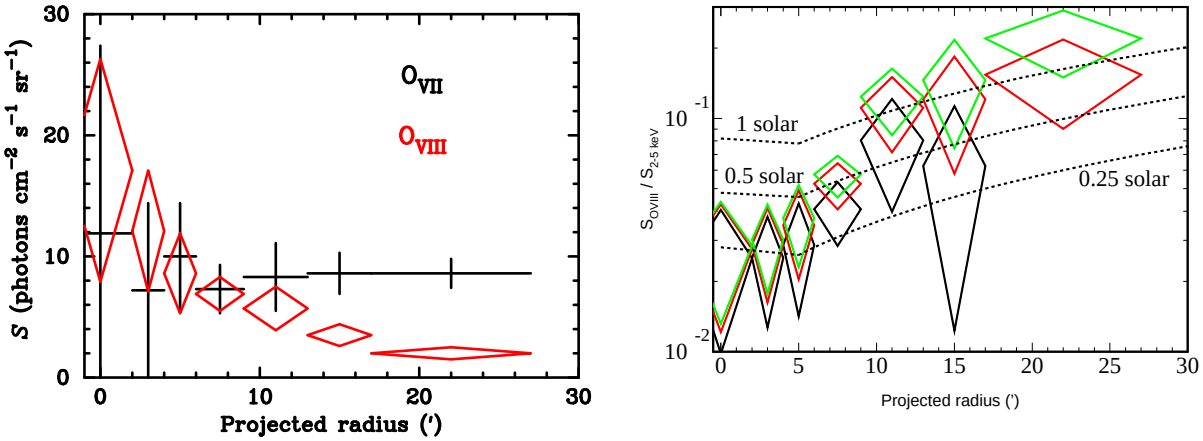

Fig. 5.7: (a) Line intensities of O VII and O VIII at each annulus of A 1060 in unit of photons cm^{-2} s^{-1} sr^{-1}. Each value is shown in table 5.6. (b) The O VIII emission line intensities in table 5.6 divided by the surface brightness of the 2–5 keV continuum are plotted in green diamonds against the radius of each annulus. The red or black diamonds correspond to the ratios when the O VIII intensities of the NGC 2992 field or the outermost annulus (17–27′) are subtracted as an offset. Dashed lines represent expected ratios for the *vapec* model with 0.25, 0.5, and 1 solar abundances, assuming the observed temperature at each annulus (table 5.5).

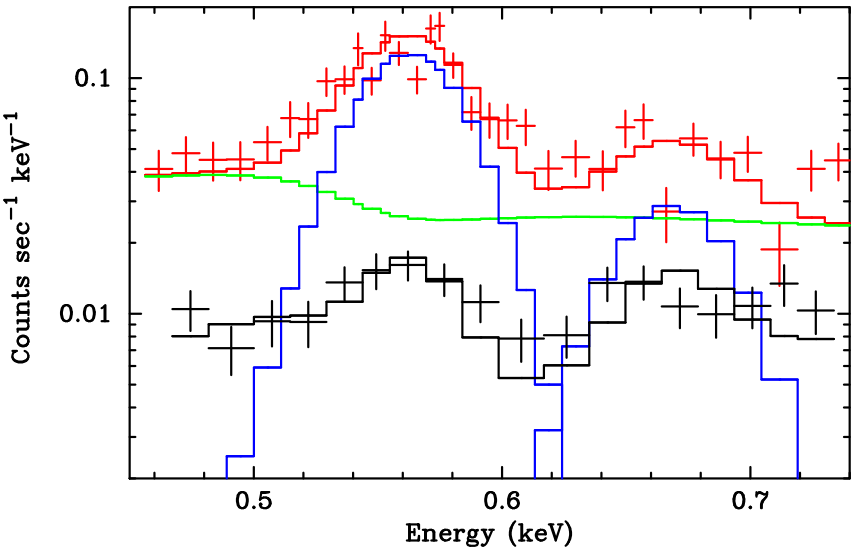

Fig. 5.8: The 0.46–0.74 keV spectra of the NGC 2992 field with BI (red) and FI (black) are fitted with the *power-law* + *gaussian* + *gaussian* model. The red and black lines represent the best-fit model, and the model components for BI are plotted by green (*power-law*) and blue (two *gaussian*) lines. The central energies of two Gaussians are constrained to be within ±5 eV range of O VII and O VIII lines, and σ of Gaussians are fixed to 0.0.

with a *power-law* + *gaussian* + *gaussian* model. In the fitting, we fixed the Gaussian σ to be 0, and allowed the energy center of the two Gaussians to vary within 555–573 eV or 648–658 eV for O VII or O VIII, respectively. The derived line intensities are summarized in table 5.6 and figure 5.7(a). There is a clear excess of the O VIII intensity towards the cluster center, while O VII is consistent with constant. This is a strong evidence that the O VIII emission is associated with the ICM itself, on the other hand, O VII might be due

mainly to the Galactic origin.

We compared the surface brightness of the oxygen lines with that at a neighbor of A 1060, the NGC 2992 field. Though NGC 2992 is located at 18° offset from A 1060, the Galactic latitude of A 1060 and NGC 2992 is similar, and the neutral hydrogen column density ($N_{\rm H} = 5.1 \times 10^{20}$ cm^{-2}; Dickey & Lockman (1990)) is comparable to A 1060. NGC 2992 ($z = 0.007710$) has an active galactic nuclei, which is expected to emit no oxygen lines. In addition, we excluded the main target with a radius of $5'$ centered on NGC 2992, and utilized the outer region for the spectral analysis in figure 5.8.

The surface brightness of the O VII and O VIII emissions in the outermost annulus of the A 1060 observation was roughly twice larger than the NGC 2992 field. Line intensities by McCammon et al. (2002) measured with a high resolution microcalorimeter array for a large sky area of ~ 1 sr are also presented in table 5.6, and the O VIII intensity was consistent with the outermost annulus (17–27′) of the A 1060. It is suggested that both the O VII and and O VIII lines in our observation are somewhat mixture of the ICM and the Galactic origin. However, we could not confirm excess O VII emission towards the cluster center, we concentrate on the O VIII emission.

Then we calculated the surface brightness ratio of the O VIII line divided by the 2–5 keV continuum at each annulus, as presented in figure 5.7(b) by green diamonds. Here, we subtracted the O VIII intensity at the NGC 2992 field (red diamonds) or the intensity at the outermost annulus (black diamonds), as an "offset" due to the Galactic component. The dashed lines represent the calculated ratio by the XSPEC simulation fixing the O abundance of ICM to 0.25, 0.5, and 1 solar. The ICM temperature at each annulus is assumed to have the measured value in figure 5.2(a). Actual value of the O abundance is supposed to lie between the black and green diamonds. The radial O abundance profile obtained in figure 5.2(b) is mostly consistent with this plot.

5.1.6 Central Cool Component of A 1060

Chandra observation resolved two central elliptical galaxies of A 1060, NGC 3311 and NGC 3309 (Yamasaki et al. 2002). We estimated the flux of an additional cool component for the central galaxies with the *vapec* model of $kT = 0.8$ keV and 0.5 solar abundance at $z = 0.0114$, and obtained an upper limit (90% confidence level) to be $L_{\rm X} = 5.2 \times 10^{40}$ erg s^{-1} (0.4–4.5 keV) in the central region within $r < 2'$. In this fit, temperatures of the Galactic components (two *apec*) were fixed at 0.146 and 0.662 keV, and only the ICM component was allowed to be free. This upper limit is consistent with the sum of the ISM flux of the two elliptical galaxies by Yamasaki et al. (2002), $L_{\rm X} = (1.8 \pm 0.6) \times 10^{40}$ erg s^{-1} (0.4–4.5 keV).

5.2 AWM 7

Analysis methods are the almost same as those of A 1060.

5.2.1 *Suzaku* XIS Spectra

We extracted spectra from seven annular regions of 0–2′, 2–4′, 4–6′, 6–9′, 9–13′, 13–17′ and 17–27′, centered on (RA, Dec) = (2h54m32.0s, +41d35′15″). The first four annuli were taken from the central observation, and the rest of thee annuli were from the two offset observations. Table 5.7 lists areas of the extraction regions (arcmin^2), coverage of the whole annulus (%), the SOURCE_RATIO_REG values (%; see caption for its definition) and the observed counts in 0.4–8.1 keV including NXB and CXB for the BI and FI sensors.

Table 5.7: Area, coverage of whole annulus, SOURCE_RATIO_ REG and observed counts for each annular region of AWM 7. SOURCE_ RATIO_REG represents the flux ratio in the assumed spatial distribution on the sky (double-β model) inside the accumulation region to the entire model, and written in the header keyword of the calculated ARF response by "xissimarfgen".

Region *	Area † (arcmin^2)	Coverage †	SOURCE_ * RATIO_REG	Counts ‡ BI	FI
0–2′	12.6	100.0%	12.0%	21,800	52,737
2–4′	37.7	100.0%	19.1%	38,654	89,901
4–6′	62.8	100.0%	15.8%	33,146	75,797
6–9′	136.1	96.3%	15.2%	34,767	74,968
9–13′	48.5	17.6%	2.1%	12,755	26,352
13–17′	76.3	20.2%	1.7%	14,577	31,750
17–27′	176.7	12.8%	1.6%	19,242	39,475
9–13′	46.3	16.7%	2.1%	10,695	23,108
13–17′	72.7	19.3%	1.6%	11,591	23,745
17–27′	182.9	13.2%	1.7%	16,295	36,026

* The first four annuli are extracted from the central observation, and second and third are from the east and west observation, respectibely.
† The largest values among four sensors are presented.
‡ Observed counts including NXB and CXB in 0.4–7.1 keV for BI and 0.4–8.1 keV for FI.

Each annular spectrum is shown in figure 5.9. The ionized Mg, Si, S, Fe lines are clearly seen in each ring. The O VII and O VIII lines are prominent in the outer rings, however, most of the O VII emission is supposed to come from the local Galactic emission, and we deal with those in the same way as A 1060.

5.2.2 Strategy of Spectral Fit

The basic strategy of the spectral fit is described in subsection 5.1.2 of A 1060.

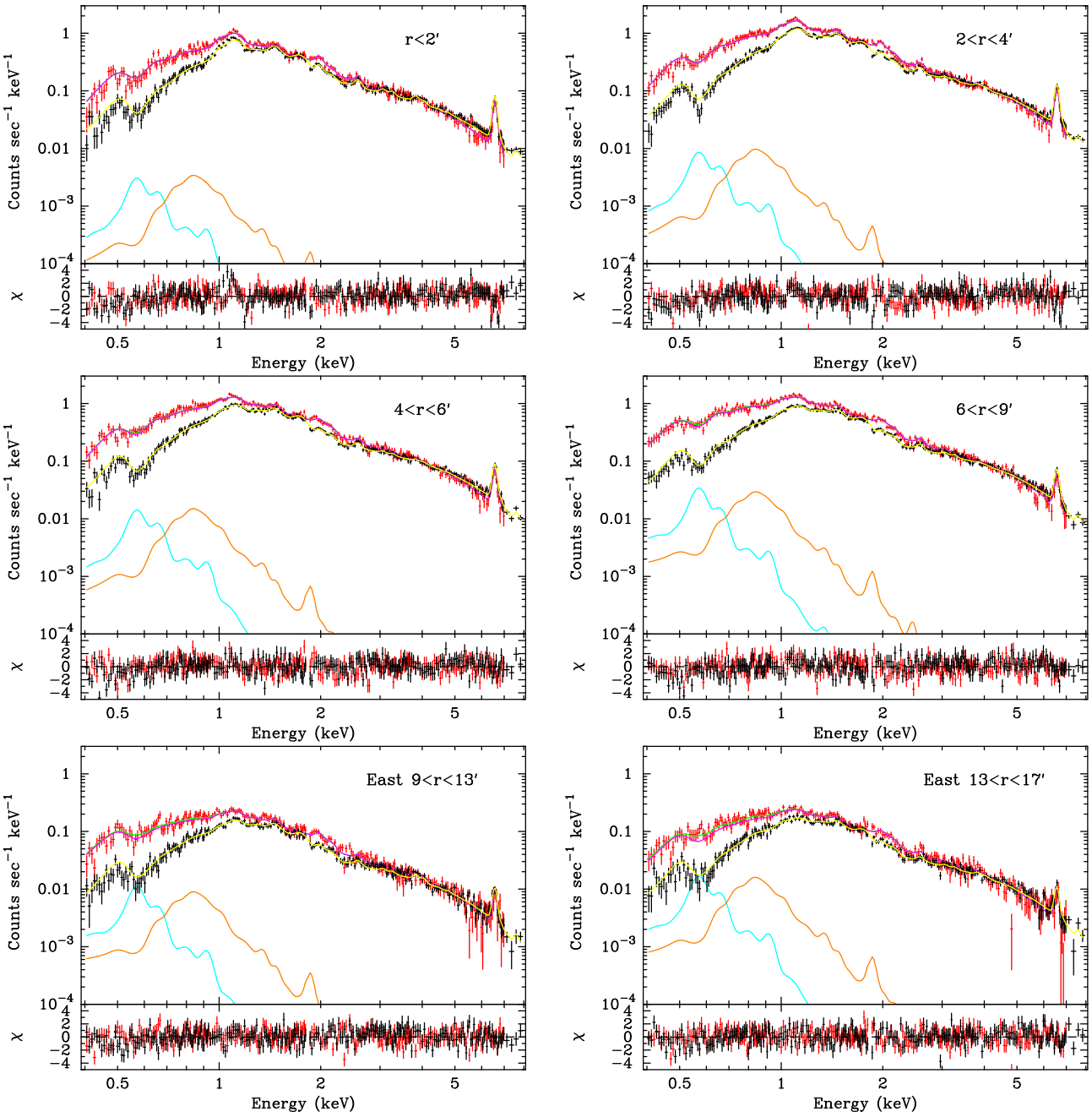

Fig. 5.9: The upper panels show the observed spectra at the annular regions which is denoted in the panels, and they are plotted by red and black crosses for BI and FI, respectively. The estimated CXB and NXB components are subtracted, and they are fitted with the $apec_1 + apec_2 + phabs \times vapec$ model drawn by green and yellow lines for the BI and FI spectra. The $apec_1$ and $apec_2$ components for the BI spectra are indicated by cyan and orange lines. The energy range around the Si K-edge (1.825–1.840 keV) is ignored for the spectral fit. The lower panels show the fit residuals in unit of σ.

We generated two different ARFs for the spectrum of each annulus, $A^{\rm U}$ and $A^{\rm B}$, which respectively assume the uniform-sky emission and $\sim 1^\circ \times 1^\circ$ size of the double-β surface brightness profile obtained with the XMM-Newton data (table 4.4).

The spectra from BI and FI are fitted simultaneously in the 0.4–8.1 keV band except for energy range of anomalous response around the Si K-edge (1.825–1.840 keV). We

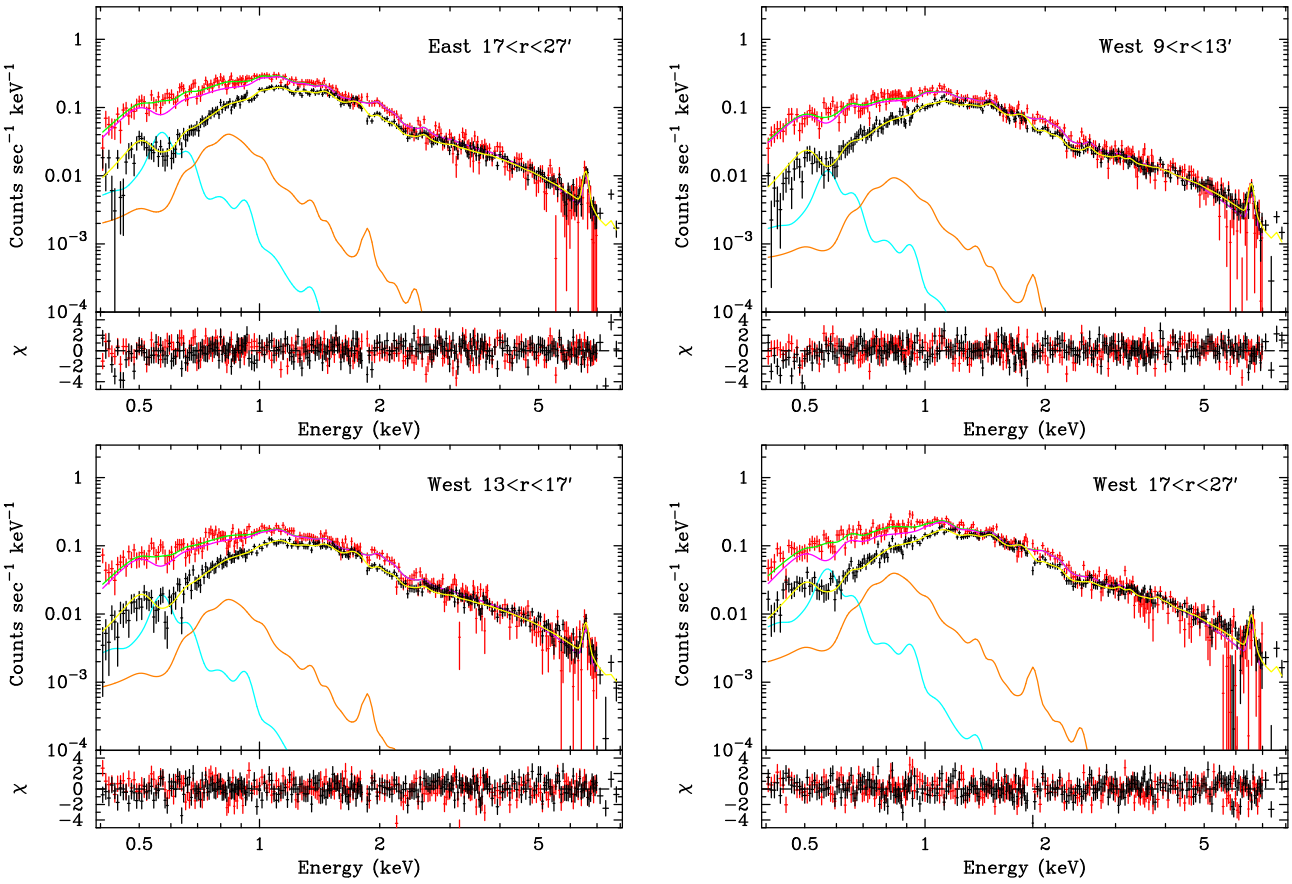

Fig. 5.9: continue of 5.9

ignored below 0.4 keV because the C edge (0.284 keV) seen in the BI spectra could not be reproduced perfectly in our data. In the simultaneous fit of BI and FI, only the normalization are allowed to be different between them, although we found that the derived normalizations are quite consistent between the two.

5.2.3 Estimation of Galactic Component

Table 5.8: The best-fit parameters of the *apec* component(s) for the simultaneous fit of the spectra in 13–17′ and 17–27′ annuli of the west offset region and in 17–27′ annulus of the east offset region.

Fit model	$Norm_1$ *	kT_1 (keV)	$Norm_2$ *	kT_2 (keV)	χ^2/dof
(a) $apec_1 + phabs \times vapec$	7.52 ± 0.70	$0.262^{+0.035}_{-0.013}$	—	—	1781/1495
(b) $apec_1 + apec_2 + phabs \times vapec$	6.59 ± 0.46	$0.157^{+0.041}_{-0.035}$	0.32 ± 0.07	$0.612^{+0.052}_{-0.055}$	1743/1493

* Normalization of the *apec* component divided by the solid angle, $\Omega^{\rm U}$, assumed in the uniform-sky ARF calculation (20′ radius), $Norm = \int n_{\rm e} n_{\rm H} dV \,/\, (4\pi\,(1+z)^2 D_{\rm A}^2) \,/\, \Omega^{\rm U} \times 10^{-20}$ cm^{-5} arcmin^{-2}, where $D_{\rm A}$ is the angular distance to the source.

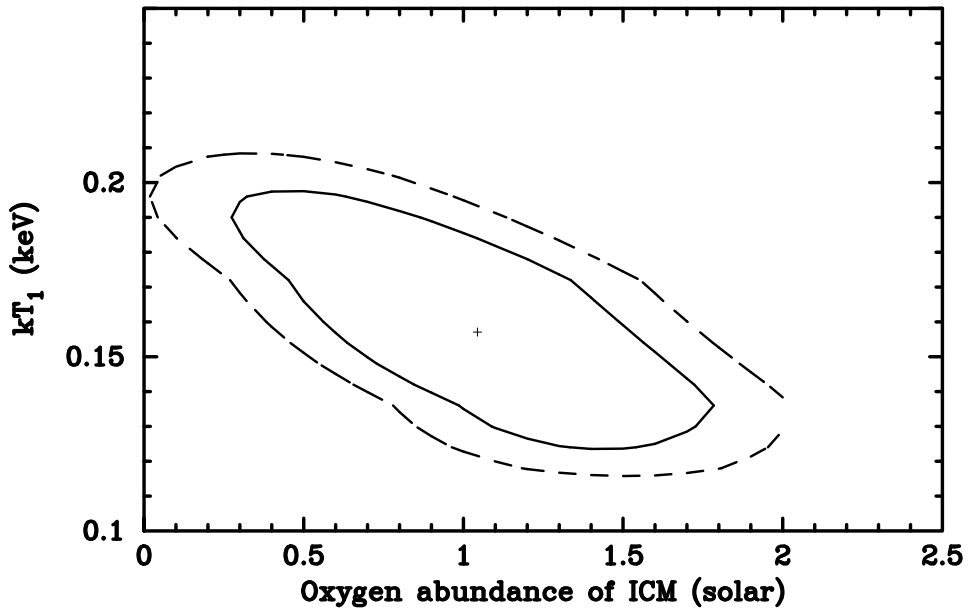

Fig. 5.10: A plot of confidence contour between kT_1 (temperature of the cooler part of the two *apec* components) and the O abundance of *vapec* for the 17–27′ annulus of the west offset region, in the simultaneous fitting of 13–17′ and 17–27′ annuli of the west offset region and 17–27′ annulus of the east offset region with the $apec_1 + apec_2 + phabs \times vapec$ model. The cross denotes the best-fit location, and the two contours represent 1σ and 90% confidence ranges, from inner to outer, respectively.

It is important to estimate the Galactic component precisely, which is possible using the offset observation of AWM 7 with *Suzaku*. In order to determine the surface brightness and the spectral shape of the Galactic component, we performed the simultaneous fit of the 13–17′ and 17–27′ annuli of the west offset region and the 17–27′ annulus of the east offset region. The Galactic component is prominent in these annuli as shown in figure 5.9, however the ICM component is still dominant almost all the energy range except for the O VII line. We made the simultaneous fit in the whole 0.4–8.1 keV range (except 1.825–1.840 keV), assuming one or two *apec* models for the Galactic component, and the fit results are presented in table 5.8. The resultant normalization of the *apec* model in table 5.8 is scaled so that it gives the surface brightness in the unit solid angle of arcmin^2.

We examined the improvement of the χ^2 ($\Delta\chi^2 = 38$) with the F-test, and adding the $apec_2$ component was justified with a large significance (false probability $\sim 10^{-7}$). We further allowed the normalization of the $apec_2$ to become free between the two annuli. We concluded that the two *apec* models are required to account for the Galactic component. Hereafter, the $apec_1 + apec_2 + phabs \times vapec$ model are utilized for the spectral fitting, otherwise stated.

To demonstrate how sensitive the O abundance of the ICM is to the assumed Galactic component model, we present a confidence contour between kT_1 (keV) of the $apec_1$ component and the O abundance (solar) of *vapec* for the outermost annulus (17–27′) of the west offset region in figure 5.10. There appears to exist a negative correlation between the two parameters, because higher temperature of the Galactic component produces more O VIII emission line relative to O VII, which contribute to reduce the O VIII line from the ICM (*vapec* component). Influences on the derived temperature and abundance by the modeling of the Galactic component will be tested in subsection 5.2.4, too.

In order to take into account both existence of the Galactic component itself and propagation of its statistical error, we simultaneously fitted each annulus with the outer-

most annulus of 17–27′ in the east and west offset regions. As mentioned in the previous subsection, the normalization of the $apec_1 + apec_2$ component are constrained to give the same surface brightness between the two annuli. The temperatures of the two *apec* models were also common between the two, however their values (two normalizations and two temperatures) themselves are left free. It is confirmed that the derived normalizations, $Norm_1$ and $Norm_2$, and temperatures, kT_1 and kT_2, are consistent with the values in table 5.8(b) within the quoted errors.

5.2.4 Radial Temperature & Abundance Profiles

Table 5.9: Summary of the best-fit parameters of the *vapec* component for each annular region of AWM 7 with the $apec_1+apec_2+phabs\times vapec$ model. Each annulus is simultaneous fitted with the the outermost 17–27′ annulus of the east and west offset regions. Errors are 90% confidence range of statistical errors, and do not include systematic errors. The solar abundance ratio of *angr* is assumed. These results are plotted in figure 5.11. The O abundance in the outer two regions becomes lower when the Galactic component is expressed by a single *apec* model, which is drawn by black, red, and green dotted lines in figure 5.11. The Ne and Ni abundances is probably not reliable because the *Suzaku* XIS cannot resolve the ionized Ne lines from the Fe-L line complex.

Region	*Norm**	kT (keV)	O (solar)	Ne (solar)	Mg (solar)	Si (solar)	S (solar)	Fe (solar)	Ni (solar)	χ^2/dof
0–2′	1007 ± 36	$3.41^{+0.04}_{-0.04}$	$0.62^{+0.34}_{-0.31}$	$2.11^{+0.40}_{-0.37}$	$1.50^{+0.32}_{-0.31}$	$1.13^{+0.18}_{-0.17}$	$1.08^{+0.20}_{-0.20}$	$0.87^{+0.05}_{-0.04}$	$1.71^{+0.61}_{-0.58}$	1872/1493
2–4′	595 ± 16	$3.66^{+0.04}_{-0.04}$	$0.57^{+0.26}_{-0.25}$	$1.65^{+0.28}_{-0.27}$	$1.18^{+0.24}_{-0.24}$	$0.94^{+0.13}_{-0.13}$	$0.85^{+0.16}_{-0.15}$	$0.73^{+0.03}_{-0.03}$	$1.47^{+0.47}_{-0.46}$	1899/1493
4–6′	342 ± 10	$3.78^{+0.05}_{-0.05}$	$0.49^{+0.28}_{-0.26}$	$1.38^{+0.29}_{-0.28}$	$1.20^{+0.27}_{-0.27}$	$0.54^{+0.14}_{-0.14}$	$0.67^{+0.17}_{-0.17}$	$0.56^{+0.03}_{-0.03}$	$0.56^{+0.53}_{-0.52}$	1805/1493
6–9′	182 ± 5	$3.82^{+0.06}_{-0.06}$	$0.63^{+0.25}_{-0.27}$	$1.33^{+0.28}_{-0.29}$	$1.05^{+0.26}_{-0.27}$	$0.57^{+0.14}_{-0.15}$	$0.74^{+0.18}_{-0.18}$	$0.50^{+0.03}_{-0.03}$	$2.11^{+0.57}_{-0.56}$	1816/1493
9–13′	115 ± 4	$3.60^{+0.10}_{-0.10}$	$0.06^{+0.36}_{-0.06}$	$0.89^{+0.44}_{-0.42}$	$1.34^{+0.44}_{-0.42}$	$0.66^{+0.23}_{-0.22}$	$0.67^{+0.28}_{-0.27}$	$0.45^{+0.05}_{-0.05}$	$2.33^{+0.93}_{-0.87}$	1739/1493
13–17′	71 ± 2	$3.55^{+0.10}_{-0.10}$	$0.11^{+0.42}_{-0.11}$	$0.97^{+0.41}_{-0.39}$	$0.89^{+0.39}_{-0.37}$	$0.50^{+0.21}_{-0.20}$	$0.50^{+0.25}_{-0.24}$	$0.34^{+0.04}_{-0.04}$	$1.63^{+0.85}_{-0.80}$	1782/1493
17–27′	30 ± 1	$3.39^{+0.09}_{-0.08}$	$0.31^{+0.56}_{-0.31}$	$1.13^{+0.44}_{-0.41}$	$0.87^{+0.38}_{-0.36}$	$0.55^{+0.20}_{-0.19}$	$0.42^{+0.24}_{-0.23}$	$0.35^{+0.05}_{-0.05}$	$1.85^{+0.85}_{-0.79}$	—†
9–13′	88 ± 5	$3.64^{+0.12}_{-0.12}$	$1.00^{+0.51}_{-0.49}$	$1.33^{+0.53}_{-0.49}$	$1.30^{+0.51}_{-0.48}$	$0.36^{+0.26}_{-0.25}$	$0.56^{+0.32}_{-0.31}$	$0.37^{+0.06}_{-0.05}$	$2.36^{+1.11}_{-1.04}$	1764/1493
13–17′	50 ± 2	$3.56^{+0.11}_{-0.11}$	$0.27^{+0.57}_{-0.27}$	$0.69^{+0.48}_{-0.45}$	$0.59^{+0.44}_{-0.42}$	$0.52^{+0.24}_{-0.23}$	$0.35^{+0.28}_{-0.28}$	$0.31^{+0.05}_{-0.05}$	$0.74^{+0.96}_{-0.74}$	1743/1493
17–27′	23 ± 2	$3.26^{+0.09}_{-0.09}$	$1.04^{+0.79}_{-0.80}$	$0.57^{+0.45}_{-0.42}$	$0.91^{+0.43}_{-0.40}$	$0.27^{+0.21}_{-0.20}$	$0.12^{+0.25}_{-0.12}$	$0.39^{+0.06}_{-0.06}$	$1.98^{+0.94}_{-0.87}$	—†

Normalization of the *vapec* model, calculated in the same way with table 5.3.
The 17–27′ annulus of the east and west offset regions were fitted simultaneously with other annuli, and the best-fit values with the 13–17′ annulus of the east and west offset regions, respectively, are presented here.

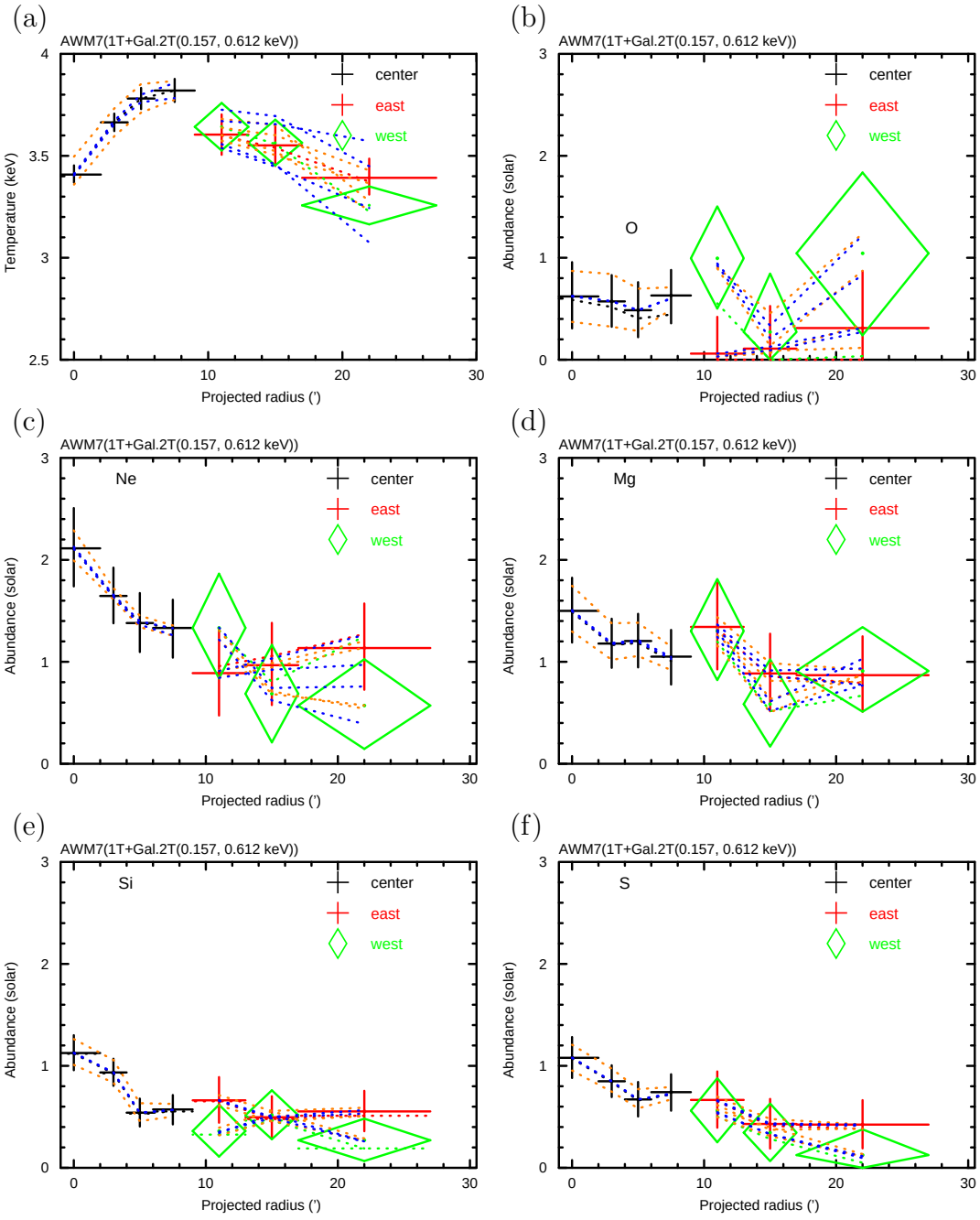

Fig. 5.11: (a) Radial temperature profiles derived from spectral fit of the *Suzaku* spectrum at each annulus. The horizontal axis denotes the projected radius and deprojection are not conducted. The same data with table 5.9 are used for *Suzaku*. The orange dotted lines correspond to shifts of the best-fit values by changing thickness of the OBF contaminant by ±10%. The blue dotted lines denote those when the estimated CXB and NXB levels are changed by ±10%. The black, red, green dotted line shows the best-fit value when the Galactic component is modeled by a single *apec*. (b)–(h) Radial abundance profiles derived and plotted in the same way as (a).

Although the fit was not acceptable due mainly to the very high photon statistics than the systematic errors in the instrumental response, this result was useful to assess whether each element abundance was reasonably determined or not. We fitted the spectra with the all metal abundances as a free parameter. Somehow, the Ne and Ni abundances were larger than other elements. This might be due to these element lines could not be resolved

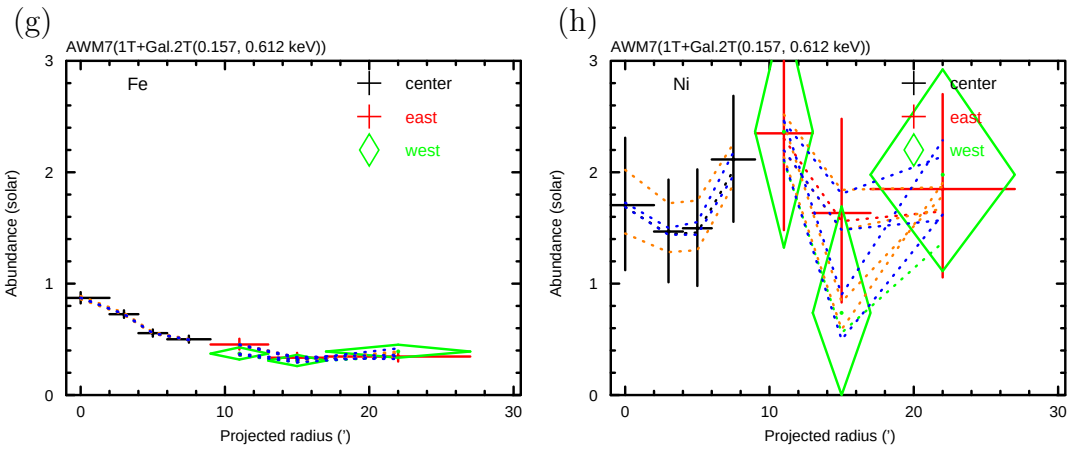

Fig. 5.11: continue of figure 5.11

from the Fe-L line complex. Anyway, we left these Ne and Ni abundances to move freely during the spectral fit.

Considering the OBF contaminants and background (CXB + NXB) systematics, results of the spectral fit at each annulus are summarized in table 5.9 and figure 5.11. We tested the results by changing the background normalization by ±10%, and they are plotted in blue dotted lines in figure 5.11. The systematic error due to the background estimation is almost negligible. Difference in the best-fit values by modeling the Galactic component with a single *apec* was investigated, and they were indicated by black, red, green dotted lines. The differences are within the statistical error for the inner five annuli, however, O abundance becomes lower than the 90% confidence error at the outer two annuli, and temperature and Fe abundance become lower at the outermost annulus. This is due mainly to the fact that the XIS cannot resolve the ICM O VIII line from the Galactic O VIII by redshift. The systematic error range due to the uncertainty in the OBF contaminant is indicated by orange dotted lines. A list of χ^2/dof is presented in table 5.10

Table 5.10: List of χ^2/dof for each fit of AWM 7.

Region	nominal	contaminant		background	
		+10%	-10%	+10%	-10%
0–2′	1872/1493	1829/1493	1939/1493	1909/1493	1871/1493
2–4′	1899/1493	1876/1493	1965/1493	1937/1493	1897/1493
4–6′	1805/1493	1789/1493	1849/1493	1844/1493	1803/1493
6–9′	1816/1493	1786/1493	1852/1493	1858/1493	1814/1493
east					
9–13′	1739/1493	1728/1493	1757/1493	1782/1493	1736/1493
13–17′	1782/1493	1774/1493	1796/1493	1827/1493	1780/1493
west					
9–13′	1764/1493	1751/1493	1784/1493	1806/1493	1762/1493
13–17′	1743/1493	1745/1493	1754/1493	1790/1493	1738/1493

Table 5.11: Line intensities of O VII and O VIII at each annulus of AWM 7 field in unit of photons cm^{-2} s^{-1} sr^{-1}. These intensities are derived from the spectral fit with *power-law* + *gaussian* + *gaussian* model assuming the uniform-sky ARF response. Intensities by McCammon et al. (2002) measured with a high resolution microcalorimeter array for a large sky area of ~ 1 sr are also presented.

Region	O VII	O VIII
AWM 7 center(0–2′)	–	79.8±40.0
AWM 7 center(2–4′)	–	44.6±22.0
AWM 7 center(4–6′)	$3.4^{+20.4}_{-3.4}$	27.7±17.2
AWM 7 center(6–9′)	–	9.9±4.4
AWM 7 east (9–13′)	$0.0^{+4.4}_{-0.0}$	5.9±5.9
AWM 7 east (13–17′)	7.2±5.5	5.9±4.8
AWM 7 east (17–27′)	$0.9^{+2.5}_{-0.9}$	$0.3^{+2.3}_{-0.3}$
AWM 7 west (9–13′)	9.9±7.8	8.4±7.7
AWM 7 west (13–17′)	6.4±5.1	$3.2^{+4.0}_{-3.2}$
AWM 7 west (17–27′)	$2.0^{+2.3}_{-2.0}$	$1.0^{+2.0}_{-1.0}$
Galactic average (McCammon et al. 2002)	4.8±0.8	1.6±0.4

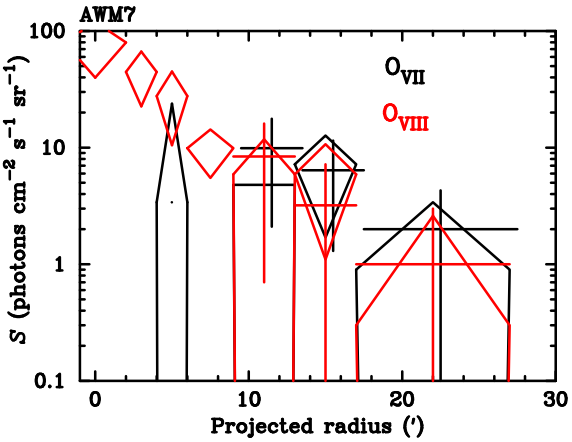

Fig. 5.12: Line intensities of O VII and O VIII at each annulus of A 1060 in unit of photons cm^{-2} s^{-1} sr^{-1}. Each value is shown in table 5.6.

5.2.5 Direct Comparison of O VII and O VIII Intensities

We also investigated the surface brightness of the O VII and O VIII emission lines in order to estimate the O abundance of the ICM directly from the line intensities. The surface brightness of the O VII and O VIII were derived by fitting the annular spectrum with a *power-law* + *gaussian* + *gaussian* model. In the fitting, we fixed the Gaussian σ to be 0, and allowed the energy center of the two Gaussians to vary within 555–573 eV or 648–658 eV for O VII or O VIII, respectively. The derived line intensities are summarized in table 5.11 and figure 5.12. There is a clear excess of the O VIII intensity towards the cluster center, while O VII is consistent with constant. This is a strong evidence that the O VIII emission is associated with the ICM itself, on the other hand, O VII might be due mainly to the Galactic origin.

5.2.6 Bulk Motions in the ICM

To search for possible bulk motions of the ICM, the central energy of He-like Fe-K line (at a rest-frame energy of 6.7 keV) was examined to look for a positional dependence.

We divided the the $18' \times 18'$ square XIS field of view into 4×4 cells (2.2×2.2 arcmin^2) for the central region, and the outer cells (4.4×4.4, or 4.4×8.8 arcmin^2) for the central and east/west offset observations. We co-added the data from XIS0, 2 and 3.

To accurately determine the iron-line energies, we fitted the background-subtracted XIS spectra with a simple model over the 5–10 keV energy range. The model we chose consists of a continuum represented by the *power-law* model and three Gaussians for the major line components: the He-like Fe-Kα line at 6.70 keV, the H-like Fe-Kα line at 6.97 keV, and a 7.83 keV line representing the blend of He-like Ni-Kα line (7.80 keV) and He-like Fe-Kβ line (7.90 keV). The quoted line energies refer to their rest-frame values.

We fitted the 5–10 keV spectra of three FI detectors from individual cells with the *power-law* plus three Gaussian line model. The central energy map of Fe-K line and the results of the fit for all cells shows in figure 5.13.

In order to search the X-ray data for larger-scale velocity gradients in the ICM, we compared the redshift in the east and west region of the central observation. The results shows in figure 5.13. We computed the confidence contour of the central energy vs. the sigma of the lines for the two regions 5.14.

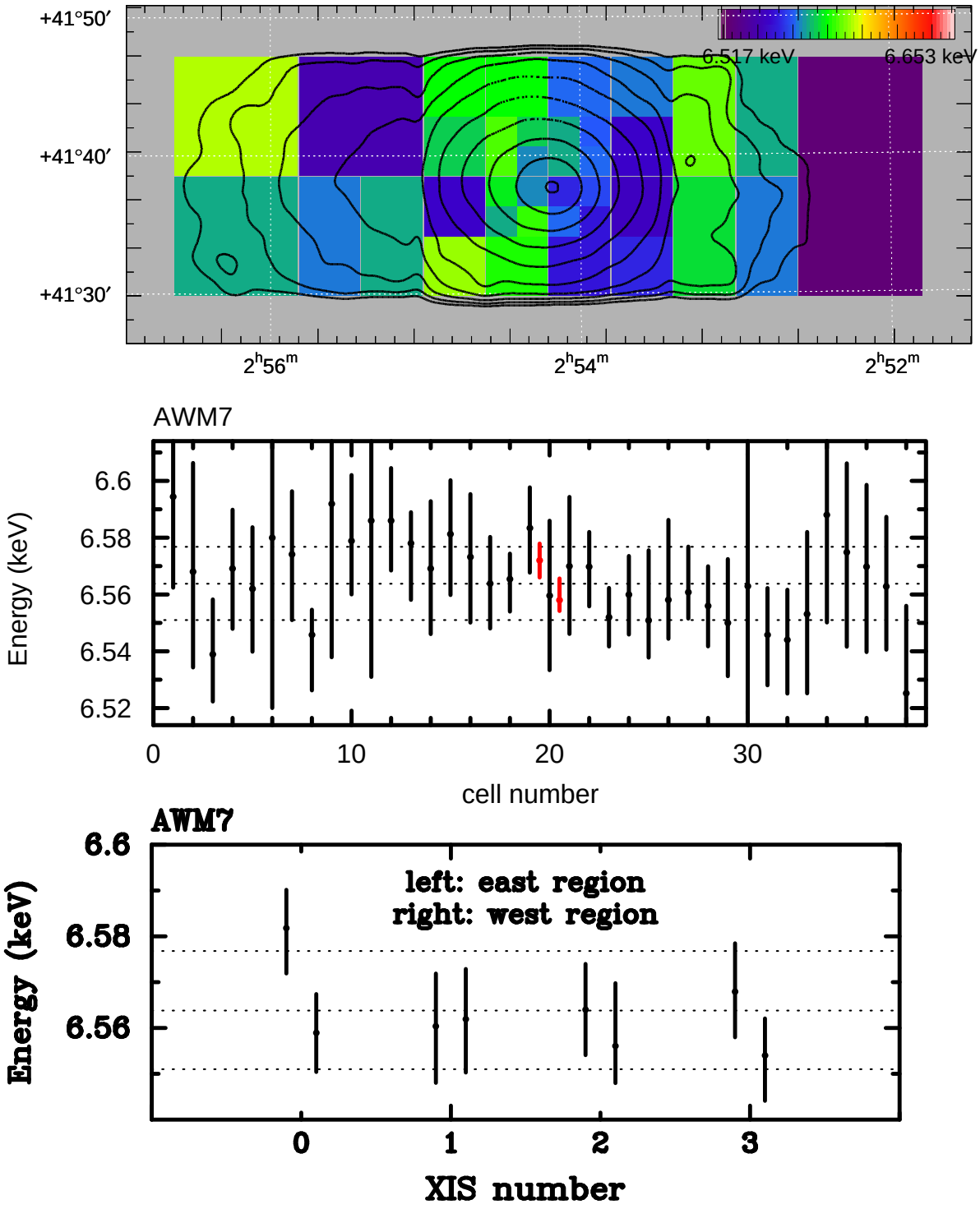

Fig. 5.13: Results of the redshift measurements using the He-like Fe-K lines. The top panel show the redshift of the each cell, which divided by 16 cells (2.2×2.2 arcmin^2) in the central region and outer cells (4.4×4.4 arcmin^2, 4.4×8.8 arcmin^2 or 8.8×8.8 arcmin^2). The middle panel show the central energy of He-like Fe-K line. The redshifted central energy of AWM 7 is 6.564 keV at z=0.01724. The middle dotted line corresponds to the redshift of the cluster, and the upper and lower dotted lines corresponds to the systematic error of XISs (Ota et al. 2006). The red points correspond to the east and west of the central observation. The bottom panel show the central energy of He-like Fe-K line of each sensor. The dotted lines are same as the middle panel.

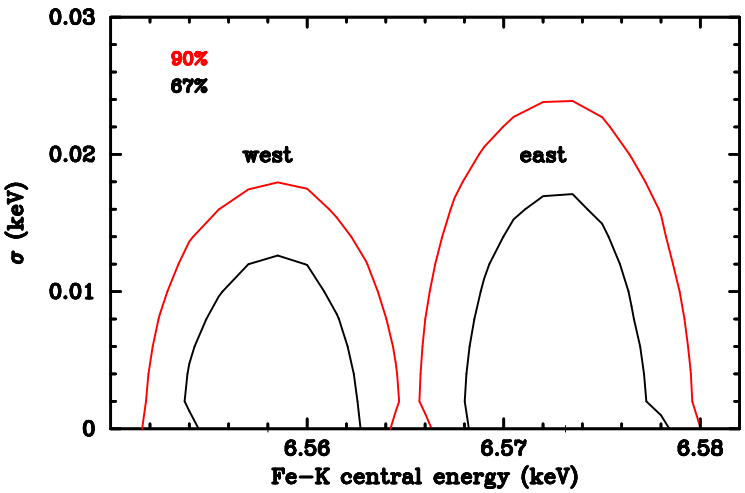

Fig. 5.14: The confidence contour of the central energy vs. the sigma of the Fe-K lines for the east and west regions of the central observation.

5.3 HCG 62

Analysis methods are the almost same as those of A 1060.

5.3.1 *Suzaku* XIS Spectra

We extracted spectra from five annular regions of 0–2′, 2–4′, 4–6′, 6–9′, $r > 9'$, centered on (RA, Dec) = ($12^{\rm h}53^{\rm m}06\overset{\rm s}{.}0$, $-9°12'15''$). Table 5.12 lists areas of the extraction regions (arcmin^2), coverage of the whole annulus (%), the SOURCE_RATIO_REG values (%; see caption for its definition) and the observed counts in 0.4–7.1 keV for the four inner regions, and 0.4–3 keV for the outermost region including NXB and CXB for the BI and FI sensors.

Table 5.12: Area, coverage of whole annulus, SOURCE_RATIO_ REG and observed counts for each annular region of HCG 62. SOURCE_ RATIO_REG represents the flux ratio in the assumed spatial distribution on the sky (triple-β model) inside the accumulation region to the entire model, and written in the header keyword of the calculated ARF response by "xissimarfgen".

Region *	Area † (arcmin^2)	Coverage †	SOURCE_ * RATIO_REG	Counts ‡ BI	FI
0–2′	12.6	100.0%	43.2%	32,041	61,778
2–4′	37.7	100.0%	12.1%	23,906	40,766
4–6′	62.8	100.0%	10.2%	16,750	28,618
6–9′	131.5	93.0%	12.5%	22,553	36,478
$r > 9'$	64.2	23.2%	4.1%	6,931	10,409

* The outermost region ($r > 9'$) include the calibration source region.

† The largest values among four sensors are presented.

‡ Observed counts including NXB and CXB in 0.4–7.1 keV for the four inner regions and in 0.4–3.0 keV for the outermost region.

Each annular spectrum is shown in figure 5.15. The ionized Mg, Si, S, Fe lines are clearly seen in each ring. The O VII and O VIII lines are prominent in the outer rings, however, most of the O VII emission is supposed to come from the local Galactic emission, and we dealt with those in the same way as A 1060.

5.3.2 Strategy of Spectral Fit

The basic strategy of the spectral fit is described in subsection 5.1.2 of A 1060.

We generated two different ARFs for the spectrum of each annulus, $A^{\rm U}$ and $A^{\rm B}$, which respectively assume the uniform-sky emission and $\sim 0.5° \times 0.5°$ size of the triple-β surface brightness profile obtained with the Chandra and XMM-Newton data (table 4.4, and Morita et al. (2006)).

The spectra from BI and FI are fitted simultaneously in the 0.4–7.1 keV band except for energy range of anomalous response around the Si K-edge (1.825–1.840 keV) for the four inner regions and in the 0.4–3.0 keV band for the outermost region. We ignored below 0.4 keV because the C edge (0.284 keV) seen in the BI spectra could not be reproduced

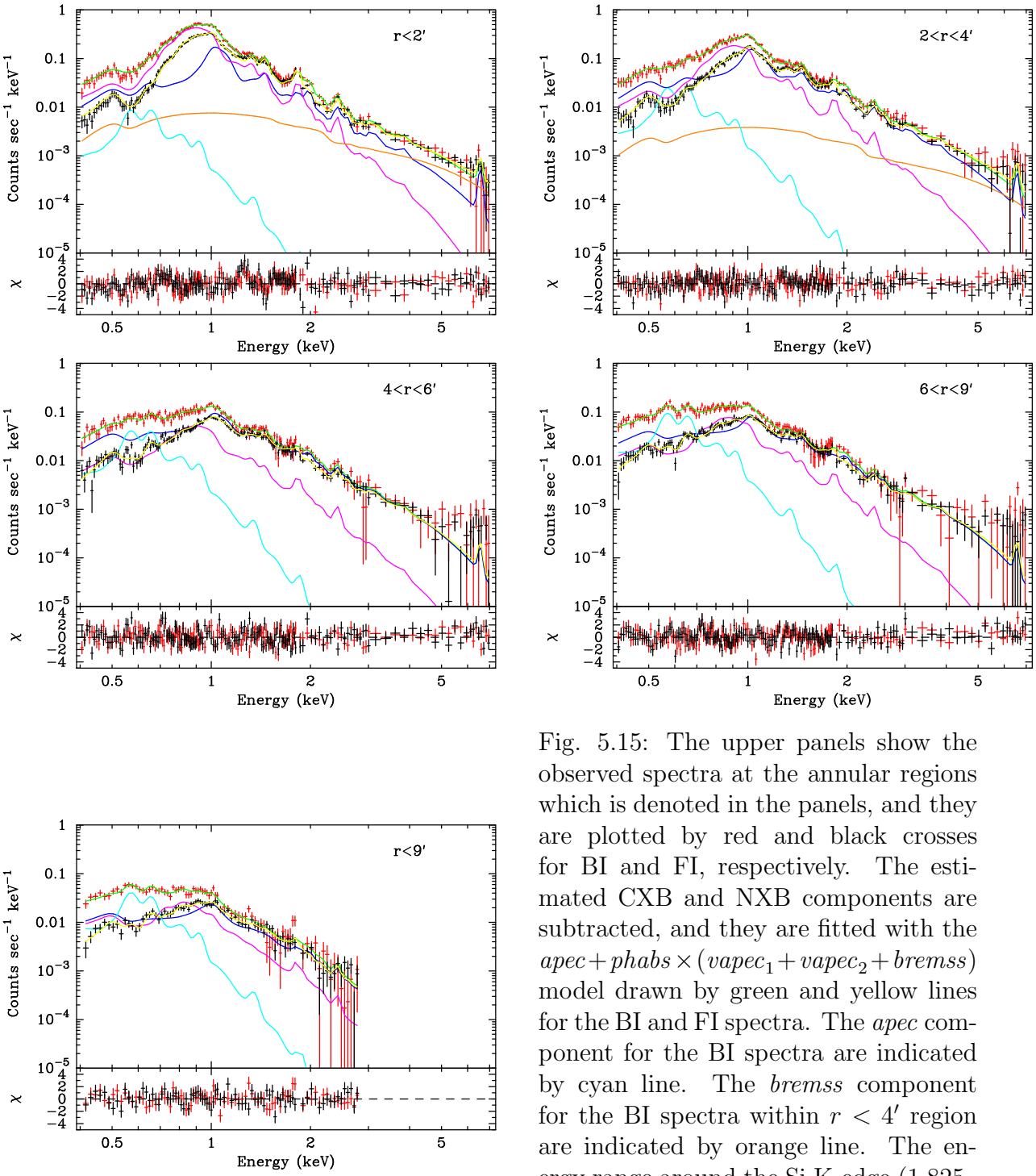

Fig. 5.15: The upper panels show the observed spectra at the annular regions which is denoted in the panels, and they are plotted by red and black crosses for BI and FI, respectively. The estimated CXB and NXB components are subtracted, and they are fitted with the $apec+phabs\times(vapec_1+vapec_2+bremss)$ model drawn by green and yellow lines for the BI and FI spectra. The *apec* component for the BI spectra are indicated by cyan line. The *bremss* component for the BI spectra within $r < 4'$ region are indicated by orange line. The energy range around the Si K-edge (1.825–1.840 keV) is ignored for the spectral fit. The lower panels show the fit residuals in unit of σ.

perfectly in our data. Energy range above 7.1 keV was also ignored because background Ni line ($\sim$ 7.5 keV) left artificial structures after the NXB subtraction at large radii. It is also known that the XIS response in $E \sim 8$ keV are not fully understood at the present stage. In the simultaneous fit of BI and FI, only the normalization are allowed to be different between them, although we found that the derived normalizations are quite consistent between the two. For the outermost region ($r > 9'$) we fitted the spectrum in

0.4–3.0 keV, because the region included the calibration source.

5.3.3 Estimation of Galactic Component

Table 5.13: The best-fit parameters of the *apec* component for the simultaneous fit of all spectra of HCG 62 with $apec + phabs \times (vapec_1 + vapec_2 + zbremss)$ model.

Fit model	*Norm* *	kT (keV)	χ^2/dof
$apec + phabs \times (vapec_1 + vapec_2)$	1.17 ± 0.04	$0.211^{+0.005}_{-0.009}$	1911/1508

* Normalization of the *apec* component divided by the solid angle, Ω^{U}, assumed in the uniform-sky ARF calculation (20′ radius), $Norm = \int n_{\mathrm{e}} n_{\mathrm{H}} dV \,/\, (4\pi\,(1+z)^2 D_{\mathrm{A}}^2) \,/\, \Omega^{\mathrm{U}}$ $\times 10^{-20}$ cm^{-5} arcmin^{-2}, where D_{A} is the angular distance to the source.

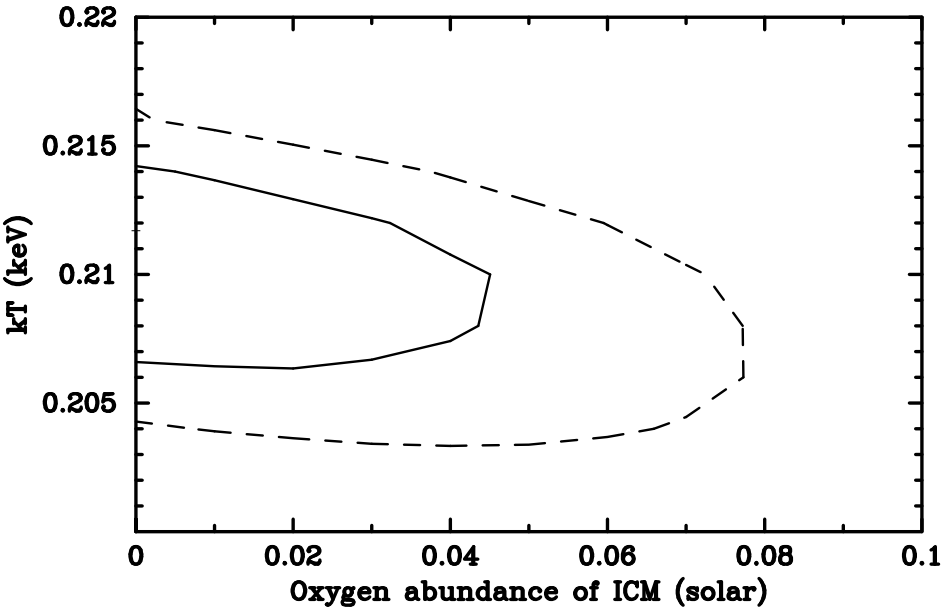

Fig. 5.16: A plot of confidence contour between kT of *apec* component and the O abundance of *vapec* for the $r > 9'$ annulus, in the simultaneous fitting of 6–9′ annulus with the $apec + phabs \times (vapec_1 + vapec_2 + zbremss)$ model. The cross denotes the best-fit location, and the two contours represent 1σ and 90% confidence ranges, from inner to outer, respectively.

It is important to estimate the Galactic component precisely, which is possible using the outermost region of HCG 62 with *Suzaku*. In order to determine the surface brightness and the spectral shape of the Galactic component, we performed the simultaneous fit of all annuli. The Galactic component is prominent in these annuli as shown in figure 5.15, however the ICM component is still dominant almost all the energy range except for the O VII line. We made the simultaneous fit in the 0.4–7.1 keV range (except 1.825–1.840 keV) for the four inner regions and in the 0.4–3.0 keV range for the $r > 9'$ region, assuming an *apec* model for the Galactic component, and the fit results are presented in table 5.13. The resultant normalization of the *apec* model in table 5.13 is scaled so that it gives the surface brightness in the unit solid angle of arcmin^2.

To demonstrate how sensitive the O abundance of the ICM is to the assumed Galactic component model, we present a confidence contour between kT (keV) of the *apec* component and the O abundance (solar) of *vapec* for the outermost annulus ($r > 9'$) in figure 5.16. There appears to exist a negative correlation between the two parameters, because higher temperature of the Galactic component produces more O VIII emission line relative to O VII, which contribute to reduce the O VIII line from the ICM (*vapec* component). Influences on the derived temperature and abundance by the modeling of the Galactic component will be tested in subsection 5.3.4, too.

In order to take into account both existence of the Galactic component itself and propagation of its statistical error, we simultaneously fitted all annuli. As mentioned in the previous subsection, the normalization of the *apec* component is constrained to give the same surface brightness in all annuli. The temperature of the *apec* model was also common in all regions.

5.3.4 Radial Temperature & Abundance Profiles

Table 5.14: Summary of the best-fit parameters of the *vapec* components for each annular region of HCG 62 with the $apec + phabs \times (vapec_1 + vapec_2 + zbremss)$ model. All annuli are simultaneous fitted. Errors are 90% confidence range of statistical errors, and do not include systematic errors. The solar abundance ratio of *angr* is assumed. These results are plotted in figure 5.18.

Region	$Norm_1$ *	kT_1 (keV)	$Norm_2$ *	kT_2 (keV)	O (solar)	Ne (solar)	Mg,Al (solar)	Si (solar)	S,Ar,Ca (solar)	Fe,Ni (solar)	χ^2/dof
0–2′	51.9 ± 2.7	$1.53^{+0.05}_{-0.06}$	50.7 ± 3.4	$0.76^{+0.06}_{-0.07}$	$0.45^{+0.10}_{-0.09}$	$1.87^{+0.33}_{-0.30}$	$1.81^{+0.22}_{-0.19}$	$1.39^{+0.09}_{-0.09}$	$1.55^{+0.20}_{-0.19}$	$1.15^{+0.09}_{-0.08}$	1911/1508
2–4′	13.5 ± 0.8	$1.54^{+0.05}_{-0.05}$	7.6 ± 0.6	$0.77^{+0.01}_{-0.02}$	$0.22^{+0.10}_{-0.09}$	$1.22^{+0.28}_{-0.25}$	$0.94^{+0.15}_{-0.13}$	$0.68^{+0.10}_{-0.09}$	$0.79^{+0.13}_{-0.12}$	$0.54^{+0.05}_{-0.04}$	–
4–6′	12.4 ± 0.9	$1.44^{+0.07}_{-0.06}$	4.1 ± 0.6	$0.76^{+0.03}_{-0.04}$	$0.10^{+0.12}_{-0.10}$	$0.33^{+0.19}_{-0.17}$	$0.35^{+0.12}_{-0.10}$	$0.30^{+0.08}_{-0.07}$	$0.50^{+0.12}_{-0.12}$	$0.24^{+0.03}_{-0.03}$	–
6–9′	6.5 ± 0.5	$1.53^{+0.08}_{-0.08}$	3.4 ± 0.5	$0.72^{+0.03}_{-0.05}$	$0.0^{+0.12}_{-0.0}$	$0.55^{+0.20}_{-0.18}$	$0.40^{+0.13}_{-0.11}$	$0.31^{+0.09}_{-0.08}$	$0.43^{+0.16}_{-0.15}$	$0.24^{+0.04}_{-0.03}$	–
$r > 9'$	5.7 ± 2.3	$1.14^{+0.15}_{-0.14}$	5.1 ± 2.0	$0.63^{+0.05}_{-0.15}$	$0.0^{+0.09}_{-0.0}$	$0.18^{+0.20}_{-0.18}$	$0.04^{+0.11}_{-0.04}$	$0.17^{+0.12}_{-0.11}$	$0.28^{+0.27}_{-0.25}$	$0.11^{+0.03}_{-0.02}$	–

* Normalization of the *vapec* model, calculated in the same way with table 5.3.

† All regions were fitted simultaneously.

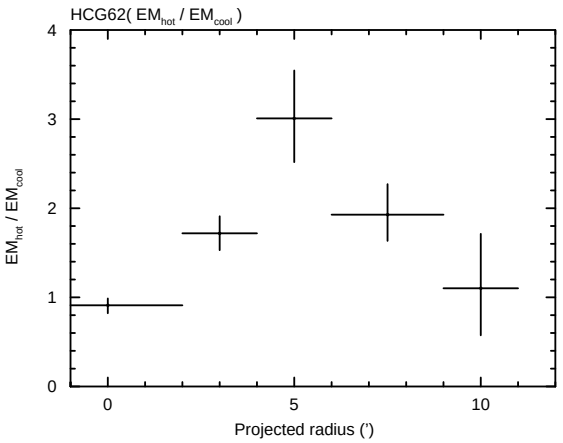

Fig. 5.17: The emission measure of the hot component of the HCG 62 to that of cool component ratio.

Although the fit was not acceptable due mainly to the very high photon statistics than the systematic errors in the instrumental response, this result was useful to assess whether each element abundance was reasonably determined or not. The abundances are linked together for Mg=Al, S=Ar=Ca, Fe=Ni, and are also linked between $vapec_1$ and $vapec_2$.

The *bremss* component represent the LMXB emission within $r < 4'$, and we adopt a $kT = 7$ keV bremsstrahlung component to model their spectra.

Considering the OBF contaminants and background (CXB + NXB) systematics, results of the spectral fit at each annulus are summarized in table 5.14 and figure 5.18. We tested the results by changing the background normalization by ±10%, and they are plotted in green dotted lines in figure 5.18. The systematic error due to the background estimation is almost negligible. The systematic error range due to the uncertainty in the OBF contaminant is indicated by black dotted lines. A list of χ^2/dof is presented in table 5.15

Table 5.15: List of χ^2/dof for each fit of HCG 62.

Region	nominal	contaminaut		background	
		+20%	-20%	+10%	-10%
All	1911/1508	1881/1508	2034/1508	1874/1508	2060/1508

5.3.5 Direct Comparison of O VII and O VIII Intensities

We also investigated the surface brightness of the O VII and O VIII emission lines in order to estimate the O abundance of the ICM directly from the line intensities. The surface brightness of the O VII and O VIII were derived by fitting the annular spectrum with a *power-law* + *gaussian* + *gaussian* model. In the fitting, we fixed the Gaussian σ to be 0, and allowed the energy center of the two Gaussians to vary within 555–573 eV or 648–658 eV for O VII or O VIII, respectively. The derived line intensities are summarized in table 5.16 and figure 5.19. There is a clear excess of the O VIII intensity towards the cluster center, while O VII is consistent with constant. This is a strong evidence that the

Table 5.16: Line intensities of O VII and O VIII at each annulus of HCG 62 field in unit of photons cm^{-2} s^{-1} sr^{-1}. These intensities are derived from the spectral fit with *power-law* + *gaussian* + *gaussian* model Intensities by McCammon et al. (2002) measured with a high resolution microcalorimeter array for a large sky area of ~ 1 sr are also presented.

Region		O VII	O VIII
HCG 62	(0–2′)	–	24.8±13.4
HCG 62	(2–4′)	4.6±2.7	5.6±3.0
HCG 62	(4–6′)	8.2±3.2	5.2±2.0
HCG 62	(6–9′)	8.7±1.2	4.9±1.1
HCG 62	($r > 9'$)	7.8±2.1	3.3±1.9
Galactic average (McCammon et al. 2002)		4.8±0.8	1.6±0.4

O VIII emission is associated with the ICM itself, on the other hand, O VII might be due mainly to the Galactic origin.

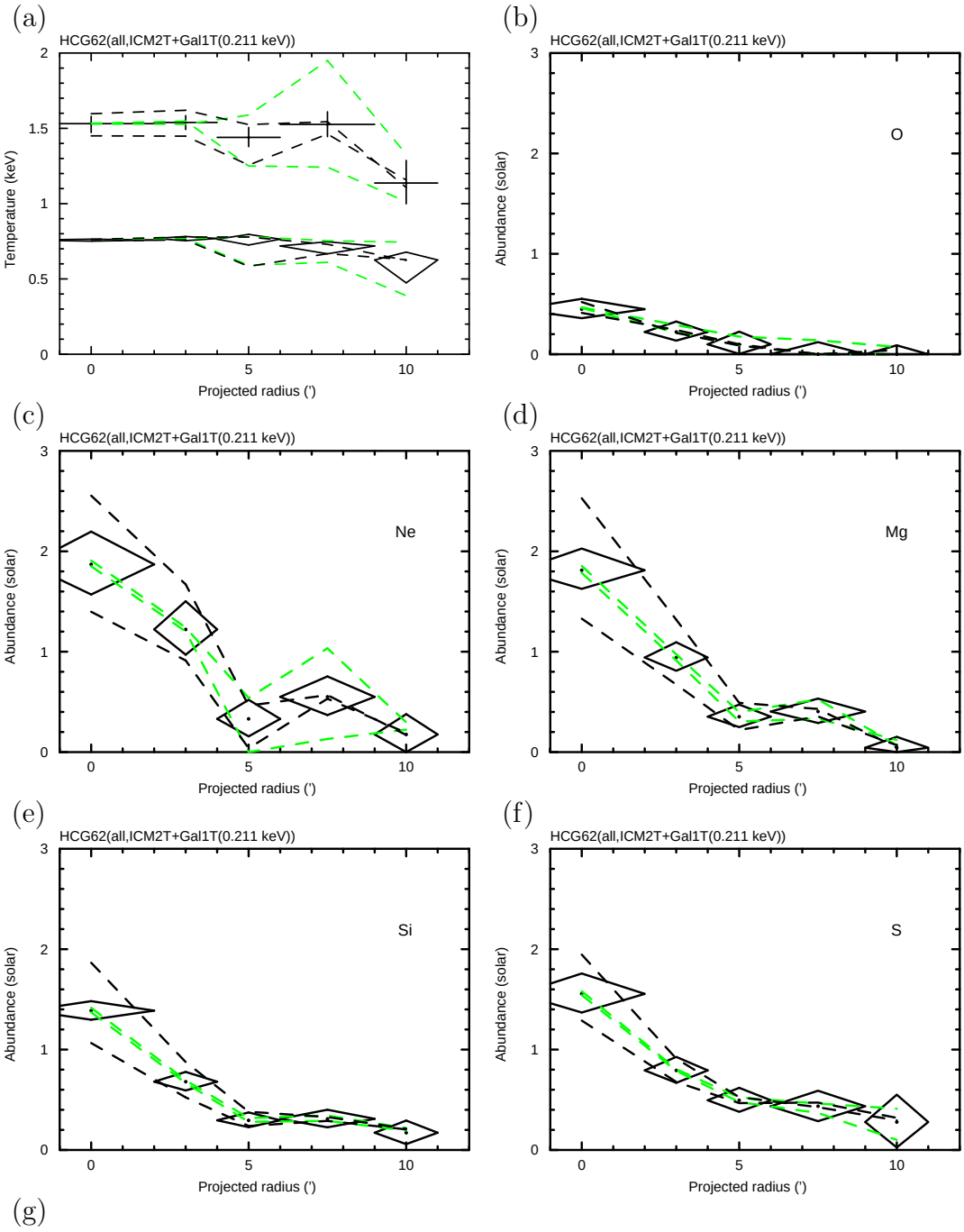

Fig. 5.18: (a) Radial temperature profiles derived from spectral fit of the *Suzaku* spectrum at each annulus. The horizontal axis denotes the projected radius and deprojection are not conducted. The same data with table 5.14 are used for *Suzaku*. The black dotted lines correspond to shifts of the best-fit values by changing thickness of the OBF contaminant by ±20%. The green dotted lines denote those when the estimated CXB and NXB levels are changed by ±10%. (b)–(g) Radial abundance profiles derived and plotted in the same way as (a).

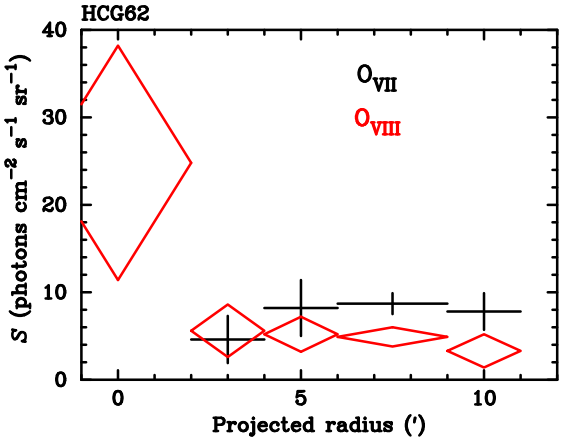

Fig. 5.19: Line intensities of O VII and O VIII at each annulus of A 1060 in unit of photons cm^{-2} s^{-1} sr^{-1}. Each value is shown in table 5.16.

5.4 NGC 507

Analysis methods are the almost same as those of HCG 62.

5.4.1 *Suzaku* XIS Spectra

We extracted spectra from five annular regions of 0–2′, 2–4′, 4–6′, 6–9′, $r > 9'$, centered on (RA, Dec) = ($1^{\rm h}23^{\rm m}40\overset{\rm s}{.}0$, $+33°15'21''$). Table 5.17 lists areas of the extraction regions (arcmin^2), coverage of the whole annulus (%), the SOURCE_RATIO_REG values (%; see caption for its definition) and the observed counts in 0.4–7.1 keV for the four inner regions, and 0.4–3 keV for the outermost region including NXB and CXB for the BI and FI sensors.

Table 5.17: Area, coverage of whole annulus, SOURCE_RATIO_ REG and observed counts for each annular region of NGC 507. SOURCE_ RATIO_REG represents the flux ratio in the assumed spatial distribution on the sky (triple-β model) inside the accumulation region to the entire model, and written in the header keyword of the calculated ARF response by "xissimarfgen".

Region *	Area † (arcmin^2)	Coverage †	SOURCE_ * RATIO_REG	Counts ‡ BI	FI
0–2′	12.6	100.0%	29.2%	23,452	49,445
2–4′	37.7	100.0%	21.9%	26,997	53,622
4–6′	62.8	100.0%	14.4%	18,274	34,960
6–9′	133.3	94.3%	13.4%	21,286	38,891
$r > 9'$	64.0	23.1%	4.0%	5,481	9,420

* The outermost region ($r > 9'$) include the calibration source region.

† The largest values among four sensors are presented.

‡ Observed counts including NXB and CXB in 0.4–7.1 keV for the four inner regions and in 0.4–3.0 keV for the outermost region.

Each annular spectrum is shown in figure 5.20. The ionized Mg, Si, S, Fe lines are clearly seen in each ring. The O VII and O VIII lines are prominent in the outer rings, however, most of the O VII emission is supposed to come from the local Galactic emission, and we dealt with those in the same way as HCG 62.

5.4.2 Strategy of Spectral Fit

The basic strategy of the spectral fit is described in subsection 5.1.2 of HCG 62.

We generated two different ARFs for the spectrum of each annulus, $A^{\rm U}$ and $A^{\rm B}$, which respectively assume the uniform-sky emission and $\sim 0.5° \times 0.5°$ size of the triple-β surface brightness profile obtained with XMM-Newton data (table 4.4).

The spectra from BI and FI are fitted simultaneously in the 0.4–7.1 keV band except for energy range of anomalous response around the Si K-edge (1.825–1.840 keV) for the four inner regions and in the 0.4–3.0 keV band for the outermost region. We ignored below 0.4 keV because the C edge (0.284 keV) seen in the BI spectra could not be reproduced perfectly in our data. Energy range above 7.1 keV was also ignored because background

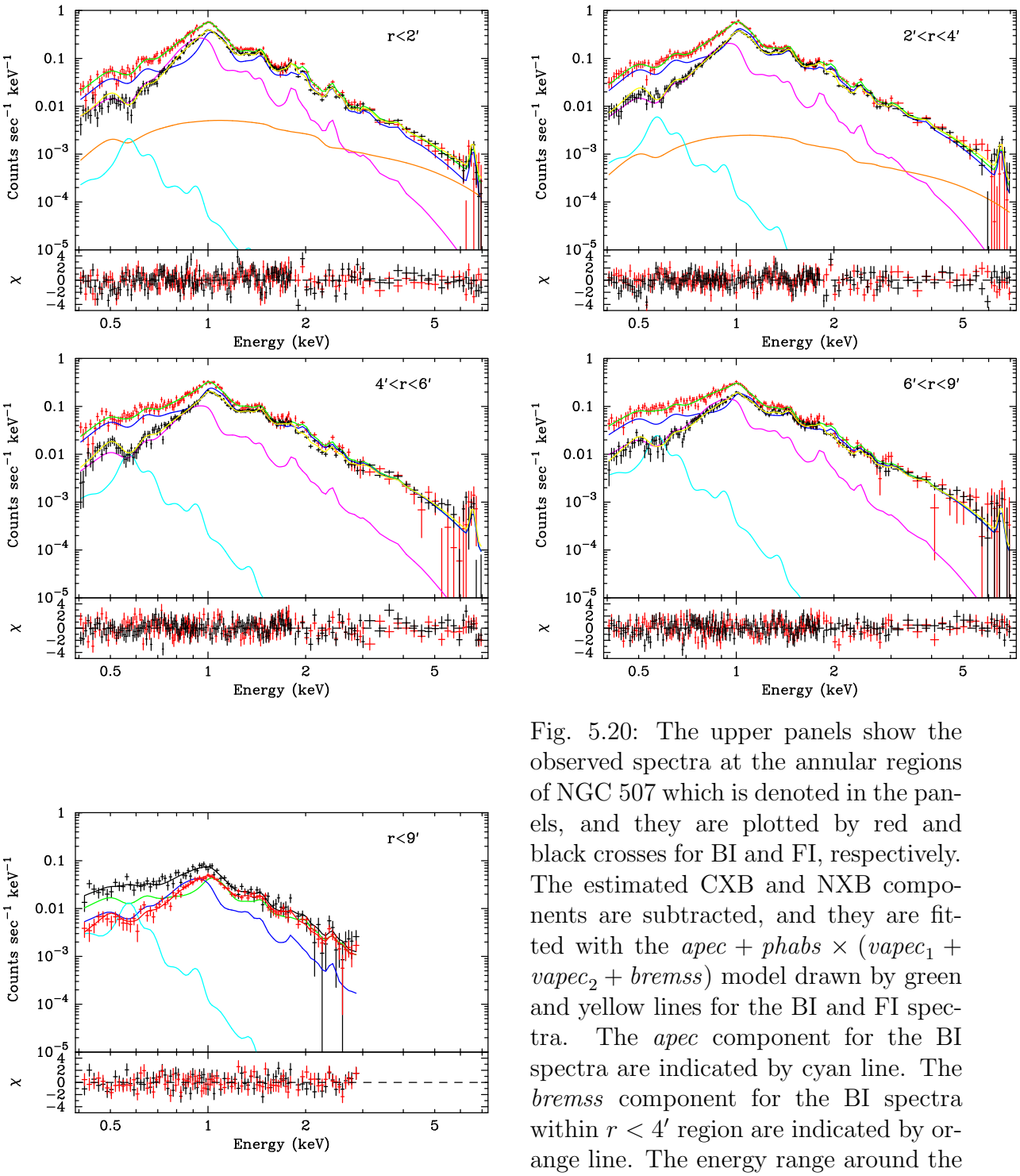

Fig. 5.20: The upper panels show the observed spectra at the annular regions of NGC 507 which is denoted in the panels, and they are plotted by red and black crosses for BI and FI, respectively. The estimated CXB and NXB components are subtracted, and they are fitted with the $apec + phabs \times (vapec_1 + vapec_2 + bremss)$ model drawn by green and yellow lines for the BI and FI spectra. The *apec* component for the BI spectra are indicated by cyan line. The *bremss* component for the BI spectra within $r < 4'$ region are indicated by orange line. The energy range around the Si K-edge (1.825–1.840 keV) is ignored for the spectral fit. The lower panels show the fit residuals in unit of σ.

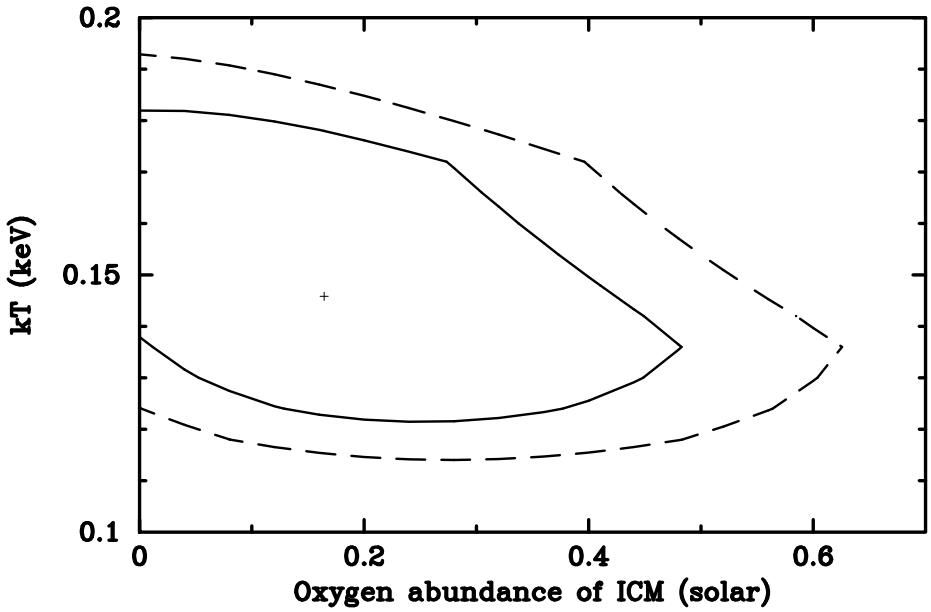

Fig. 5.21: A plot of confidence contour between kT of *apec* component and the O abundance of *vapec* for the $r > 9'$ annulus, in the simultaneous fitting of 6–9′ annulus with the $apec + phabs \times (vapec_1 + vapec_2 + bremss)$ model. The cross denotes the best-fit location, and the two contours represent 1σ and 90% confidence ranges, from inner to outer, respectively.

Ni line ($\sim$ 7.5 keV) left artificial structures after the NXB subtraction at large radii. It is also known that the XIS response in $E \sim 8$ keV are not fully understood at the present stage. In the simultaneous fit of BI and FI, only the normalization are allowed to be different between them, although we found that the derived normalizations are quite consistent between the two. For the outermost region ($r > 9'$) we fitted the spectrum in 0.4–3.0 keV, because the region included the calibration source.

5.4.3 Estimation of Galactic Component

Table 5.18: The best-fit parameters of the *apec* component for the simultaneous fit of all spectra of NGC 507 with $apec + phabs \times (vapec_1 + vapec_2 + bremss)$ model.

Fit model	*Norm* *	kT (keV)	χ^2/dof
$apec + phabs \times (vapec_1 + vapec_2 + bremss)$	0.42 ± 0.14	$0.159^{+0.034}_{-0.037}$	2067/1510

* Normalization of the *apec* component divided by the solid angle, $\Omega^{\rm U}$, assumed in the uniform-sky ARF calculation (20′ radius), $Norm = \int n_{\rm e} n_{\rm H} dV \,/\, (4\pi\,(1+z)^2 D_{\rm A}^2) \,/\, \Omega^{\rm U} \times 10^{-20}$ cm^{-5} arcmin^{-2}, where $D_{\rm A}$ is the angular distance to the source.

It is important to estimate the Galactic component precisely, which is possible using the outermost region of NGC 507 with *Suzaku*. In order to determine the surface brightness and the spectral shape of the Galactic component, we performed the simultaneous fit of all annuli. The Galactic component is prominent in these annuli as shown in figure 5.20, however the ICM component is still dominant almost all the energy range except

for the O VII line. We made the simultaneous fit in the 0.4–7.1 keV range (except 1.825–1.840 keV) for the four inner regions and in the 0.4–3.0 keV range for the $r > 9'$ region, assuming an *apec* model for the Galactic component, and the fit results are presented in table 5.18. The resultant normalization of the *apec* model in table 5.18 is scaled so that it gives the surface brightness in the unit solid angle of arcmin^2.

To demonstrate how sensitive the O abundance of the ICM is to the assumed Galactic component model, we present a confidence contour between kT (keV) of the *apec* component and the O abundance (solar) of *vapec* for the outermost annulus ($r > 9'$) in figure 5.21. There appears to exist a negative correlation between the two parameters, because higher temperature of the Galactic component produces more O VIII emission line relative to O VII, which contribute to reduce the O VIII line from the ICM (*vapec* component). Influences on the derived temperature and abundance by the modeling of the Galactic component will be tested in subsection 5.4.4, too.

In order to take into account both existence of the Galactic component itself and propagation of its statistical error, we simultaneously fitted all annuli. As mentioned in the previous subsection, the normalization of the *apec* component is constrained to give the same surface brightness in all annuli. The temperature of the *apec* model was also common in all regions.

5.4.4 Radial Temperature & Abundance Profiles

Table 5.19: Summary of the best-fit parameters of the *vapec* components for each annular region of NGC 507 with the $apec + phabs \times (vapec_1 + vapec_2 + zbremss)$ model. All annuli are simultaneous fitted. Errors are 90% confidence range of statistical errors, and do not include systematic errors. The solar abundance ratio of *angr* is assumed. These results are plotted in figure 5.23.

Region	$Norm_1$ *	kT_1 (keV)	$Norm_2$ *	kT_2 (keV)	O (solar)	Ne (solar)	Mg,Al (solar)	Si (solar)	S,Ar,Ca (solar)	Fe,Ni (solar)	χ^2/dof
0–2′	115.4 ± 7.0	$1.54^{+0.02}_{-0.02}$	38.0 ± 3.2	$0.83^{+0.01}_{-0.01}$	$0.58^{+0.16}_{-0.14}$	$2.02^{+0.41}_{-0.36}$	$1.61^{+0.22}_{-0.19}$	$1.33^{+0.15}_{-0.13}$	$1.36^{+0.17}_{-0.15}$	$0.96^{+0.09}_{-0.08}$	2067/1510
2–4′	49.0 ± 2.8	$1.53^{+0.04}_{-0.02}$	11.3 ± 0.8	$0.85^{+0.01}_{-0.01}$	$0.50^{+0.13}_{-0.12}$	$1.34^{+0.20}_{-0.20}$	$1.08^{+0.14}_{-0.14}$	$0.83^{+0.09}_{-0.08}$	$0.82^{+0.10}_{-0.10}$	$0.61^{+0.05}_{-0.05}$	–
4–6′	26.1 ± 1.7	$1.51^{+0.05}_{-0.04}$	5.7 ± 0.6	$0.84^{+0.06}_{-0.03}$	$0.36^{+0.15}_{-0.13}$	$1.00^{+0.28}_{-0.26}$	$0.67^{+0.15}_{-0.13}$	$0.45^{+0.08}_{-0.07}$	$0.51^{+0.10}_{-0.10}$	$0.40^{+0.05}_{-0.04}$	–
6–9′	12.6 ± 0.9	$1.65^{+0.06}_{-0.06}$	4.2 ± 0.4	$0.81^{+0.02}_{-0.02}$	$0.34^{+0.17}_{-0.14}$	$1.19^{+0.32}_{-0.29}$	$0.77^{+0.17}_{-0.15}$	$0.54^{+0.10}_{-0.10}$	$0.52^{+0.13}_{-0.13}$	$0.41^{+0.05}_{-0.04}$	–
$r > 9'$	8.5 ± 1.2	$1.49^{+0.17}_{-0.18}$	4.1 ± 0.8	$0.82^{+0.03}_{-0.04}$	$0.22^{+0.27}_{-0.20}$	$0.39^{+0.52}_{-0.39}$	$0.58^{+0.28}_{-0.23}$	$0.34^{+0.17}_{-0.15}$	$0.53^{+0.31}_{-0.29}$	$0.35^{+0.10}_{-0.07}$	–

* Normalization of the *vapec* model, calculated in the same way with table 5.3.

† All regions were fitted simultaneously.

Table 5.20: List of χ^2/dof for each fit of NGC 507.

Region	nominal	contaminaut		background	
		+10%	-10%	+10%	-10%
All	2067/1510	2004/1510	2148/1510	2104/1510	2094/1510

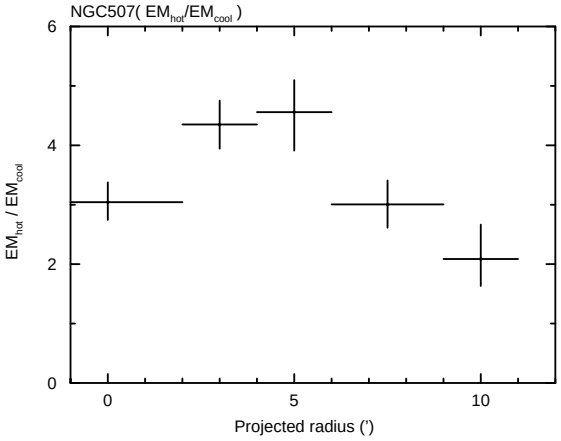

Fig. 5.22: The emission measure of the hot component of the NGC 507 to that of cool component ratio.

Although the fit was not acceptable due mainly to the very high photon statistics than the systematic errors in the instrumental response, this result was useful to assess whether each element abundance was reasonably determined or not. The abundances are linked together for Mg=Al, S=Ar=Ca, Fe=Ni, and are also linked between $vapec_1$ and $vapec_2$.

The *bremss* component represent the LMXB emission within $r < 4'$ (Kim & Fabbiano 2004), and we adopt a $kT = 7$ keV bremsstrahlung component to model their spectra.

Considering the OBF contaminants and background (CXB + NXB) systematics, results of the spectral fit at each annulus are summarized in table 5.19 and figure 5.23. We tested the results by changing the background normalization by $\pm 10\%$, and they are plotted in green dotted lines in figure 5.23. The systematic error due to the background estimation is almost negligible. The systematic error range due to the uncertainty in the OBF contaminant is indicated by black dotted lines. A list of χ^2/dof is presented in table 5.20

5.4.5 Direct Comparison of O VII and O VIII Intensities

We also investigated the surface brightness of the O VII and O VIII emission lines in order to estimate the O abundance of the ICM directly from the line intensities. The surface brightness of the O VII and O VIII were derived by fitting the annular spectrum with a *power-law + gaussian + gaussian* model. In the fitting, we fixed the Gaussian σ to be 0, and allowed the energy center of the two Gaussians to vary within 555–573 eV or 648–658 eV for O VII or O VIII, respectively. The derived line intensities are summarized in table 5.21 and figure 5.24. There is a clear excess of the O VIII intensity towards the cluster center, while O VII is consistent with constant. This is a strong evidence that the O VIII emission is associated with the ICM itself, on the other hand, O VII might be due

Table 5.21: Line intensities of O VII and O VIII at each annulus of NGC 507 field in unit of photons cm^{-2} s^{-1} sr^{-1}. These intensities are derived from the spectral fit with *power-law* + *gaussian* + *gaussian* model Intensities by McCammon et al. (2002) measured with a high resolution microcalorimeter array for a large sky area of ~ 1 sr are also presented.

Region		O VII	O VIII
NGC 507	(0–2′)	$14.5^{+82.8}_{-14.5}$	26.0±8.4
NGC 507	(2–4′)	8.9±4.0	11.3±4.0
NGC 507	(4–6′)	2.5±2.5	3.1±2.4
NGC 507	(6–9′)	4.4±1.7	3.9±1.6
NGC 507	($r > 9'$)	3.7±2.7	3.3±2.4
Galactic average (McCammon et al. 2002)		4.8±0.8	1.6±0.4

mainly to the Galactic origin.

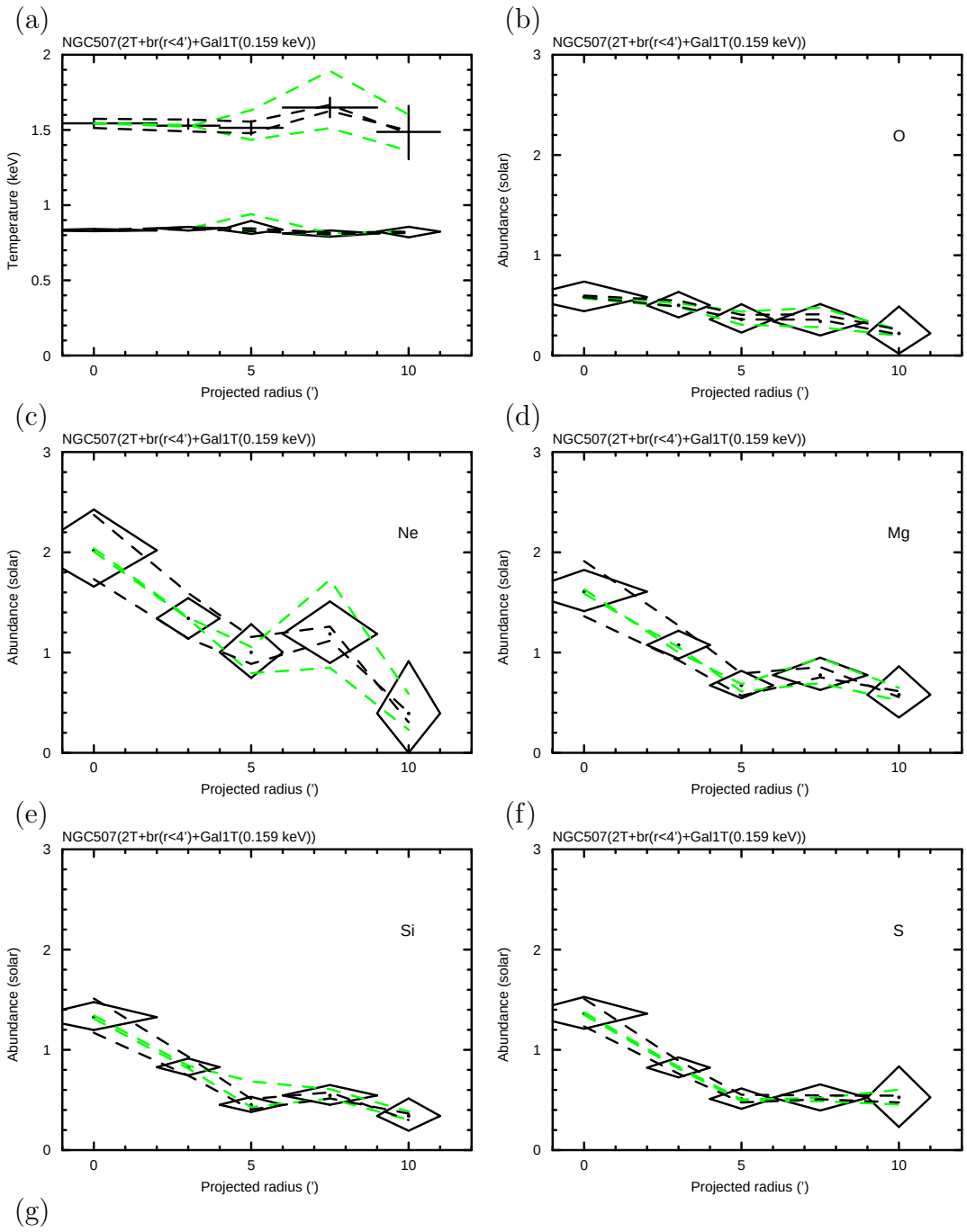

Fig. 5.23: (a) Radial temperature profiles derived from spectral fit of the *Suzaku* spectrum at each annulus. The horizontal axis denotes the projected radius and deprojection are not conducted. The same data with table 5.19 are used for *Suzaku*. The black dotted lines correspond to shifts of the best-fit values by changing thickness of the OBF contaminant by ±10%. The green dotted lines denote those when the estimated CXB and NXB levels are changed by ±10%. (b)–(g) Radial abundance profiles derived and plotted in the same way as (a).

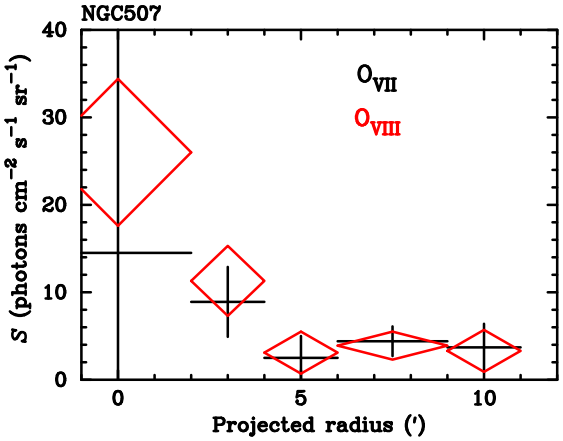

Fig. 5.24: Line intensities of O VII and O VIII at each annulus of A 1060 in unit of photons cm^{-2} s^{-1} sr^{-1}. Each value is shown in table 5.21.

5.5 NGC 720

Analysis methods are the almost same as those of HCG 62. Our results of NGC 720 are almost same as that reported by Tawara (2007).

5.5.1 *Suzaku* XIS Spectra

We extracted spectra from four annular regions of 0–2′, 2–4′, 4–6′, 6–9′, centered on (RA, Dec) = ($1^{\rm h}53^{\rm m}00\overset{\rm s}{.}5$, $-13°44'19''$). Table 5.22 lists areas of the extraction regions (arcmin^2), coverage of the whole annulus (%), the SOURCE_RATIO_REG values (%; see caption for its definition) and the observed counts in 0.4–7.0 keV for the two inner regions, and 0.4–4 and 0.4–2.0 keV for the 4–6′ and 6–9′ region including NXB and CXB for the BI and FI sensors, respectively.

Table 5.22: Area, coverage of whole annulus, SOURCE_RATIO_ REG and observed counts for each annular region of NGC 720. SOURCE_RATIO_REG represents the flux ratio in the assumed spatial distribution on the sky (triple-β model) inside the accumulation region to the entire model, and written in the header keyword of the calculated ARF response by "xissimarfgen".

Region	Area * (arcmin^2)	Coverage *	SOURCE_} RATIO_REG	Counts † BI	FI
0–2′	12.6	100.0%	33.2%	13,884	22,813
2–4′	37.7	100.0%	16.5%	13,201	20,404
4–6′	62.8	100.0%	12.6%	9,834	13,916
6–9′	137.1	97.0%	14.9%	13,078	17,183

* The largest values among four sensors are presented.
† Observed counts including NXB and CXB in 0.4–7.0 keV for the two inner regions and in 0.4–4.0 and 0.4–2.0 keV for the 4–6′ and 6–9′ region.

Each annular spectrum is shown in figure 5.25. The ionized Mg, Si, S, Fe lines are clearly seen in each ring. The O VII and O VIII lines are prominent in the outer rings, however, most of the O VII emission is supposed to come from the local Galactic emission, and we dealt with those in the same way as HCG 62.

5.5.2 Strategy of Spectral Fit

The basic strategy of the spectral fit is described in subsection 5.1.2 of HCG 62.

We generated two different ARFs for the spectrum of each annulus, $A^{\rm U}$ and $A^{\rm B}$, which respectively assume the uniform-sky emission and $\sim 0.5° \times 0.5°$ size of the triple-β surface brightness profile by Buote et al. (2002).

The spectra from BI and FI are fitted simultaneously in the 0.4–7.0 keV band except for energy range of anomalous response around the Si K-edge (1.825–1.840 keV) for the two inner regions and in the 0.4–4.0 and 0.4 –2.0 keV band for the 4–6′ and 6–9′ region. We ignored below 0.4 keV because the C edge (0.284 keV) seen in the BI spectra could not be reproduced perfectly in our data. Energy range above 7.0 keV was also ignored because

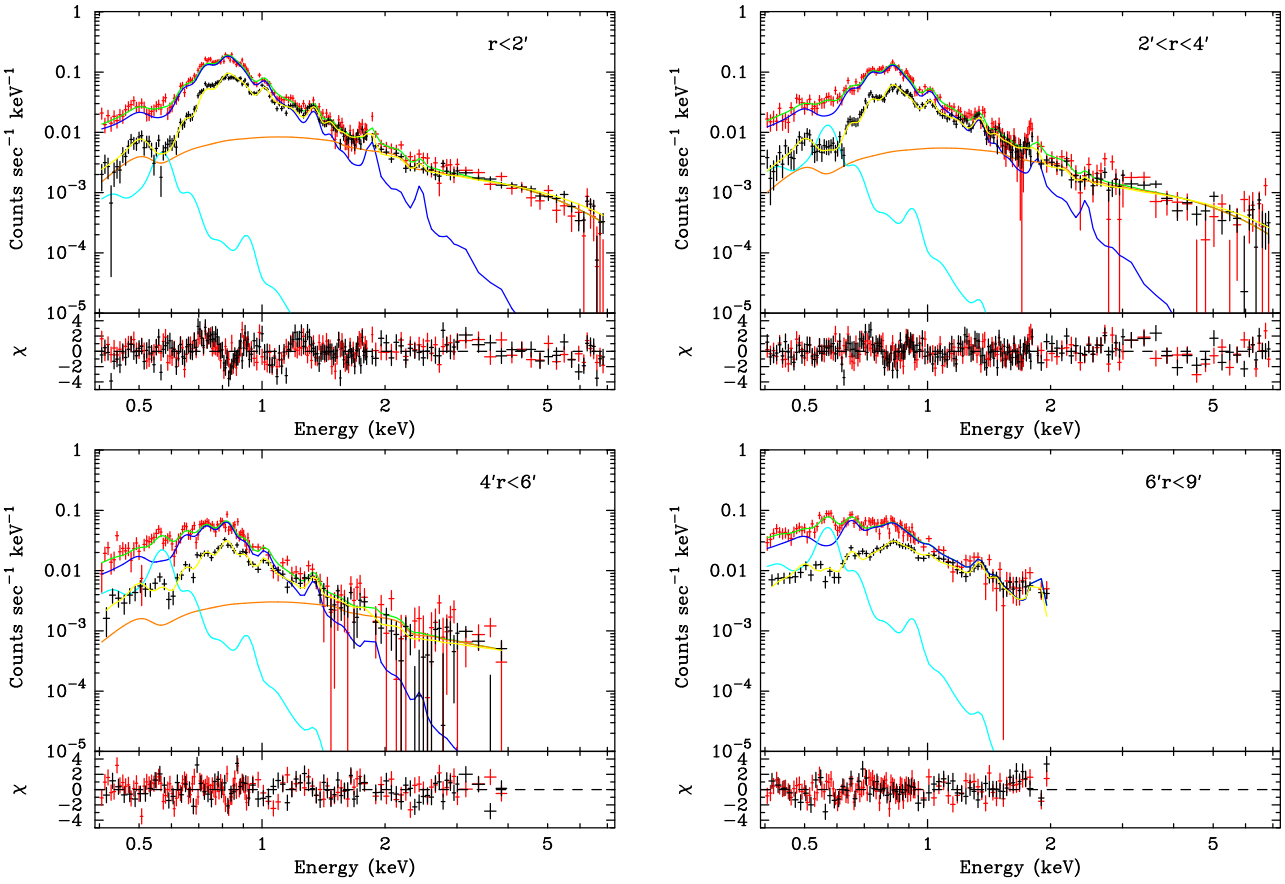

Fig. 5.25: The upper panels show the observed spectra at the annular regions of NGC 720 which is denoted in the panels, and they are plotted by red and black crosses for BI and FI, respectively. The estimated CXB and NXB components are subtracted, and they are fitted with the $apec + phabs \times vapec) + phabs \times zbremss$ model drawn by green and yellow lines for the BI and FI spectra. The *apec* component for the BI spectra are indicated by cyan line. The *bremss* component for the BI spectra within $r < 6'$ region are indicated by orange line. The energy range around the Si K-edge (1.825–1.840 keV) is ignored for the spectral fit. The lower panels show the fit residuals in unit of σ.

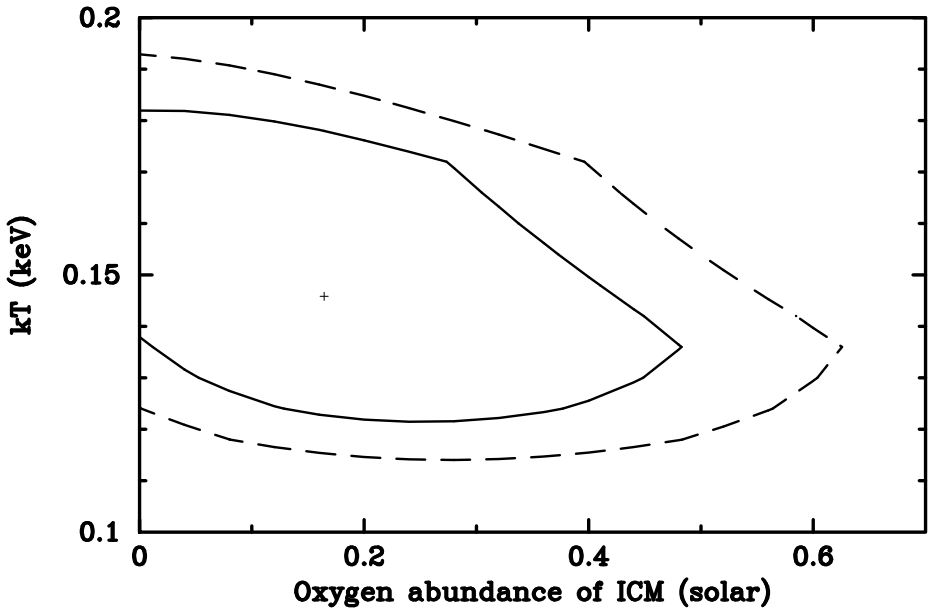

Fig. 5.26: A plot of confidence contour between kT of *apec* component and the O abundance of *vapec* for the $r > 9'$ annulus, in the simultaneous fitting of 6–9′ annulus with the *apec* + *phabs* × *vapec* + *itphabs* × *bremss* model. The cross denotes the best-fit location, and the two contours represent 1σ and 90% confidence ranges, from inner to outer, respectively.

background Ni line (~ 7.5 keV) left artificial structures after the NXB subtraction at large radii. It is also known that the XIS response in $E \sim 8$ keV are not fully understood at the present stage. In the simultaneous fit of BI and FI, only the normalization are allowed to be different between them, although we found that the derived normalizations are quite consistent between the two. However, for the 4–6′ and 6–9′ region, the spectra were not fitted well.

5.5.3 Estimation of Galactic Component

Table 5.23: The best-fit parameters of the *apec* component for the simultaneous fit of all spectra of NGC 720 with *apec* + *phabs* × *vapec* + *phabs* × *zbremss* model.

Fit model	*Norm* *	kT (keV)	χ^2/dof
apec + *phabs* × *vapec* + *phabs* × *bremss*	0.79 ± 0.35	$0.136^{+0.058}_{-0.012}$	1468/1041

* Normalization of the *apec* component divided by the solid angle, $\Omega^{\rm U}$, assumed in the uniform-sky ARF calculation (20′ radius), $Norm = \int n_{\rm e} n_{\rm H} dV \,/\, (4\pi\,(1+z)^2 D_{\rm A}^2) \,/\, \Omega^{\rm U} \times 10^{-20}$ cm^{-5} arcmin^{-2}, where $D_{\rm A}$ is the angular distance to the source.

It is important to estimate the Galactic component precisely, which is possible using the outermost region of NGC 720 with *Suzaku*. In order to determine the surface brightness and the spectral shape of the Galactic component, we performed the simultaneous fit of all annuli. The Galactic component is prominent in these annuli as shown in figure 5.25, however the ICM component is still dominant almost all the energy range except

for the O VII line. We made the simultaneous fit in the 0.4–7.0 keV range (except 1.825–1.840 keV) for the two inner regions and in the 0.4–4.0 and 0.4–2.0 keV range for the 4–6′ and 6–9′ region, respectively, assuming an *apec* model for the Galactic component, and the fit results are presented in table 5.23. The resultant normalization of the *apec* model in table 5.23 is scaled so that it gives the surface brightness in the unit solid angle of arcmin^2.

To demonstrate how sensitive the O abundance of the ICM is to the assumed Galactic component model, we present a confidence contour between kT (keV) of the *apec* component and the O abundance (solar) of *vapec* for the outermost annulus ($r > 9'$) in figure 5.26. There appears to exist a negative correlation between the two parameters, because higher temperature of the Galactic component produces more O VIII emission line relative to O VII, which contribute to reduce the O VIII line from the ICM (*vapec* component). Influences on the derived temperature and abundance by the modeling of the Galactic component will be tested in subsection 5.5.4, too.

In order to take into account both existence of the Galactic component itself and propagation of its statistical error, we simultaneously fitted all annuli. As mentioned in the previous subsection, the normalization of the *apec* component is constrained to give the same surface brightness in all annuli. The temperature of the *apec* model was also common in all regions.

5.5.4 Radial Temperature & Abundance Profiles

Table 5.24: Summary of the best-fit parameters of the *vapec* components for each annular region of NGC 720 with the $apec + phabs \times vapec + itphabs \times bremss$ model. All annuli are simultaneous fitted. Errors are 90% confidence range of statistical errors, and do not include systematic errors. The solar abundance ratio of *angr* is assumed. These results are plotted in figure 5.27.

Region	$Norm_1$ *	kT_1 (keV)	O (solar)	Ne (solar)	Mg,Al (solar)	Si (solar)	S,Ar,Ca (solar)	Fe,Ni (solar)	χ^2/dof
0–2′	28.8 ± 6.2	$0.55^{+0.01}_{-0.01}$	$0.57^{+0.14}_{-0.09}$	$0.63^{+0.13}_{-0.12}$	$0.72^{+0.11}_{-0.13}$	$0.64^{+0.16}_{-0.18}$	$1.22^{+0.72}_{-0.55}$	$0.58^{+0.10}_{-0.08}$	1468/1041
2–4′	8.7 ± 0.8	$0.51^{+0.16}_{-0.16}$	$0.33^{+0.09}_{-0.04}$	$0.28^{+0.09}_{-0.07}$	$0.39^{+0.12}_{-0.09}$	$0.26^{+0.18}_{-0.16}$	$0.64^{+0.75}_{-0.58}$	$0.31^{+0.07}_{-0.05}$	–

* Normalization of the *vapec* model, calculated in the same way with table 5.3.

† All regions were fitted simultaneously.

Table 5.25: List of χ^2/dof for each fit of NGC 720.

Region	nominal	contaminaut		background	
		+20%	-20%	+10%	-10%
All	1468/1041	1477/1041	1432/1041	1457/1041	1509/1041

Although the fit was not acceptable due mainly to the very high photon statistics than the systematic errors in the instrumental response, this result was useful to assess whether each element abundance was reasonably determined or not. The abundances are linked together for Mg=Al, S=Ar=Ca, Fe=Ni.

The *bremss* component represent the LMXB emission within $r < 6'$ (Jeltema et al. 2003), and we adopt a $kT = 11$ keV and $N_{\rm H} = 0.8 \times 10^{21}$ cm^{-2} absorbed bremsstrahlung component to model their spectra.

Considering the OBF contaminants and background (CXB + NXB) systematics, results of the spectral fit at each annulus are summarized in table 5.24 and figure 5.27. We tested the results by changing the background normalization by ±10%, and they are plotted in green dotted lines in figure 5.27. The systematic error due to the background estimation is almost negligible. The systematic error range due to the uncertainty in the OBF contaminant is indicated by black dotted lines. A list of χ^2/dof is presented in table 5.25

5.5.5 Direct Comparison of O VII and O VIII Intensities

Table 5.26: Line intensities of O VII and O VIII at each annulus of NGC 720 field in unit of photons cm^{-2} s^{-1} sr^{-1}. These intensities are derived from the spectral fit with *power-law + gaussian + gaussian* model Intensities by McCammon et al. (2002) measured with a high resolution microcalorimeter array for a large sky area of ~ 1 sr are also presented.

Region		O VII	O VIII
NGC 720	(0–2′)	–	18.3±3.1
NGC 720	(2–4′)	2.4±1.8	4.4±1.4
NGC 720	(4–6′)	6.1±1.2	4.4±0.9
NGC 720	(6–9′)	4.3±0.7	2.9±1.0
Galactic average (McCammon et al. 2002)		4.8±0.8	1.6±0.4

We also investigated the surface brightness of the O VII and O VIII emission lines in order to estimate the O abundance of the ICM directly from the line intensities. The surface brightness of the O VII and O VIII were derived by fitting the annular spectrum with a *power-law + gaussian + gaussian* model. In the fitting, we fixed the Gaussian σ to be 0, and allowed the energy center of the two Gaussians to vary within 555–573 eV or 648–658 eV for O VII or O VIII, respectively. The derived line intensities are summarized in table 5.26 and figure 5.28. There is a clear excess of the O VIII intensity towards the cluster center, while O VII is consistent with constant. This is a strong evidence that the O VIII emission is associated with the ICM itself, on the other hand, O VII might be due mainly to the Galactic origin.

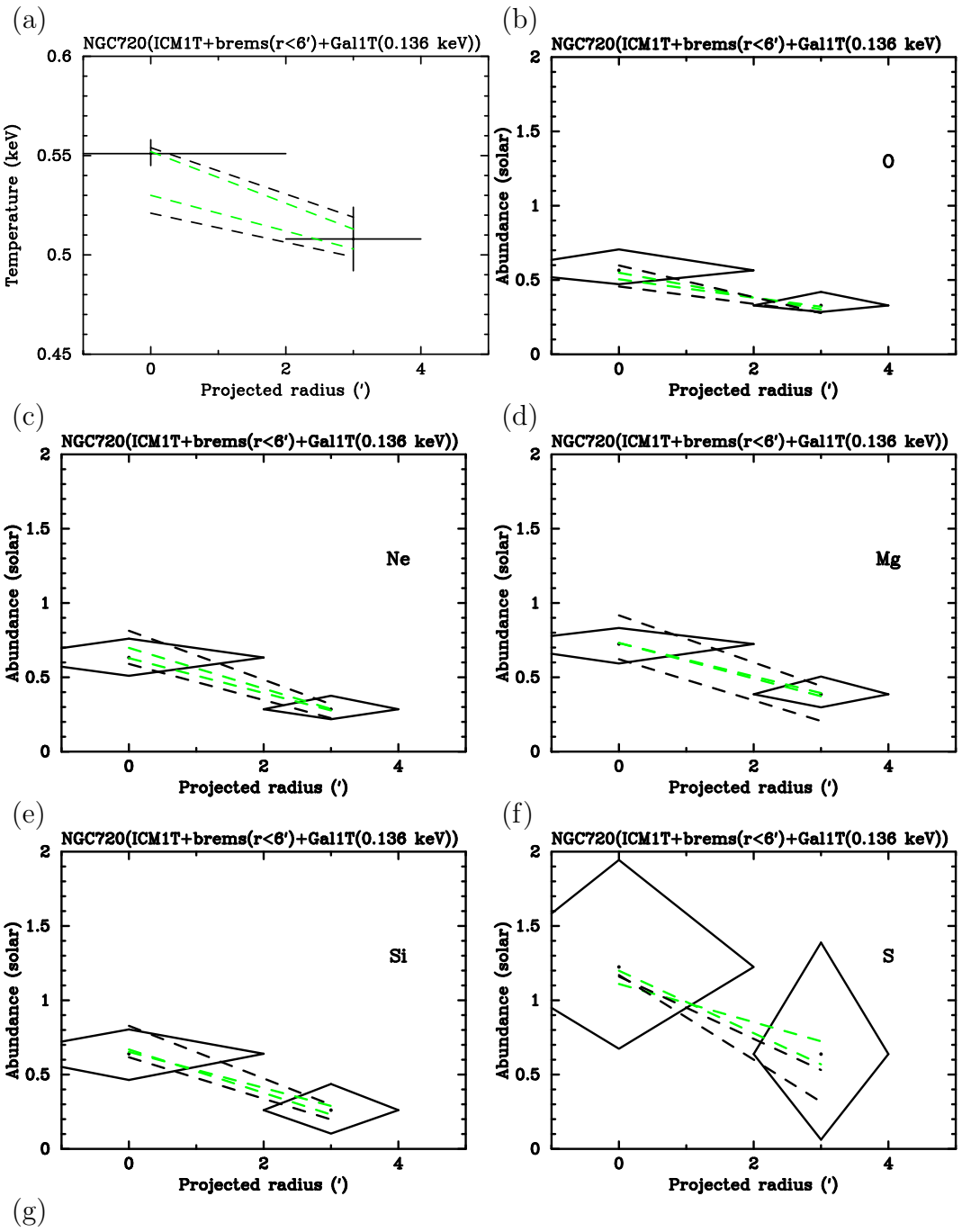

Fig. 5.27: (a) Radial temperature profiles derived from spectral fit of the *Suzaku* spectrum at each annulus. The horizontal axis denotes the projected radius and deprojection are not conducted. The same data with table 5.24 are used for *Suzaku*. The black dotted lines correspond to shifts of the best-fit values by changing thickness of the OBF contaminant by ±20%. The green dotted lines denote those when the estimated CXB and NXB levels are changed by ±10%. (b)–(g) Radial abundance profiles derived and plotted in the same way as (a).

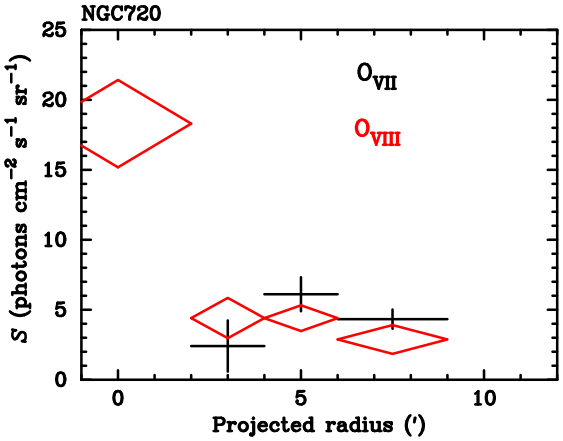

Fig. 5.28: Line intensities of O VII and O VIII at each annulus of A 1060 in unit of photons cm^{-2} s^{-1} sr^{-1}. Each value is shown in table 5.26.

Chapter 6

Discussion and Conclusion

6.1 Summary of results

In this section we summarize the observed distributions of temperature and metal abundance for clusters and groups of galaxies, and then briefly discuss on their properties.

6.1.1 Temperature Profile

A 1060

The temperature in A 1060 observed with *Suzaku* shows a decline from ~ 3.4 keV in the central region of $r \leq 5'(\sim 70$ kpc) to ~ 2.2 keV in the outermost annulus of 17–27′ ($\sim$ 240–380 kpc ~ 0.16–$0.25\ r_{180}$). This feature is roughly consistent with the previous result for the inner region ($r < 13'$) measured with *XMM-Newton* Hayakawa et al. 2006, although our *Suzaku* result indicate slight flattening of the temperature profile in the outer annuli. Hayakawa et al. (2006) suggested a faster decline of the temperature profile of A 1060 than the average $T/\langle T\rangle$ curve by Markevitch et al. (1998) obtained from 30 nearby clusters (excluding A 1060) with *ASCA* observations. However, now it appears more consistent with them by taking the emission-weighted average temperature, $k\langle T\rangle = 2.5$ keV.

AWM 7

The temperature profile in AWM 7 shows a mild cooling core in the central region ($r \lesssim 6'$), and declines from ~ 3.8 keV at 6–9′ region ($\sim$ 130 kpc) to ~ 3.3 keV in the outermost annulus of 17–27′ ($\sim$ 360–570 kpc ~ 0.22–$0.35\ r_{180}$). This feature is roughly consistent with the previous result for the inner region ($r < 13'$) measured with *XMM-Newton* (Hayakawa 2006). Previous *ASCA* observation showed fairly uniform temperature distribution in the whole cluster (Furusho et al. 2001), however this may be caused by the wide and energy-dependent point-spread function of the telescope.

HCG 62

For the two temperature model, the temperature of the hotter and the cooler component are nearly constant at 0.15 and 0.7 keV, respectively. We also note that the fraction of the cool component in the surface brightness is 50% at the center and drops to 25% at $r = 6'$. These features are generally consistent with the previous result measured with *Chandra* and *XMM-Newton* (Morita et al. 2006).

NGC 507

For the two temperature model, the temperature of the hotter and the cooler component are nearly constant at 0.15 and 0.7 keV, respectively. We also note that the fraction of the cool component in the surface brightness is 25% at the center and drops to 15% at $r = 6'$. The observed features also agree with the previous results obtained with *XMM-Newton* (Kim & Fabbiano 2004).

NGC 720

The temperature in NGC 720 is nearly constant in the central region at $r \lesssim 4'(\sim 30$ kpc), while the temperature for $r \geq 4'$ is undetermined due to the faintness of the emission. The significant X-ray emission is observed only within the optical elliptical galaxy. Consistent results are reported based on the same *Suzaku* observation by Tawara (2007).

6.1.2 Comparison of the temperature profiles

We summarized the temperature profiles of A 1060, AWM 7, HCG 62, NGC 507, and NGC 720 in figure 6.1. We scaled the temperature and radius using the average temperature and the virial radius for each cluster and group (table 6.1), respectively. Figure 6.1(b) shows that these profiles are consistent with the range of theoretical simulations summarized by Markevitch et al. (1998).

Table 6.1: The average temperature and virial radius for each cluster and group

object	$k\langle T\rangle$ (keV)	$1'$ (kpc)	r_{180} (Mpc)
A 1060	3.0	14.0	1.53
AWM 7	3.5	21.0	1.65
HCG 62	1.5	17.8	1.08
NGC 507	1.5	20.1	1.08
NGC 720	0.55	7.20	0.65
Fornax	1.3	5.48	0.98
NGC 1404	0.60	7.80	0.66

Recent measurements of 13 nearby relaxed clusters (excluding A 1060) with *Chandra* by Vikhlinin et al. (2005) show that the temperature reaches at a peak at $r \sim 0.15\ r_{180}$ and then declines to ~ 0.5 of its peak value at $r \simeq 0.5\ r_{180}$, in good agreement with Markevitch et al. (1998). They also found that clusters whose temperature profiles peak at $r < 70$ kpc ($\ll 0.15\ r_{180}$; MKW4 and RX J1159+5531) show a larger peak-temperature-ratio of $T_{\rm p}/\langle T\rangle \sim 1.35$. This is exactly the case for A 1060, which shows the peak temperature of $kT_{\rm p} = 3.42 \pm 0.04$ keV at $r = 4$–$6'(\sim 70$ kpc) with our *Suzaku* measurement. Using the relation of $T_{\rm p}/\langle T\rangle \sim 1.35$, the emission-weighted average temperature is calculated to be $k\langle T\rangle = 2.5$ keV, as suggested by the Suzaku observation. These three clusters, MKW4, RX J1159+5531 and A1060, correspond to objects without cooling cores, hence this apparent steep temperature decline at $r \leq 0.2\ r_{180}$ might be a common feature for non-cooling flow clusters.

In order to determine actual value of $k\langle T\rangle$ for nearby clusters, further offset observations toward r_{180} are required. Since the wide and energy-dependent point-spread function of *ASCA* tended to give a flatter temperature profiles, as mentioned earlier, studies of the

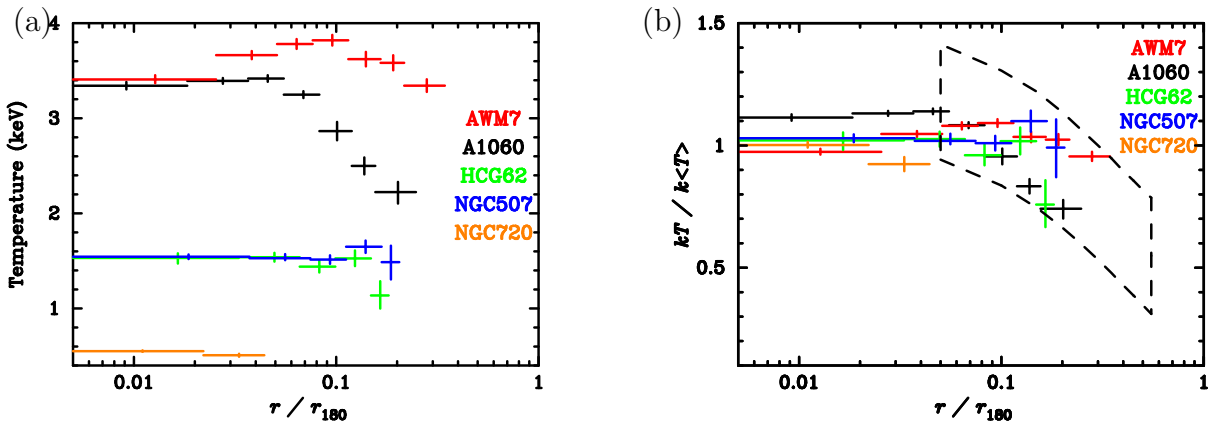

Fig. 6.1: (a) Temperature profiles of A 1060, AWM 7, HCG 62, NGC 507, and NGC 720 to the scaled radius using the virial radius for each cluster and group. (b) The scaled temperature profiles using the average temperature to the scaled radius. The dashed square corresponds to the simulation value of Markevitch et al. (1998).

$T/\langle T\rangle$ curve in cluster outskirts with *Suzaku* will be useful to look at the true temperature features.

Dolag et al. (2004) conducted a smoothed particle hydrodynamics (SPH) simulation to reconstruct the structure of the Local Universe, which well reproduces the position, mass, and temperature of A 1060 ("Hydra" of table 1 in Yoshikawa et al. (2004)) and other nearby clusters. The simulated temperature of A 1060 was 3.4 keV within $r < 20' \sim 0.18\ r_{180}$. The radial temperature profile of the simulated A 1060 is examined by Kawahara (2007), based on the updated version of the SPH simulation by Dolag et al. (2005). The predicted temperature profile agrees with our *Suzaku* result pretty well, although the simulated temperatures are higher than the observation. This is partly because our temperature profile in figure 5.6(a) is plotted against the projected radius, in which the ICM emission is integrated along the line of sight, while the simulated temperature is plotted against the spherical radius. The projected temperature drops by ∼3% than the 3-dimensional value in the central 2′. It is pointed out that the spectroscopic temperature in the real X-ray observation tend to give lower values than the emission-weighted temperature calculated in the simulation. This is due to the multi-phase nature of the ICM, resulted not only from the radial temperature gradients but also from the local inhomogeneities (Mazzotta et al. 2004; Kawahara 2007).

There is a small flat-top in the observed temperature profile of A 1060 within $r \leq 5' \sim 70$ kpc in figure 5.6(a). This feature might indicate an initial phase in the formation of cooling core. The SPH simulation predicts that the period of the last major merger occurred at an age of ~ 3 Gyr ago ($z \sim 0.3$). This implies that the temperature flat-top has been produced within the recent ~ 3 Gyr. The scale length of the thermal conduction is calculated as

$$r_{\rm cond} = 155 \left(\frac{t}{3\ {\rm Gyr}}\right)^{\frac{1}{2}} \left(\frac{n_{\rm e}}{0.001\ {\rm cm^{-3}}}\right)^{-\frac{1}{2}} \left(\frac{kT}{3\ {\rm keV}}\right)^{\frac{5}{4}}\ {\rm kpc},$$

where t is the time after the last merger, $n_{\rm e}$ is the electron density, assuming the classical Spitzer conductivity. This length scale is similar to the size of the flat-top.

In subsection 5.1.6, only an upper limit of 5×10^{40} erg s^{-1} for the cool component in A 1060 was obtained. It confirms that the sharp cusp structure in the *Chandra* image of A 1060 (Hayakawa et al. 2004) really reflects the gravitational mass concentration and

does not come from cool gas of high emissivity.

6.1.3 Abundance Profiles

Based on the good XIS sensitivity to emission lines, especially below 2 keV, we directly measured oxygen and magnesium abundances, although mainly iron was measured with the past satellites. As a common feature in the abundance determination, Ni and Ne values are not reliable due to the strong and complex Fe-L line emissions. Also, we have to note that the O abundances depend on the estimation of the Galactic component as described in subsection 5.1.3.

A 1060

We obtained emissivity weighted abundance profiles of Ni, Fe, Si, S, Mg, Ne and O in the ICM of A 1060 up to a radius of $27' \simeq 380$ kpc as shown in figure 5.6. Abundances of Si, S, and Fe decrease from ~ 0.7, 0.8 and 0.5 solar in the central region, to ~ 0.3, 0.2 and 0.2 solar, respectively, in the outskirts of the cluster. De Grandi & Molendi (2001) showed that non-cooling flow clusters do not exhibit a steep abundance gradient due possibly to disruption of the central cool cores after major merger events. A 1060 shows clear gradients for Fe, Si, and S, even though it is a very relaxed system without the cD galaxy and cooling core.

The other elements, Mg and O, show somewhat flatter radial distributions. The measured Mg abundance is consistent with constant up to the 13–17′ annulus, namely out to 240 kpc from the cluster center. Oxygen also exhibits a flat distribution or a slight increase at $r \simeq 10'$. The O abundance in the outer annuli is particularly affected by the surface brightness and temperature of the cooler Galactic component ($kT_1 \sim 0.15$ keV). The O and Mg abundances at $r \leq 6'$ are also affected by the uncertainties in the OBF contaminant (subsection 5.1.4). We have tried to take into account all the possible systematic errors, and the results are presented in figure 5.6. In addition, systematic effects caused by the definition of the solar abundances were addressed and described in appendix B.

AWM 7

Abundance profiles of Ni, Fe, Si, S, Mg, Ne and O are obtained up to a radius of $27' \simeq 570$ kpc. Abundances of Mg, Si, S, and Fe decrease from ~ 1.5, 1.1, 1.1 and 0.9 solar in the central region, to ~ 0.9, 0.6, 0.4 and 0.4 solar in the east region and ~ 0.9, 0.3, 0.1 and 0.4 solar in the west region, respectively, in the outskirts of the cluster. The O abundance shows somewhat flatter radial distributions.

HCG 62

Abundance profiles are obtained up to a radius of $13' \simeq 230$ kpc. Abundances of O, Mg, Si, S, and Fe decrease from ~ 0.4, 1.7, 1.3, 1.4 and 1.1 solar in the central region, to ~ 0.0, 0.1, 0.2, 0.3 and 0.1 solar, respectively, in the group outskirts.

NGC 507

Abundance profiles are obtained up to a radius of $13' \simeq 260$ kpc. Abundances of O, Mg, Si, S, and Fe decrease from ~ 0.6, 1.6, 1.3, 1.4 and 1.0 solar in the central region, to ~ 0.2, 0.6, 0.4, 0.5 and 0.4 solar, respectively, in the outskirts.

NGC 720

Abundance profiles are obtained up to a radius of $4' \simeq 30$ kpc. The He-like and H-like Ne lines are strong in the spectra, although Fe-L line emissions are in the same energy ranges. Abundances of O, Ne, Mg, Si, S, and Fe decrease from $\sim$ 0.6, 0.6, 0.7, 0.7, 1.2 and 0.6 solar at 0–2′, to $\sim$ 0.3, 0.3, 0.4, 0.3, 0.6 and 0.3 solar, respectively, at 2–4′. The observed region is within the elliptical galaxy.

6.1.4 Comparison of the abundance profiles

In order to compare the relative variation in the abundance profiles, we show abundance ratios of O, Mg, and Si divided by Fe as a function of projected radius in figure 6.2. Apparently, the profiles of Si/Fe, O/Fe, and Mg/Fe show different gradients. The Si/Fe ratio is consistent with a constant value for all objects, while the O/Fe and Mg/Fe ratios seem to increase to the outer region for A 1060 and AWM7-WEST.

Recent *Suzaku* observations also show the O and Mg abundances in poorer systems: an elliptical galaxy NGC 720 (Tawara 2007), the Fornax cluster, and NGC 1404 (Matsushita et al. 2006). The Fe ratios of elements for these systems are compared in figure 6.3.

The similar behavior of the O/Fe ratio, characterized by the central low values with some increase in outer regions, has been reported by (Tamura et al. 2004) with *XMM-Newton* as an average of 19 clusters which are mainly composed of X-ray bright and relaxed clusters with cD galaxies. The O/Fe ratio is $\sim$ 0.7 solar within $r \leq 50$ kpc, which increases to $\sim$ 1.5 solar at $r \sim 100$ kpc, and more at $r \geq 200$ kpc, as shown in figure 5(b) of Tamura et al. (2004), assuming the solar abundance ratio of *angr* (Anders & Grevesse 1989). This is much alike the O/Fe plot in figure 6.2.

Since these differences are not simply explained by the ion mass, we need to consider that the enrichment processes have a significant difference between O and Fe, for example. It is generally considered that enrichment of O and other SN II originated metals has occurred in the early stage of cluster formation, certainly before the last merger epoch. The relatively flat distributions of O and Mg indicate that the early metal enrichment has caused these features. One plausible explanation is the enrichment in the form of starburst-driven galactic winds (e.g. Strickland & Stevens (2000)). Recent numerical simulation of the cluster metal enrichment indicates that even a metallicity peak in an intermediate radius can be created by enrichment through galactic winds (Kepferer et al. 2006, priv. comm.), which resembles our oxygen feature.

6.1.5 The number ratio of each metal to iron

In order to examine the abundance pattern of the ICM in the 4 systems studied here, we plotted number ratios for the α-elements to iron in figure 6.4 as a function of the atomic number. The abundance patterns are compared with solar abundance elemental ratios (Anders & Grevesse 1989; Feldman 1992; Lodders 2003) and with the theoretical calculations of the elements produced by SN II, SN Ia (W7) and SN Ia (WDD1) by Iwamoto et al. (1999). The observed abundance ratios are quite similar to the solar abundance ones, however O/Fe ratio in the central region (figure 6.4:left) is about half $\sim 3/4$ of the solar level, while the that at 0.1 $r_{\rm vir}$ is much closer to the solar value. These plots indicate that the observed ICM metals are produced by some combination of SN Ia and SN II.

6.1.6 Comparison to the *ASCA* observation

Fukazawa et al. (1998) shows the temperature, Si and Fe abundance for 40 nearby galaxies with *ASCA*, and reveal that Si abundance of the richer clusters is higher than the poorer clusters while Fe abundance is almost the same between the two systems. In other words, the higher temperature the clusters have, the higher Si to Fe abundance ratio they have. Although Fukazawa et al. (1998) select the region from 0.1 h_{50}^{-1} Mpc to 0.4 h_{50}^{-1} Mpc from the cluster center, our observed regions are narrower than that because the filed of view of *Suzaku* is smaller than that of *ASCA*. Thus, using the results of each annular region around 0.1 $r_{\rm vir}$ of our results from the cluster center, we compare with the results in figure 6.5. Except for the temperature and Si abundance of A 1060, the values of our results are slightly higher than those of Fukazawa et al. (1998). In addition, as far as we see figure 6.3, Si/Fe abundance ratios do not become higher with the higher temperature of the systems. However, because the systems of our observations are poor clusters (A 1060, AWM 7, Fornax), groups (HCG 62 and NGC 507) and individual elliptical galaxies (NGC 720, NGC 1404), we need to investigate more samples such as the rich clusters.

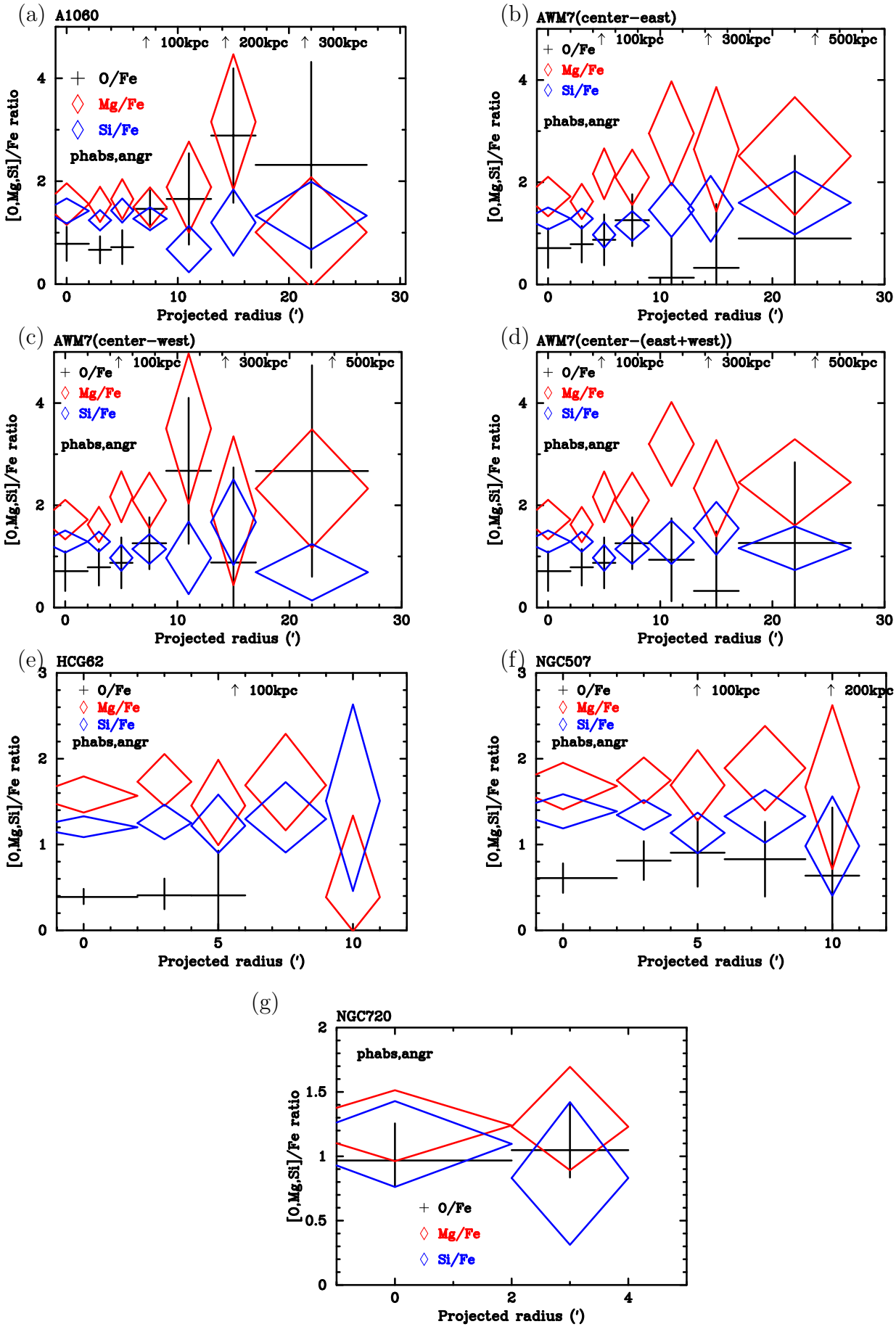

Fig. 6.2: (a)-(f) Abundance ratios of O (black), Mg (red) and Si (blue) divided by Fe, for A 1060, AWM 7(from center to east and west, and to east and west region fitted simultaneously), HCG 62, NGC 507, and NGC 720 respectively.

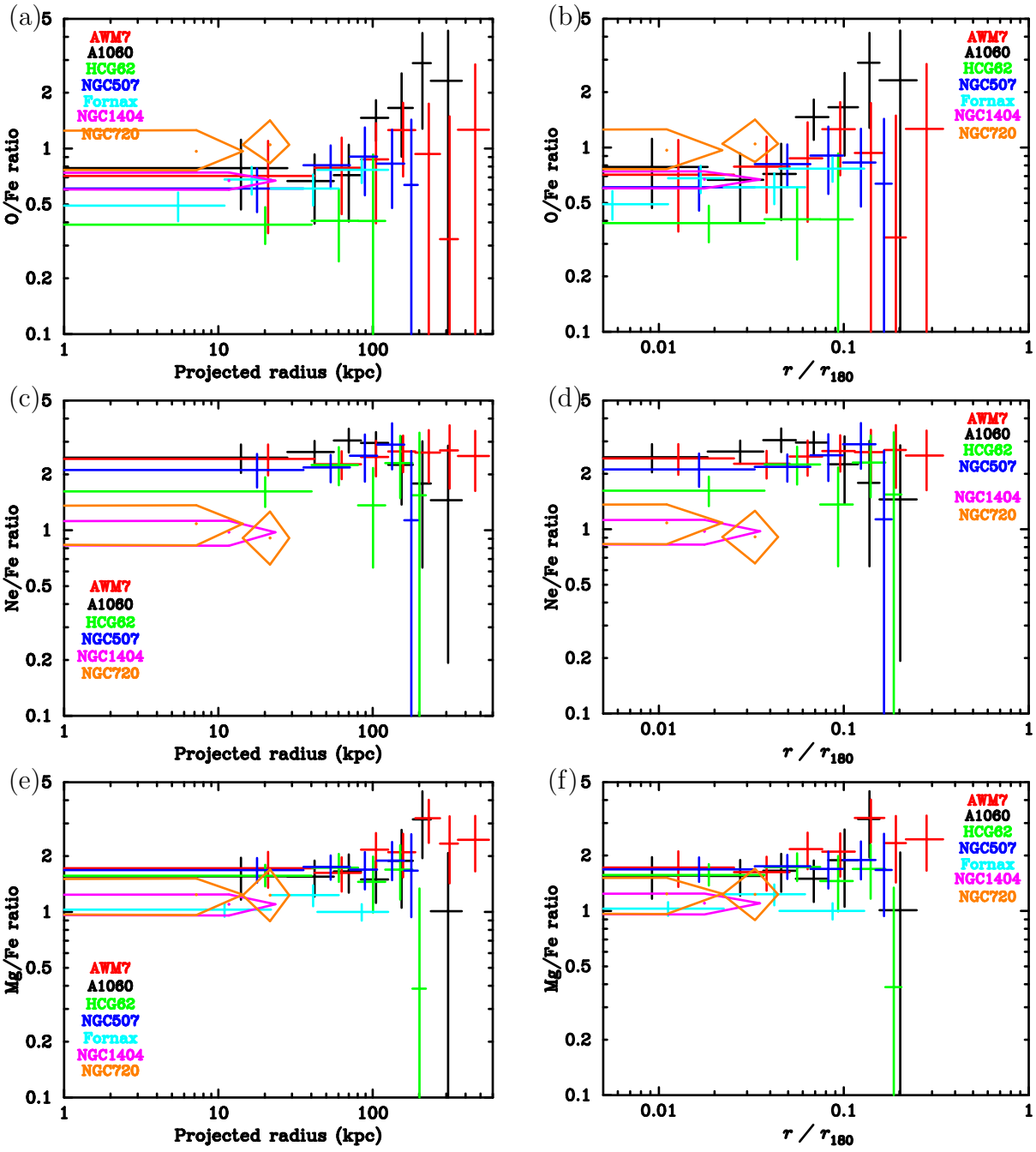

Fig. 6.3: (a)-(f) Abundance ratios of O, Ne and Mg divided by Fe, for A 1060, AWM 7, HCG 62, NGC 507, Fornax cluster, NGC 1404, NGC 720. Left panels shows the dependence of the distance from the cluster/group center, and right panels shows that of the scaled distance using each virial radius.

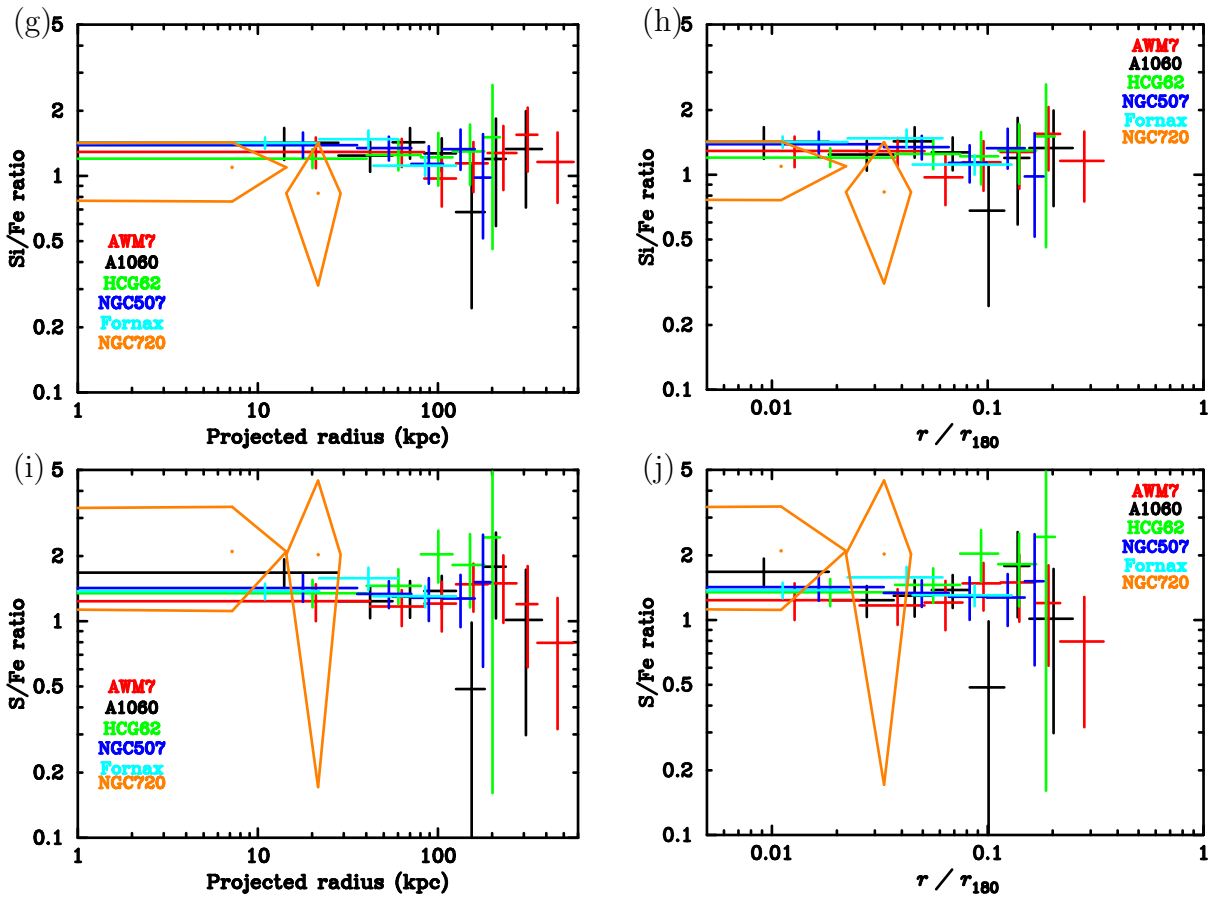

Fig. 6.3: (g)-(j) Abundance ratios of Si and S divided by Fe, for A 1060, AWM 7, HCG 62, NGC 507, Fornax cluster, NGC 1404, NGC 720. Left panels shows the dependence of the distance from the cluster/group center, and right panels shows that of the scaled distance using each virial radius.

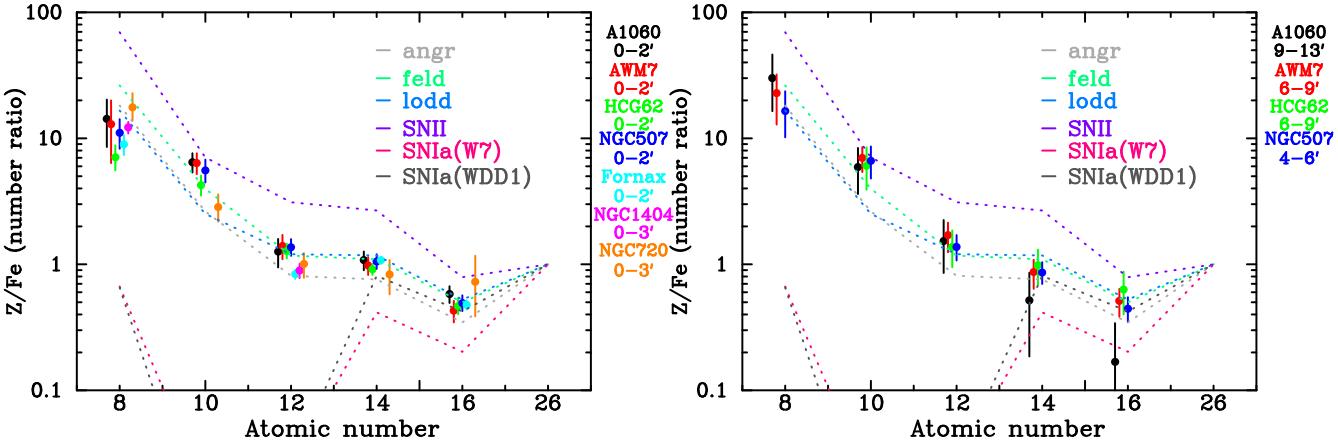

Fig. 6.4: The Z/Fe number ratio in the central region (left) and 0.1 $r_{\rm vir}$ region. The dashed lines shows the Z/Fe number ratio of the solar abundance tables, black:Anders & Grevesse (1989), red:Feldman (1992), green:Lodders (2003), and theoretical calculations of SN II, SN Ia (W7), and SN Ia (WDD1) by Iwamoto et al. (1999).

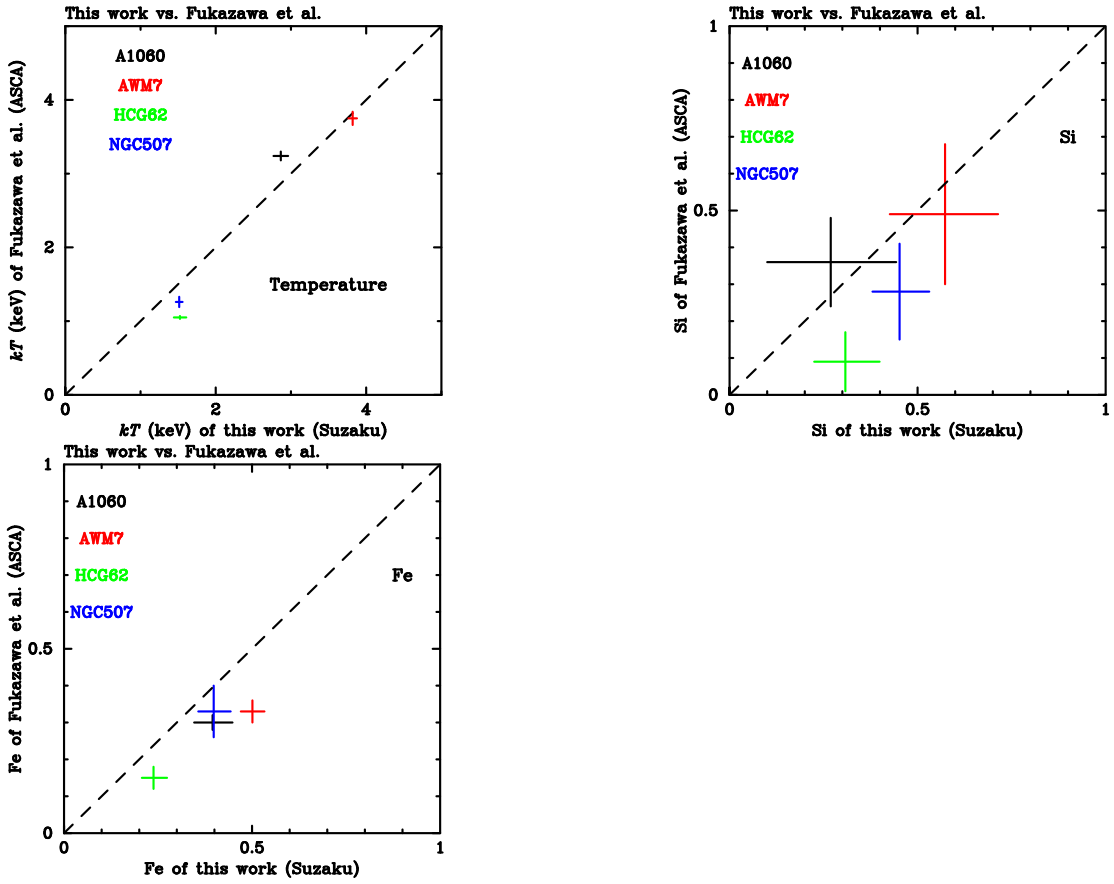

Fig. 6.5: Comparison this work with Fukazawa et al. (1998) about the temperature, Si and Fe abundance of A 1060, AWM 7, HCG 62, NGC 507. Our results use the results of each annulus region around 0.1 $r_{\rm vir}$, while Fukazawa et al. (1998) use the region from 0.1 h_{50}^{-1} Mpc to 0.4 h_{50}^{-1} Mpc from the cluster center.

6.2 Metal distribution

6.2.1 Metal mass profiles

Combining the X-ray luminous gas mass profile of A 1060 and AWM 7 by Hayakawa (2006), and HCG 62 by Morita et al. (2006) with *XMM-Newton* and the abundance profiles obtained with *Suzaku*, we calculated the cumulative metal mass profiles in figure 6.6 and 6.7. The gas mass profile of NGC 507 was calculated from the surface brightness obtained with *XMM-Newton*. If we strictly concern about the data, the abundance profile used here is derived from the projected spectrum along the line of sight, which is approximated to represent the spherical distribution. The abundance derived from the projected spectrum is constant with that from the deprojected spectrum by the 90% confidence level. The iron and oxygen masses within respective radii are shown in table 6.2.

Table 6.2: Fe and O Masses for the observed clusters

	A 1060	AWM 7	HCG 62	NGC507
r (kpc)	380	570	230	260
$M_{\rm Fe}$ ($M_\odot$)	1.4×10^9	8.1×10^9	2.7×10^8	3.4×10^8
$M_{\rm O}$ ($M_\odot$)	1.6×10^{10}	4.4×10^{10}	1.8×10^8	1.3×10^9

6.2.2 The number ratio of SN II to SN Ia

In order to examine the relative contributions from SN Ia and SN II in producing the observed amount of elements, we compare observed metal masses with the theoretical supernova yields. Although the metals produced by SN are contained not only in the ICM but also in the stars, we do not consider the latter component here, noting that the ratio of iron in the ICM to the star is about 5:1 (Arimoto et al. 1997).

We adopt the SN Ia (W7) yields by Nomoto et al. (1984), and the SN II ones by Iwamoto et al. (1999) assuming the Salpeter initial mass function (IMF) for stellar mass of 10 to 50 $M_\odot$ as the model, respectively. Combination of these models are fitted with the observed metal mass patterns in the central region ($r < 2'$) and in the whole region, respectively, for each object. However, neon was excluded from the fit because of its large uncertainty in the abundance than the other metals.

Figure 6.8 shows the results of the fit. The results indicate the following features;

- Iron is mainly produced by SN Ia in both the central and the whole region for all the objects. The ratio of iron produced by SN Ia to SN II is $\sim 3:1$.
- The amount of oxygen in the whole region is much better fitted with the model than that in the central region.
- The amount of magnesium in both the regions is twice as much as that predicted by the models.
- Silicon is produced by both SN Ia and SN II, and the ratio of silicon produced by SN Ia to SN II is $\sim 1:3$.

The fits, especially for HCG 62, were not acceptable based on the χ^2 values. This is probably because the models adopted here are too simple and also the present abundance

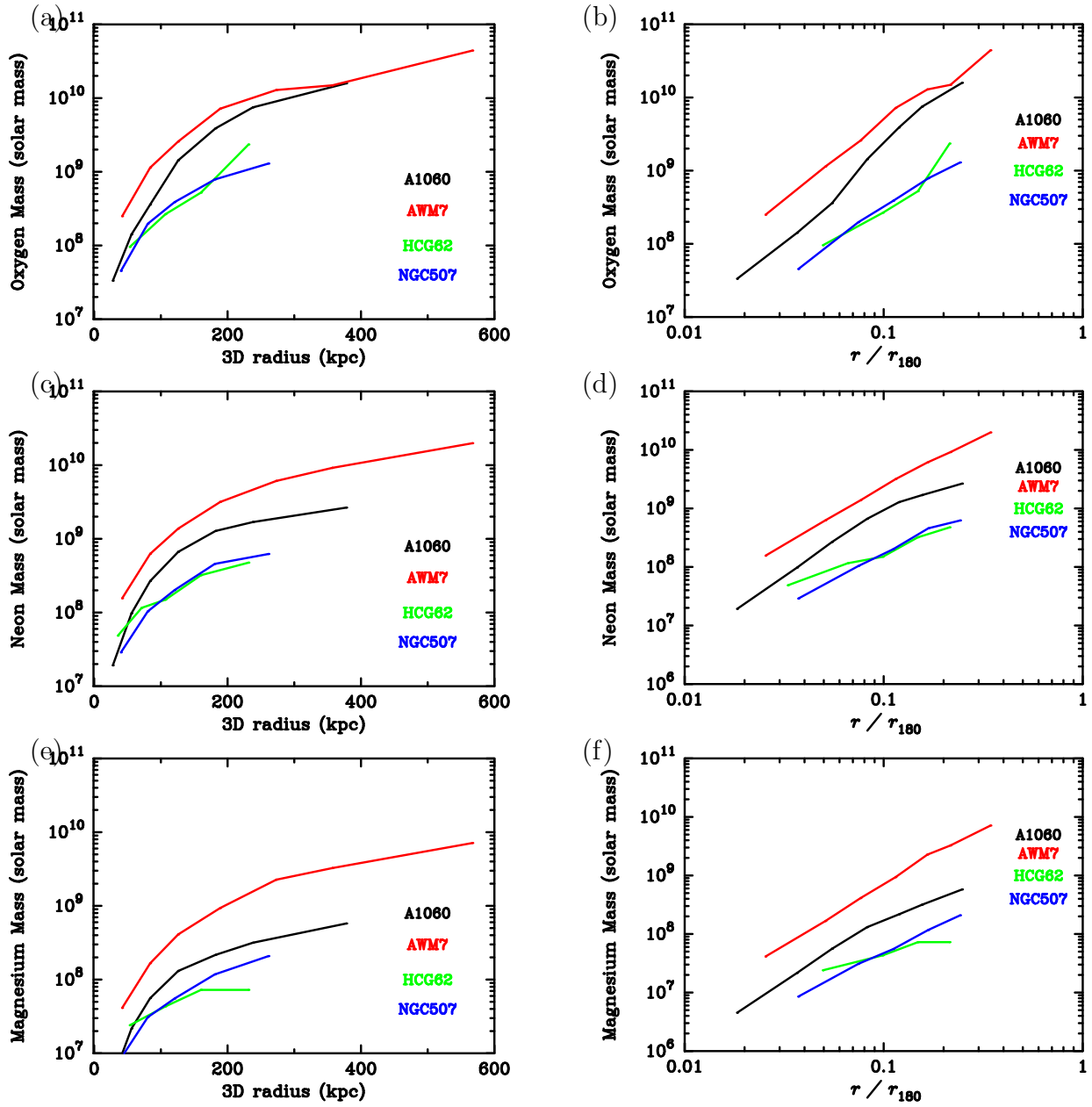

Fig. 6.6: (a)-(f) show the radial profiles of the integrated oxygen, neon and magnesium mass of A 1060, AWM 7 , HCG 62, NGC 720. The errors of the mass profiles almost corresponds to the errors of each abundance profile.

results may have some systematic errors. Here, we assume the Salpeter IMF from 10 to 50 $M_{\odot}$. Since a flatter slope than the Salpeter IMF tends to yield lager amount of oxygen, the fits for oxygen and magnesium may be somewhat improved by taking different IMF and mass range.

Figure 6.9 shows the number ratio of SN II to SN Ia to be ~ 3 (excluding HCG 62), and the number of SN Ia, which is almost proportional to the gas mass.

Figure 6.10 shows the abundance pattern of ICM, and the dotted lines in this figure indicate the number ratio of SN II to SN Ia to be ~ 3.

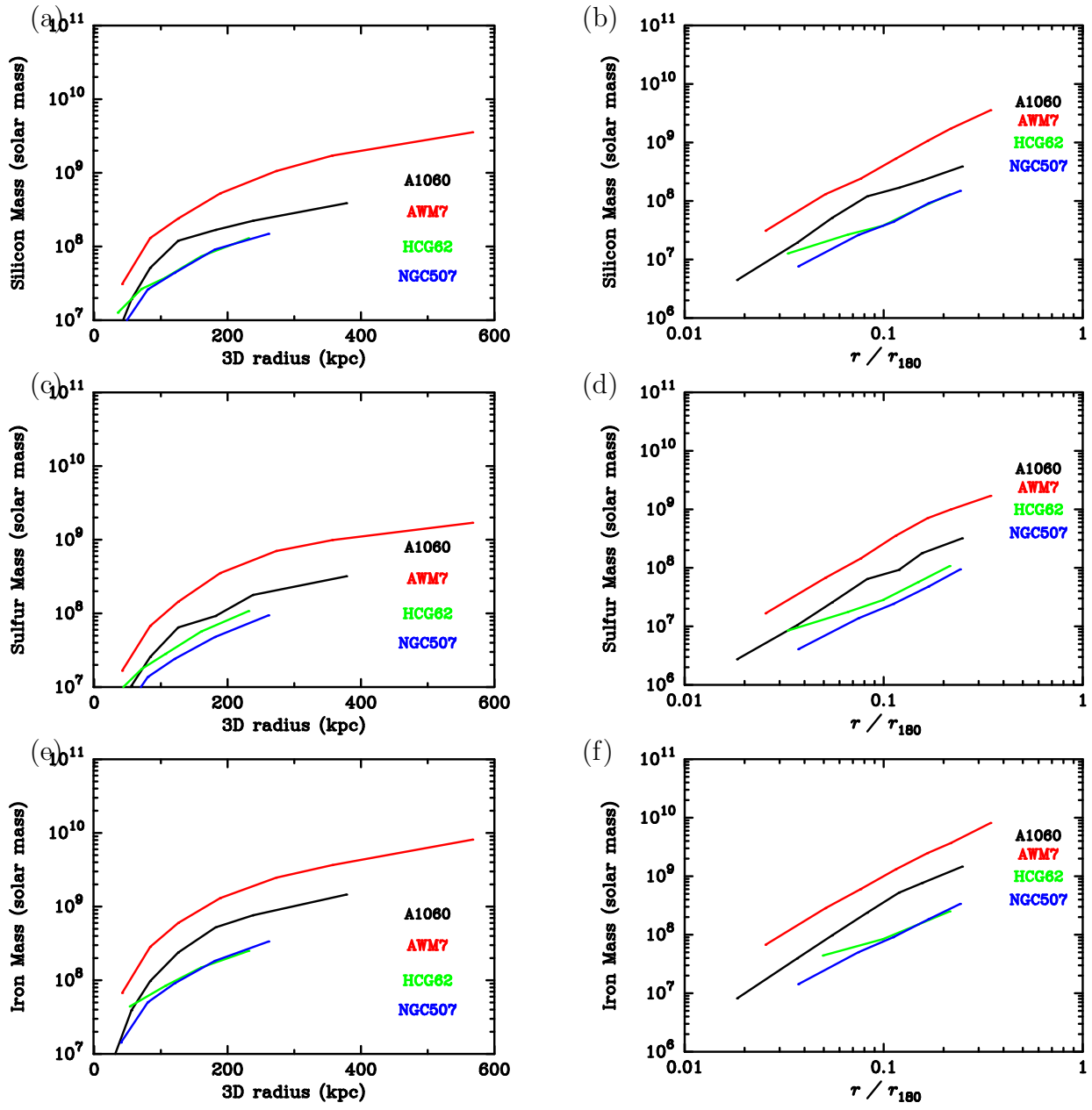

Fig. 6.7: (a)-(f) show the radial profiles of the integrated silicon, sulfur and iron mass of A 1060, AWM 7 , HCG 62, NGC 720. The errors of the mass profiles almost corresponds to the errors of each abundance profile.

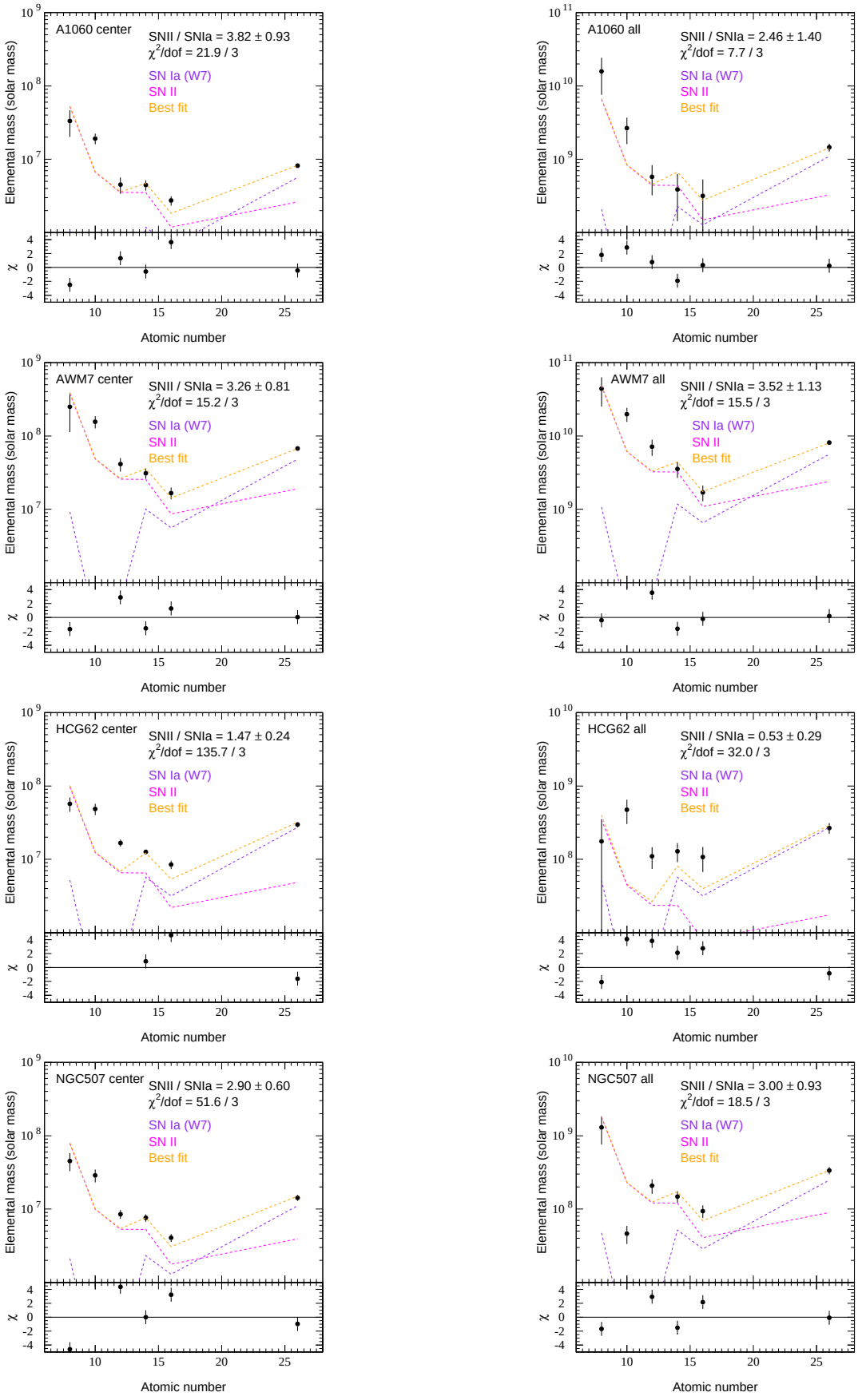

Fig. 6.8: The results of the fit of the metal mass patterns. The metal mass patterns were fitted by the SN Ia model (W7) and SN II model, which assume the Salpeter IMF. Although the fits were not acceptable, the reasons were thought that the uncertainties of SN models or the amount of the metals from the observations.

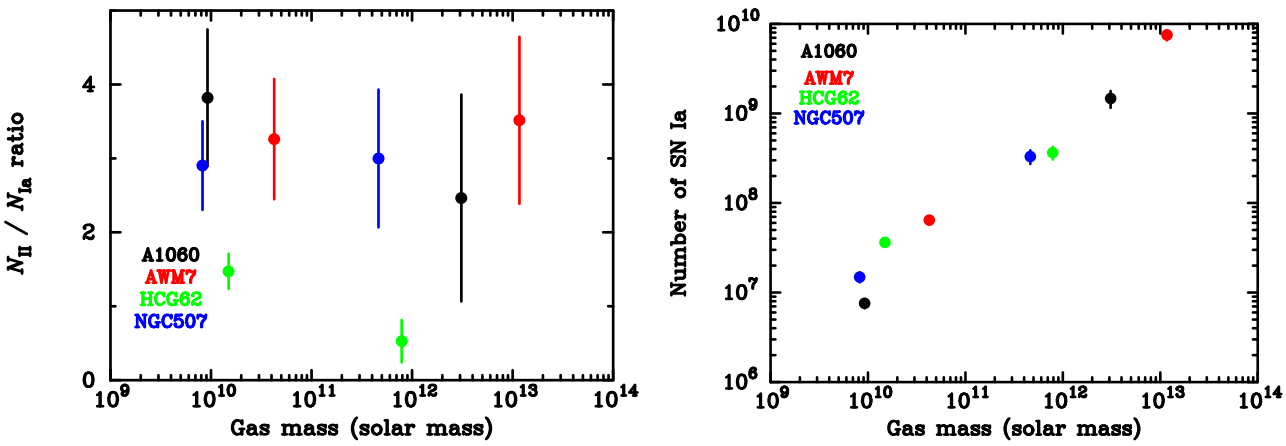

Fig. 6.9: Left: The number ratio of SN II to SN Ia. It is almost ~ 3. Right: The number of SN Ia to gas mass.

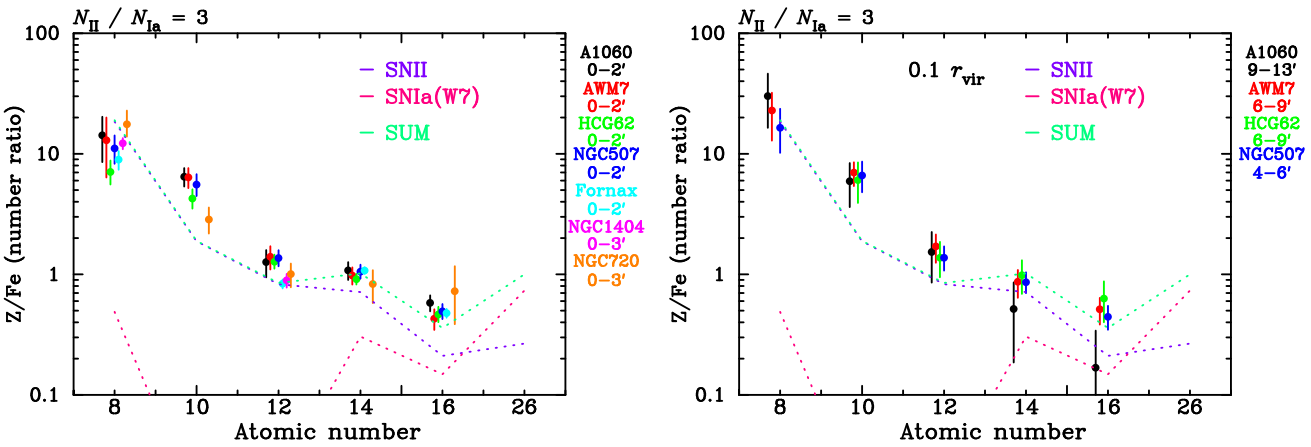

Fig. 6.10: The Z/Fe number ratio in the central region (left) and 0.1 $r_{\rm vir}$ region, when the number ratio of SN II to SN Ia is ~ 3.

6.2.3 Mass-to-light ratio

Table 6.3: Comparison of IMLR and OMLR with all systems.

	IMLR	OMLR	r	kT	Reference
NGC 720	1×10^{-4}	4×10^{-4}	25 kpc	~ 0.56 keV	Tawara et al. (2007)
Fornax ...	4×10^{-4}	2×10^{-3}	130 kpc	~ 1.3 keV	Matsushita et al. (2006)
HCG 62 ..	9.7×10^{-4}	6.4×10^{-4}	240(90) kpc	~ 1.5 keV	HCG 62 in this work
A 1060 ...	4.0×10^{-3}	4.3×10^{-2}	380 kpc	~ 3 keV	A 1060 in this work
AWM 7 ..	1.2×10^{-2}	6.8×10^{-2}	570 kpc	~ 3.5 keV	AWM7 in this work
XMM					
Centaurus	4×10^{-3}	3×10^{-2}	190 kpc	~ 4 keV	Matsushita et al. (2007)

We introduce the parameter of cluster metal mass-to-light ratio and estimate its value for both the ICM and the stars (see 2.4.5). For the integrated optical luminosity, we refer to the member galaxy catalog by Christlein & Zabludoff (2003) for A 1060 (69 galaxies within the projected radius, $r < 27' \sim 380$ kpc), by Koranyi et al. (1998) for AWM 7 (49 galaxies in $r < 27' \sim 570$ kpc), and by Zabludoff & Mulchaey (2000) for HCG 62 (12 galaxies in $r < 13' \sim 230$ kpc). We calculated the iron mass-to-light ratio (IMLR), oxygen mass-to-light ratio (OMLR), and magnesium mass-to-light ratio (MMLR) as shown in figure 6.11 and 6.12. We utilized the observed redshift to estimated the 3-dimensional distribution of the galaxy, assuming the spherical symmetry. The estimated optical luminosity and the metal abundance are both subjected to large errors, and we tentatively adopt factors of two, three, and two for IMLR, OMLR and MMLR, respectively.

We summarize recent measurements of IMLR and OMLR in table 6.3 and figure 6.11 and 6.12, and compare these values with those in other systems, Fornax cluster, NGC 1404 and NGC 720. In order to investigate the temperature dependence of the IMLR and OMLR, we plotted the data in 6.13. It is suggested that the smaller systems with lower gas temperature tend to show not only lower IMLR in Makishima et al. (2001) but also lower OMLR, even though the scatter of the data is large.

All the integrated IMLR, OMLR, and MMLR show a steep increase up to a radius of $\sim$ 100 kpc and seem to reach almost the maximum at 100–200 kpc. This trend is similar to the IMLR obtained with *XMM-Newton* for M 87 and the Centaurus cluster by Matsushita et al. (2007) within $r \lesssim 100$ kpc. The steep increase in the $r \lesssim 100$ kpc region suggests that the Fe and O ions which were synthesized in the central galaxies have been distributed to a wide region in the ICM. On the other hand, as pointed out in Ezawa et al. (1997), abundance gradient over a few hundred kpc scale in clusters of galaxies follows the mass ratio between the ICM and the galaxies. This is because heavy ions released from galaxies without much kinetic energy would not diffuse out more than 10 kpc over the Hubble time. (Böhringer et al. 2004) showed that it takes about 10^{10} yr to synthesize Fe mass within $r \lesssim 100$ kpc range. These considerations suggest that the gas enriched by Fe and O was released to the cluster space with significant kinetic energy and/or the gas stripping was efficiently occurred in the $\sim$ 100 kpc range due to the galactic motion.

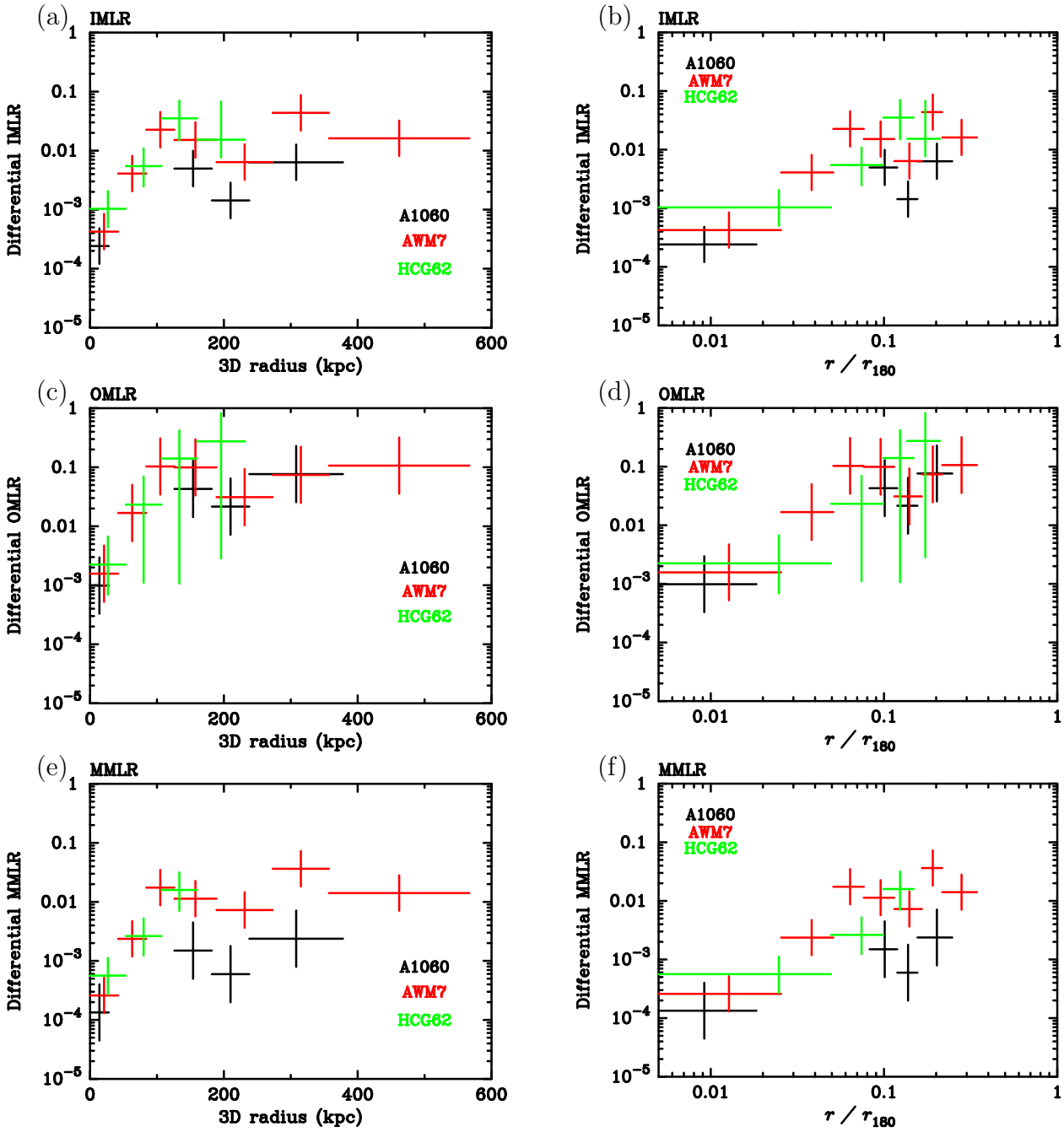

Fig. 6.11: (a)-(d) show the radial profiles of the differential iron , oxygen, magnesium mass to light ratio of A 1060, AWM 7, HCG 62.

6.2.4 SN rate and mass loss rate

We estimate the amount of metal in the central region from the SN Ia rate . Equation 2.11 gives the amount of metals produced by SN Ia in elliptical galaxies. The SN Ia rate is 0.18 per 100 years per $10^{10} L_{\odot}^{\mathrm{B}}$ (Cappellaro et al. 1999), and we take W7 model by Nomoto et al. (1984). Integrating the yield over the Hubble time, taking 1.5×10^{10} yr, IMLR and OMLR become $\sim 2.0 \times 10^{-3}$ and $\sim 3.9 \times 10^{-4}$, respectively. Comparing these values with the observed results in the central region, IMLR and OMLR are about one order and a few times higher than the observed ones, respective. For the whole region of the observed clusters, the predicted IMLR and OMLR are about one and two orders lower than the observed levels, respectively. This feature indicates that the amount of O produced by

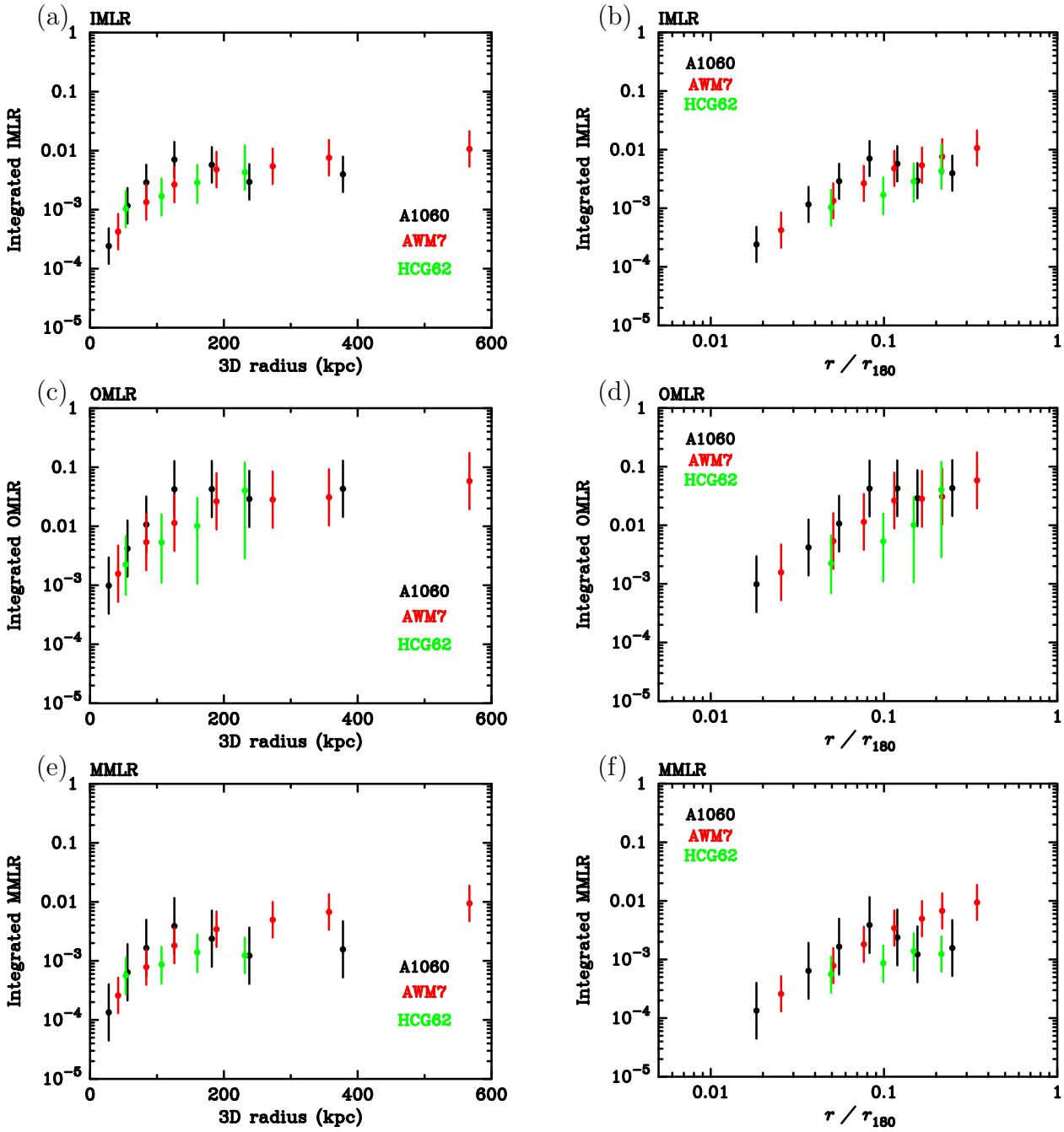

Fig. 6.12: (a)-(f) show the radial profiles of the integrated iron, oxygen and magnesium mass to light ratio of A 1060, AWM 7 and HCG 62.

SN II has to be lager than that by SN Ia, and the amount of excess Fe (or other metals) concentrated in the central region, corresponding to the IMLR of a few times 10^{-4}, can be produced in a time scale of $\tau \sim 10^9$ yr.

On the other hand, Renzini et al. (1993) suggests that the SN Ia rate was higher in the past or the ratio of SN Ia to stellar mass loss rate was higher in the past. The observed Fe in the gas at the core of clusters is also a mixture of those in the ICM and the recent supply from the cD or elliptical galaxies in the central region. The latter contains Fe synthesized by mainly SN Ia and those coming from stars through stellar mass loss, since Fe can be produced by both SN Ia and SN II. The Fe abundance of gas from SN Ia in an elliptical galaxy is proportional to $M_{\rm SN}^{\rm Fe}\theta_{\rm SN}/\alpha_*$ (Matsushita et al. 2003). Here $M_{\rm SN}^{\rm Fe}\theta_{\rm SN}/\alpha_*$

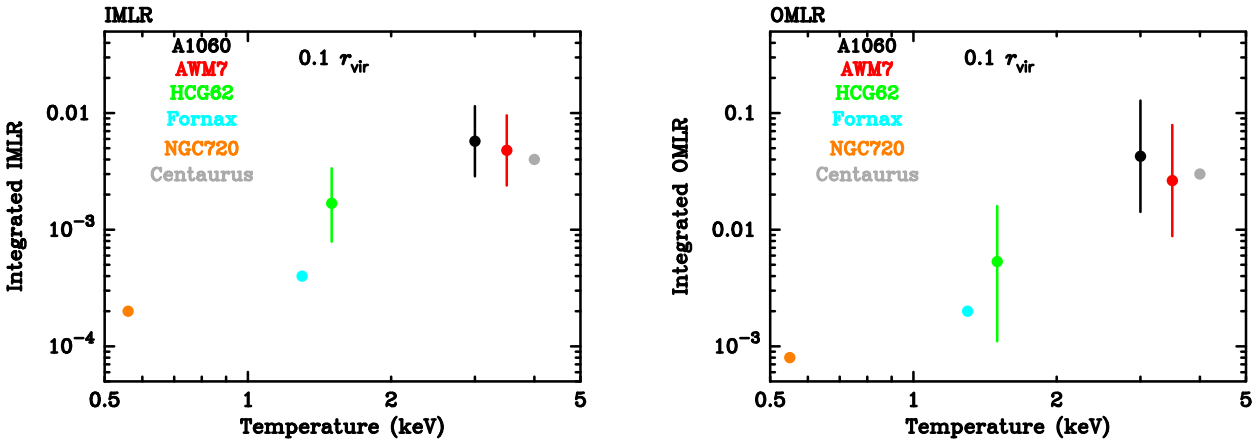

Fig. 6.13: Temperature dependence of IMLR (left) and OMLR (right) normalized the 0.1 virial radius.

is the mass of Fe synthesized by SN Ia, $\theta_{\rm SN}$ is SN Ia rate, and α_* is stellar mass loss rate. From theoretical stellar evolutionally models of stellar population, the stellar mass loss rate is approximated by $1.5 \times 10^{-11} L_{\rm B} \tau_{15}^{-1.3}$ $M_\odot$/yr, where τ_{15} is the age in unit of 15 Gyr, and $L_{\rm B}$ is the B-band luminosity (Ciotti et al. 1991). Böhringer et al. (2004) tested the standard cooling flow model by examining the Fe mass profile of 4 clusters with cooling cores. They concluded that we need long enrichment times (> 5 Gyr) in order to accumulate the observed Fe abundance peak even if the SN Ia rate was high in the past.

Actually, our results indicate that, while the metals produced by SN Ia and SN II show abundance concentration in the central region, the amount of metals in the central region is actually lower than the predicted level. In other words, metal outflow from the central galaxies is more efficient than the cooling flow effect.

6.2.5 Scenario of metal enrichment

We consider the scenario of chemical evolution of the clusters and groups based on our results.

The main features from the present observations are summarized as follows.

1. The metal mass-to-light ratios (OMLR, IMLR etc.) decrease toward the central region of the clusters and groups, even though the metal to hydrogen number ratios (abundances) generally increase to the center.

2. The number ratio of SN II to SN Ia is about ~ 3, based on the fit of the observed abundance patterns. However, the fit is not acceptable because of the rather simple assumption of the SN yields and/or the systematic error in the observed metal abundance.

3. The abundance of oxygen is lower than those of other elements and about half the solar value in the central region. This is partly because oxygen may be contained in the stars or dusts, and because of the simple assumption of the Salpeter IMF.

4. The predicted IMLR, assuming the present SN Ia rate over the Hubble time, is much lower than the observed values for the whole cluster regions. Renzini et al. (1993) suggest that the SN Ia rate was higher in the past.

These results indicate the following scenario for the metal enrichment.

1. In the early stage of the cluster formation, a large number of SN II, as indicated by the 3 to 1 ratio of SN II to SN Ia in total, were occurred. And, a wide region in or around the cluster space was enriched by galactic winds and/or mass loss from stars.

2. Then, as the gravitational collapse of clusters of galaxies proceeds, the enhanced SN II activity ceases and the metals produced in galaxies are brought in to the cluster space by mild outflows and/or ram pressure strippings. In this epoch, the metals are mainly produced by SN Ia and the high metal production in the central elliptical galaxies causes abundance gradient in clusters.

Suzaku enabled efficient determination of various emission lines, especially those of O and Mg, and we could estimate the fractional contribution to the metal production by SN Ia and SN II for the first time. Such an estimation was attempted based only with the iron abundance in the past. We hope that future sensitive observations of emission lines from various clusters and groups at different redshifts will enable us to look directly into the enrichment process of the cluster space. For those studies, X-ray microcalorimeters are expected to play a major role.

Appendix A

Fraction from Corresponding Sky

Since angular resolution of X-Ray Telescopes (XRT; Serlemitsos (2007)) of Suzaku ($\sim 2'$ in half power diameter; HPD) is not as good as those of Chandra ($\sim 0.5''$) and XMM-Newton ($\sim 15''$), fraction of photons may become significant that come from outside of the sky direction corresponding to the extraction region of spectra on the XIS detector plane. This was a severe problem for the ASCA GIS (Ohashi et al. 1996; Makishima et al. 1996), which employs similar type of thin-foil-nested reflectors for the XRT (Serlemitsos et al. 1995) with $\sim 3.6'$ HPD, and the fraction sometimes became more than half of total detected photons as seen in figure 4 of Kikuchi et al. (1999) for the MKW 3s and 2A 0335+096 clusters. It made the cluster analysis further complicated that energy dependence of the fraction could not be neglected with the ASCA XRT/GIS system.

The situation has been much improved for Suzaku than ASCA. The Suzaku XRT/XIS system adopts longer focal length of 4.75 m than ASCA (3.5 m) and the sky coverage of the XIS detector ($18' \times 18'$) is smaller than the GIS ($\sim 22'$ radius), so that the energy-dependent vignetting effect is much smaller. Moreover, improvement of the mirror surface has reduced scatters on the reflector and equipment of the pre-collimator dramatically decreased the so-called "stray-lights" mainly from outside of the XIS field of view (Serlemitsos 2007).[1]

We therefore estimated the fraction of photons outside the extraction region using a simulator of the Suzaku XRT/XIS system, "xissim" version 2006-08-26 (Ishisaki et al. 2006) for A 1060 and version 2006-10-26 for AWM 7, HCG 62, NGC507, and NGC 720, in the following way: *(1)* Assuming the surface brightness profile for each object, 2,000,000 count of monochromatic incident-photons (in 0.5, 1, 2, 4, or 8 keV) were generated by a "mkphlist" task. *(2)* Simulated event files were created for both the central and offset observations using the "xissim" task, with the xis_efficiency parameter set to "no" to save photon statistics. *(3)* Using the RA and DEC columns in the simulated event files, the event files were splitted into 7+1 sky regions corresponding to the extraction annuli of 0–$2'$, 2–$4'$, 4–$6'$, 6–$9'$, 9–$13'$, 13–$17'$, and 17–$27'$, plus outside of them, $r > 27'$ for A 1060 and AWM 7, the extaction anuuli of 0–$2'$, 2–$4'$, 4–$6'$, 6–$9'$, 9–$13'$ plus outside of them, $r > 13'$ for HCG 62, NGC 507, and NGC 720.[2] *(4)* The detected photon count at each extraction region on the XIS detector plane was calculated for each splitted event file using the "xselect" task.

In this way, we estimated the fraction of photons for the 7, 5 extraction annuli from the 8, 6 sky regions for the clusters and groups, respectively, in 5 energies for the 4

[1]The "stray-lights" reach to the focal plain through abnormal paths, e.g., reflection by only the secondary mirror, or the mirror backside reflection (Mori et al. 2005).

[2]The "fselect" task with the *angsep* function was utilized to calculated the angular separation of events from the assumed center of the clusters and groups.

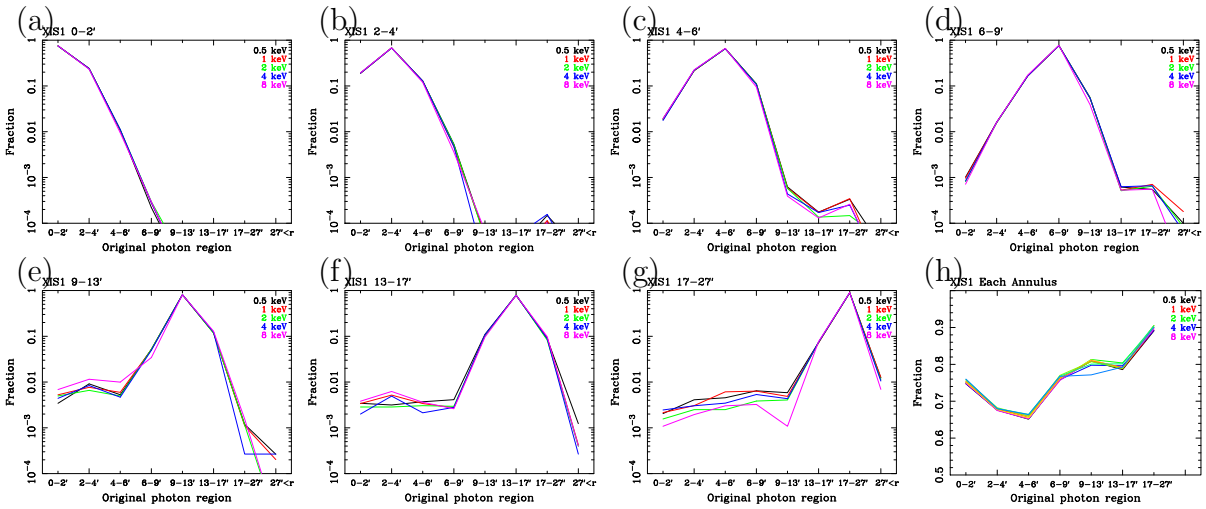

Fig. A.1: (a)–(g) Fraction of photons detected in the 0–2′ to 17–27′ extraction regions of A 1060 on the XIS1 detector plotted against the original sky directions of incidence, which is estimated by the "xissim" simulation. Different energies are plotted in different colors. (h) Photon fraction of each annulus coming from the corresponding sky region, i.e., maximum values of panels (a)–(g) are plotted.

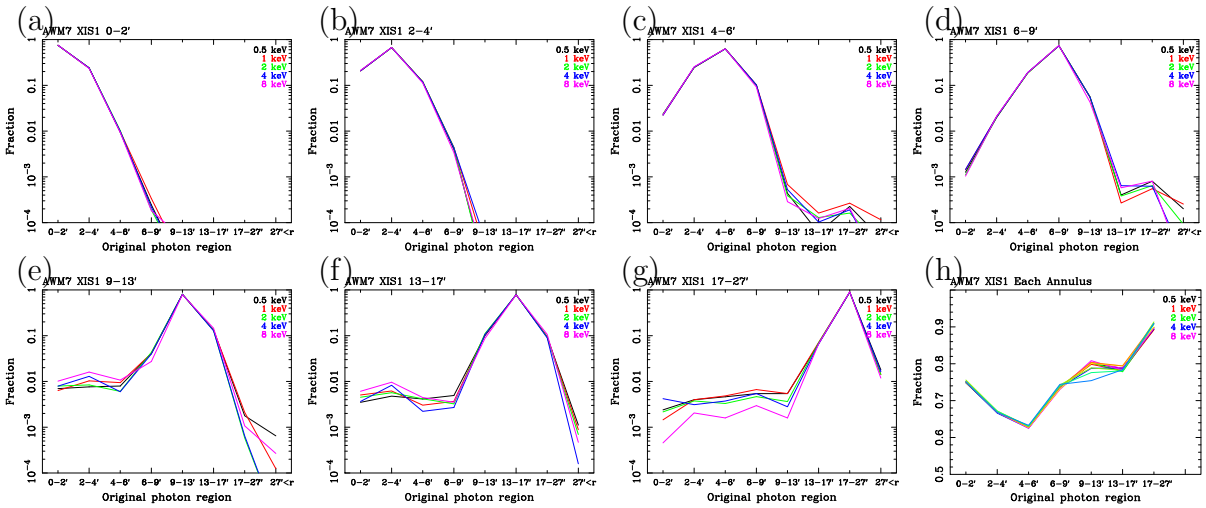

Fig. A.2: (a)–(g) Fraction of photons detected in the 0–2′ to 17–27′ extraction regions of AWM 7 on the XIS1 detector. The concept is same as A 1060.

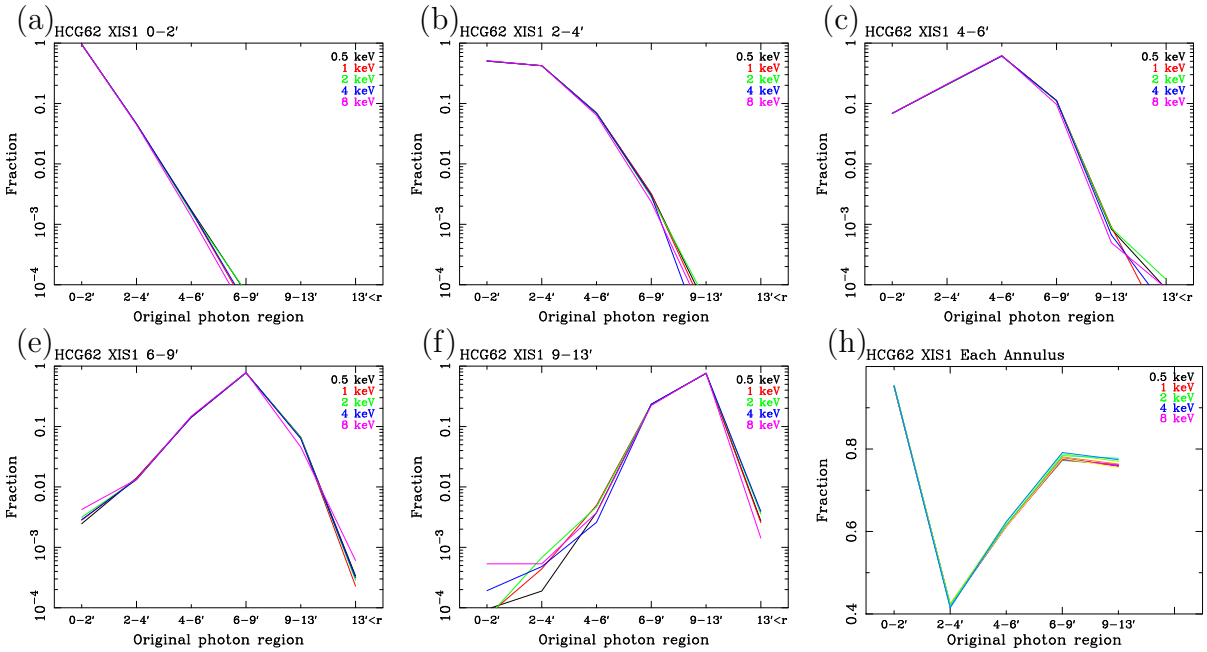

Fig. A.3: (a)–(f) Fraction of photons detected in the 0–2′ to 9–13′ extraction regions of HCG 62 on the XIS1 detector. The concept is same as A 1060.

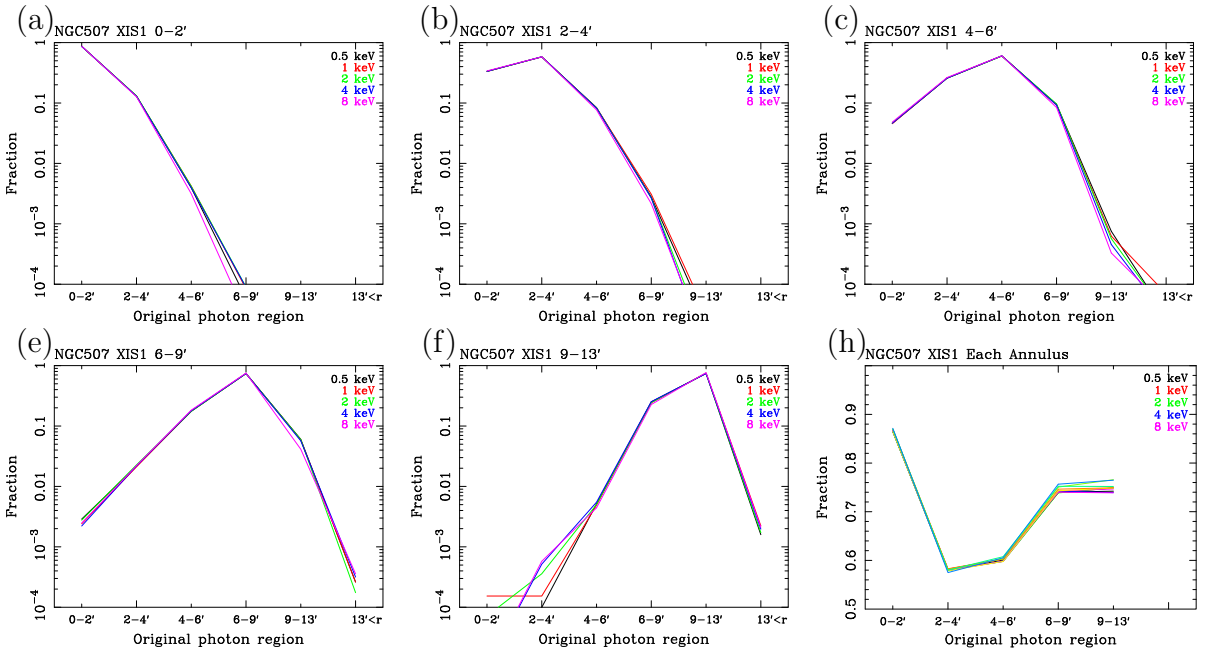

Fig. A.4: (a)–(f) Fraction of photons detected in the 0–2′ to 9–13′ extraction regions of HCG 62 on the XIS1 detector. The concept is same as A 1060.

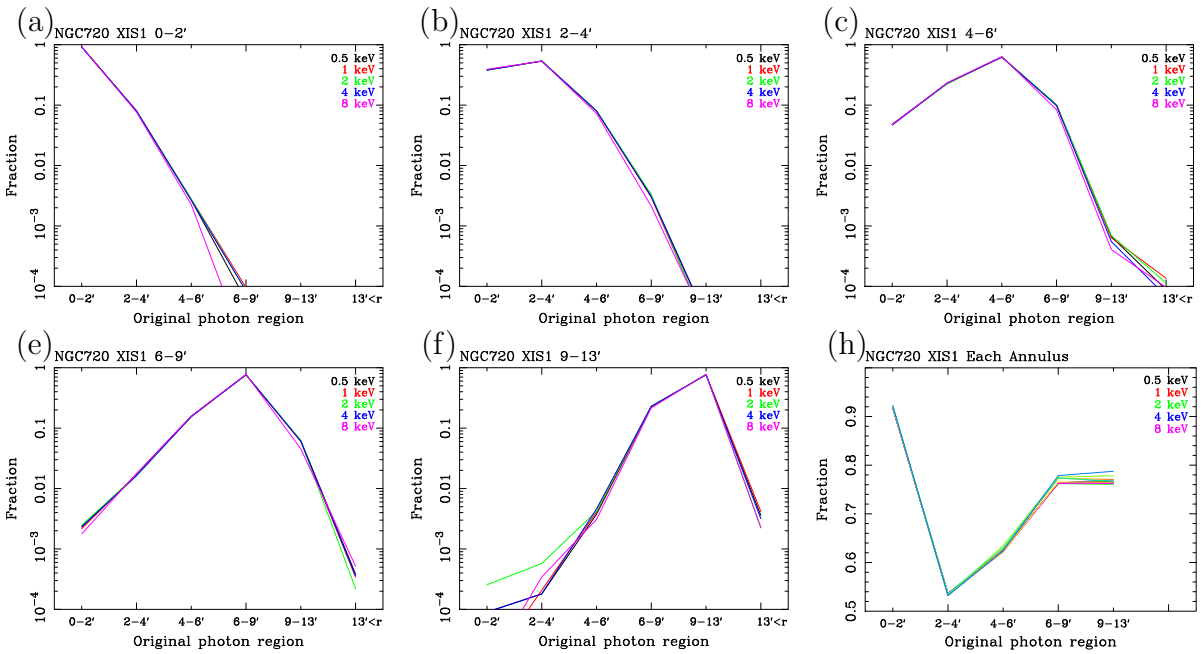

Fig. A.5: (a)–(f) Fraction of photons detected in the 0–2′ to 9–13′ extraction regions of HCG 62 on the XIS1 detector. The concept is same as A 1060.

XIS sensors. We plot examples of XIS1 in figure A.1-A.5. The energy dependence is almost negligible within $\sim 5\%$ in figure A.1(h). This is primarily owing to the existence of the pre-collimator for the Suzaku XRT. These results are almost the same with the other XIS sensors. Note that this simulation does not include the CXB and the Galactic background, which are almost uniform on the sky so that the spatial response is different from figure A.1.

Appendix B

Dependence on Abundance Tables

There are several abundance tables usable in XSPEC, such as *angr* (Anders & Grevesse 1989), *aneb* (Anders & Ebihara 1982), *feld* (Feldman 1992), and *lodd* (Lodders 2003). The elemental abundances relative to hydrogen in number defined by these tables are plotted in figure B.1(a), and ratios of each element to *angr* is shown in figure B.1(b). Although *feld* is not used in our spectral analysis, it is added to compare recent Suzaku results (Matsushita et al. 2007; Tawara 2007) which adopt this table. As seen in figure B.1(b), *angr* and *feld* are essentially the same except for Fe abundance, which is 1.44 times larger for *angr* than *feld*.

The *angr* table is the de facto of XSPEC, however, Fe abundance is significantly different from others. This is because *angr* is based on the solar photospheric measurement of Fe I (Blackwell et al. 1984), which disagrees with the meteorites measurement adopted in *aneb*. Discussions afterwards seem to prefer the lower abundance by meteorites, because Fe abundance determined by Fe II, which is dominant in the solar photosphere, is consistent with the meteorites value (Biemont et al. 1991; Raassen & Uylings 1998).

It is notable that C, N, O, and Ne abundances in *lodd* is significantly lower ($\sim 60\%$ of *angr*). These values are based on the three-dimensional time-dependent hydrodynamical model solar atmosphere, in which departures from local thermodynamical equilibrium (LTE) and blend of Ni I line with the forbidden [O I] λ6300 are considered (Allende Prieto et al. 2001; Allende Prieto et al. 2002). The *lodd* table in XSPEC is the recommended elemental abundance of the solar photosphere (table 1 in Lodders (2003)), however, he states that the photo-solar abundances as representative of the solar system should be slightly larger (by ~ 1.2 times for C, N, and O) for helium and heavy-element due to the settling effects.

The decrease of these abundant elements in the Inter Stellar Medium (ISM) also leads to the difference in the assumed Galactic absorption as seen in figure B.1(c). The *phabs* absorption model with *lodd* abundance table gives by $\sim 15\%$ smaller absorption at the maximum in our noticed energy range of 0.4–7.1 keV in the spectral fitting, while the difference between *wabs* and *phabs* with *angr* is negligible. This is because we have assumed the neutral hydrogen column density of $N_{\rm H} = 4.9\times10^{20}$ cm^{-2} (Dickey & Lockman 1990) with "1 solar" abundance for the ISM. In fact, the ISM consists of monoatomic gas, molecules, and grains, so that it is suggested to have smaller abundance than the solar abundance by Wilms et al. (2000). Shaver et al. (1983) have reported a radial abundance gradient in the Milky Way Galaxy of $\sim 16\%$ per kpc.

Considering these uncertainties, we have tested the spectral fit of A 1060 with four kinds of combinations in the absorption model and the abundance table, *phabs angr*, *wabs angr*, *wabs lodd*, and *phabs angr*. We further tested the fit when the abundances of O, Ne, and Mg are linked to have the same value relative to the assumed "solar" abundance,

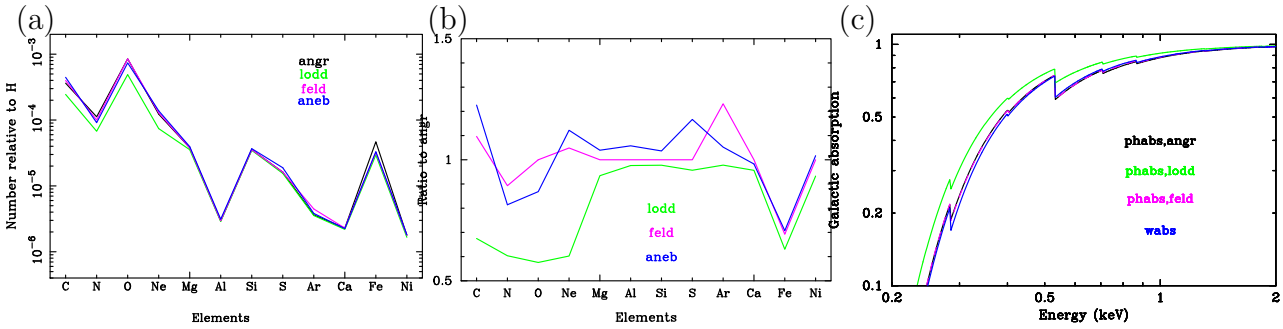

Fig. B.1: (a) The assumed metal abundances relative to H in number by the *angr*, *lodd*, *feld*, and *aneb* tables of XSPEC v11.3.0t. (b) Same as (a) but normalized by the *angr* abundances. (c) Comparison of absorption by the *phabs* model with *angr* abundance table, *phabs* with *lodd*, and the *wabs* model in XSPEC. The *wabs* model assumes the abundance ratio of *aneb* built-in the code. Neutral hydrogen column density of $N_{\rm H} = 4.9 \times 10^{20}$ cm^{-2} and "1 solar" abundance, which is different among the tables, are assumed. The photoelectric absorption cross-section of *bcmc* (Balucinska-Church & McCammon 1992; Yan et al. 1998) is used.

in two reasons: they are all supposed to be primarily the SN II products; O and Ne abundances are susceptible to the Galactic component in outer annuli. Note that the O : Ne : Mg ratios are significantly different between *angr* (1 : 0.145 : 0.045) and *lodd* (1 : 0.151 : 0.072).

Results are summarized in figures B.2–B.4 and a list of χ^2/dof is presented in table B.1. As expected from figure B.1(c), the *phabs angr* and *wabs angr* results are almost identical. The *phabs lodd* gives slightly larger temperature than others, which leads the O abundance profile in figure B.2(b) to be different behavior from others. Other discrepancies in the derived abundances can be explained by difference in the definition of "1 solar".

Since χ^2 values for *phabs lodd* are generally larger than other models, the Galactic absorption model by *phabs lodd* is considered to be inappropriate with our X-ray data. On the other hand, *wabs lodd* model shows the minimum χ^2 in table B.1. This is interesting because the *wabs* absorption model assumes *aneb* abundance table built-in the code. This may indicates that our modeling of the Galactic component is too naive, and/or the Galactic abundance gradient is responsible so that effective elemental abundance between absorption and emission are different.

It is notable that shape of the radial abundance profiles are quite similar among these four models in figure B.4 when O = Ne = Mg is assumed. Difference from Fe or Si is evident as seen in figures B.3(c) and B.4(c): Fe and Si abundances decreases with radius with roughly constant Si/Fe ratio, while O = Ne = Mg are almost constant within $r \lesssim 17'$. The higher (O = Ne = Mg)/Fe ratio than "1 solar" is also suggested for both *angr* and *lodd* abundance tables.

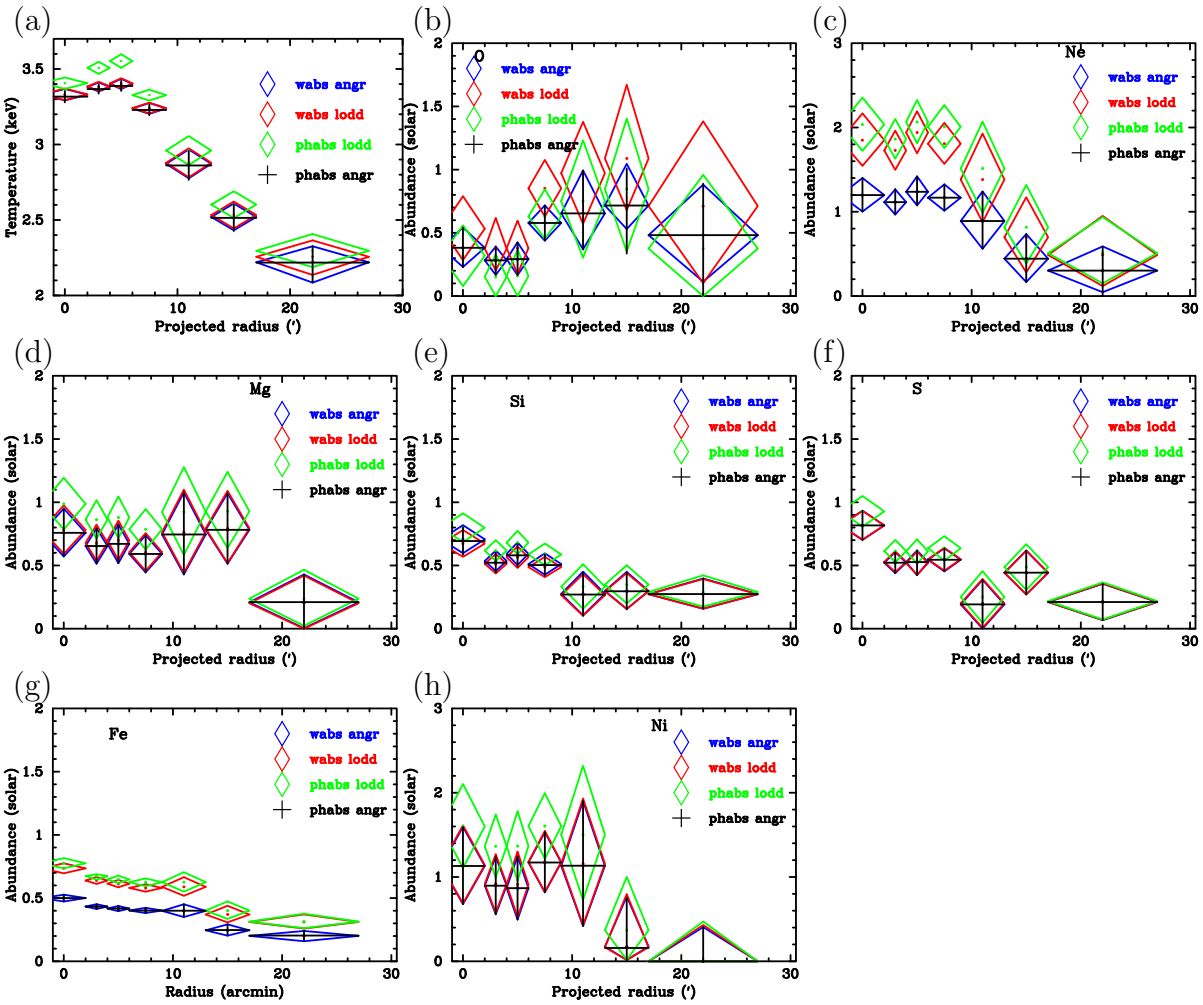

Fig. B.2: Same as figure 5.6 of the Suzaku result for the black crosses (*phabs angr*). Other fit results are also plotted in blue, red, and green diamonds, when different abundance ratio (*lodd*) and/or different absorption model (*wabs*) are assumed.

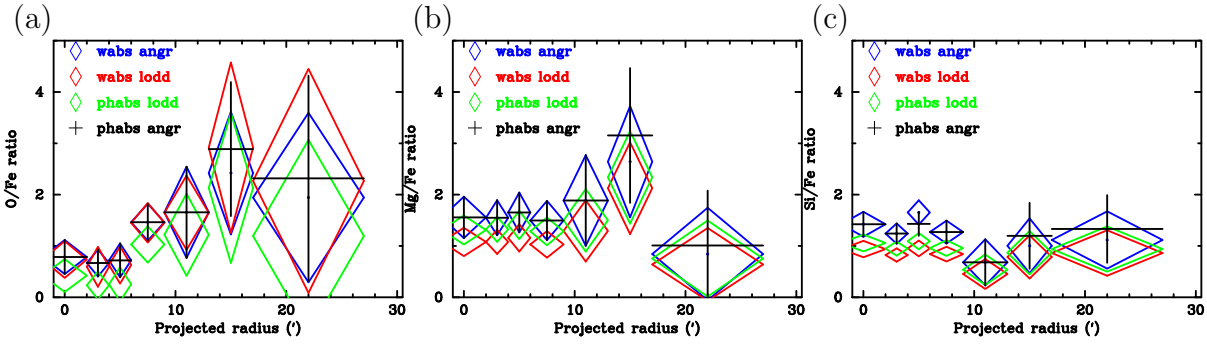

Fig. B.3: (a) O/Fe ratio, (b) Mg/Fe ratio, and (c) Si/Fe ratio, which are same as figure 6.2(a) for the black crosses (*phabs angr*) in these figures (a)–(c). Other fit results are also plotted in blue, red, and green diamonds, when different abundance ratio (*lodd*) and/or different absorption model (*wabs*) are assumed.

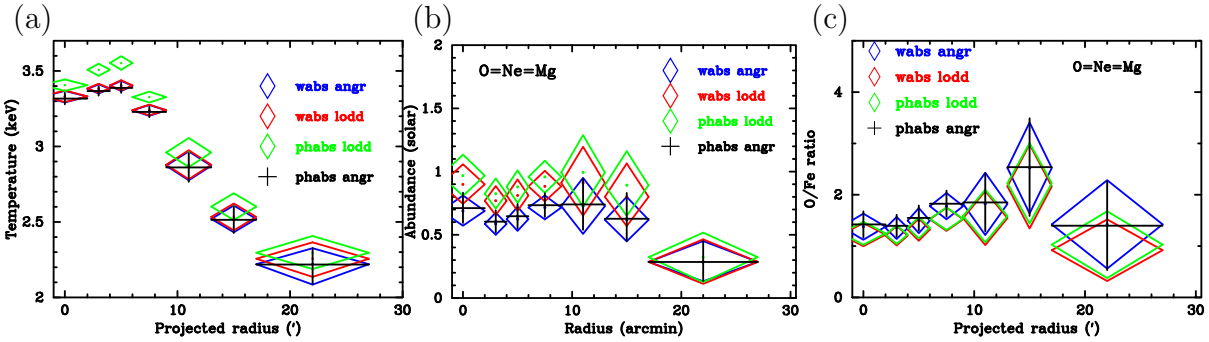

Fig. B.4: Radial profiles of (a) temperature, (b) O = Ne = Mg abundance, and (c) abundance ratio to Fe, when the abundances of O, Ne, and Mg are constrained to have the same value for the assumed abundance tables of *angr* or *lodd*. Meaning of the markers are same as figures B.2 and B.3.

Table B.1: List of χ^2/dof for each fit.

Region	O, Ne, Mg independent				Constrained to be O=Ne=Mg			
	phabs angr	*wabs angr*	*wabs lodd*	*phabs lodd*	*phabs angr*	*wabs angr*	*wabs lodd*	*phabs lodd*
0–2′	1240/992	1240/992	1215/992	1274/992	1278/996	1260/996	1258/996	1335/996
2–4′	1290/992	1290/992	1267/992	1356/992	1358/996	1346/996	1343/996	1464/996
4–6′	1345/992	1345/992	1312/992	1400/992	1418/996	1396/996	1397/996	1513/996
6–9′	1329/992	1329/992	1298/992	1395/992	1365/996	1340/996	1359/996	1464/996
9–13′	1057/992	1057/992	1053/992	1059/992	1058/996	1057/996	1057/996	1063/996
13–17′	1082/992	1082/992	1077/992	1078/992	1086/996	1085/996	1080/996	1080/996

Appendix C

Deprojection

C.1 the concept of deprojection

In order to estimate the 3-dimensional effects of the emission from the objects, we need to calculate the effects from the flux of the outer shell to that of the inner shell of the object. We estimate the effects the following method. In figure C.1, the volume, V_N, is calculated as,

$$V_N = \frac{4}{3}\pi\left(r_N^2 - r_{N-1}^2\right)^{\frac{3}{2}}, \tag{C.1}$$

and the volume, V_N^m, for $m < N$ is

$$V_N^m = \frac{4}{3}\pi\left\{(r_N^2 - r_{m-1}^2)^{\frac{3}{2}} - (r_N^2 - r_m^2)^{\frac{3}{2}} - (r_{N-1}^2 - r_{m-1}^2)^{\frac{3}{2}} + (r_{N-1}^2 - r_m^2)^{\frac{3}{2}}\right\}. \tag{C.2}$$

The observed flux $F_m^{\rm obs}$ in the projected $r_{m-1} < r < r_m$ annulus is the sum of flux from the volumes, V_m, V_{m+1}^m, ..., V_N^m. If we define the flux from the volume V_i as f_i,

$$F_m^{\rm obs} = f_m + \frac{V_{m+1}^m}{V_{m+1}} f_{m+1} + ... + \frac{V_N^m}{V_N} f_N = \sum_{i=m}^{N} \frac{V_i^m}{V_i} f_i, \tag{C.3}$$

assuming the spherical symmetry and $V_i^i \equiv V_i$. Because the volume of the $r_{m-1} < r < r_m$ crust is $W_m = \frac{4}{3}\pi\left(r_m^3 - r_{m-1}^3\right)$, the flux contribution in the 3-dimensional range of $r_{m-1} < r < r_m$ is

$$F_m^{\rm 3D} = \frac{W_m}{V_m} f_m = \frac{r_m^3 - r_{m-1}^3}{(r_m^2 - r_{m-1}^2)^{3/2}}\, f_m. \tag{C.4}$$

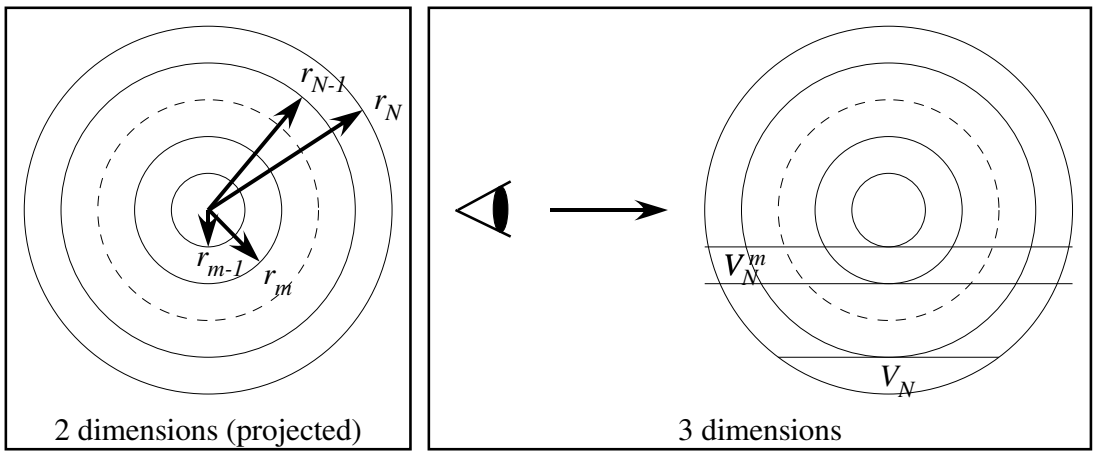

Fig. C.1: deprojection image

C.2 HCG 62

Using the deprojection method in the previous section, we estimated the effects for HCG 62. We summarized the conversion factor from the outer shells to the inner shells in table C.1.

The deprojected spectra is shown in figure C.2. The spectra are fitted with the $apec + phabs \times (vapec_1 + vapec_2)$ model (see section 5.3.2), the obtained temperature and abundance profiles show in figure C.3. The obtain results are almost same as the results of the fitting of the projected spectra, although the values in the central region are slightly higher than those of the results for the projected spectra. We also compare the value of χ^2 and normalization for the deprojected spectra with those for the projected spectra. These values also have the same tendencies as those for the projected results.

Because the spatial resolution of *Suzaku* is inferior to that of *Chandra* or *XMM-Newton*, if you calculation the effects of the deprojection correctly, you need to take the fraction of photons in consideration.

Table C.1: Fractional contribution of the outer shells to the inner shells in the deprojection analysis.

	6–9′	4–6′	2–4′	0–2′
9–13′	0.492	0.165	0.091	0.029
6–9′	.....	0.440	0.199	0.061
4–6′	.....	.....	0.559	0.140
2–4′	.....	.....	.....	0.347

Table C.2: left: The χ^2 and dof of the each annuli for the results of the projected spectra. right: The χ^2 and dof of the each annuli for the results of the deprojected spectra.

projection		
region	XIS	χ^2/dof
0-2′	BI	222.2362/175
	FI	277.0044/175
2-4′	BI	181.6976/175
	FI	208.4201/175
4-6′	BI	192.0910/175
	FI	256.0377/175
6-9′	BI	200.622/175
	FI	205.839/175
9-13′	BI	77.815/86
	FI	89.232/86
all		1910.995/1508

deprojection		
region	XIS	χ^2/dof
0-2′	BI	222.0826/175
	FI	275.8482/175
2-4′	BI	180.4348/175
	FI	208.0382/175
4-6′	BI	191.7936/175
	FI	255.7254/175
6-9′	BI	199.6856/175
	FI	205.1819/175
9-13′	BI	77.815/86
	FI	89.232/86
all		1905.8373/1508

Table C.3: The normalization of the hot and cool components of the projected spectra (left) and the deprojected spectra.

projection		
region	XIS	normalization
0-2′	hot	1.231e-3
	cool	1.352e-3
2-4′	hot	3.982e-3
	cool	2.317e-3
4-6′	hot	7.636e-3
	cool	2.538e-3
6-9′	hot	6.848e-3
	cool	3.552e-3
9-13′	hot	8.862e-3
	cool	8.041e-3

deprojection		
region	XIS	normalization
0-2′	hot	9.510e-4
	cool	1.101e-3
2-4′	hot	3.239e-3
	cool	1.954e-3
4-6′	hot	6.976e-3
	cool	2.120e-3
6-9′	hot	6.105e-3
	cool	2.909e-3
9-13′	hot	8.862e-3
	cool	8.041e-3

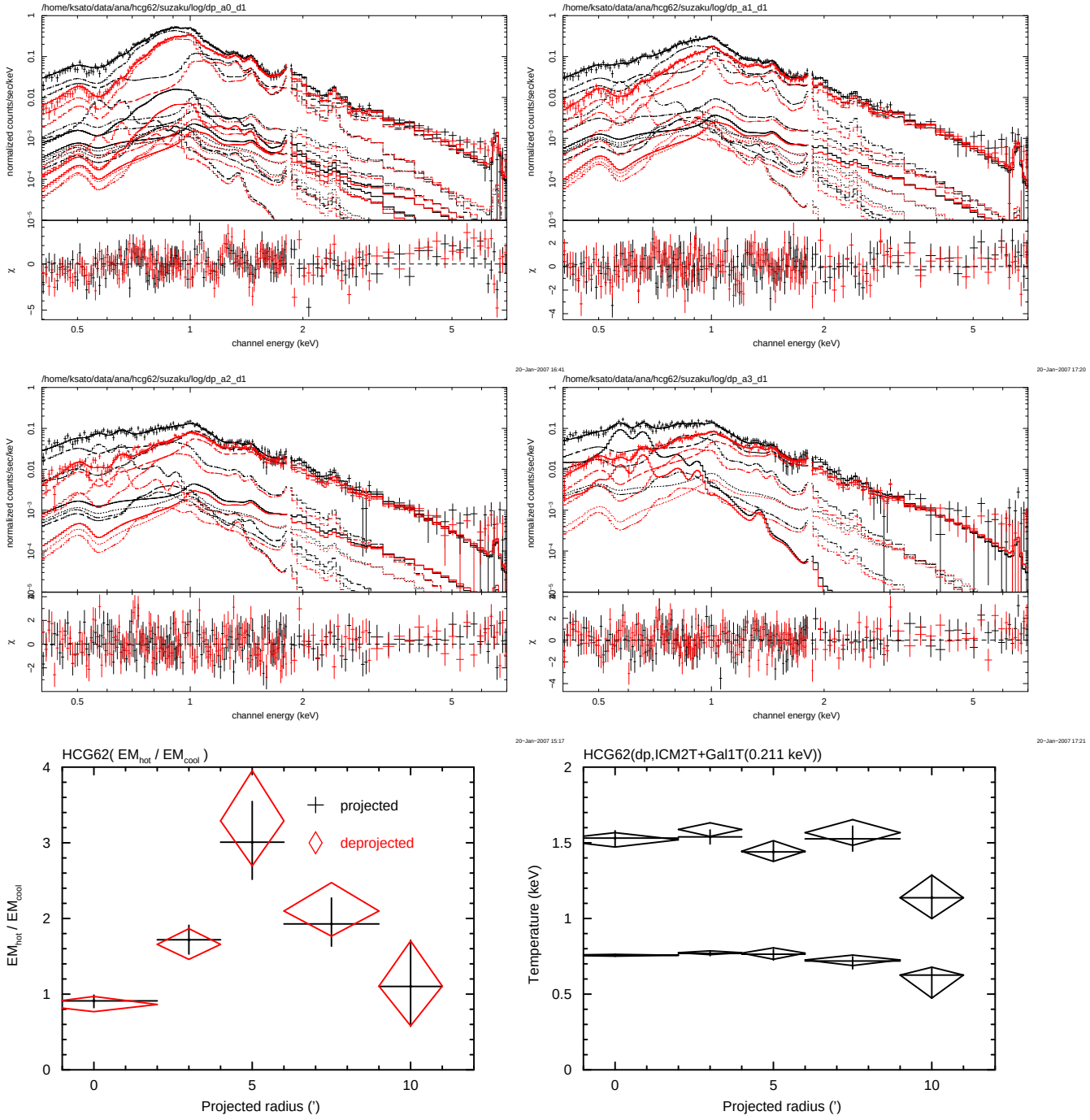

Fig. C.2: The upper four panels show the deprojected spectra at the annular regions which is denoted in the panels, and they are plotted by black and red crosses for BI and FI, respectively. The estimated CXB and NXB components are subtracted, and they are fitted with the $apec + phabs \times (vapec_1 + vapec_2)$ model. The lower left panel shows the emission measure of hot component to that of cool component ratio of the results of the projected spectra (black crosses) and the results of the deprojected (red diamonds). The lower right panel shows the temperature profile of the results of the projected spectra (crosses) and the results of the deprojected spectra (black diamonds).

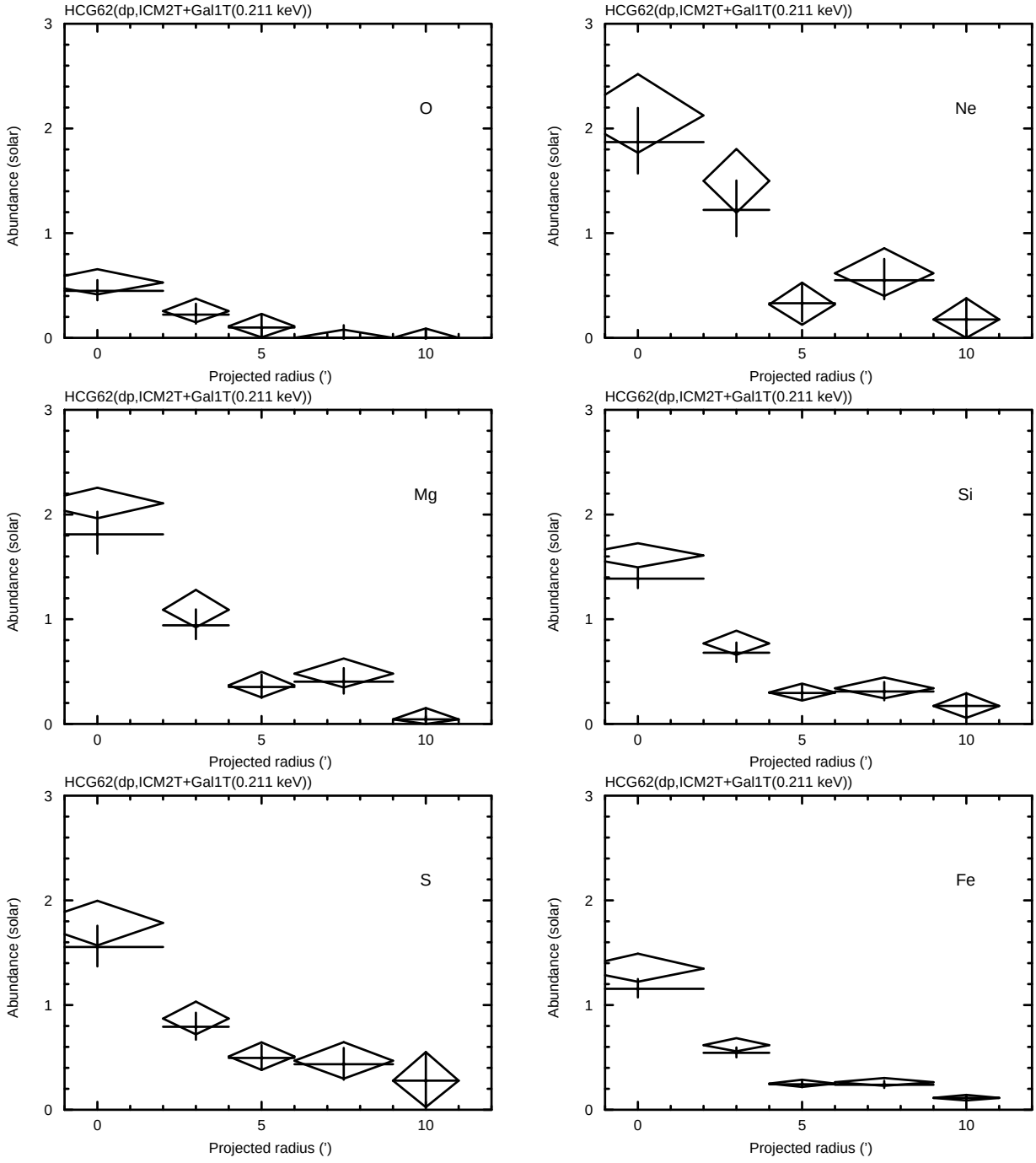

Fig. C.3: Radial abundance profiles of the results of the projected spectra (black crosses) and the results of the deprojected spectra (black diamonds).

Bibliography

Allende Prieto, C., Lambert, D. L., & Asplund, M. 2001, ApJL, 556, L63

—. 2002, ApJL, 573, L137

Anders, E., & Ebihara, M. 1982, Geochim. Cosmochim. Acta, 46, 2363

Anders, E., & Grevesse, N. 1989, Geochim. Cosmochim. Acta, 53, 197

Arimoto, N., Matsushita, K., Ishimaru, Y., Ohashi, T., & Renzini, A. 1997, ApJ, 477, 128

Arnaud, M., Maurogordato, S., Slezak, E., & Rho, J. 2000, A&A, 355, 461

Arnaud, M., Rothenflug, R., Boulade, O., Vigroux, L., & Vangioni-Flam, E. 1992, A&A, 254, 49

Balucinska-Church, M., & McCammon, D. 1992, ApJ, 400, 699

Biemont, E., Baudoux, M., Kurucz, R. L., Ansbacher, W., & Pinnington, E. H. 1991, A&A, 249, 539

Blackwell, D. E., Booth, A. J., & Petford, A. D. 1984, A&A, 132, 236

Böhringer, H., Matsushita, K., Churazov, E., Finoguenov, A., & Ikebe, Y. 2004, A&A, 416, L21

Brandt, W. N., & Hasinger, G. 2005, ARA&A, 43, 827

Buote, D. A., Jeltema, T. E., Canizares, C. R., & Garmire, G. P. 2002, ApJ, 577, 183

Cappellaro, E., Evans, R., & Turatto, M. 1999, A&A, 351, 459

Christlein, D., & Zabludoff, A. I. 2003, ApJ, 591, 764

Ciotti, L., Pellegrini, S., Renzini, A., & D'Ercole, A. 1991, ApJ, 376, 380

David, L. P., Jones, C., & Forman, W. 1996, ApJ, 473, 692

De Grandi, S., Ettori, S., Longhetti, M., & Molendi, S. 2004, A&A, 419, 7

De Grandi, S., & Molendi, S. 2001, ApJ, 551, 153

—. 2002, ApJ, 567, 163

Diaferio, A., Geller, M. J., & Ramella, M. 1994, AJ, 107, 868

Dickey, J. M., & Lockman, F. J. 1990, ARA&A, 28, 215

Dolag, K., Grasso, D., Springel, V., & Tkachev, I. 2004, Journal of Experimental and Theoretical Physics Letteres, 79, 583

Dolag, K., Hansen, F. K., Roncarelli, M., & Moscardini, L. 2005, MNRAS, 363, 29

Ezawa, H., Fukazawa, Y., Makishima, K., Ohashi, T., Takahara, F., Xu, H., & Yamasaki, N. Y. 1997, ApJL, 490, L33+

Feldman, U. 1992, Physica Scripta Volume T, 46, 202

Finoguenov, A., Arnaud, M., & David, L. P. 2001, ApJ, 555, 191

Finoguenov, A., David, L. P., & Ponman, T. J. 2000, ApJ, 544, 188

Finoguenov, A., Matsushita, K., Böhringer, H., Ikebe, Y., & Arnaud, M. 2002, A&A, 381, 21

Forman, W., & Jones, C. 1982, ARA&A, 20, 547

Fujimoto, R., Mitsuda, K., McCammon, D., Takei, Y., Bauer, M., Ishisaki, Y., Porter, F. S., Yamaguchi, H., Hayashida, K., & Yamasaki, N. Y. 2006, ArXiv Astrophysics e-prints

Fukazawa, Y. 1997, PhD thesis, , Univ. Tokyo, (1997)

Fukazawa, Y., Kawano, N., & Kawashima, K. 2004, ApJL, 606, L109

Fukazawa, Y., Makishima, K., Tamura, T., Ezawa, H., Xu, H., Ikebe, Y., Kikuchi, K., & Ohashi, T. 1998, PASJ, 50, 187

Fukazawa, Y., Makishima, K., Tamura, T., Nakazawa, K., Ezawa, H., Ikebe, Y., Kikuchi, K., & Ohashi, T. 2000, MNRAS, 313, 21

Fukazawa, Y., Ohashi, T., Fabian, A. C., Canizares, C. R., Ikebe, Y., Makishima, K., Mushotzky, R. F., & Yamashita, K. 1994, PASJ, 46, L55

Furusho, T., Yamasaki, N. Y., & Ohashi, T. 2003, ApJ, 596, 181

Furusho, T., Yamasaki, N. Y., Ohashi, T. S. R., Kagei, T., Ishisaki, Y., Kikuchi, K., Ezawa, H., & Ikebe, Y. 2001, PASJ, 53, 421

Gehrels, N., & Williams, E. D. 1993, ApJL, 418, L25+

Governato, F., Tozzi, P., & Cavaliere, A. 1996, ApJ, 458, 18

Hayakawa, A. 2006, PhD thesis, Tyokyo Metropolitan Univ., (2006)

Hayakawa, A., Furusho, T., Yamasaki, N. Y., Ishida, M., & Ohashi, T. 2004, PASJ, 56, 743

Hayakawa, A., Hoshino, A., Ishida, M., Furusho, T., Yamasaki, N. Y., & Ohashi, T. 2006, PASJ, 58, 695

Helsdon, S. F., & Ponman, T. J. 2000, MNRAS, 319, 933

Hickson, P. 1982, ApJ, 255, 382

—. 1997, ARA&A, 35, 357

Ishisaki, Y., Maeda, Y., Fujimoto, R., Ozaki, M., Ebisawa, K., Takahashi, T., Ueda, Y., Ogasaka, Y., Ptak, A., Mukai, K., Hamaguchi, K., Hirayama, M., Kotani, T., Kubo, H., Shibata, R., Ebara, M., Furuzawa, A., Iizuka, R., Inoue, H., Mori, H., Okada, S., Yokoyama, Y., Matsumoto, H., Nakajima, H., Yamaguchi, H., Anabuki, N., Tawa, N., Nagai, M., Katsuda, S., Hayashida, K., Bamba, A., Miller, E. D., Sato, K., & Yamasaki, N. Y. 2006, ArXiv Astrophysics e-prints

Iwamoto, K., Brachwitz, F., Nomoto, K., Kishimoto, N., Umeda, H., Hix, W. R., & Thielemann, F.-K. 1999, ApJS, 125, 439

Jansen, F., Lumb, D., Altieri, B., Clavel, J., Ehle, M., Erd, C., Gabriel, C., Guainazzi, M., Gondoin, P., Much, R., Munoz, R., Santos, M., Schartel, N., Texier, D., & Vacanti, G. 2001, A&A, 365, L1

Jeltema, T. E., Canizares, C. R., Buote, D. A., & Garmire, G. P. 2003, ApJ, 585, 756

Jones, C., & Forman, W. 1984, ApJ, 276, 38

Kawahara, H. e. a. 2007, ApJ, 51, 301

Kikuchi, K., Furusho, T., Ezawa, H., Yamasaki, N. Y., Ohashi, T., Fukazawa, Y., & Ikebe, Y. 1999, PASJ, 51, 301

Kim, D.-W., & Fabbiano, G. 2004, ApJ, 613, 933

Kokubun, M., Makishima, K., Takahashi, T., Murakami, T., Tashiro, M., Fukazawa, Y., Kamae, T., Madejski, G. M., Nakazawa, K., Yamaoka, K., Terada, Y., Yonetoku, D., Watanabe, S., Tamagawa, T., Mizuno, T., Kubota, A., Isobe, N., Takahashi, I., Sato, G., Takahashi, H., Hong, S., Kawaharada, M., Kawano, N., Mitani, T., Murashima, M., Suzuki, M., Abe, K., Miyawaki, R., Ohno, M., Tanaka, T., Yanagida, T., Itoh, T., Ohnuki, K., Tamura, K., Endo, Y., Hirakuri, S., Hiruta, T., Kitaguchi, T., Kishishita, T., Sugita, S., Takahashi, T., Takeda, S., Enoto, T., Hirasawa, A., Katsuta, J., Matsumura, S., Onda, K., Sato, M., Ushio, M., Ishikawa, S., Murase, K., Odaka, H., Suzuki, M., Yaji, Y., Yamada, S., Yamasaki, T., & Yuasa, T. 2006, ArXiv Astrophysics e-prints

Koranyi, D. M., Geller, M. J., Mohr, J. J., & Wegner, G. 1998, AJ, 116, 2108

Koyama, K., Takano, S., & Tawara, Y. 1991, Nature, 350, 135

Koyama, K. e. a. 2007, PASJ, 28, 215

Kushino, A., Ishisaki, Y., Morita, U., Yamasaki, N. Y., Ishida, M., Ohashi, T., & Ueda, Y. 2002, PASJ, 54, 327

Lodders, K. 2003, ApJ, 591, 1220

Madau, P. 1999, in AIP Conf. Proc. 470: After the Dark Ages: When Galaxies were Young (the Universe at 2 Z 5), ed. S. Holt & E. Smith, 299–+

Makishima, K., Ezawa, H., Fukuzawa, Y., Honda, H., Ikebe, Y., Kamae, T., Kikuchi, K., Matsushita, K., Nakazawa, K., Ohashi, T., Takahashi, T., Tamura, T., & Xu, H. 2001, PASJ, 53, 401

Makishima, K., Tashiro, M., Ebisawa, K., Ezawa, H., Fukazawa, Y., Gunji, S., Hirayama, M., Idesawa, E., Ikebe, Y., Ishida, M., Ishisaki, Y., Iyomoto, N., Kamae, T., Kaneda, H., Kikuchi, K., Kohmura, Y., Kubo, H., Matsushita, K., Matsuzaki, K., Mihara, T., Nakagawa, K., Ohashi, T., Saito, Y., Sekimoto, Y., Takahashi, T., Tamura, T., Tsuru, T., Ueda, Y., & Yamasaki, N. Y. 1996, PASJ, 48, 171

Mamon, G. A. 1986, ApJ, 307, 426

Markevitch, M., Forman, W. R., Sarazin, C. L., & Vikhlinin, A. 1998, ApJ, 503, 77

Markevitch, M., Ponman, T. J., Nulsen, P. E. J., Bautz, M. W., Burke, D. J., David, L. P., Davis, D., Donnelly, R. H., Forman, W. R., Jones, C., Kaastra, J., Kellogg, E., Kim, D.-W., Kolodziejczak, J., Mazzotta, P., Pagliaro, A., Patel, S., Van Speybroeck, L., Vikhlinin, A., Vrtilek, J., Wise, M., & Zhao, P. 2000, ApJ, 541, 542

Matsushita, K. 1997, PhD thesis, Ph. D. thesis, Univ. Tokyo, (1997)

Matsushita, K., Böhringer, H., Takahashi, I., & Ikebe, Y. 2007, A&A, 462, 953

Matsushita, K., Finoguenov, A., & Böhringer, H. 2003, A&A, 401, 443

Matsushita, K., Fukazawa, Y., Hughes, J. P., Kitaguchi, T., Makishima, K., Nakazawa, K., Ohashi, T., Ota, N., Tamura, T., Tozuka, M., Tsuru, T. G., Urata, Y., & Yamasaki, N. Y. 2006, ArXiv Astrophysics e-prints

Mazzotta, P., Rasia, E., Moscardini, L., & Tormen, G. 2004, MNRAS, 354, 10

McCammon, D., Almy, R., Apodaca, E., Bergmann Tiest, W., Cui, W., Deiker, S., Galeazzi, M., Juda, M., Lesser, A., Mihara, T., Morgenthaler, J. P., Sanders, W. T., Zhang, J., Figueroa-Feliciano, E., Kelley, R. L., Moseley, S. H., Mushotzky, R. F., Porter, F. S., Stahle, C. K., & Szymkowiak, A. E. 2002, ApJ, 576, 188

Mewe, R., Gronenschild, E. H. B. M., & van den Oord, G. H. J. 1985, A&AS, 62, 197

Mewe, R., Lemen, J. R., & van den Oord, G. H. J. 1986, A&AS, 65, 511

Misaki, K., Kunieda, H., Maeda, Y., Haba, Y., Itoh, K., Mori, H., Iizuka, R., Itoh, A., Inoue, H., Okada, S., Yokoyama, Y., Ogasaka, Y., Tamura, K., Furuzawa, A., Shibata, R., Tanaka, T., Naitou, M., Ishida, M., Hayakawa, A., Inoue, C., Hayashi, A., Shimizu, T., Serlemitsos, P. J., Soong, Y., Chan, K.-W., Okajima, T., & Lehan, J. P. 2004, in Optics for EUV, X-Ray, and Gamma-Ray Astronomy. Edited by Citterio, Oberto; O'Dell, Stephen L. Proceedings of the SPIE, Volume 5168, pp. 294-305 (2004)., ed. O. Citterio & S. L. O'Dell, 294–305

Mitsuda, K. e. a. 2007, PASJ, 28, 215

Mori, H., Iizuka, R., Shibata, R., Haba, Y., Hayakawa, A., Hayashi, A., Inoue, C., Inoue, H., Ishida, M., Itoh, A., Itoh, K., Kunieda, H., Maeda, Y., Misaki, K., Naitou, M., Okada, S., Shimizu, T., & Yokoyama, Y. 2005, PASJ, 57, 245

Morita, U., Ishisaki, Y., Yamasaki, N. Y., Ota, N., Kawano, N., Fukazawa, Y., & Ohashi, T. 2006, PASJ, 58, 719

Morrison, R., & McCammon, D. 1983, ApJ, 270, 119

Mulchaey, J. S. 2000, ARA&A, 38, 289

Mulchaey, J. S., Davis, D. S., Mushotzky, R. F., & Burstein, D. 1996, ApJ, 456, 80

Mulchaey, J. S., & Zabludoff, A. I. 1998, ApJ, 496, 73

Nomoto, K., Thielemann, F.-K., & Yokoi, K. 1984, ApJ, 286, 644

Ohashi, T., Ebisawa, K., Fukazawa, Y., Hiyoshi, K., Horii, M., Ikebe, Y., Ikeda, H., Inoue, H., Ishida, M., Ishisaki, Y., Ishizuka, T., Kamijo, S., Kaneda, H., Kohmura, Y., Makishima, K., Mihara, T., Tashiro, M., Murakami, T., Shoumura, R., Tanaka, Y., Ueda, Y., Taguchi, K., Tsuru, T., & Takeshima, T. 1996, PASJ, 48, 157

Ota, N., Fukazawa, Y., Fabian, A. C., Kanemaru, T., Kawaharada, M., Kawano, N., Kelley, R. L., Kitaguchi, T., Makishima, K., Matsushita, K., Murase, K., Nakazawa, K., Ohashi, T., Sanders, J. S., Tamura, T., & Urata, Y. 2006, ArXiv Astrophysics e-prints

Ponman, T. J., Bourner, P. D. J., Ebeling, H., & Bohringer, H. 1996, MNRAS, 283, 690

Raassen, A. J. J., & Uylings, P. H. M. 1998, A&A, 340, 300

Renzini, A., Ciotti, L., D'Ercole, A., & Pellegrini, S. 1993, ApJ, 419, 52

Richstone, D., Loeb, A., & Turner, E. L. 1992, ApJ, 393, 477

Roettiger, K., Stone, J. M., & Mushotzky, R. F. 1998, ApJ, 493, 62

Sato, K., Furusho, T., Yamasaki, N. Y., Ishida, M., Matsushita, K., & Ohashi, T. 2005, PASJ, 57, 743

Serlemitsos, e. a. 2007, PASJ, 57, 743

Serlemitsos, P. J., Jalota, L., Soong, Y., Kunieda, H., Tawara, Y., Tsusaka, Y., Suzuki, H., Sakima, Y., Yamazaki, T., Yoshioka, H., Furuzawa, A., Yamashita, K., Awaki, H., Itoh, M., Ogasaka, Y., Honda, H., & Uchibori, Y. 1995, PASJ, 47, 105

Shaver, P. A., McGee, R. X., Newton, L. M., Danks, A. C., & Pottasch, S. R. 1983, MNRAS, 204, 53

Smith, R. K., Brickhouse, N. S., Liedahl, D. A., & Raymond, J. C. 2001, ApJL, 556, L91

Strickland, D. K., & Stevens, I. R. 2000, MNRAS, 314, 511

Takahashi, T. e. a. 2007, PASJ, 57, 743

Tamura, T., Kaastra, J. S., den Herder, J. W. A., Bleeker, J. A. M., & Peterson, J. R. 2004, A&A, 420, 135

Tamura, T., Kaastra, J. S., Makishima, K., & Takahashi, I. 2003, A&A, 399, 497

Tawara, Y. e. a. 2007, PASJ

Thielemann, F.-K., Nomoto, K., & Hashimoto, M.-A. 1996, ApJ, 460, 408

Tsujimoto, T., Nomoto, K., Yoshii, Y., Hashimoto, M., Yanagida, S., & Thielemann, F.-K. 1995, MNRAS, 277, 945

Turner, M. J. L., Reeves, J. N., Ponman, T. J., Arnaud, M., Barbera, M., Bennie, P. J., Boer, M., Briel, U., Butler, I., Clavel, J., Dhez, P., Cordova, F., Dos Santos, S., Ferrando, P., Ghizzardi, S., Goodall, C. V., Griffiths, R. G., Hochedez, J. F., Holland, A. D., Jansen, F., Kendziorra, E., Lagostina, A., Laine, R., La Palombara, N., Lortholary, M., Mason, K. O., Molendi, S., Pigot, C., Priedhorsky, W., Reppin, C., Rothenflug, R., Salvetat, P., Sauvageot, J., Schmitt, D., Sembay, S., Short, A., Strüder, L., Trifoglio, M., Trümper, J., Vercellone, S., Vigroux, L., Villa, G., & Ward, M. 2001, A&A, 365, L110

Vikhlinin, A., Markevitch, M., Murray, S. S., Jones, C., Forman, W., & Van Speybroeck, L. 2005, ApJ, 628, 655

Walke, D. G., & Mamon, G. A. 1989, A&A, 225, 291

Watanabe, M., Yamashita, K., Furuzawa, A., Kunieda, H., Tawara, Y., & Honda, H. 1999, ApJ, 527, 80

Wilms, J., Allen, A., & McCray, R. 2000, ApJ, 542, 914

Xu, H., Ezawa, H., Fukazawa, Y., Kikuchi, K., Makishima, K., Ohashi, T., & Tamura, T. 1997, PASJ, 49, 9

Yamasaki, N. Y., Ohashi, T., & Furusho, T. 2002, ApJ, 578, 833

Yan, M., Sadeghpour, H. R., & Dalgarno, A. 1998, ApJ, 496, 1044

Yoshikawa, K., Dolag, K., Suto, Y., Sasaki, S., Yamasaki, N. Y., Ohashi, T., Mitsuda, K., Tawara, Y., Fujimoto, R., Furusho, T., Furuzawa, A., Ishida, M., Ishisaki, Y., & Takei, Y. 2004, PASJ, 56, 939

Yoshikawa, K., Yamasaki, N. Y., Suto, Y., Ohashi, T., Mitsuda, K., Tawara, Y., & Furuzawa, A. 2003, PASJ, 55, 879

Zabludoff, A. I., & Mulchaey, J. S. 2000, ApJ, 539, 136

Acknowledgement

First of all, I would like to express my best gratitude to Prof. T. Ohashi for his continuous support, leading and encouragement throughout the five years of my graduate course. I also grateful to Prof. N. Y. Yamasaki for her constructive discussions and cooperations. I also deeply appreciate Dr. Y. Ishisaki for his powerful support on technical process, data analysis and experiments. I am so much obliged to Prof. M. Ishida, Prof. N. Ariomoto, Prof. K. Masai, Dr. S. Sasaki, and Dr. K. Matsushita for valuable comments and suggestions.

I am also deeply grateful to Dr. T. Furusho, Dr. N. Ota, Dr. T. Oshima, Dr. A. Hayakawa, Dr. K. Shinozaki, Dr. Y. Takei, and Dr. U. Morita. They encouraged me to finish this work with useful advice, discussions on analysis methods and experiments.

I wish to thank all the members, past and present of our laboratory: Mr. T. Ishikawa, Mr. C. Inoue, Mr. T. Koga, Mr. A. Hoshino, Mr. S. Okuma, Mr. Y. Yamakawa, Mr. T. Fujimori, Mr. H. Kurabayashi, Mr. R. Kubota, Mr. M. Suzuki, Mr. T. Osawa and Ms. K. Tokoi.

Finally, I thank my parents and friends for their hearty support and encouragement.